SANDIA REPORT

SAND2007-0059
Unlimited Release
Printed January 2007

Recyclable Transmission Line (RTL) and Linear Transformer Driver (LTD) Development for Z-Pinch Inertial Fusion Energy (Z-IFE) and High Yield

Craig L. Olson, Michael G. Mazarakis, William E. Fowler, Robin A. Sharpe,
David L. Smith, Matthew C. Turgeon, William L. Langston, Timothy D. Pointon,
Paul F. Ottinger, Joseph W. Schumer, Dale R. Welch, David V. Rose,
Thomas C. Genoni, Nicki L. Bruner, Carsten Thoma, Mark E. Barkey,
Michael Guthrie, Daniel C. Kammer, Gerald L. Kulcinski, Yuri G. Kalinin,
Alexander S. Kingsep, Sergei L. Nedoseev, Valentin P. Smirnov,
and Alexander Kim

Prepared by
Sandia National Laboratories
Albuquerque, New Mexico 87185 and Livermore, California 94550

Sandia is a multiprogram laboratory operated by Sandia Corporation,
a Lockheed Martin Company, for the United States Department of Energy's
National Nuclear Security Administration under Contract DE-AC04-94AL85000.

Sandia National Laboratories

Issued by Sandia National Laboratories, operated for the United States Department of Energy by Sandia Corporation.

Printed in the United States of America. This report has been reproduced directly from the best available copy.

Available to DOE and DOE contractors from
U.S. Department of Energy
Office of Scientific and Technical Information
P.O. Box 62
Oak Ridge, TN 37831

Telephone: (865) 576-8401
Facsimile: (865) 576-5728
E-Mail: reports@adonis.osti.gov
Online ordering: http://www.osti.gov/bridge

Available to the public from
U.S. Department of Commerce
National Technical Information Service
5285 Port Royal Rd.
Springfield, VA 22161

Telephone: (800) 553-6847
Facsimile: (703) 605-6900
E-Mail: orders@ntis.fedworld.gov
Online order: http://www.ntis.gov/help/ordermethods.asp?loc=7-4-0#online

SAND2007-0059
Unlimited Release
Printed January 2007

Recyclable Transmission Line (RTL) and Linear Transformer Driver (LTD) Development for Z-Pinch Inertial Fusion Energy (Z-IFE) and High Yield

Craig L. Olson[1], Michael G. Mazarakis[1], William E. Fowler[1], Robin A. Sharpe[1],
David L. Smith[1], Matthew C. Turgeon[1], William L. Langston[1],
Timothy D. Pointon[1], Paul F. Ottinger[2], Joseph W. Schumer[2], Dale R. Welch[3],
David V. Rose[3], Thomas C. Genoni[3], Nicki L. Bruner[3], Carsten Thoma[3],
Mark E. Barkey[4], Michael Guthrie[5], Daniel C. Kammer[5], Gerald L. Kulcinski[5],
Yuri G. Kalinin[6], Alexander S. Kingsep[6], Sergei L. Nedoseev[6],
Valentin P. Smirnov[6], and Alexander Kim[7]

[1] Sandia National Laboratories, Albuquerque, NM
[2] Naval Research Laboratory, Washington, DC
[3] Voss Scientific, Albuquerque, NM
[4] University of Alabama, Tuscaloosa, AL
[5] University of Wisconsin, Madison, WI
[6] Kurchatov Institute, Moscow, Russia
[7] High Current Electronics Institute, Tomsk, Russia

Abstract

Z-Pinch Inertial Fusion Energy (Z-IFE) complements and extends the *single-shot* z-pinch fusion program on Z to a *repetitive*, high-yield, power plant scenario that can be used for the production of electricity, transmutation of nuclear waste, and hydrogen production, all with no CO_2 production and no long-lived radioactive nuclear waste. The Z-IFE concept uses a Linear Transformer Driver (LTD) accelerator, and a Recyclable Transmission Line (RTL) to connect the LTD driver to a high-yield fusion target inside a thick-liquid-wall power plant chamber.

Results of RTL and LTD research are reported here, that include: (1) The key physics issues for RTLs involve the power flow at the high linear current densities that occur near the target (up to 5 MA/cm). These issues include surface heating, melting, ablation, plasma formation, electron flow, magnetic insulation, conductivity changes, magnetic field diffusion changes, possible ion flow, and RTL mass motion. These issues are studied theoretically, computationally (with the ALEGRA and LSP codes), and

will work at 5 MA/cm or higher, with anode-cathode gaps as small as 2 mm. (2) An RTL misalignment sensitivity study has been performed using a 3D circuit model. Results show very small load current variations for significant RTL misalignments. (3) The key structural issues for RTLs involve optimizing the RTL strength (varying shape, ribs, etc.) while minimizing the RTL mass. Optimization studies show RTL mass reductions by factors of three or more. (4) Fabrication and pressure testing of Z-PoP (Proof-of-Principle) size RTLs are successfully reported here. (5) Modeling of the effect of initial RTL imperfections on the buckling pressure has been performed. Results show that the curved RTL offers a much greater buckling pressure as well as less sensitivity to imperfections than three other RTL designs. (6) Repetitive operation of a 0.5 MA, 100 kV, 100 ns, LTD cavity with gas purging between shots and automated operation is demonstrated at the SNL Z-IFE LTD laboratory with rep-rates up to 10.3 seconds between shots (this is essentially at the goal of 10 seconds for Z-IFE). (7) A single LTD switch at Tomsk was fired repetitively every 12 seconds for 36,000 shots with no failures. (8) Five 1.0 MA, 100 kV, 100 ns, LTD cavities have been combined into a voltage adder configuration with a test load to successfully study the system operation. (9) The combination of multiple LTD coaxial lines into a tri-plate transmission line is examined. The 3D Quicksilver code is used to study the electron flow losses produced near the magnetic nulls that occur where coax LTD lines are added together. (10) Circuit model codes are used to model the complete power flow circuit with an inductive isolator cavity. (11) LTD architectures are presented for drivers for Z-IFE and high yield. A 60 MA LTD driver and a 90 MA LTD driver are proposed.

Present results from all of these power flow studies validate the whole LTD/RTL concept for single-shot ICF high yield, and for repetitive-shot IFE.

Acknowledgments

We would like to acknowledge Rick Stulen (V.P. 1000) for his strong support of this Laboratory Directed Research and Development Project 101817 on Z-IFE.

Contents

Figures

Tables

(This page intentionally left blank.)

Recyclable Transmission Line (RTL) and Linear Transformer Driver (LTD) Development for Z-Pinch Inertial Fusion Energy (Z-IFE) and High Yield

1.0 Introduction *(C. L. Olson, SNL)*

Z-Pinch Inertial Fusion Energy (Z-IFE) complements and extends the single-shot z-pinch fusion program on Z to a repetitive, high-yield, power plant scenario that can be used for the production of electricity, transmutation of nuclear waste, hydrogen production, desalination of water, etc., all with no CO_2 production and no long-lived radioactive nuclear waste. Initial research (supported by Congressional Initiative in FY04 and FY05) has addressed critical issues and led to acceptance of Z-IFE by the broader fusion community. This Report presents new results on Z-IFE obtained by FY06 SNL LDRD support.

The z-pinch approach to IFE is the newest of the three major approaches to IFE. Z-IFE began about seven years ago, and has played a major role in IFE at the 1999 Snowmass Fusion Summer Study, the IAEA Cooperative Research Project on IFE Power Plants, the 2002 Snowmass Fusion Summer Study, the Fusion Energy Sciences Advisory Committee (FESAC) 35-year Plan Panel Report (2003), and the FESAC IFE Panel Report (2003). A comprehensive publication on Z-IFE includes 93 references describing the initial development of Z-IFE [1]. Reports on extensive results obtained in FY04, FY05, and beyond are now available [2-4].

The goal of Z-IFE is to extend the *single-shot* z-pinch Inertial Confinement Fusion (ICF) results on Z to a *repetitive-shot* z-pinch power plant concept for the economical production of electricity, and other applications. The Recyclable Transmission Line (RTL) is key to this concept [5]. The RTL is made from a solid coolant (e.g., Flibe) or a material that is easily separable from the coolant (e.g., carbon steel). The later is the present preferred choice for z-pinch IFE. As shown in Figure 1.1, the RTL would enter the chamber through a single hole at the top of the chamber (~1 meter radius), and extend into the chamber a distance of two or more meters. The RTL would bend at the top of the chamber, and upper shielding would be placed above it. In operation, the RTL/target assembly is inserted, the shot is fired, portions of the RTL are vaporized and end up mixed with the coolant to be recycled, the upper remnant of the RTL is removed, and the cycle is repeated. The present strategy for Z- IFE is to use high-yield targets (~3 GJ/shot) and low repetition rate per chamber (~0.1 Hz). Initial experiments at the 10 MA level on Saturn have been successfully used to study the electrical current initiation in the RTL, the RTL low-mass limit, and the RTL electrical conductivity.

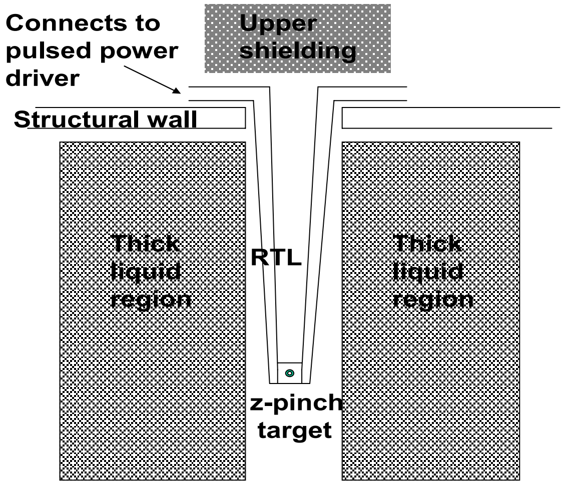

Figure 1.1. The Recyclable Transmission Line (RTL) concept for Z-IFE.

The Z-IFE concept uses a thick liquid wall chamber. The coolant (typically Flibe - a binary salt) is used to absorb the neutron energy, breed tritium, and shield the structural wall from neutrons. Present neutronics studies indicate 40 year wall lifetimes are possible now. Thick liquid walls essentially eliminate the "first wall problem" (which is common to all magnetic fusion schemes and dry-wall IFE schemes) and leads to a faster development path for fusion energy. No new neutron test facilities are required.

The Z-IFE concept uses a Linear Transformer Driver (LTD) accelerator, and a Recyclable Transmission Line (RTL) to connect the LTD driver to a high-yield fusion target inside a thick-liquid-wall power plant chamber. This Report investigates power flow issues in the LTD driver, the intermediate adder/transmission lines, and the RTL. All of these issues are also applicable to a single-shot Inertial Confinement Fusion (ICF) high-yield fusion facility, as is envisioned by SNL. This research is vital to producing a credible, cost-effective, path to high yield and IFE.

RTL Research in this FY06 LDRD Report:

The key physics and engineering issues for RTLs continue to be investigated. The key *physics issues* for RTLs are the power flow issues at the high linear current densities that occur near the target (up to 5 MA/cm). These issues include surface heating, melting, ablation, plasma formation, electron flow, magnetic insulation, conductivity changes, magnetic field diffusion changes, possible ion flow, and RTL mass motion. These issues are being studied theoretically, computationally (with the ALEGRA and LSP codes), and experimentally (at the Kurchatov Institute, Moscow). The key *engineering issues* for RTLs involve optimum structural design with sufficient structural strength with low mass; fabrication; and pressure testing. RTL results in all of these areas are included in this Report.

In addition to RTLs, this LDRD has investigated Linear Transformer Driver (LTD) technology. LTD technology is very different than the Marx generator/water line technology used on Z/ZR. Marx generators and pulse forming lines are eliminated altogether. In the LTD concept, a series of compact, low-inductance, capacitors are charged directly in parallel, in a cylindrical formation, at a moderate voltage (~100 kV). A series of switches next to the capacitors, and in the same cylindrical formation, switches the charged capacitors directly to apply voltage to a single, inductively-isolated gap. By proper selection of compact, low inductance capacitors, pulse lengths of the order of 100 ns can be achieved directly - and this is the typical pulse length desired to drive a z-pinch fusion target. To reach higher voltages, a series of modules is stacked into an inductive voltage-adder configuration. The LTD concept was pioneered at the High Current Electronics Institute (HCEI) in Tomsk, Russia.

LTDs are well-suited for repetitive operation. For z-pinch IFE, a repetitive LTD is needed, with about 10 seconds between shots.

LTD Research in this FY06 LDRD Report:

This LDRD has investigated repetitive operation with LTD cavities at the 0.5 MA level, and voltage adding with multiple cavities at the 1 MA level. Repetitive switching operation, electrode erosion effects, and heating effects due to the high average power, are issues that are being addressed. The complete power flow includes the LTD driver, the intermediate adder/transmission lines, and the RTL. Particle-in-cell codes have been used to study the electron flow losses produced near the magnetic nulls that occur when coax LTD lines are added together. Circuit model codes have been used to model the complete power flow circuit. LTD architectures have been proposed for drivers for high yield and for IFE.

All of the goals proposed for this FY06 LDRD have been exceeded:

Goal 1: Operate 0.5 MA LTD cavity at SNL repetitively at up to once every 25 seconds for 1000 shots or more.

Results: At SNL, this 0.5 MA cavity has been fired in repetitive mode for ~3000 shots; the last set of 50 shots with one shot every 10.25 seconds (~0.1 Hz) - we are already at the desired goal of 0.1 Hz for Z-IFE. At HCEI, Tomsk, a single switch has been fired 37,000 shots with one shot every 12 seconds (~0.08 Hz)

Goal 2: Combine four SNL LTD 1.0 MA cavities at HCEI, Tomsk, Russia to produce a 400 kV, 1 MA pulse to a load.

Results: Five 1 MA LTD cavities (four belong to SNL and one belongs to U. Michigan) have been successfully tested in a voltage-adder configuration at HCEI, Tomsk.

Goal 3: Perform detailed study of the power flow in an RTL near the load at high linear current densities (up to 5 MA/cm).

Results: Analytic results, code simulation results (LSP and other codes), and experiments have been used to study power flow at high linear current densities above 5 MA/cm.

Goal 4: Propose LTD architectures for drivers for high yield and for IFE.

Results: Two LTD architectures have been proposed: A 60 MA LTD driver with one layer of LTDs, and a 90 MA LTD driver with multiple layers of LTDs.

Goal 5: Develop and use circuit model codes and particle-in-cell codes to study power flow from the LTD driver, to the intermediate adder/transmission lines, to the RTL, to the load.

Results: Quicksilver simulations have been used to study electron losses at the magnetic nulls that occur where LTD driven coax lines add together at the entrance to a flat tri-plate transmission line. Circuit codes have been used to assess the complete circuit operation (driver, RTL, load).

Results from all of these power flow studies validate the whole LTD/RTL concept for single-shot ICF high yield, and for repetitive-shot IFE.

In the following, RTL results are presented in Section 2; LTD results are presented in Section 3; and conclusions are presented in Section 4.

2.0 Recyclable Transmission Line (RTL)

(C. L. Olson, SNL)

There are many physics and engineering tradeoffs in optimizing RTL operation. A brief listing of several of these tradeoffs, together with the current mainline choice of parameters (given in red) is as follows:

RTL gap size: as small as possible to minimize RTL inductance; as large as possible to minimize potential electron, ion, and plasma issues (minimum gap 2 mm or larger)

RTL material: electrical conductivity, structural properties, low activation, interaction with coolant, recycling, etc. (carbon steel or frozen Flibe)

RTL mass: movement, size/cost of recycle plant, total inventory mass, etc. (32 kg)

RTL radius at top: minimum inductance, vacuum and electrical connections, minimal hole into chamber, etc. (100 cm for power plant)

RTL radius at bottom: about target radius, ~ 2- 5 cm. (5 cm for power plant)

RTL length: long for blast, short for inductance, affects voltage requirement of driver, etc. (200 – 500 cm for power plant)

RTL shape: Quickly flare to large radius from the target: best for low inductance
Flare like a trumpet from the target: best for structural strength
(using conical RTL for now)

RTL interface with power flow: many LTD modules (coax), to triplate, to biplate, to connection with RTL (using biplate to coax RTL for now)

The actual RTL sizes that are being considered are summarized in Figure 2.1. Test RTLs have been fabricated and pressure tested. Z-PoP RTLs have been fabricated and pressure tested (results included in this Report).

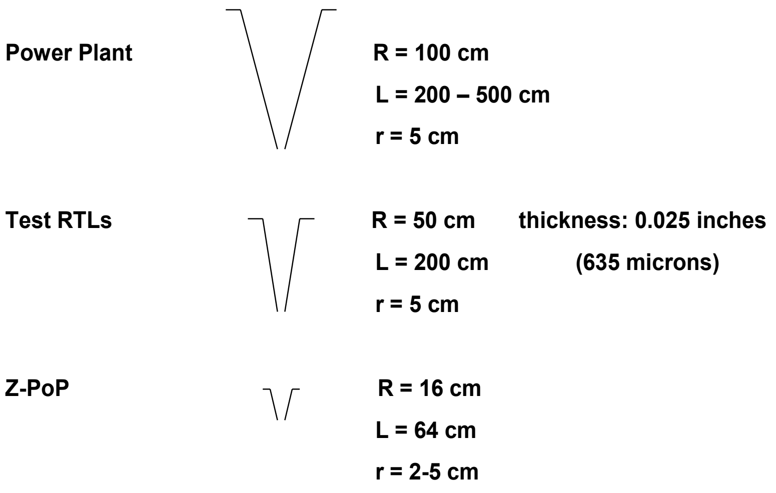

Figure 2.1. RTL sizes.

In the following sections, summaries of research are given on:

2.1 Self-consistent magnetically-insulated power flow in RTLs.
2.2 Plasma effects in power flow in an RTL near a Z-pinch load.
2.3 LSP simulations of RTL power flow in the presence of plasma.
2.4 Experiments at high linear current densities to study potential RTL power flow loss mechanisms.
2.5 RTL misalignment sensitivity study using a 3D circuit model.
2.6 RTL structural analysis, fabrication, and pressure testing of Z-PoP RTLs.
2.7 Modeling the effect of initial RTL imperfections on the RTL bucking pressure.

2.1 Self-Consistent Magnetically-Insulated Power Flow in RTLs [6] *(P. F. Ottinger and J. W. Schumer, NRL)*

This report documents FY06 work studying power flow in the recyclable transmission line (RTL) of a z-pinch driven inertial fusion energy (IFE) system [1,7]. The RTL is a conical magnetically insulated transmission line (MITL) [8] that connects the pulsed power driver to the inertial confinement fusion (ICF) target in the center of the reactor chamber. The RTL is illustrated in Figure 2.2. Electrons emitted from the cathode are magnetically insulated [9-14] from crossing the anode-cathode (AK) gap and flow axially in the direction of power flow as illustrated in Figure 2.3. A low MITL impedance is advantageous for a z-pinch IFE system as it minimizes the inductance between the driver and the load; thus, the voltage generated by dI/dt (required to drive the z-pinch) is minimized [15]. The effective impedance of the MITL is described best by the flow impedance Z_f, which is a function of both the geometry and the voltage [16-24] and is less than the vacuum impedance of the line Z_0 because of the distributed electron current. Additionally, high current resistively heats the electrode surfaces; when the anode surface is heated above T = 400° C [25-30], ions are emitted. Ions are emitted where the RTL radius is smallest and the current density is highest (and therefore the heating is strongest); thus, ion emission starts at the load end of the RTL and gradually expands up the line as the anode continues to heat during the pulse. Ions emitted from the anode affect the power flow near the end of the pulse, resulting in a loss current and causing addition electron emission and flow current [31]. Although ion losses are expected, good power flow coupling can still be achieved as evidenced on the Z machine at SNL where the current density near the load is comparable to that expected here [32]. This ion current can be magnetically insulated as well if the voltage is low enough and the total current and RTL gap are large enough [33]. Magnetically insulated ion flow is illustrated in Figure 2.4. In Figures 2.3 and 2.4, I_c and I_a are the currents that flow in the cathode and anode, respectively, and $I_f = I_a - I_c$ is the current in the particle flows. The purpose of this work is to first determine the effect of ion emission on power flow in a RTL coupled to a time-varying inductance and then use this insight to specify RTL design parameters that both satisfy the overall system constraints and deliver the required power for a z-pinch-driven IFE reactor.

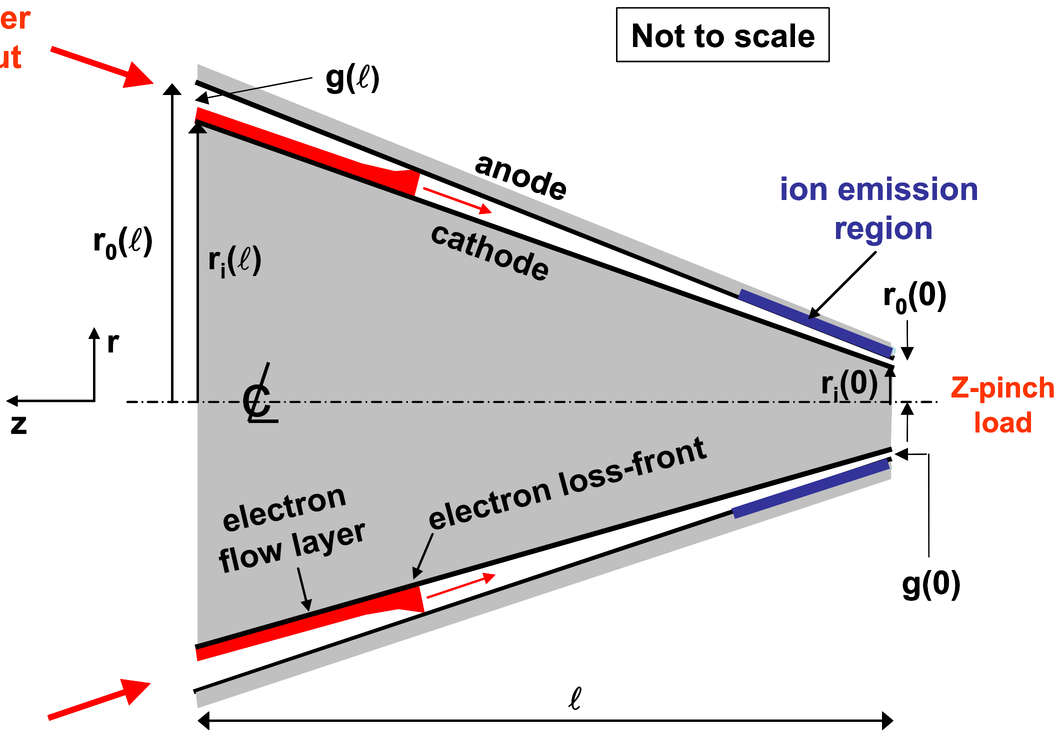

Figure 2.2. Schematic of the conical RTL showing the baseline design. Power is fed in from the left and the load is connected to the right end of the line.

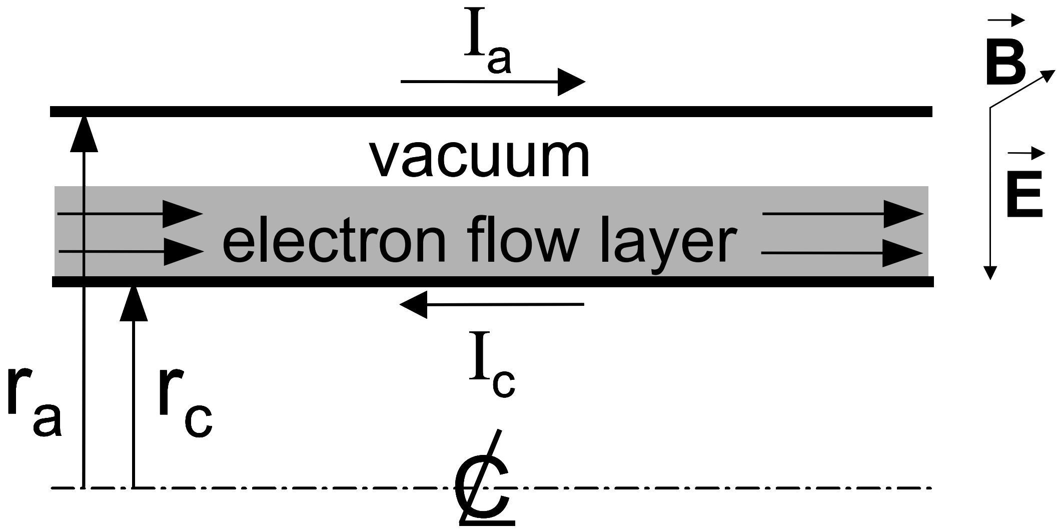

Figure 2.3. Schematic of electron MITL flow in negative polarity (i.e., the cathode is the center conductor).

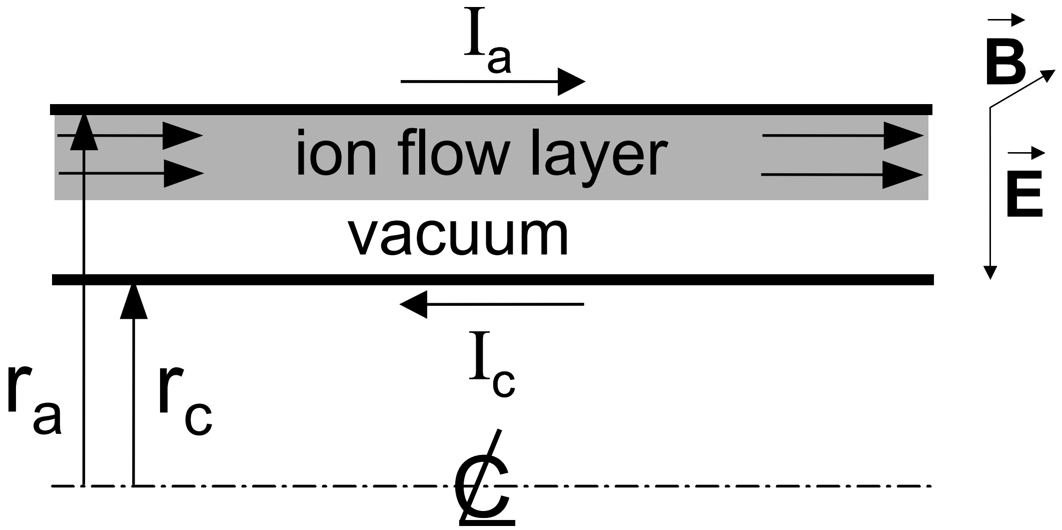

Figure 2.4. Schematic of ion MITL flow in negative polarity (i.e., the cathode is the center conductor).

2.1.1 RTL Power Flow Optimization including Electrons and Ions

Previous work has demonstrated that ion emission at the load end of the RTL can seriously degrade the z-pinch implosion if the gap at the load end of the RTL is too small. In the absence of ion emission, the condition for load-limited operation of the line can be used to determine the impedance of the RTL required for maintaining magnetic insulation of the electron flow. For example, if the load voltage and current at the end of the full z-pinch implosion shown are 40 MV and 45 MA, respectively, this condition yields $V/I_a \leq 0.9Z_f^{SL}$, implying that $Z_0 \geq 1.09\ \Omega$ (where $Z_f^{SL} \sim 0.9Z_0$ at 40 MV)[19]. This vacuum line impedance corresponds to g(0) = 1 mm for the baseline RTL with r(0) = 5 cm. With ion emission, however, a gap of g(0) > 2 mm was found to be necessary to reduce ion current losses to a tolerable level. But, with this larger impedance, the inductance of the RTL is increased driving up the voltage at the driver end of the RTL. In order to maintain a reasonable voltage, this leads to using a variable impedance RTL. Here, the impedance at the load end of the RTL is larger than at the driver end, so that the RTL inductance is kept at an acceptable value to control the voltage at the driver end, while ion current losses at the load end of the RTL are controlled as well. However, an increasing MITL impedance can lead to electron flow losses. Thus, the design of the optimal RTL requires controlling both electron and ion losses while achieving an acceptable RTL inductance.

There are three distinct phases of the power delivery to the z-pinch load: the *run-down* phase, the *short-circuit* phase, and the *implosion* phase. The run-down and short-circuit phases were initially studied in FY04 [34]. During the run-down phase, self-limited electron MITL flow is established and power propagates down the line to the load. Once the power reaches the load (initially a short circuit), a re-trapping wave propagates back up the line lowering the voltage and driving the flow impedance up toward super-insulated flow [23,35]. The arrival of the re-trapping wave indicates the beginning of the short-circuit phase.

This re-trapping wave moves backward at about 0.85c, quickly limiting the voltage and driving most of the electron flow current back into the cathode. However, some of the electrons that were emitted to establish self-limited flow during the run-down phase form circulating clumps or vortices that drift slowly downstream toward the load and persist through the short-circuit phase. These charge clumps do account for a small flow current and remain as space charge in the line for a long time. Consequently, the transient flow impedance calculated from the PIC simulation does not rise instantaneously toward Z_0 near the load end and, in fact, actually drops for a while until the excess charge can clear from the line. This leads to a discrepancy between the Z_f predicted by an equilibrium MITL model and that observed in the simulations even well after 30 ns into the run, particularly near the load. Although the MITL flow model significantly overestimates Z_f, the error in predicting I_c is small because the voltage has been driven down. Eventually this space charge does clear the system and Z_f approaches Z_0 along the entire line.

During the run-down and short-circuit phase the current resistively heats the anode, ultimately forming an anode plasma at the small-radius load end of the RTL when the temperature threshold is exceeded. Ions are emitted from this anode plasma in a space-charged-limited (SCL) fashion with the emission expanding up the line in time as more of the anode surface exceeds the ion turn-on temperature threshold. Once the z-pinch implosion causes a significant dL/dt voltage to develop, the short-circuit phase ends and the implosion phase begins. This voltage increase leads to additional electron emission and flow current as well as a decrease in Z_f. Simultaneously, the increase in emitted ion space further enhances the electron emission and flow current along the RTL where ion emission occurs.

The initial FY06 work carried out at the beginning of the year involved completing the analysis of simulations done in FY05. This work is documented in Ref. 36. Because a self-consistent z-pinch load model was not available at the time, a simplified load model was used that limited the study to constant impedance RTLs. The accuracy of this model also degraded as the ion loss current increased, making the results with large ions loss currents only qualitatively correct. In spite of these shortcomings, a qualitative picture of RTL performance was obtained.

A summary of the results present in Ref. 36 is now provided. This work showed that the ion current could become insulated during the short-circuit phase but generally that ion insulation will be lost when the voltage increases during the z-pinch implosion phase. This is illustrated in Figure 2.5, which compares magnetically insulated flow theory [33] with data from two of the simulations in Ref. 36, showing that ion insulation is marginal at best until the gap at the load end of the RTL, g(0), is larger than about 4 mm.

Although there is some ion current flow into the load region in the simulations, there are significant ion current losses in the RTL, particularly for the case with a 1-mm gap at the end of the RTL. During the short-circuit phase, these ion current losses are modest but are enhanced by transit time voltage fluctuations in the line and by residual electron space charge clumps in the line (generated by the retrapping wave during the short-circuit phase). Significant ion current losses occur during the implosion phase when the increasing inductance of the z-pinch load drives the voltage up.

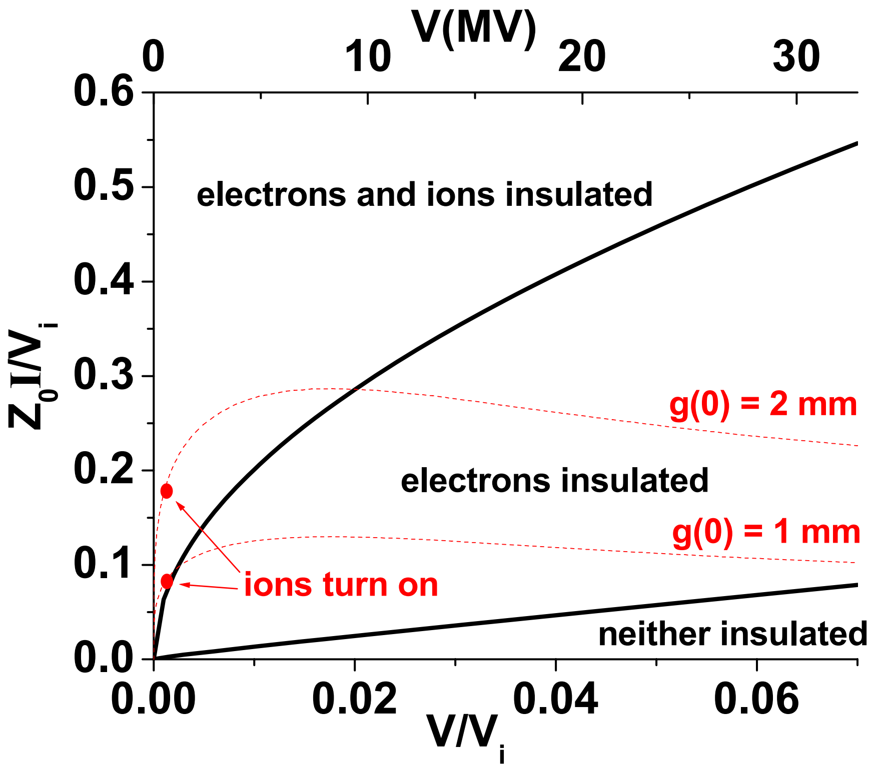

Figure 2.5. Plot of $Z_0I_1^{SL}/V_{0i}$ vs V/V_{0i} for electrons and ions with $g_i = g_e = 1$ showing regions where insulated flow applies for each species as discussed in Ref. 31. I_1 is the total current. The dotted curves are from constant impedance simulations in Ref. 34 for g(0) = 1 and 2 mm.

The electron space charge in the gap is also enhanced by the presence of ions in the gap. On the other hand, once electron flow is established in the RTL it remains well insulated in these simulations, even in the presence of ions and during the z-pinch implosion phase. Electron MITL theory predicts electron insulation can be maintained up to voltage levels that are above the levels reached in these simulations. However, when the impedance of the RTL is small enough that the effective impedance of the imploding load approaches the electron self-limited impedance of the line, large electron flow current is launched during the implosion phase and electron flow current losses can occur if the RTL transitions to the line-limited regime. For the baseline designs considered in these simulations, this occurs when the gap at the load end of the RTL is < 2 mm.

When the g(0) = 1 mm, results indicate that significant ion loss currents and flow currents (both ions and electrons) are generated in this constant-impedance RTL geometry. In spite of this, the load current is only marginally reduced from the full z-pinch current assumed in the z-pinch load model. However, the questions that remain are (a) whether the flow currents that enter the load region couple to the implosion or represent a reduction in the current driving the z-pinch implosion, and (b) whether the flow currents disrupt the z-pinch dynamics in any manner. If only the bound current drives the z-pinch load and the flow currents do not participate, then this introduces a polarity effect with significantly more current flowing in the anode than the cathode. These questions could not be addressed here but will be studied in the future.

When the gap at the load end of the RTL is increased from 1 mm to 2 mm, the ion loss currents and ion and electron flow currents are significantly reduced. In this case, the load current is also nearly equal to the full z-pinch current assumed in the z-pinch load model; however, the load voltage is suppressed by the parallel load impedance presented by the ion loss current. Although the questions raised above concerning the flow currents entering the load region still remain, these issues are greatly alleviated because the current flowing into the load region is greatly reduced with this larger gap. Continuing to increase the gap will further mitigate these issues but must be balanced against the impact of increasing the RTL inductance. Overall, this was a very encouraging result but it needed to be confirmed using the more accurate self-consistent z-pinch load model described below.

These results indicate that gaps at the end of the RTL of < 2 mm will be problematic, both in terms of ion loss current and launched ion and electron flows that enter the load region. Gap closure, which was not addressed, will also be more worrisome for smaller gaps. All of these concerns are mitigated by using a gap of ≥ 2 mm. However, the RTL inductance is limited by constraints on the driver voltage required to achieve the 60 MA z-pinch current in 100 ns. Based on a minimum AK gap of 2 mm at the load end of the RTL and an inductance limit for the RTL of about 10 nH, an acceptable RTL can easily be designed with a length of up to about 5 m, provided the RTL impedance is allowed to vary along its length. The minimum inductance RTL would have a constant gap rather than constant impedance. However, electron flow in the RTL may be disrupted if the impedance of the RTL varies too rapidly along its length. This issue is addressed below. A shorter length RTL allows for a larger AK gap at the load end of the RTL, which will further reduce concerns about ion loss current, ion and electron flows launched into the load region, and gap closure; however, the shortness of the RTL is constrained by other system design issues such as the chamber size required to confine the IFE target explosion.

The remainder of this work describes results from new simulations carried out in FY06 which addresses these concerns. A new self-consistent z-pinch load model is developed here and is coupled to a particle-in-cell simulation to study power flow in a recyclable transmission line (RTL) for a z-pinch-driven inertial fusion energy (IFE) system. This self-consistent model allows for the treatment of variable impedance transmission lines, which provides the flexibility to choose an appropriate inductance for the RTL in matching to the overall IFE system. In addition, the simulations are driven by a voltage wave appropriate for the IFE target implosion when there is no particle emission from the walls of the RTL. When models for both electron and ion emission from the RTL walls are included in the simulations, results indicate the effect of particle emissions on power coupled to the load. The combination of the self-consistent load model, this new driver model, and the particle emission models provides a considerably more accurate simulation of RTL power flow than previously available. In particular, quantitative insight is obtained for designing an efficient IFE system which satisfies system constraints on RTL inductance and driver voltage.

2.1.2 Summary of LSP Simulations of RTL Power Flow including Electrons and Ions

This section documents FY06 work studying power flow in the recyclable transmission line (RTL) of a z-pinch driven inertial fusion energy (IFE) system. The purpose of this work is to first determine the effect of ion emission on power flow in a RTL coupled to a time-varying inductance and then use this insight to specify RTL design parameters that both satisfy the overall system constraints and deliver the required power for a z-pinch-driven IFE reactor. Previous work has demonstrated that ion emission at the load end of the RTL can seriously degrade the z-pinch implosion if the gap at the load end of the RTL is too small. In the absence of ion emission, the condition for load-limited operation of the line can be used to determine the impedance of the RTL required for maintaining magnetic insulation of the electron flow. For example, if the load voltage and current at the end of the full z-pinch implosion are 40 MV and 45 MA, respectively, this condition yields $V/I_a \leq 0.9Z_f^{SL}$, implying that $Z_0 \geq 1.09\ \Omega$ (where $Z_f^{SL} \sim 0.9Z_0$ at 40 MV). This vacuum line impedance corresponds to g(0) = 1 mm for the baseline RTL with r(0) = 5 cm. However, resistive heating of the anode during the run-down and short-circuit phase of the z-pinch implosion cause anode plasma formation and ion emission at the load end of the RTL where the current density is large. This emitting region expands up the RTL during the implosion phase ultimately turning on about 30 cm of the anode. With ion emission, a gap of g(0) > 2 mm was found to be necessary to reduce ion current losses to a tolerable level. But, with this larger impedance, the inductance of the RTL is increased, driving up the voltage at the driver end of the RTL. In order to maintain a reasonable voltage, a variable impedance RTL is needed where the impedance at the load end of the RTL is larger than at the driver end. Thus, the RTL inductance is kept at an acceptable value to control the voltage at the driver end, while ion current losses at the load end of the RTL are controlled by maintaining a gap of > 2 mm at the load end of the RTL. However, an RTL with an impedance that increases along its length, which is considered a *bad transition* in MITL flow theory, can lead to electron flow current losses. Thus, the design of the optimal RTL requires controlling both electron and ion losses while achieving an acceptable RTL inductance.

In order to obtain a quantitative assessment of this problem, a self consistent z-pinch load model was implemented in LSP [37,38] along with an ion emission turn-on model based on resistive heating along the anode. Five different cases were considered, each driving a z-pinch implosion to a compression ratio of 10 in 100 ns when no electron or ion emission was allowed. Appropriate forward-going voltage waveforms for driving the system were established using the BERTHA transmission line model [39]. Three LSP simulations are run for each case: the first with no particle emission, the second with only electron emission, and the third with electron and ion emission. All three simulations for a given case use the same driver and load parameters determined from the BETRHA simulation for that case so that contrasting the results shows the effect of the particle emissions.

The parameters for the simulations are listed in Table 2.1 along with a summary of the results. Case A uses the same parameters as those in the baseline case of Ref. [36] in order to compare with those results. The RTL has a constant impedance. Results from this case demonstrate the efficacy of the new models and illustrates some of the shortcomings of the models used previously in Ref. [36]. Case B looks at power flow in a constant-gap RTL. These results are contrasted with Case A and dramatically show how magnetic insulation of the electron flow can be disrupted when the impedance varies too rapidly along the RTL. Case C is a compromise between the constant-impedance RTL and the constant-gap RTL of Cases A and B. The gap at the load end of the RTL is

Table 2.1. Summary of simulation parameters and results. Each simulation is labeled by its case followed by "v" for vacuum (i.e., no electron or ion emission), "e" for electron emission only, or "ei" for electron and ion emission. Also, $g(0)$ and $g(\ell)$ are the gaps at the load and driver ends of the RTL, $Z(0)$ and $Z(\ell)$ are the impedances at the load and driver ends of the RTL, L is the RTL inductance, V_{1p} is the peak voltage at the driver end of the RTL, I_{loadp} is the peak load current, $I_{load}(t_{impv})$ is the load current at the time t_{impv} when C_r reaches 10 in the vacuum simulation for each case, and C_r is the z-pinch compression ratio at t_{impv}.

Case	$g(0)$ cm	$g(\ell)$ cm	$Z(0)$ Ω	$Z(\ell)$ Ω	$\frac{Z(0)-Z(\ell)}{Z(0)}$	L nH	V_{1p} MV	I_{loadp} MA	$I_{load}(t_{impv})$ MA	C_r @ $t=t_{impv}$
Av	0.2	4	2.1	2.1	0	15.7	19.0	60.4	35.4	10
Ae	0.2	4	2.1	2.1	0	15.7	18.9	56.9	34.7	4.4
Aei	0.2	4	2.1	2.1	0	15.7	18.4	48.6	26.7	2.6
Bv	0.2	0.2	2.1	0.11	0.95	2.5	9.7	61.1	24.7	10
Be	0.2	0.2	2.1	0.11	0.95	2.5	4.1	48.7	38.9	1.6
Bei	0.2	0.2	2.1	0.11	0.95	2.5	4.0	38.3	32.5	1.4
Cv	0.4	3.49	4.15	1.85	0.55	15.7	20.6	60.8	30.4	10
Ce	0.4	3.49	4.15	1.85	0.55	15.7	19.4	57.6	35.0	3.6
Cei	0.4	3.49	4.15	1.85	0.55	15.7	19.4	54.7	31.7	3.1
Dv	0.4	3.49	4.15	1.85	0.55	15.7	30.9	90.6	47.3	10
De	0.4	3.49	4.15	1.85	0.55	15.7	29.2	85.1	56.1	3.3
Dei	0.4	3.49	4.15	1.85	0.55	15.7	28.9	80.4	52.5	2.8
Ev	0.5	2	5.17	1.07	0.79	11.4	16.1	60.3	31.9	10
Ee	0.5	2	5.17	1.07	0.79	11.4	15.4	58.1	36.2	3.4
Eei	0.5	2	5.17	1.07	0.79	11.4	15.7	53.9	34.5	2.7

increased to better match the RTL to the load (and keep ion current losses down), while maintaining a reasonable inductance by allowing the gap at the driver end of the RTL to increase. Although there is some electron current loss, this variable-impedance RTL provides good load coupling characteristics. Case D uses the same variable-impedance RTL as Case C, but increases the peak load current. This case illustrates scaling of driver voltage with load current. Even with earlier ion turn-on and the larger ion emission area generated by the higher current, reasonable load coupling is maintained. Finally, Case E considers a more extreme variable-impedance RTL than Case C. The gap at the load end of the RTL is further increased and the gap at the driver end of the RTL is further decreased compared to Case C, and the RTL inductance is decreased. The change in impedance along the RTL in this case is larger than that used in Case C but less than Case B. Thus, this case investigates the scaling of power coupling with impedance variation along the RTL.

The results in Table 2.1 for Case A show that ion losses are manageable when $g(0) \geq 2$ mm. A full implosion could be achieved by increasing the input voltage waveform by about 20% so that a peak current of 60 MA is obtained even with ion current losses. On the other hand, the results of Case B show that electron flow current losses are excessive for a 2-mm constant-gap RTL. If a lower inductance RTL (for a given length ℓ) is required to reduce the voltage at the driver than can be obtained with a constant-impedance RTL with a gap of ≥ 2 mm at the load end of the RTL, then a variable impedance RTL is needed. However, the extreme impedance change presented by a constant-gap RTL is not the solution.

Cases C and E are variable impedance RTLs, which are intermediate to the two extremes presented in Cases A and B, and were used to investigate the electron losses in variable-impedance RTLs. In both cases, $g(0)$ is increased to further control the ion losses, while $g(\ell)$ is decreased to maintain or reduce the RTL inductance. A plot of the z-pinch compression ratio $C_r(t_{impv})$ as a function of the variation in impedance along the RTL as measured by $[Z(0) - Z(\ell)]/Z(0)$ is shown in Figure 2.6. Here, t_{impv} is the time when C_r reaches 10 for the simulation with no electron or ion emission for each case. The top curve relates to simulations with only electron emission and the bottom curve relates to simulations with electron and ion emission. Here, it is seen that electron current losses increase slowly until $[Z(0) - Z(\ell)]/Z(0)$ exceeds about 0.8, after which they increase rapidly. Note that the difference between $C_r = 10$ for Case Av and $C_r = 4.4$ for Case Ae results from a number of effects associated with MITL flow. Most important is a small electron flow current loss that occurs at the load end of the RTL. At mid-pulse, this loss results from small radial ∇B and polarization drifts. Such effects are not included in equilibrium MITL flow theory for a straight cylindrical transmission line, however, in this dynamic problem in conical geometry they can play a role, particularly when the gap is very small (such as in the case here where $g(0) = 2$ mm). Near the end of the pulse, the rising impedance of the load also causes electron flow current losses. For $Z_0 = 2.1\ \Omega$ and $V \sim 15$ MV, $Z_f^{SL} \sim 1.8\ \Omega$ while the load impedance dL_p/dt reaches about $2.5\ \Omega$ at the end of the implosion. Thus, by this time the RTL has transitioned from running load-limited to line-limited and electron loss current at the end of the RTL is expected. The small current loss (compared to the load current in Case Av with no electron emission) reduces the current driving the z-pinch load, resulting in a lower compression ratio at t_{impv}. The additional drop in C_r observed in the top curve for Cases Ce, Ee, and Be results from electron current losses caused by the increasing impedance along the RTL. The current losses associated with this increasing impedance are largest at the load end of the RTL because the impedance increases more rapidly there for walls defined by straight lines as used here. The difference between the two curves results mostly from ion loss current.

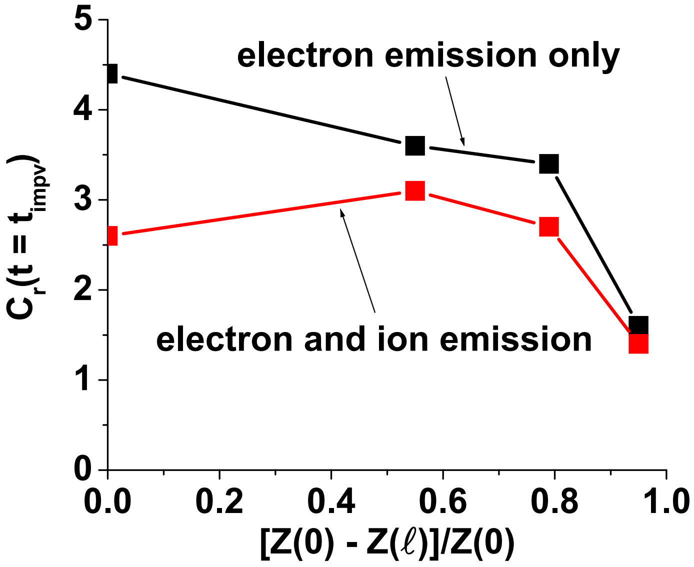

Figure 2.6. Plot of the z-pinch compression ratio $C_r(t_{impv})$ as a function of the variation in impedance along the RTL as measured by $[Z(0) – Z(\ell)]/Z(0)$. Here, t_{impv} is the time when C_r reaches 10 for the simulation with no electron or ion emission for each case. The top curve relates to simulations with only electron emission and the bottom curve relates to simulations with electron and ion emission.

The larger difference between the curves at $[Z(0) – Z(\ell)]/Z(0) = 0$ reflects the larger ion losses with the smaller 2-mm gap at the load end of the RTL in Case A compared to the 4 to 5 mm gaps in Cases B, C, and E.

Case D illustrates scaling in current. Although the currents losses observed in Case D are somewhat larger than in Case C, they are not excessive and a reasonable compression ratio is achieved at t_{impv}. Thus, for the most part, RTL designs that satisfy power flow requirements for a lower current system can be applied directly to higher current system. However, one issue must be considered is that the voltage at the driver end of the RTL increases linearly with current when the inductance remains constant.

A number of issues still require additional investigation. These issues include the following:

(a) The accuracy of simulations when the gap is very small may be compromised by the grid resolution and stair-stepping used here, particularly when the effects of ∇B and polarization drifts cause electron flow current loss. The resolution problem can be resolved by using a smaller radial cell-size at the expense of computational effort. Although it is only possible to completely resolve the problem of stair-stepping by using spherical geometry when both RTL walls are straight lines that fall on radii of a common circle (corresponding to a constant impedance RTL), it may still reduce the stair-stepping in a variable-impedance RTL.

(b) Using 2D simulations may mask 3D effects. For example, a 3D simulation may be required to uncover instability of the electron flow layer in the presence of ions such as observed in ion diodes. Effects of an instability could impact the thickness of the electron flow layer and electron current losses. This could be studied by doing 3D simulations but would be very computer intensive.

(c) In a variable-impedance RTL electron flow current losses are observed that are associated with the increasing impedance along the line. These losses are largest at the load end of the RTL because the impedance increases more rapidly there for walls defined by straight lines as used here. Shaping the walls to more smoothly change the impedance along the line may reduce these current losses and improve power coupling to the load.

(d) Questions also remain about whether the flow currents that enter the load region couple to the implosion or represent a reduction in the current driving the z-pinch implosion, and whether the flow currents disrupt the z-pinch dynamics in any manner. If only the bound current drives the z-pinch load and the flow currents do not participate, then this introduces a polarity effect with significantly more current flowing in the anode than the cathode. These questions could only be addressed by examining the z-pinch load region itself driven by boundary and flow currents.

(e) Finally, issues associated with gap closure and with power flow in a non-concentric RTL need to be evaluated. Non-concentricity studies will require 3D simulations, while specialized fluid and PIC simulation techniques are required to study gap closure.

These issues are left for future work. However, the work presented here indicates that RTL designs can be achieved for a z-pinch-driven IFE system that will provide good power coupling to a z-pinch load while maintaining a reasonable inductance if the gap at the load end of the RTL satisfies $g(0) \geq 2$ mm and the impedance along the RTL does not vary by more than $[Z(0) - Z(\ell)]/Z(0) \sim 0.8$. The models developed here can be used to evaluate specific RTL designs once baselines have been established for the driver and load.

2.2 Plasma Effects on Power Flow in an RTL near a Z-Pinch Load [40] *(D. W. Welch, D. V. Rose, T. C. Genoni, N. Bruner, C. Thoma, VOSS Scientific)*

In the feed of a magnetically insulated transmission line (MITL) for Z-pinch driven inertial fusion energy (IFE) [1], a crucial issue is the delivery of an intense pulse of energy to the load. The Z-pinch produces copious x-rays which then drive ignition in a fusion target. Such a Z-pinch load may require > 90 MA current to achieve 4 GJ target yield, but with vacuum gaps of the order of millimeters [41].

The key enabling technology for Z-pinch IFE is the recyclable transmission line (RTL) [5] which comprises a low-mass MITL from the edge of the containment vessel to the load and is largely vaporized in the target explosion. Higher power levels and larger Z-pinch compression ratios will drive increased voltages across the RTL gap. Recent MHD work has shown that the 50 kg RTL bulk (high β) material does not appreciably move on the 100--200 ns time scales of the Z-pinch implosion. The impact of fast, largely contaminant electrode plasmas must also be considered. Ultimately, these considerations will limit the minimum RTL gap that, in turn, affects the machine inductance and power requirements.

Earlier work has sketched out a simple, but fairly realistic, geometry to investigate the impact of plasma in the MITL gap near the load [42]. Here, we continue along this research path by considering the impact of plasma with various effective loads. The plasma constituents are considered to be that of electrode contaminants. An electron-H^+ plasma is actually modeled. Other than load impedance, no feedback from the load such as x-ray heating is considered. This feedback will be the subject of future work.

The evolution of electrode plasma in the MITL gap near the Z-pinch load is studied in a series of 2D LSP simulations. The plasma is injected at a rate consistent with a 10--20 contaminant monolayer (ml) release in 10--20 ns. No external heating mechanisms are considered such as that from UV or x-rays emitted from the load or other electrode plasmas. These simulations are made possible with the implicit/collisional algorithms in LSP. The cathode plasma penetration is seen to affect the power flow into the load most strongly.

2.2.1 Simulation Model

The LSP code [38,43] uses a robust energy conserving implicit algorithm including particle collision models. A fully 3D implementation of the direct implicit PIC algorithm [44] has been developed. The benefits of this treatment are that the usual charged particle limitations on time step, namely the need to resolve the cyclotron and plasma frequencies, are relaxed although both frequencies cannot be under resolved at the same time and position. It is important to note that in regimes where $\omega_p \Delta t > 1$, high-frequency interactions are not temporally resolved. Plasma electrons and ions are described with PIC methods using kinetic equations. Unlike most implicit algorithms, the LSP algorithm does not require resolution of the Debye length to avoid grid heating even when the time steps are small, $\omega_p \Delta t < 1$, where ω_p is the plasma frequency and Δt is the simulation time step. Also, for $\omega_p \Delta t >> 1$, the algorithm does not demonstrate numerical cooling.

The LSP simulations include an algorithm to model electron-electron, ion-ion and electron-ion collisions. This involves first constructing drifting Maxwellian distributions at each grid cell in each direction by summing over all particles for the mean momentum for each species i, $<p>_i = \sum q_i p_i / \sum q_i$, and random component $T_i = 1/(3\gamma m_i)\sum q_i (p_i - <p>_i)^2 / \sum q_i$. A particle of a given species is then elastically scattered isotropically in the center-of-mass frame off a particle obtained by sampling this distribution. The collision probability is determined by the Spitzer collision frequency. Collisions between different species (both kinetic and fluid) are separated into an energy push and a frictional momentum push. The energy and momentum transfers from one species to another are accomplished by summing the changes from each interaction on the grid. In these electrode plasma simulations, we inject a dense 3-eV hydrogen plasma through the electrode surface. Details of the implementation of the implicit and collision algorithm are described elsewhere [45].

2.2.2 Static-Load Plasma Simulations

We now examine the power flow into a static impedance load including sheath electron flow with cathode or anode plasmas. The simulation geometry is similar to that found in reference [42] but varies the outlet gap *d* from 0-0.5 cm as seen in Figure 2.7. The voltage is fed at the upper left assuming the voltage source is far away. The effective load impedance is controlled by varying *d*. In these simulations, cathode plasma is injected from the bottom ($r = 0.98$ cm, $z = 0.5\text{-}1.5$ cm) and anode plasma from the top ($r = 1.2$ cm, $z = 0.7\text{-}1.5$ cm). Vacuum electron flow is enabled via space-charge-limited (SCL) emission of electrons over the entire cathode up to $z = 1.5$ cm. SCL emission of protons is permitted only where anode plasma is in contact with the anode. A summary of the simulation parameters is shown in Table 2.2.

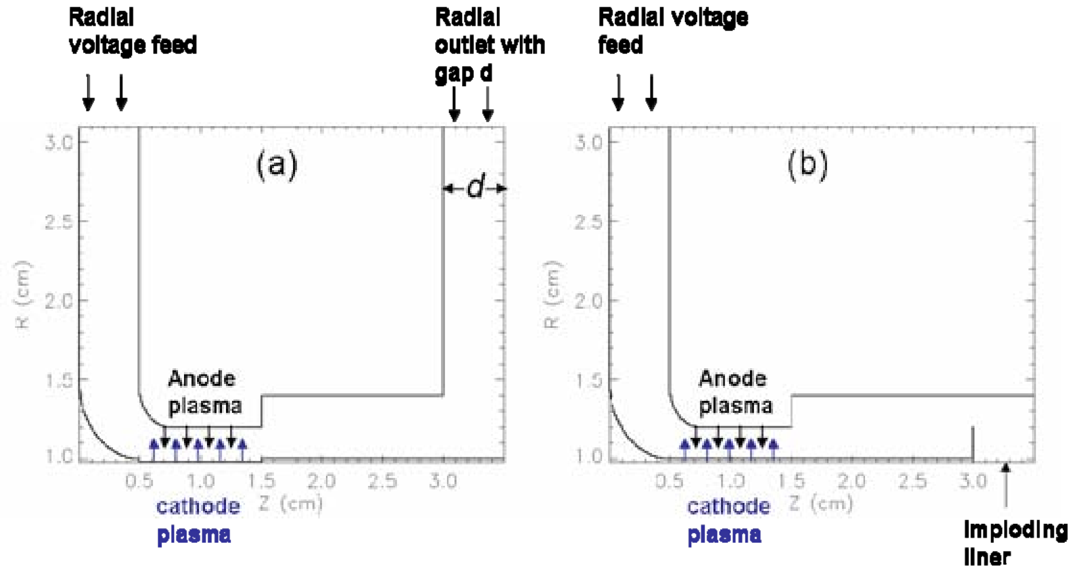

Figure 2.7. Simulation geometries employed in the static load simulation (a) and dynamic imploding liner simulations (b) are shown. In each case infinitely long radial transmission line voltage feeds are assumed.

Table 2.2. Summary of static load LSP simulations.

Run	Gap, d (cm)	V at 20 ns (MV)	I_f at 20 ns (MA)	Z_f (Ω)	I_l / I_f
Load4	0.5	9.1	1.23	7.4	0.73
Load7	0.1	3.3	1.74	1.9	0.94
Load9	0.05	1.93	1.84	2.0	1
Load8	0	0.28	2.04	2.03	0.99
Kplasma4	0.5	7.9	1.2	0.31	0.26
Kplasma6	0.1	3.0	1.8	0.78	0.43
Kplasma9	0.05	1.63	1.94	0.95	0.49
Kplasma10	0.03	1.03	1.91	1.67	0.87
Kplasma8	0	0.29	2.03	2.02	0.99
Aplasma4	0.5	8.0	1.26	0.61	0.484
Aplasma7	0.1	3.20	1.72	1.59	0.92
Aplasma9	0.05	1.93	1.86	1.83	0.98
Aplasma8	0.0	0.28	2.03	2.03	1

As expected, as the gap closes, the impedance drops due to a simultaneous increase in current and decrease in voltage. The best measure of the plasma effect is found in the last column of Table 2.2 which gives the ratio of the load to the feed current (measured at r = 3.1 cm) I_l/I_f. In general, this ratio decreases with increasing feed impedance Z_f. The most precipitous decrease is found in the cathode plasma simulations. Plotting the ratio versus impedance in Figure 2.8, we see that for each type of simulation (vacuum flow only, anode plasma, and cathode plasma) above some Z_f the I_l/I_f drops. For the case with vacuum electron flow only, the ratio drops below unity near roughly 6Ω. Adding an anode plasma with 0.6 ml/ns hydrogen plasma give a threshold of near 4Ω. With vacuum flow and cathode plasma (0.6 ml/ns), the threshold is close to 1Ω. Clearly, the effect of the cathode plasma entering the AK gap is the most severe with anode plasma effects being just slightly worse than vacuum flow only. From Figure 2.9, we see that as d increases, the plasma density in the wire array region increases from 10^{13} to $3x10^{15}$ cm^{-3}. The higher density plasma can shunt an increasingly higher current with 74% of the current flowing in the plasma for the highest Z_f. The moderate impedance simulations show an interesting enclosed current profile where more of the current actually flows into the load at r = 1 cm than mid-gap at higher radii indicating a sheath effect just off the load. This is likely the results of Hall current along the inner conductor yielding fast magnetic field penetration to the load.

The density and enclosed current after 20 ns for the series of anode plasma simulations are shown in Figure 2.10. In these simulations, except for the d = 0.5 cm case, the anode plasma remains well confined by the magnetic field. The load region fills with mostly electron flow exhibiting strong vortices that can locally suppress the enclosed current. In these simulations, the electron density doesn't exceed $3x10^{14}$ cm^{-3} in the center of the gap.

2.2.3 Dynamic Liner Simulation

In the next series of simulations, we use the geometry shown in Figure 2.7(b), which shows an additional structure in the lower right hand corner. This structure enables a transmission line boundary at the correct radius for the imploding liner model in LSP but serves roughly the same purpose as the outlet in the simulation discussed in Section 2.2.2. The "washer" that extends up at the z = 3 cm plane has a stabilizing effect on the liner boundary by both shielding the boundary from much of the plasma and by guiding the TEM waves normally through the boundary. The input for this model includes the liner mass and length (2 cm), initial radius (1 cm), final radius (0.1 cm), and the outer wall radius (1.4 cm). The time dependent impedance of the liner is determined from the geometry of the dynamic liner radius and outer radius.

For the initial simulations, we used a mass that was too large (5 mg) to implode on the 20--30 ns time scale and the load was essentially a short. The current drive rate was increased from 0.2--0.8 MA/ns --- in the range of that expected for an IFE driver. This augmented drive increases the feed impedance due to the higher induced electric field. In all these cases, both anode and cathode plasmas are included in addition to vacuum electron flow. As we see in Figure 2.11, the gap in the load region fills with a 10^{15} cm^{-3} plasma 16 ns into the simulation. Because the liner had not yet moved appreciably,

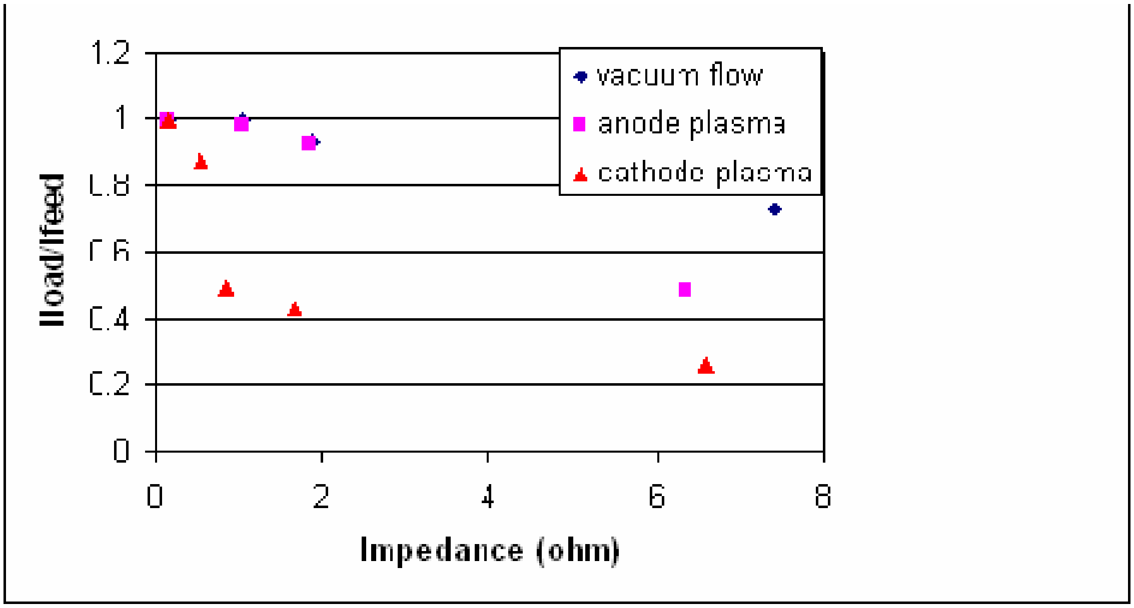

Figure 2.8. The ratio of the load to feed current is plotted versus feed impedance differentiating between simulations with vacuum electron flow only, flow with anode plasma and flow with cathode plasma.

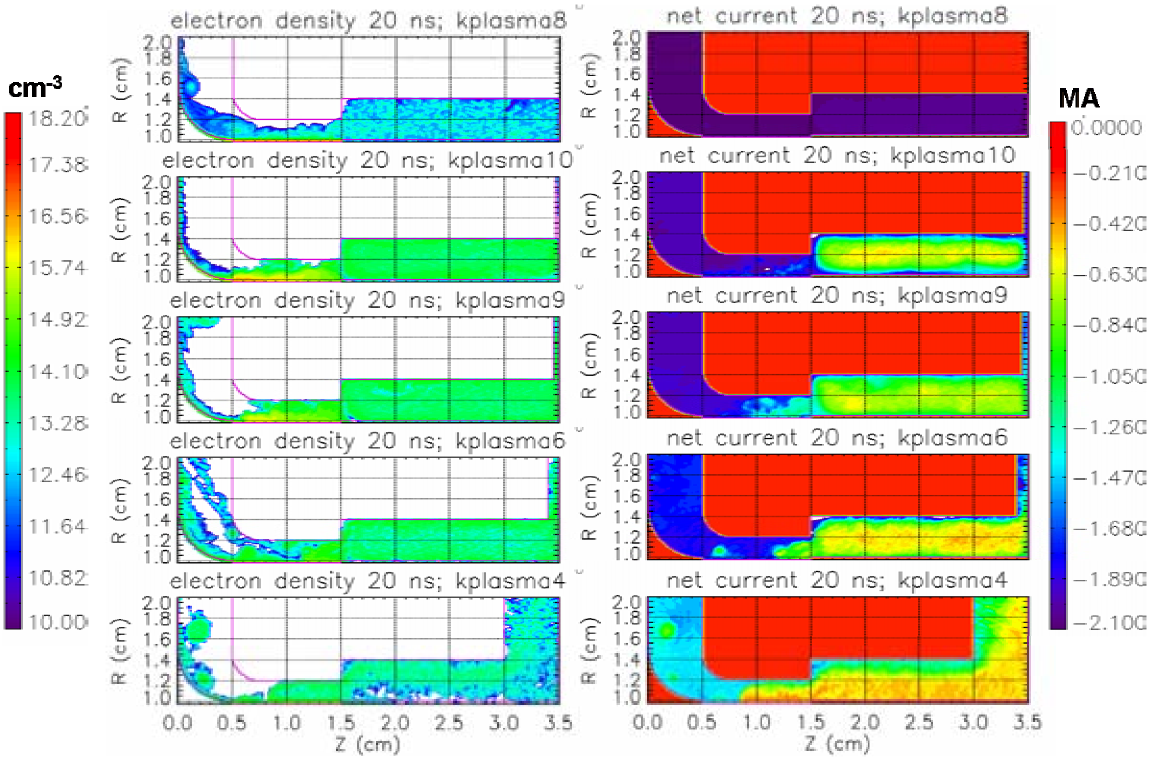

Figure 2.9. The plasma number density (on left) and the enclosed net current contours (on right) are plotted 20 ns in the series of cathode plasma simulations. The impedance increases from top to bottom.

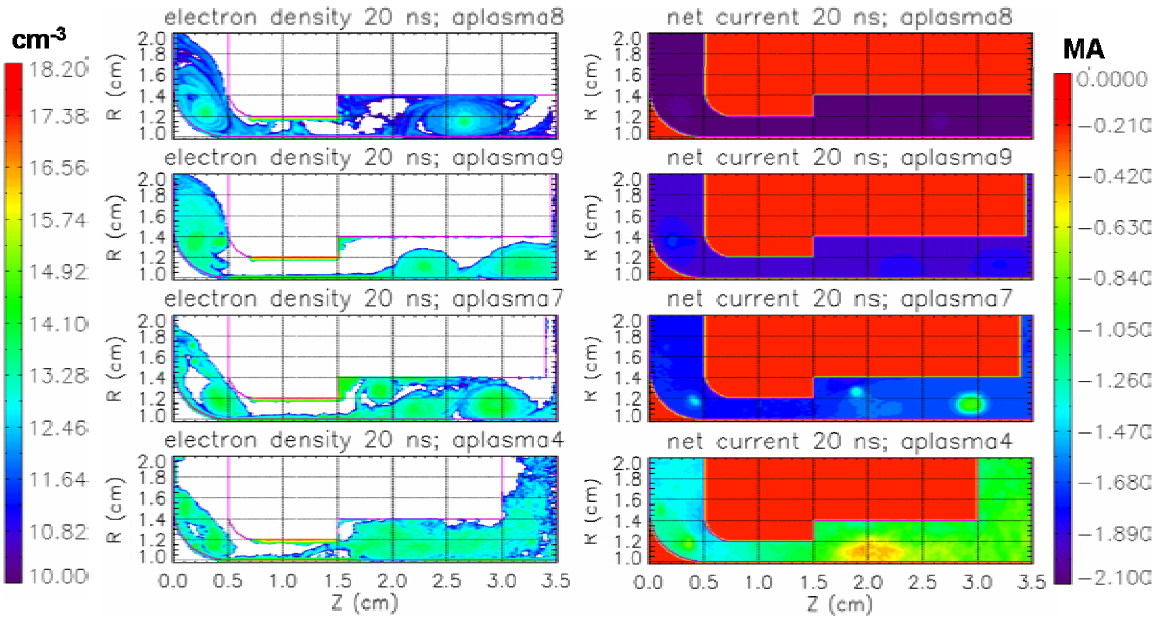

Figure 2.10. The plasma number density (on left) and the enclosed net current contours (on right) are plotted 20 ns in the series of anode plasma simulations which also include vacuum electron flow. The impedance increases from top to bottom.

the impedance at the feed position remains too low for plasma to shunt much current and indeed only 5% of the current does not make it to the load regardless of drive rate. The highest impedance at 16 ns for the 0.8 MA/ns was 0.4 Ω --- well below the threshold for significant plasma shunting. A comparison of the nominal 0.6 ml/ns with the 1.2 ml/ns plasma injection rate is shown in Figure 2.12. Doubling the plasma injection rate resulted in little additional shunting of the current. As in some of the earlier simulations, the plasma actually shields out 2 MA out of 12 MA in the gap center, but along the cathode surface the field has mostly penetrated. In the cathode plasma region, it is interesting to note the fingers of higher density (> 10^{16} cm^{-3}) plasma that extend into the 2-mm gap with roughly 0.5-mm spatial scale. The scale of these fingers is consistent with analytic estimates. In the higher plasma injection rate simulation, a plasma channel is evident that spans the gap right at the z = 1.5 cm position. This behavior indicates that we are on the edge of losing the power coupling to the load.

In the final series of simulations in hopes of driving a higher voltage and stress plasma confinement, we reduce the liner mass to 0.5 mg while keeping the current drive rate at 0.8 MA/ns. In this case without any particle current, the liner implodes by t = 24 ns with 16.4 MA peak current and 63 MV peak voltage. The full simulation including all plasma sources is compared with the vacuum case in Figure 2.13. Due to the shunting of some of the current from the load, the liner implodes 0.4 ns later in simulation with plasmas. The peak current is reduced by 4 MA from that of the vacuum simulation. This level of power lost to the load (20%) for the 2--3 Ω transient impedance at the feed is not as bad as the static simulation would suggest (60% loss). Additionally, for realistic final currents, the impedance will be down a factor 2--3 which will improve confinement.

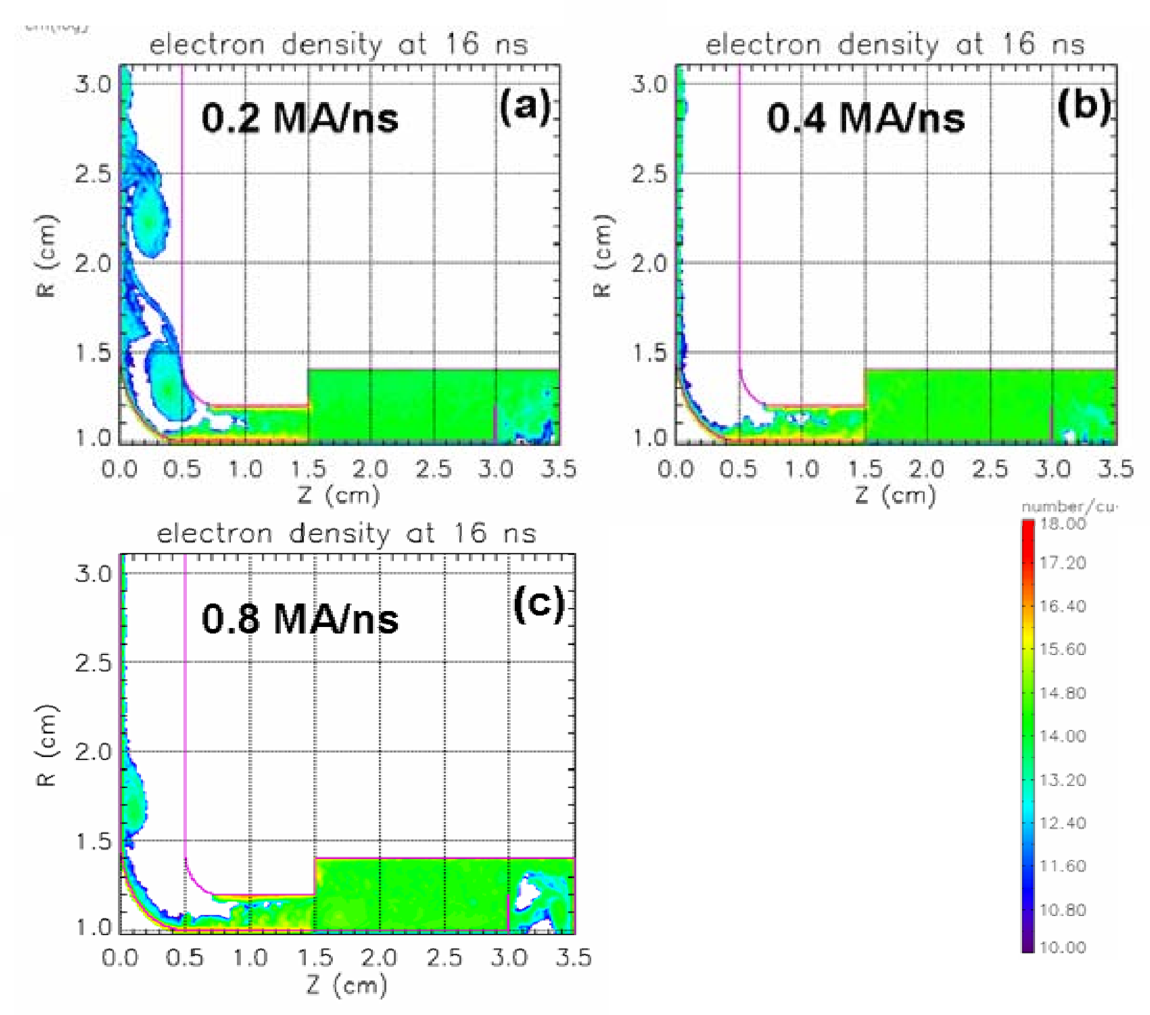

Figure 2.11. The electron number density is plotted in the simulation with (a) 0.2 , (b) 0.4, and (c) 0.8 MA/ns current drive rate. The simulation included vacuum electron flow and cathode and anode plasma.

Using the implicit and collision algorithms in LSP, we have examined the impact of evolving electrode plasmas in the AK gap of the RTL near the Z-pinch load region. As a first look, we injected hydrogen plasma from an assumed contaminant surface layer neglecting heating from radiation from the source and surrounding plasma. We varied the load characteristics (in both static and dynamic boundary models), the current rise rate, and plasma injection parameters. The cathode plasma was found to have the strongest impact of the power coupling to the load by carrying a significant fraction of the current when the feed impedance increased above 1 Ω. The anode plasma and simple sheath flow had little impact on power coupling until the impedance increased above 4 Ω. Increasing the plasma injection rate from 0.6 to 1.2 ml/ns show some increased susceptibility to current loss as well.

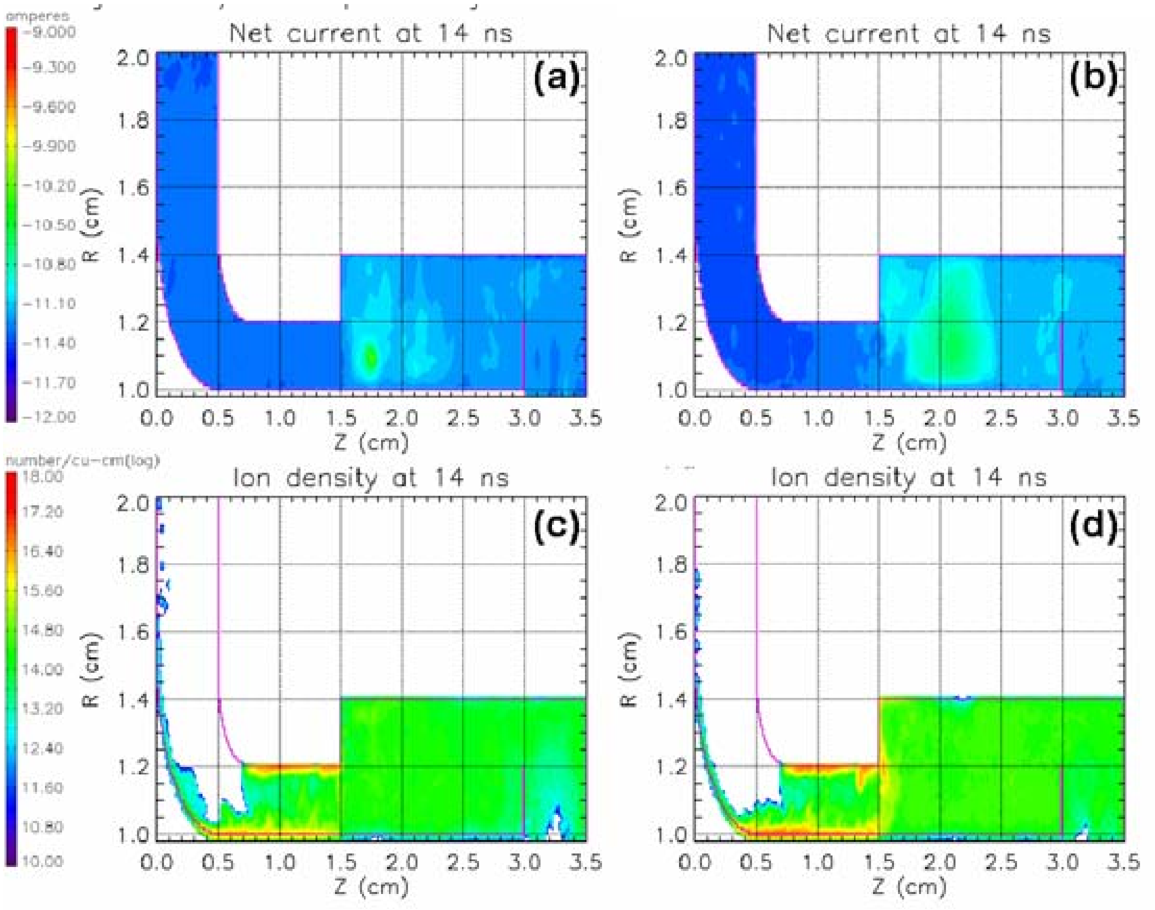

Figure 2.12. A comparison of the simulation with 0.6 ml/ns (on left) and 1.2 ml/ns (on right) plasma injection rates is shown. The 0.8-MA/ns current rise rate is used. The top figures (a) and (b) show the enclosed current contours and the bottom figures (c) and (d) show the ion density.

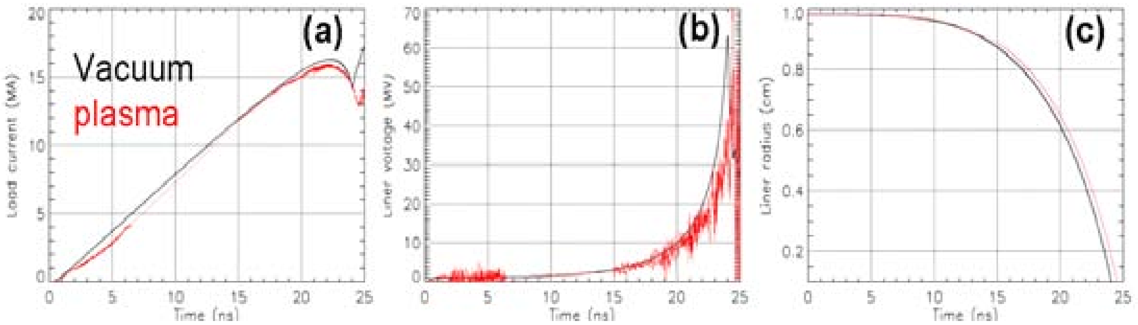

Figure 2.13. The vacuum and full plasma simulations with a 0.5-mg liner mass are compared. The (a) load current, (b) voltage at the load, and (c) liner radius are plotted versus time with vacuum in black and plasma simulation in red.

A dynamic imploding liner load simulation exhibited a less dramatic dependence with the impedance of the system. The implosion time was increased from 24 to 24.5 ns when plasma evolution was included in the simulation despite reaching a 2--3 Ω feed impedance near the time of minimum liner radius. Indicative of an instability with > 1 ns e-fold time, only 20% current loss to the load as the liner imploded was calculated. The rapid evolution of the impedance apparently slows the shunting of current relative to the static load simulations.

Although these results are encouraging for efficient power delivery to an IFE-scale Z-pinch load, future simulations need to be carried out with the full current (> 60 MA) and implosion time of order 100 ns. To resolve the electron cyclotron frequency, simulation of 60 MA currents will require as much as 10× more computer power than those discussed in this paper. In addition, radiatively-driven ablation from the load will increase the plasma beta and possibly results in a more sudden loss of power to the load. The impact of the more dense electrode material could also be added to the calculation.

2.3 LSP Simulations of RTL Power Flow in the Presence of a Plasma [40] *(N. Bruner, D. R. Welch, D. V. Rose, VOSS Scientific)*

Updated results of power flow modeling for the Z-IFE recyclable transmission line (RTL) are presented. Simulations were conducted using LSP which included the imploding load and space-charge-limited emission of electrons. Although the simulations had micron resolution, the electron sheath was not fully resolved over the duration of the pulse. However, changes from previous, lower-resolution studies were modest and it does not appear that further simulations which neglect plasma effects are required. Studies of the effect of a localized plasma in the A-K gap of the RTL were also conducted. It is shown that the presence of plasma diverts some cathode current across the gap and away from the load. For a 10^{15} cm^{-3} plasma, this current was less than 10% of the total, but it is in the 20% range for a 10^{16} cm^{-3} plasma.

2.3.1 Introduction

As reported in Ref. [46], it is expected that a plasma will form in the A-K gap of the RTL ramping to 60 MA due to ohmic heating of the conductors and may also form via x-ray ionization of neutrals in the gap or on the conductor surface. Regardless of how a plasma is be formed, it is important to understand how it affects power flow. The analytical results from Ref. [46] indicate that for a transmission line operating at 1.3 MV, a modest 10^{12} ions/cm^{-3} should double the sheath current. Progress toward understanding the effect of plasma as a function of density is reported in this section.

2.3.2 Model

A smaller segment of the RTL is modeled here than in the previous section. The simulation geometry (Figure 2.14) includes last 5 cm of the transmission line with the same resolution but with a short-circuit load. In cylindrical coordinates, the radial range of the inner RTL radius is $4.8 < R_i < 6.9$ cm, but the simulations were conducted in 2-D spherical ($11.7 < r < 16.7$ cm).

The pulse is the same as in the previous section, 100-ns pulse rise to 60 MA, but the new physics occurs before 10 ns. In this short transmission line segment, sheath current retrapping is complete in less than 1 ns. After allowing a few more nanoseconds for fields to establish, a plasma is introduced spanning the A-K gap between $12.2 < r < 13.0$ cm ($5.1 < R_i < 5.4$ cm). Unlike the analytic model, the ion motion is not constrained to be transverse to the A-K gap (the polar direction), but may also drift radially.

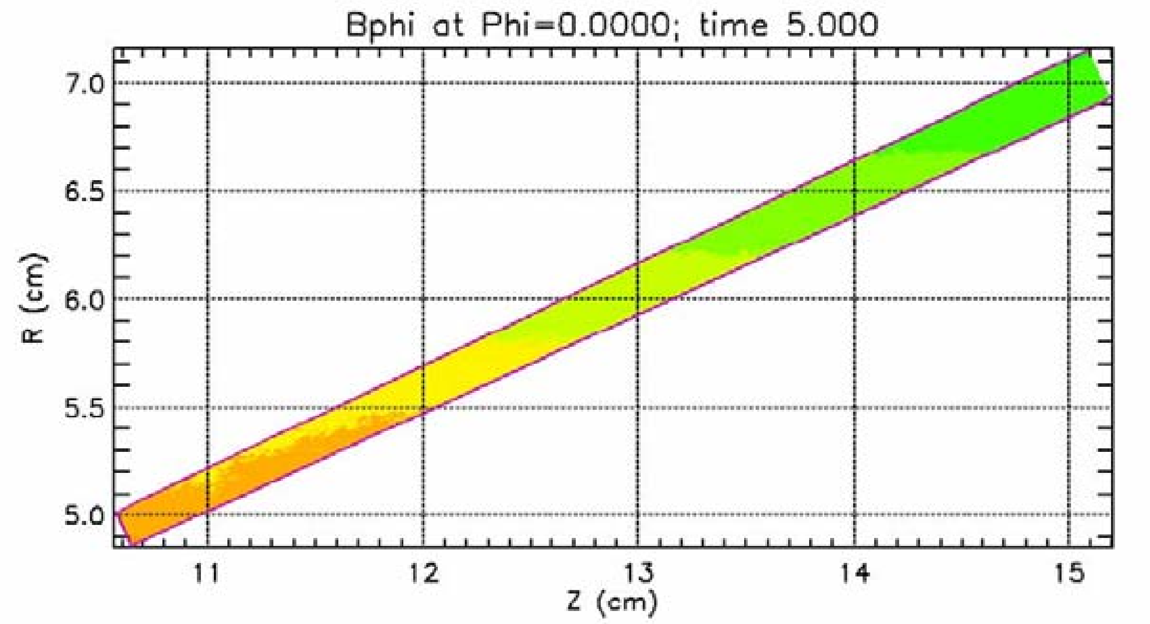

Figure 2.14: Diagram of the LSP simulation of the conical transmission line used in simulations of a plasma in the A-K gap. The diagram is represented in cylindrical coordinates but was simulated in spherical.

The LSP results from Ref. [46] reported that a 10^{16} cm^{-3} density plasma diverted some portion of the cathode current across the A-K gap and away from the load. In an effort to approach the threshold density for this effect, two densities were modeled; 10^{15} and 10^{16} cm^{-3}.

2.3.3 Simulations results

The cathode currents upstream and downstream of the plasma region are plotted in Figure 2.15, along with a polar current (I_θ or I_{shunt}) to quantify the amount of current diverted across the A-K gap. Both plasma densities are shown in Figure 2.15, and it appears that the 10^{15} cm^{-3} density does not significantly lower current delivered to the load. The ratios of shunt current to anode current for both densities are shown in Figure 2.16. The shunt current recorded before 1 ns occurs with retrapping. After the plasma is introduced, there is an initial jump in $I_{\mathrm{shunt}}/I_{\mathrm{a}}$ (where I_{a} is the anode or total current) followed by a slower decay for both plasma densities. At 10^{15} cm^{-3} this ratio drops from 7% to below 2%, while at 10^{16} cm^{-3} it drops from 23% to 6%. The actual transient behavior of the shunt current will depend on the duration of plasma production. Without resupply, the transient behavior in simulation is reminiscent of an opening switch.

To compare this LSP prediction of threshold density to the analytic model presented in Ref. [46], the equation relating γ_{m} (maximum electron γ in sheath) and the cathode and anode magnetic fields for static ions can be rewritten:

$$\frac{I_s}{I_a} = \left(\frac{1}{\gamma_m^2} - \frac{2m_e}{\varepsilon_0} \frac{\gamma_m - 1}{B_a^2} n_i \right)^{1/2}, \tag{2.1}$$

where n_{i} is the ion density and B_{a} is the field at the anode. (Note the conversion from field to current generalizes the result from Cartesian to any coordinate system.) A value of B_{a} can be assumed from a 100-ns rise to 60 MA, but a determination of γ_{m} is not as straightforward since for the short circuit γ_{m} approaches 0. γ_{m} can be assumed to be near 5 when operating at line impedance. Figure 2.17 shows the behavior of Eq. 2.1 as a function of n_{i} for a few values of $\gamma_{\mathrm{m}} < 5$. The relative sheath current is seen to drop with γ_{m} while the threshold ion density rises. This is consistent with the LSP result.

2.3.4 Conclusions

Updated results of power flow modeling for the Z-IFE RTL have been presented. Simulations were conducted using LSP with increased resolution over the study in Ref. [46]. A 40-cm long segment of the RTL including the imploding load and SCL emission of electrons was modeled with a resolution of 2.3 µm at the cathode. While this is an order of magnitude increase in resolution over Ref. [46], the electron sheath was not fully resolved over the duration of the pulse. However, changes from previous simulations were modest and it does not appear that further simulations which neglect plasma effects are required.

The effect of a localized plasma in the A-K gap were modeled for a 5-cm long segment of the RTL. The presence of plasma diverts some cathode current across the gap and away from the load. For a 10^{15} cm^{-3} plasma, this current was less than 10% of the total, but it is in the 20% range for a 10^{16} cm^{-3} plasma.

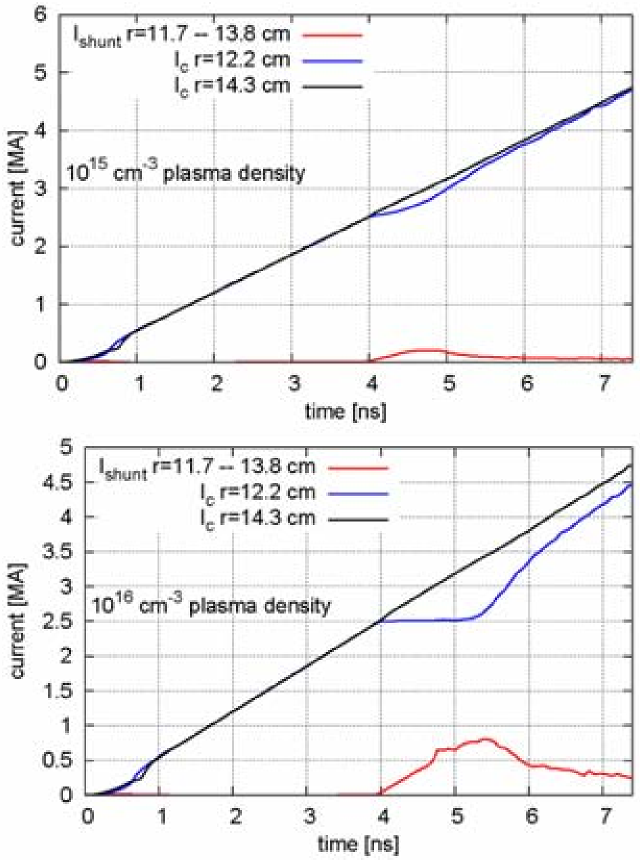

Figure 2.15: Cathode boundary currents upstream and downstream of a plasma region (5.1 < *r* < 9.1 cm) inserted at 4 ns into the simulation. Currents are shown for two plasma densities, 10^{15} (top) and 10^{16} cm^{-3} (bottom).

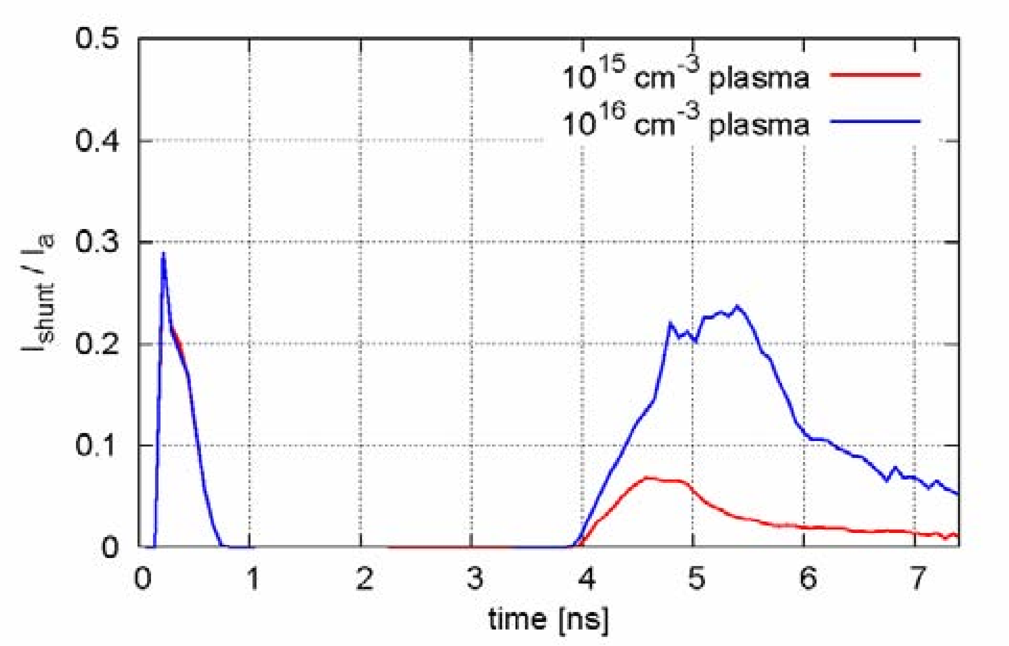

Figure 2.16: Ratio of shunt current to total before and after plasma insertion at 4 ns. Fractional shunt current is shown for two plasma densities, 10^{15} and 10^{16} cm^{-3}.

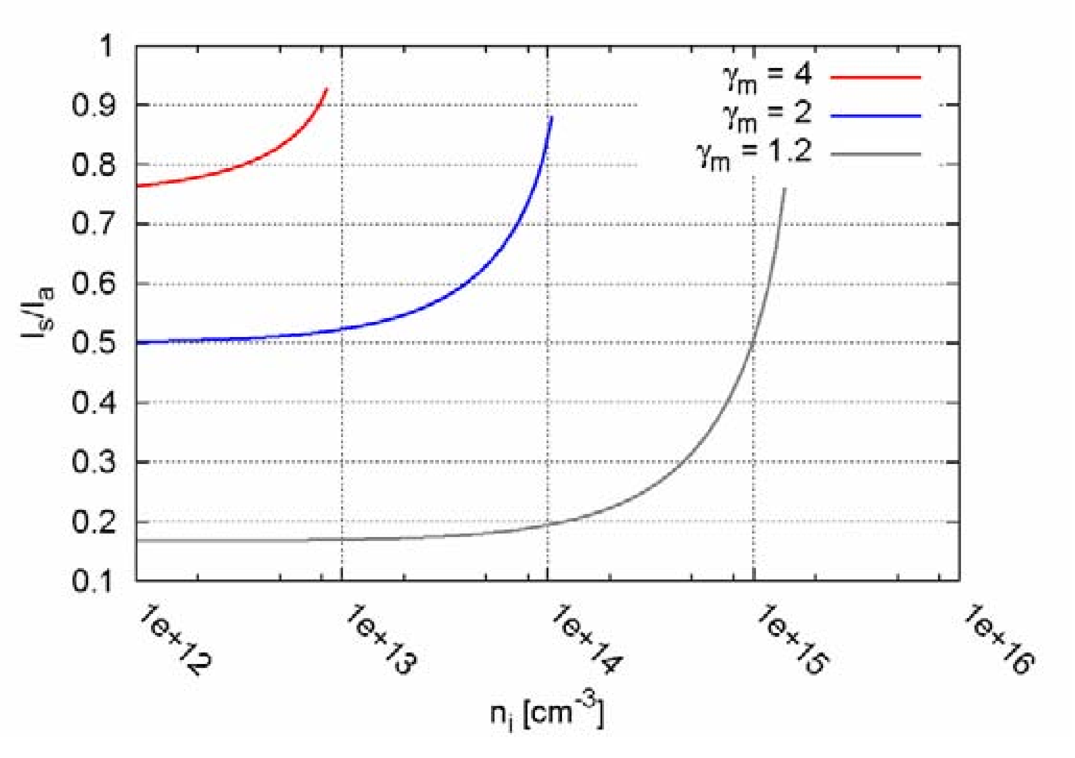

Figure 2.17: From Eq. 2.1, the ratio of sheath current to total as a function of n_i for various values of γ_m is shown.

2.4 Experiments at High Linear Current Densities to Study Potential RTL Power Flow Loss Mechanisms [47] *(Yu. G. Kalinin, A. S. Kingsep, S. L. Nedoseev, V. P. Smirnov, Kurchatov Institute, Moscow)*

The two purposes of this research performed by the Kurchatov Institute in Moscow were to:

(A) Perform experiments on the S-300 machine to study experimentally the inter-electrode plasma behavior by the current flow along the Recyclable Transmission Lines (RTLs) for linear current flow densities of several (up to 7) MA/cm and different electrode materials (Al, Cu, Ni, and Bi). Study near-electrode plasma sheath dynamics using the electrodes with the absorbed gas removed by means of electrode pre-heating.

(B) Perform experiments on the ANGARA-5-1 facility to study the current-carrying electrodes expansion under the effect of soft x-ray radiation (SXR), by the different electrode materials.

2.4.1 Experiments on the S-300 Machine

1. On the S-300 pulsed power generator, a series of experiments has been carried out devoted to the study of cathode material effect, as well as that of gases and oil layer absorbed by its surface, on the near-electrode plasma dynamics and the current pulse transport along the short MITL segment. The “cold” linear current flow density reached 6 MA/cm. As the previous experiments show that the current transport efficiency actually does not depend on the form of outer electrode, we have used the output device identical to that used in FY05. The return conductor consists of three rods, 3 mm in diameter, made of the stainless steel and situated at the radius 7.5 mm (Figure 2.18). Both dimensions and material of surface of the inner electrode were varied; to wit, Al, Au, W, Pb were used, as well as Ni (with and without a heating).

Both input and output current were measured by means of calibrated magnetic loops and shunt (NiCr, 200 μm), respectively. In this experimental series, the basic information on the near-electrode plasma dynamics has been used by means of the ICT chronography in visible range. Besides, 5-frame shadow photography in the light of second YAG:Nd laser harmonics was used ($\lambda = 532$ nm, $\tau = 0.3$ ns), as well as frame ICT photography in both visible and SXR ranges, with the time resolution 5 ns. In some experiments, the Bremsstrahlung from the anode rods was recorded by means of the collimated probe, in the range of $E > 30$ keV.

2. In the first experimental series, the effect of cathode surface purity on the gap reconnection rate was studied. As a cathode, the Ni tube was used with the diameter 0.75 mm and thickness 100 μm. To exclude the influence of plasma formed of surface oil layer (which cannot help arising because of the pumping out by the diffusive oil pump), as well as the gas absorbed by the surface, the inner conductor (cathode) was supported

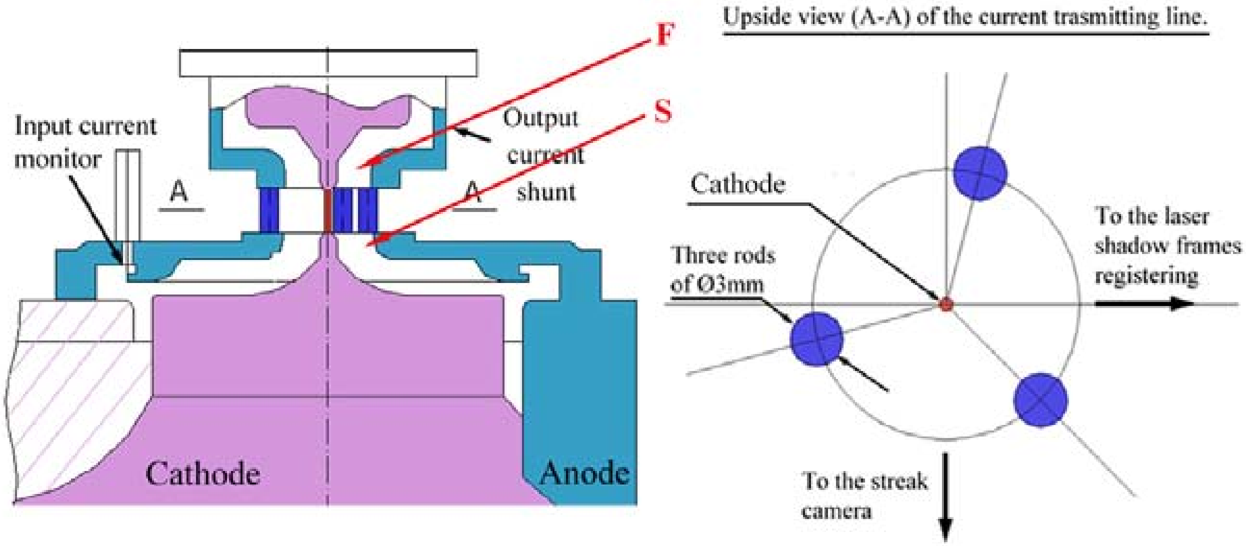

Figure 2.18. Schematic of the output unit.

heated starting from the beginning of high-vacuum pumping out till the shot, by the temperature 200-600 C. Such heating removes the oil layer and decreases the concentration of gas absorbed some 2 orders of magnitude. The heating was brought about by passing the direct current ~ 10-40 A through the conductor. This current was provided by the separate rectifier connected via the filtering inductances. To protect the low- voltage fragments of the scheme from the breakdown by passing the working pulse, the solid-state switch was also used. Just before the pulse, the feeding of low-voltage circuit was switched on the isolated source (accumulator). Figure 2.19 demonstrates the oscillograms of both input and output current in the experiments with and without heating. The feature of these two experiments is the very good (with the accuracy better than 10%) coincidence of temporal dependences of input and output current up to the moment 240-260 ns. The chronograms of cathode plasma (Figure 2.20) show the same dynamics of its expansion in both variants of experiment. The only difference is the following one: the expanding plasma of "unheated" electrodes has more diffusive boundary.

The experiments carried out with the aluminum cathode have demonstrated no essential difference as well, neither in plasma dynamics, nor in the time of reconnection. Thus, one may conclude that in our conditions, by high current flow densities, presence or absence of the oil layer on the electrode surface does not affect essentially plasma dynamics in MITL, and, accordingly, the transport properties of the latter.

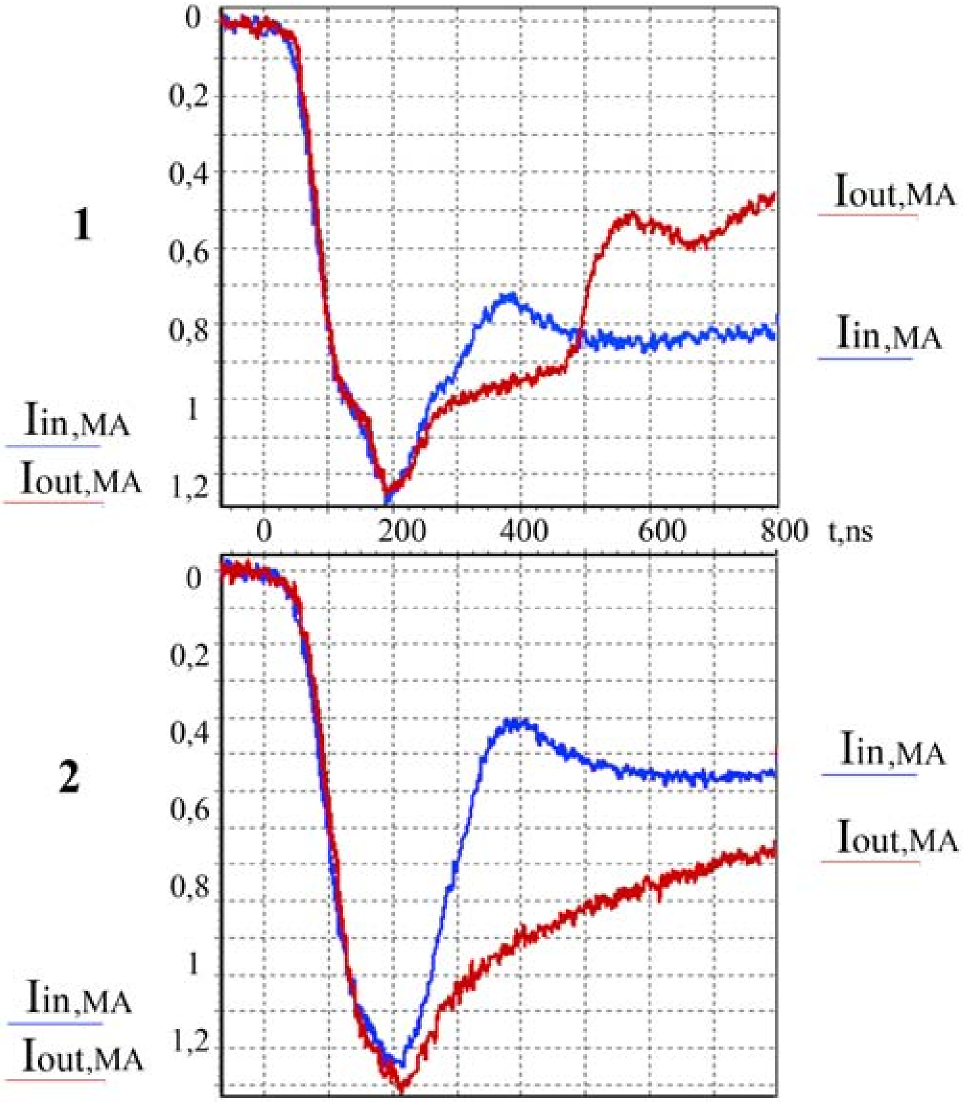

Figure 2.19. Oscillograms of both currents, input one (I_{in} , blue curve) and output one (I_{out} , red curve): 1 – without preheating, 2 – with preheating. The cathode is the Ni tube with the diameter 0.75 mm and wall thickness 100 μm.

Let us note, however, that some peculiarities in plasma behavior by the cathode preheating still do exist. In particular, according to the statistics, the Bremsstrahlung in X-ray range appeared earlier (in the beginning of the current front) in the experiments with the heated cathode, compared to cold one. To some extent, that is true also for the luminosity of plasma adjacent to the cathode. Perhaps, it may be conditioned by earlier generation of the rare plasma on the electrode and/or in the gap in the case of preheating. In the experiments with heated cathode, no periodic structure has been formed described in our reports for FY04 (see Ref. 2) and FY05 (see Ref. 3). Let us, however, emphasize that no essential difference in the MITL (used in FY04 or FY05) transport properties has been observed.

Similar results were obtained in the experiments with aluminum loads: the heating did not affect essentially on the current and plasma dynamics.

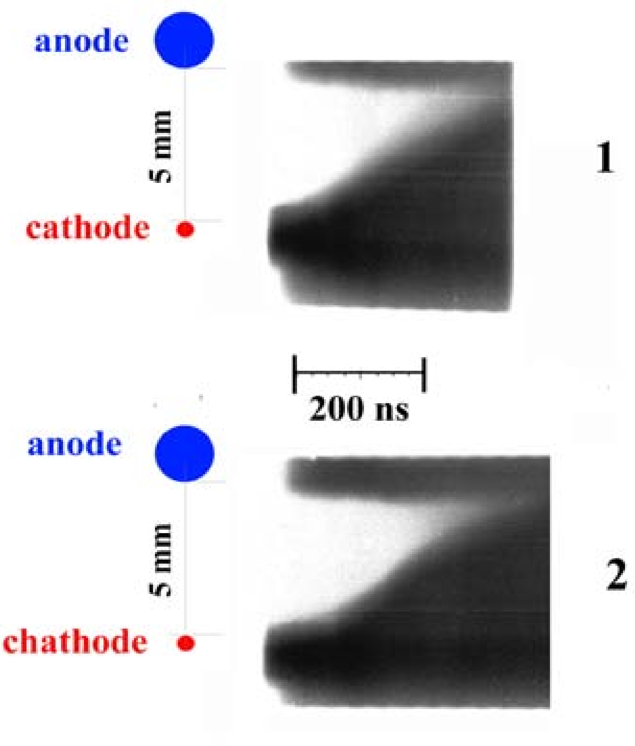

Figure 2.20. The chronograms of near-electrode plasma expansion (negative picture): 1 – without preheating, 2 – with preheating. The cathode is the Ni tube with the diameter 0.75 mm and wall thickness 100 μm.

3. In the second experimental series on S-300 machine, the effect of electrode material on the plasma expansion velocity and, hence, the time of gap reconnection was studied. The material of electrode with maximal linear current flow density (i.e. that of cathode) was varied. This experimental activity was based on the assumption of less expansion velocity of plasmas of heavier elements. Unlike the conventional problem of plasma expansion into a vacuum, in the strong magnetic field, this statement is not obvious a priori and demands the experimental verification.

In the experimental series described below, except of Ni and Al, both lead and gold were used as the inner electrode material. The former is appropriate to be used as the material of recycled fragments of transporting lines since the reactor chamber is assumed to be filled, to the great extent, by the melted lead (see our report for FY05 in Ref. 3). The latter is interesting as the metal with very low gas absorption ability, compared to other metals. The loads were performed as tubes with the outer diameter 200-250 μm, that is more or of the order of skin depth. Inside the aluminum or lead tubes, sometimes, golden tubes as well, the nickel tubes were situated as kern, aimed at the simplification of production and enhanced mechanical strength. The diameter of these inner tubes was 0.75 mm and the wall thickness 0.1 mm. In some shots, the tungsten rod was used as the inner electrode.

Experiments have confirmed the assumption about slower expansion of plasmas with greater Z. In Figure 2.21, the oscillograms of both input and output current are presented, synchronized with the chronogram of Pb plasma expansion started from the lead cathode, without a preheating.

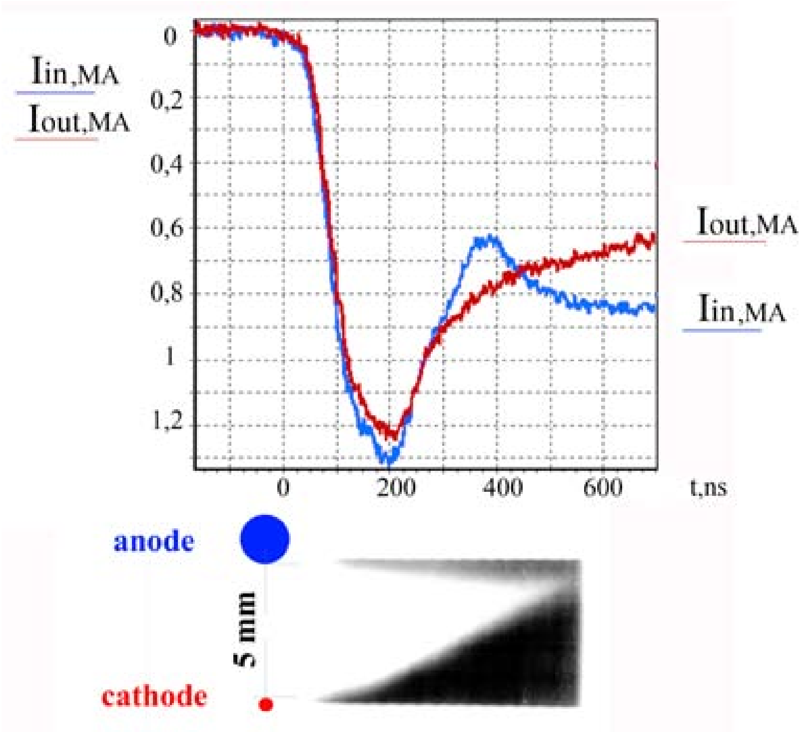

Figure 2.21. Oscillograms of the input (I $_{in}$) and output (I $_{out}$) currents by the lead cathode. Bottom: chronogram of Pb plasma expansion (negative).

These oscillograms show the divergence of input and output currents as late in time, as at 300-320 ns from the current start, i.e. 50-70 ns after corresponding moment for the nickel tube. The visible overlap of electrode plasma clouds on the chronogram occurs after 500 ns from the current start.

Even more obvious is the difference in plasma behavior for different materials, if one compares visible dynamics of Pb and Al plasmas. The results for the latter are shown in Figure 2.22. In this case, the divergence of currents starts already at 250 ns, and the visible overlap of the gap happens at 400 ns.

Even more pure experiment on the heavy plasma dynamics was carried out with the golden cathode heated from the start of high vacuum pumping out, up to the basic current pulse. Thereby we eliminated the effect of thin oil layer (as we have already noticed, the absorption ability of Au is very low).

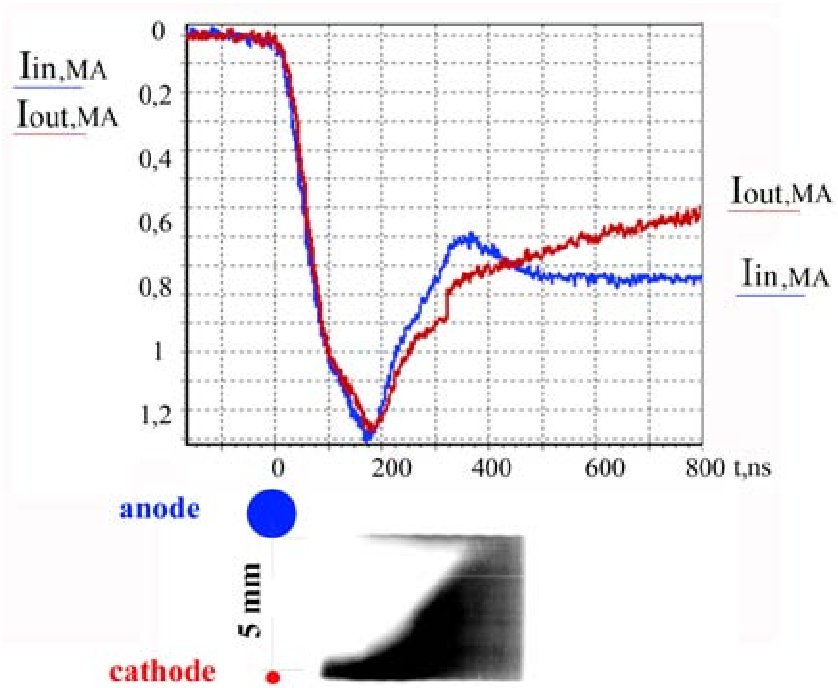

Figure 2.22. Oscillograms of the input (I_{in}) and output (I_{out}) currents by the aluminum cathode. Bottom: chronogram of Al plasma expansion (negative).

The results of this experimental series are shown in Figure 2.23 and Figure 2.24. The difference was only conditioned by the cathode construction: either the inner tube coated by the golden foil (Figure 2.23), or the hollow golden tube with the wall thickness 200 µm (Figure 2.24). In both cases, the oscillograms are very close to each other. The coincidence of input and output current behavior is kept up to 400 ns from the current start. The overlap of electrode plasmas happens after 600 ns, however, the plasma dynamics turns out to be different. In the case of cathode with Ni tube inside, the radial plasma velocity is varied smoothly and, quantitatively, not so much. In the case of hollow golden tube, two segments of time exist, with the essential difference in expansion velocities, from $8 \cdot 10^5$ cm/s at the first one, till $1.7 \cdot 10^6$ cm/s at the second. The transition from the smaller velocity to the greater one occurs as the jump at 430 ns from the current start. Perhaps, this point corresponds to the shock conditioned by the golden tube compression coming out onto the tube surface. One may assume that in the case of planar MITL electrodes, which should be used at the end part of MITL, the expansion velocity could not be changed, that would result even in longer time scales of the gap reconnection.

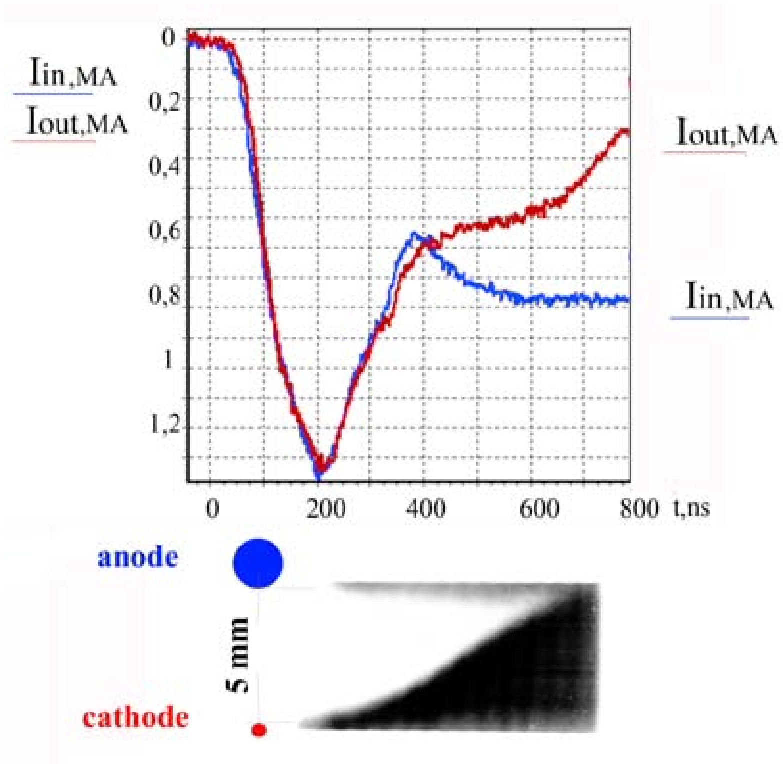

Figure 2.23. Oscillograms of the input (I_{in}) and output (I_{out}) currents by the golden cathode with the Ni tube inside. Bottom: chronogram of electrode plasma expansion (negative).

The different expansion dynamics of dense plasmas of different materials, to wit, Al, Ni, Au, is demonstrated by laser shadow photographs shown in Figures 2.25 - 2.27, respectively. Except of expansion velocity decrease by increasing atomic number, the different degree of the dense plasma instability is obvious: the boundary of aluminum plasma (Figure 2.25) is much more ripped, compared to nickel plasma (Figure 2.26); in turn, the boundary of golden plasma (Figure 2.27) is the most smoothed one.

One more peculiarity has been noticed, namely, dense plasmas with greater velocities close the gap in both beginning and end of the line segment, i.e. in the points S (the transition from diode to the line) and F (the transition from the line to the shunt unit) in Figures 2.18 and 2.25 where some inhomogeneities cannot help existing. The greater plasma velocity in the vicinity of these points, including respectively rare plasma, may be just the reason of the input/output current divergence earlier than closure the gap in the chronograms since the middle cross section of the line segment is usually projected on the chronograph slit. Hence, one could suppose that in uniform lines the efficient time of operation would be even greater than that in our experiments.

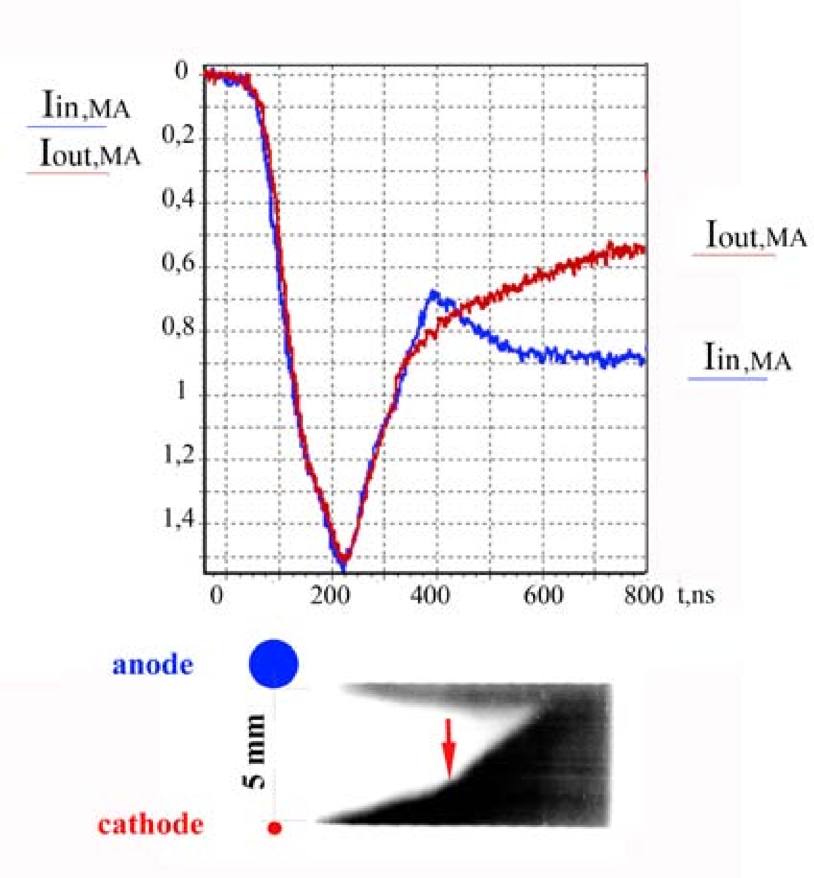

Figure 2.24. Oscillograms of the input (I_{in}) and output (I_{out}) currents by using the hollow golden cathode. Bottom: chronogram of electrode plasma expansion; the read arrow shows the jump in the expansion velocity.

The conclusions for these S-300 experiments are:

1. It has been proved experimentally that by pass of the current with the linear current flow density up to 6 MA/cm along the MITL model, the input and output current coincide, within the frames of experimental accuracy, depending on the experimental conditions, during 200 to 400 ns from the current start.
2. It has been proved that the duration of such coincidence depends essentially on the electrode material. To wit, it is minimal in the case of light metals (200 ns for Al) and greater for heavier materials (320 ns and 400 ns for Pb and Au, respectively). We have not revealed any essential dependence upon the presence of light impurities on the electrode surface.
3. Thus, the electric explosion at the final recycled segment of magnetically insulated transporting line does not prevent from the energy transport towards the target. Apparently, it is reasonable to construct the electrodes of this fraction of MITL of lead. On the one hand, this material is favorable from the standpoint of energy transport, on the other hand, conceptual reactor project already includes rather great amount of melted lead in the reactor chamber.

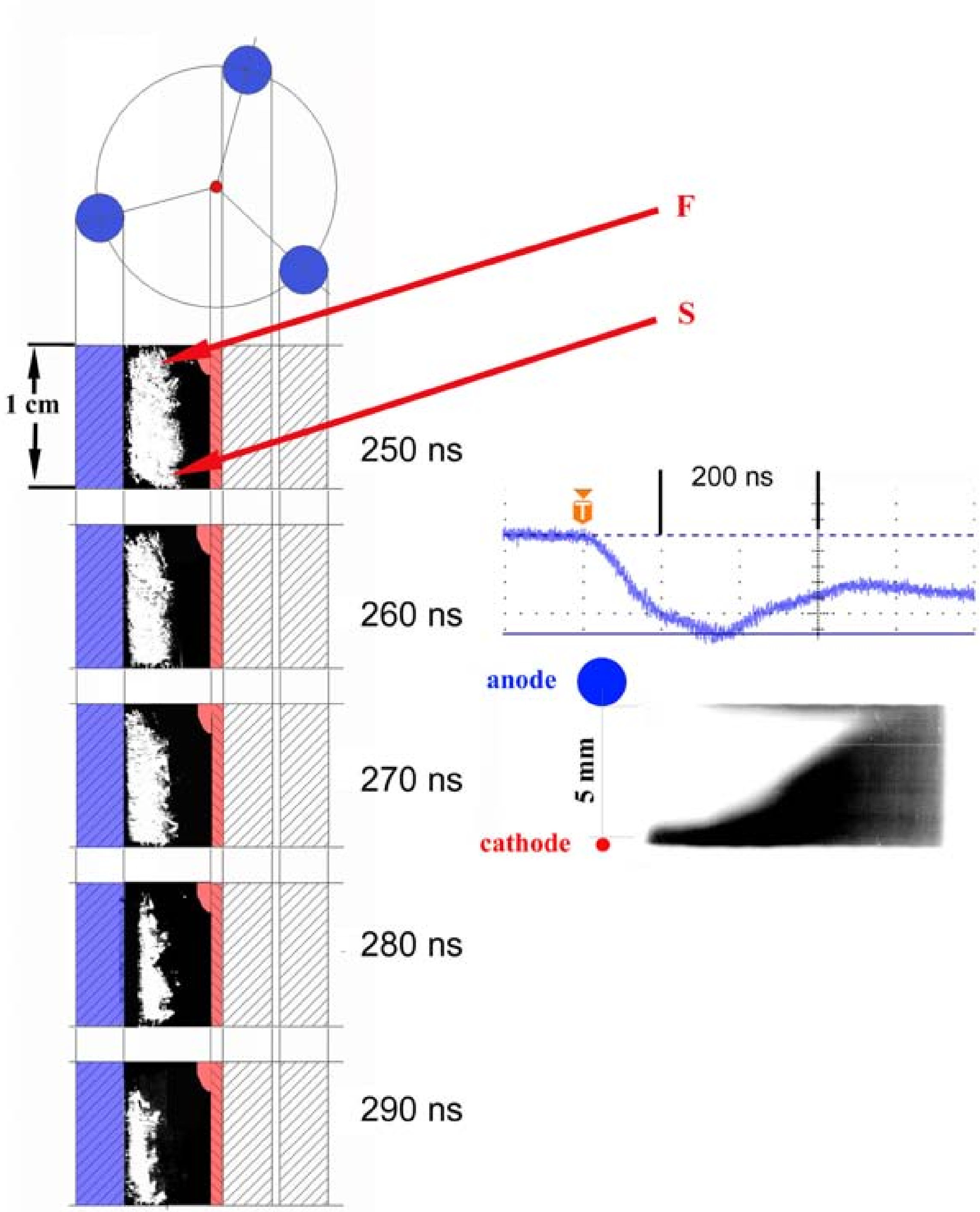

Figure 2.25. Left: laser shadow photographs of expanding electrode plasma in the case of Al cathode (red); the zero point of time is the current start. S and F points are the points of line segment connection to the diode and shunt, respectively. Right: the oscillogram of input current and the chronogram of plasma expansion.

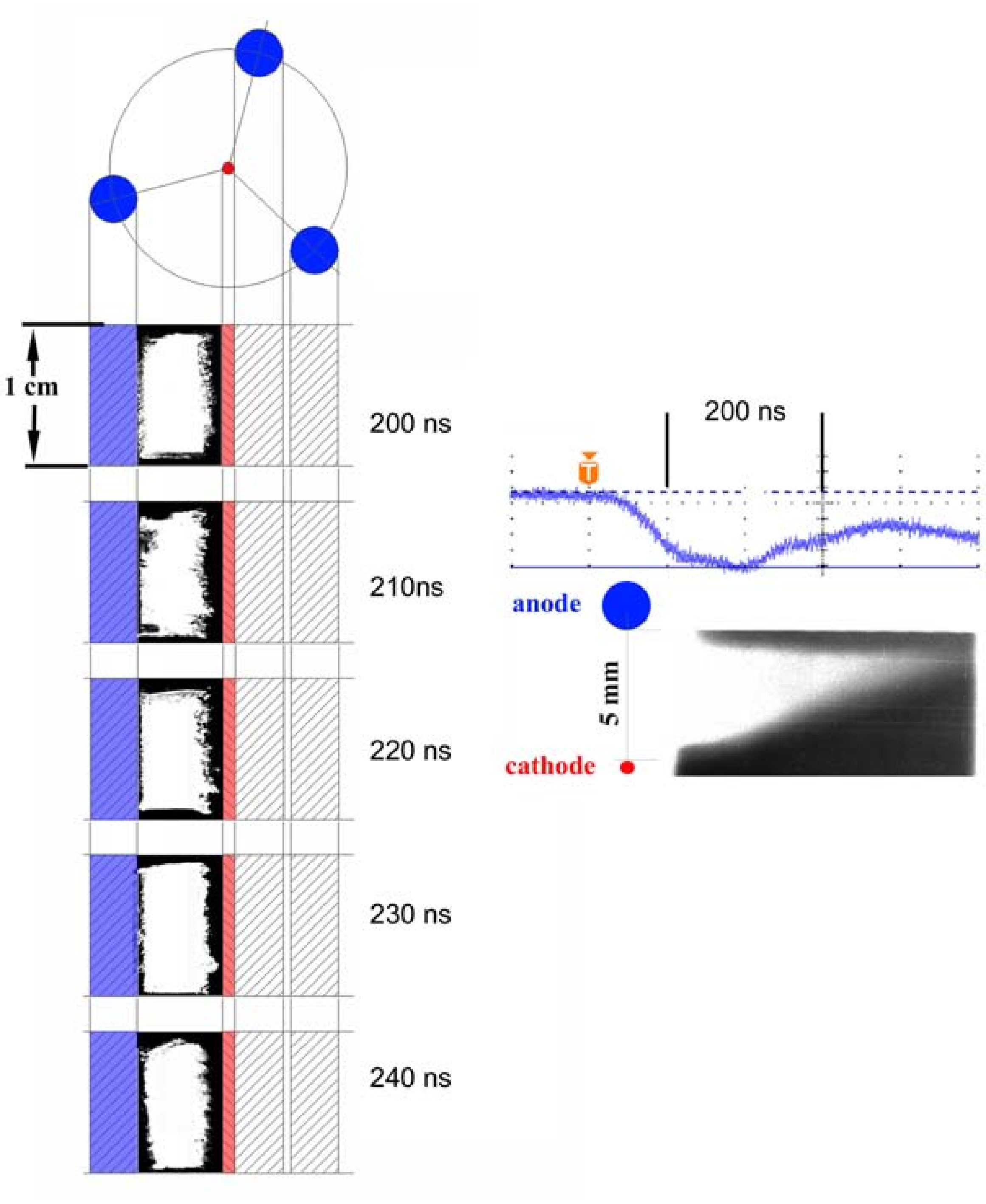

Figure 2.26. Left: laser shadow photographs of expanding electrode plasma in the case of Ni cathode (red); the zero point of time is the current start. Right: the oscillogram of input current and the chronogram of plasma expansion.

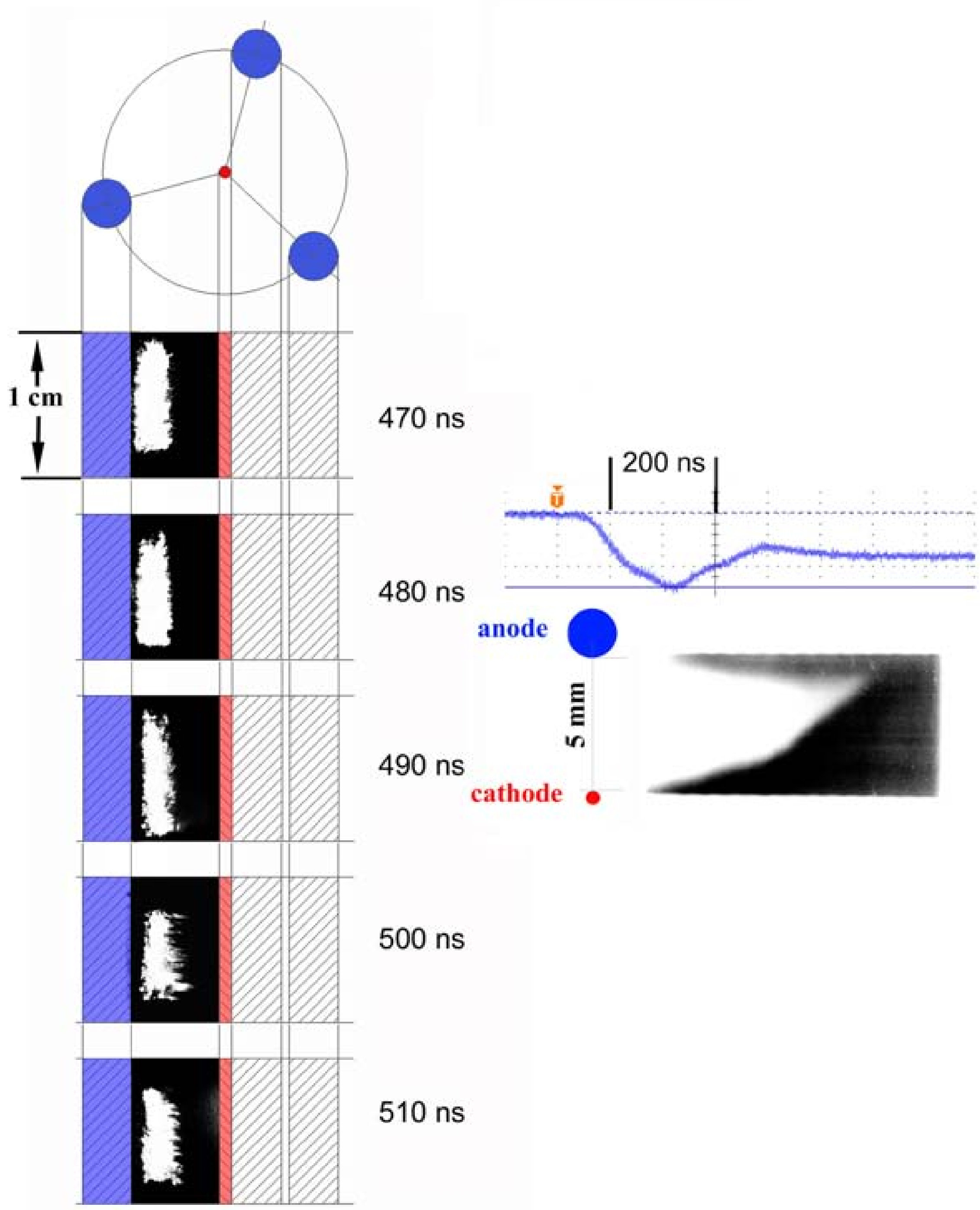

Figure 2.27. Left: laser shadow photographs of expanding electrode plasma in the case of Au cathode (red); the zero point of time is the current start. Right: the oscillogram of input current and the chronogram of plasma expansion.

2.4.2 Angara-5-1 Experiments to study the current-carrying electrodes expansion under the effect of SXR, by the different electrode materials [47]

In the concept of the rep-rate Z-pinch-based IFE reactor [1,5], it is necessary that the processes proceeding on the surface of vacuum magnetically insulated transmission lines (MITL) used to deliver electromagnetic power to the load should be investigated. The linear current density at the electrode can achieve 10 MA/cm. At these linear densities the electrode will explode forming a plasma layer on its surface. A normal operation of such MITL, to the great extent, depends on the parameters of the arising plasma layer. The plasma layer formation can result in ion and electron current leakage through a vacuum gap of MITL and in shunting by plasma. The rate of plasma production on the electrode surface could be also raised by soft X-radiation arising at current flowing across the load. Our preceding contract included an experiment on the plasma production on stainless steel electrodes under conditions of both high current density and their irradiation with soft X-rays (SXR) from the array being compressed. Some alternatives of a generator for a repetitive facility are considered where the MITL electrodes are made from different materials. In the given work we are to perform some experiments similar to those conducted earlier, but with lead and aluminum electrodes.

The present work is devoted to an experimental investigation into the process of the plasma production on SXR - radiated electrodes of stainless steel, lead and aluminum at linear current densities of an order of 1 MA/cm. The work is aimed at developing and refining the results of work [5] and the contract report.

2.4.2.1 Experimental Arrangement

The experiments were carried out on the Angara-5-1 facility [48]. The SXR source was Z-pinch produced at current implosion of a wire array. The megaampere current flowing is provided with a generator of the Angara-5-1 facility. The wire array is 18 mm in height and 8 or 12 mm in diameter. The array contains 40-60 tungsten wires 6-7 μm in diameter. To locate the wire array there are symmetrical cavities with their diameters of 10 or 14 mm in the investigated anode and cathode parts, respectively. The wire array is 1 mm distant from the electrode. The distance between the investigated anode and cathode parts is 3-5 mm.

The work is aimed at investigating the processes of plasma production on the surface of electrodes made from different materials. In the previous work the investigated electrodes were made from stainless steel. In the present work they are from lead and aluminum. That is why the experiment was carried out in two variants. In the first variant lead electrodes were used, in the second they were aluminum.

Figure 2.28 displays a layout of the wire array and the studied electrodes in the first

Variant I - lead electrodes

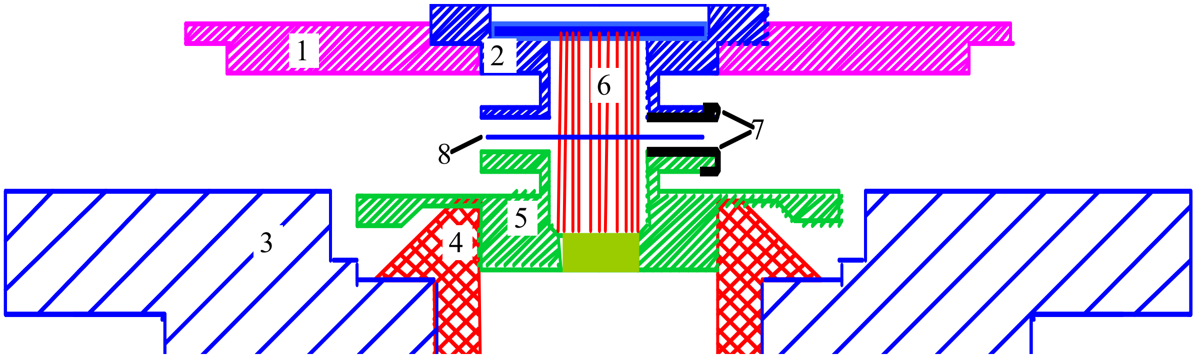

Figure 2.28. The layout of the wire array and electrodes under study in variant 1.
1 - anode
2 - expendable anode electrode;
3 – cathode;
4 - prepulse switch;
5 - expendable cathode electrode;
6 - wire array 8 mm in diameter;
7 - lead-covered electrode part;
8 - image of the inlet slit of the optic streak camera, i.e. the area from which an optical emission is detected with time resolution and with spatial resolution along indicated line 8.

Figure 2.29. Photos of expendable electrodes, left - anode, right cathode. The central hole diameter is 10 mm, the square size on paper is 5 mm. The left half of the studied surfaces (24 mm diameter) of each electrode is covered with lead.

variant. In this case a comparison of the plasma expansion from the electrodes from stainless steel and lead in one shot was made. To juxtapose the plasma expansion dynamics in only one shot half of the studied stainless steel anode was covered with lead foil 100 μm thick. The line separating the covered and uncovered electrode part passed through the electrode axis. To keep the anode surface flat a sample 100 μm thick was taken in the very point of the electrode where lead is to be fixed. The same lead foil was fixed on the cathode in the same manner. The photos of the expendable anode and cathode electrodes studied are shown in Figure 2.29. On mounting the electrodes were oriented so that the anode part covered with lead was over the cathode part covered with lead. Besides, the line separating the covered and uncovered electrode parts was oriented in the direction of observation. In Figure 2.28, this direction is normal to the drawing plane.

Such variant of the experiment made it possible to observe the difference in the plasma parameters in one shot that improves the experiment reliability.

Variant 2 - aluminum electrodes

Figure 2.30 shows a layout of the wire array and the electrodes studied in the second variant. In this case an investigation of the plasma expansion from the aluminum electrodes was carried out.

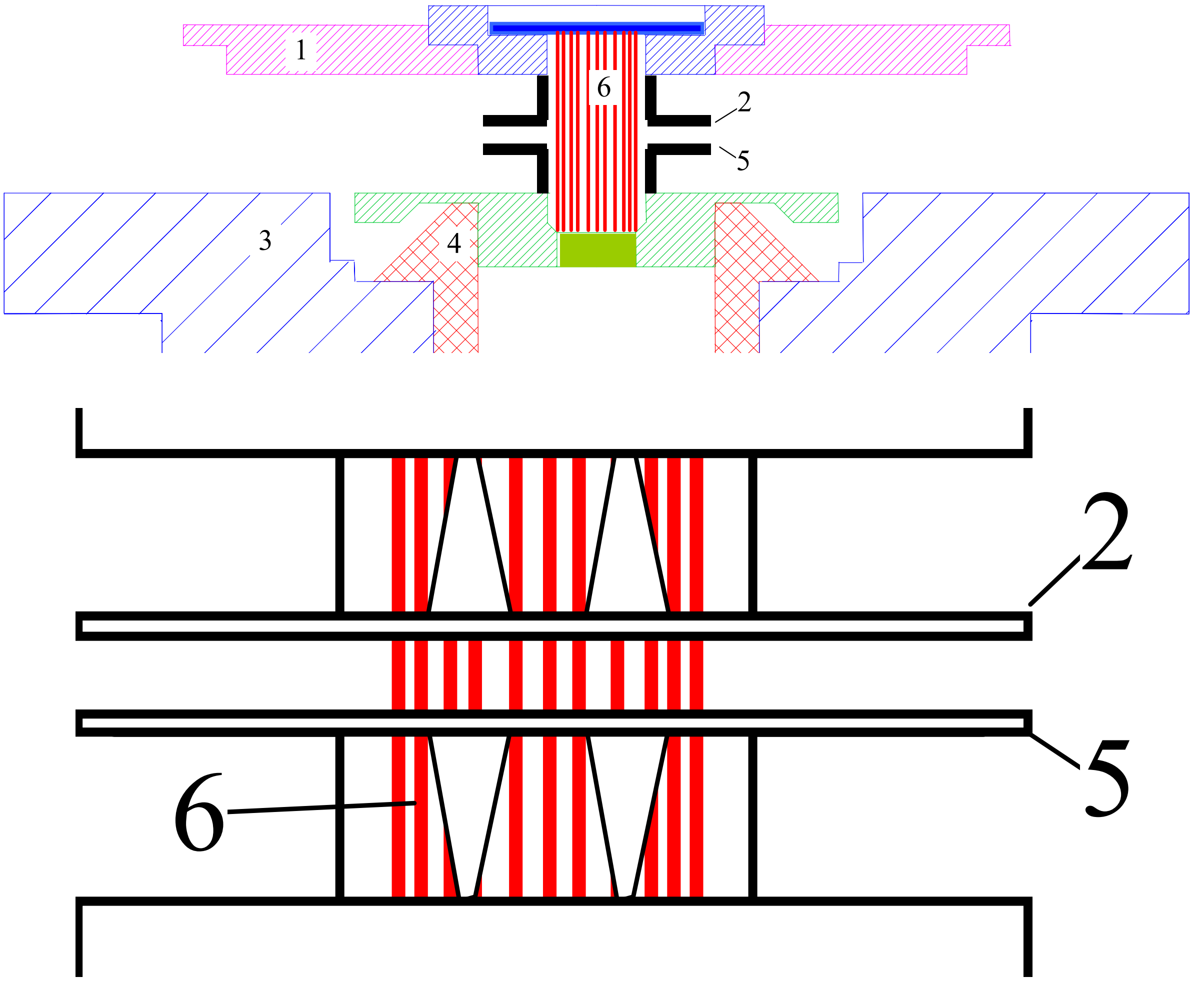

Figure 2.30. A layout of the wire array and the electrodes studied in variant 2. In the lower part of the drawing the wire array and the studied electrodes with trapezium form holes are presented in a close-up view.

1 – anode;
2 - expendable anode electrode;
3 – cathode;
4 - prepulse switch;
5 - expendable cathode electrode;
6 - wire array 12 mm in diameter.

The expendable anode and cathode electrodes under study were made from aluminum 300 μm thick. Their vertical cylindrical surfaces had trapezium-form holes that was defined by their construction and fixing. It should be noted that the time of the magnetic field diffusion in aluminum 150 μm thick (it is half-width of the electrodes) is about 400 ns. Since the current duration is about 100 ns, the current appears to flow over the entire surface of the studied electrodes even with holes.

Diagnosis techniques

The set of diagnosis techniques used in the test involved the following.

- The full current flowing through the liner load was detected by eight B-dot probes located on a radius of 55 mm from the liner axis.
- The voltage drop between the anode and cathode near the wire array was taken on a radius of 6 cm with an inductive divider [49].
- The set of four XRD was 3.5 m distant from the wire array in the radial direction. The time resolution was 0.7 ns.
- An X-ray pinhole camera was employed to obtain integral-in-time images. The spatial resolution on the object was 30 μm mm for the energy quanta of 700 eV. A small inlet hole in the camera prevented the fixation of the image details in quanta below 60 eV.

In variant 1, the optical streak camera was employed to detect the glow in the visual spectral range in the process of implosion. The time resolution of the optical streak camera of the visual range was 0.3 ns. The spatial resolution on the object was under 80 μm, while the depth of sharpness in the object area was + 23 mm in the radial direction. The device was adjusted so that the light can fall into its slit from a narrow region (90 μm) 24 mm long spaced 1.5 mm over the cathode (see Figure 2.28(8)). Such location permitted the comparison of the produced plasma glow over the cathodes of stainless steel and lead to be made simultaneously in one shot.

In variant 2, the plasma production on the electrode surfaces was detected by taking frame pictures of the surfaces in the SXR of with a nanosecond resolution using an X-ray optical converter on the basis of a pinhole camera and micro-channel plates (MCP). A 4-frame X-ray camera on the basis of a MCP brightness amplifier was used to detect 4 images in SXR by means of four pinhole cameras. The time of frame exposure was 3 ns. The frame X-ray camera is sensitive to X-quanta of energy in the range from 20 to several thousand eV with a maximum spectral response in the range of 200 eV. The spatial resolution of the technique is 85-150 μm on the object for the X-ray energy quanta ranging from 250 to 600 eV.

2.4.2.2 Experimental Results

Results of variant 1: lead irradiation

In this experiment in different shots the lead foil position varied. In some shots the electrode parts covered with lead foil were located at the right and uncovered ones at the left when viewed from the observation side. In other shots the situation was the opposite one. This made possible the test of the technique and exception of uncertainties attributed to a possible dependence of the relative aperture of the detector upon the position of the object studied and the difference in the realization of implosion processes in different shots.

Figure 2.31 presents a comparison of two detected optic streak camera images of the liner optic glow and the plasma generated on the electrodes. In the first shot (left part of the Figure 2.31) the electrode parts covered with lead foil were located at the right and those uncovered at the left when viewed from the side of observation. In the second shot (left part of the Figure 2.31) their position was quite contrary. A conventional representation of the lead foil position is given in the upper part of the Figure 2.31.

In the middle of Figure 2.31 a comparison of two detected images of the liner optic glow and the plasma generated over the electrodes is presented. The upper part on the images corresponds with the right part of the object studied, while the bottom with the left part. Thus in the left part of the Figure 2.31 the glow over lead is consistent with the upper part of the streak image, and in the right - the lower part of the streak image. It is easy to see in both images the appearance of plasma glow near the cathode just after final compression of pinch.

The bottom part of Figure 2.31 shows time dependencies of the current derivative through the discharge, voltage on the liner unit and SXR power. The current amplitude for both cases is around 2 MA, its rise time is ~ 95 ns. The minimum radius of the investigated electrodes is 5 mm, so the maximum linear current density was found to be 0.6 MA/cm. The maximum magnetic field on the electrode surface proved to be 0.8 MG. The detected SXR power for both cases was about 1.5 TW. Since in the given construction at a distance of 3.5 m from the wire array one could observe only 5 mm of the entire Z-pinch length, it can be considered that the linear SXR source emits 1.5 TW/0.5 cm = 3 TW/cm. For such a source at a distance of 5 mm from it the density of power flux was estimated as a maximum of 0.9 TW/cm^2.

In this variant several shots were fired. There the position of the lead part of the electrode varied, i.e. at the right or at the left relative to the liner axis, when viewed from the optic streak camera. The obtained images evidence the absence of any reliable difference in the plasma glow over the both stainless steel and lead cathodes.

Results of variant 2: aluminum irradiation

Figure 2.32 presents three subsequent soft X-ray frame images of the investigated aluminum electrodes in the process of current flowing through them and soft X-irradiation. The distance between the investigated anode and cathode parts was about 3.5 mm. The time synchronization of frames with current and SXR is in Figure 2.33. Figure 2.33 shows time dependencies of the current derivative through the charge (bottom curve), SXR power (upper curve) and three narrow peaks corresponding in time with three frames of Figure 2.32. The current amplitude is around 3 MA rising up to its maximum in ~ 95 ns. The minimum radius of the investigated electrodes is 7 mm, so the maximum linear current density was 0.7 MA/cm. The maximum magnetic field on the electrode surface was 0.85 MG.

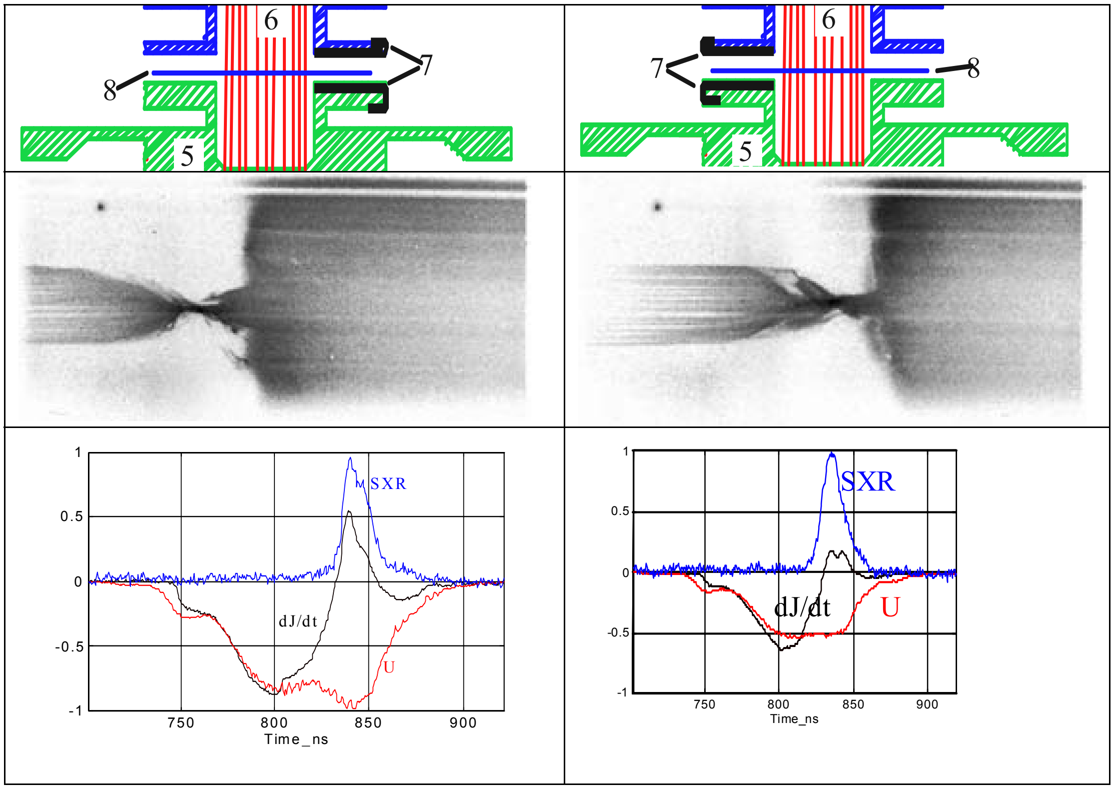

Figure 2.31. Comparison of two optic streak camera images of the optical glow from the both liner and plasma on the electrodes for different foil position. Upper part: a conventional representation of the lead foil position. Middle part: two optic streak camera pictures. In the left streak image the glow over lead is consistent with the upper part of the streak image, while in the right - with the bottom part of the streak image. The duration of these streak images is 145 ns, the time axis is directed from left to right. Its vertical size is 24 mm. Bottom part: time dependencies for two cases of the current derivative through the discharge (dJ/dt, negative amplitude 4*10^{13} A/s), SXR power (SXR, Amplitude 1.5 TW/4 π) and voltage on the liner unit (U, amplitude 500 kV).

The detected SXR power was about 2 TW. Since in the present construction at a distance of 3.5 m from the wire array observable were only 3.5 mm of the full pinch length, it may be considered that the linear SXR source emits 2TW/0.35cm =5.7 TW/cm. For such a source at a distance of 7 mm from it the density of power flux was estimated as 1.2 TW/cm^2 at a maximum. The radiated energy is 1, 16 and 38 kJ for frames 1, 2 and 3. The density of energy flux at a distance of 7 mm from the source is 0.6, 10 and 25 kJ/cm^2 for frames 1, 2 and 3.

The first frame of the images available was taken at the very beginning of the SXR rise. The plasma glow inside the wire array 12 mm in diameter is clearly seen on the

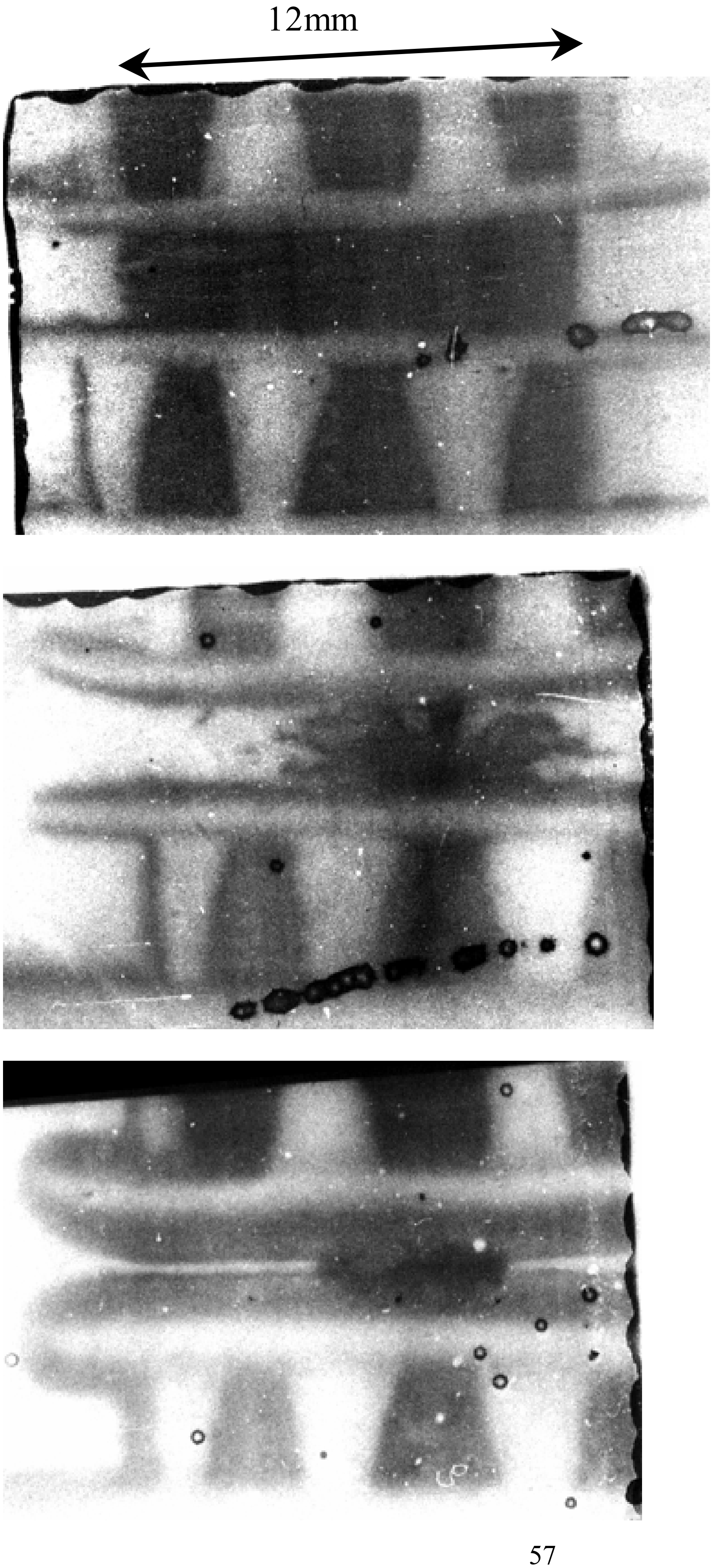

Figure 2.32. Three subsequent SXR frame images of the studied aluminum electrodes.

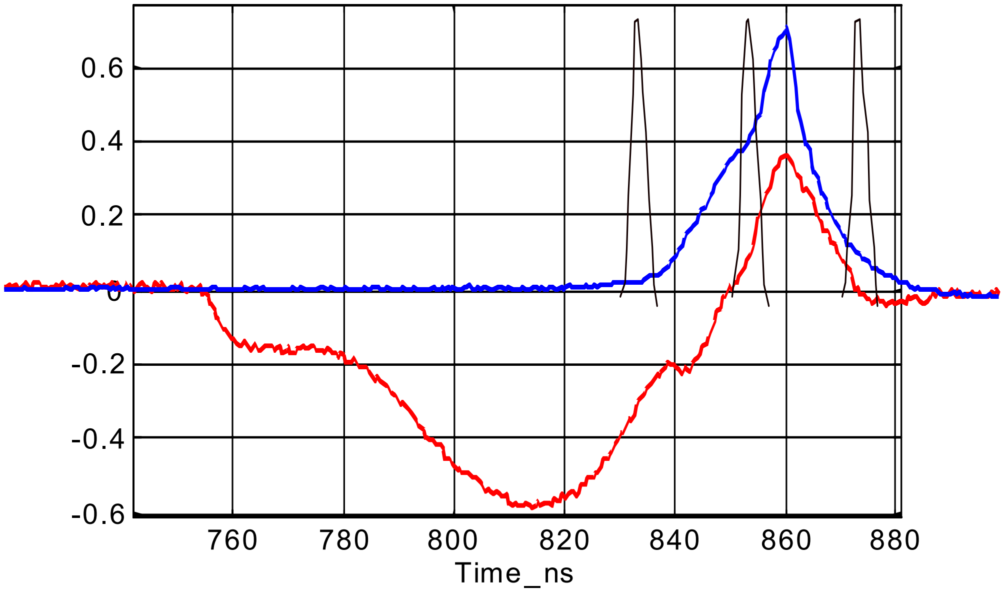

Figure 2.33. Time dependencies of the current derivative through the discharge, (bottom curve), SXR power (upper curve) and three narrow peaks corresponding in time with three frames in Figure 2.31. Vertical units are arbitrary.

image. In addition, through the trapezium form holes in the vertical cylindrical electrode surfaces one can also see the plasma glow inside the wire array.

The maximum diameter of the cathode and anode surfaces investigated was 19 mm in this scenario. The energy flux density at the 19 mm diameter is 0.4kJ/cm^2 for frame 1. On this diameter one can clearly observe the plasma layer glow about 0.8 mm thick. Note, that the plasma production process proceeds on both sides of the electrode as the rear side of the electrodes is irradiated through the trapezium form holes in the cylindrical electrode part. Since the thickness of the electrode itself is 0.3 mm, the thickness of the plasma layer formed by this moment may be considered as 300 μm. The visible gap reduced from 3.5 mm to 3 mm.

The second frame is taken on the leading front of the SXR rise. The plasma glow of the forming pinch is clearly seen in the center of the image. The plasma in the form of jets is carried to the axis. On the axis there occur their collisions and formation of the emitting Z-pinch. Just as in frame 1, the plasma glow inside the wire array is seen through the trapezium form holes in the vertical cylindrical electrode surfaces. The visible gap reduced to 2 mm.

Frame 3 shows the moment of the pinch recession. The visible gap reduced to 0.3 mm. The value of the average rate of the plasma expansion (visible in SXR) between frames 1 and 2 is 25 km/s on each of the electrodes. The value of the average rate of the plasma expansion (visible in SXR) between frames 2 and 3 is 42 km/s on each of the electrodes. The inner and outer radii of the electrodes in this scenario were 7 and 9.5

mm. It should be noted, the visible plasma expansion was independent on the radius within these limits.

The conclusions for these Angara-5-1 experiments are as follows. In the current experiment the production and dynamics of the near-electrode plasma on the electrodes from different materials, i.e. aluminum, stainless steel and lead have been investigated. The distance between the investigated anode and cathode parts was 3-5 mm. The maximum linear current density was 0.7 MA/cm and the time of rising to its maximum was about 100 ns. The results obtained show no indication of any detected difference in the plasma glow over the stainless steel cathode and the lead cathode.

As to the aluminum electrodes, it turned out that at an energy flux density of 10-25 kJ/cm^2 the average rate of plasma expansion was 42 km/s. At this the linear current density was 0.7 MA/cm. The maximum magnetic field on the electrode surface was 0.85 MG.

Hence, the experiments performed allow us to believe that under conditions of [1] at a current density of 0.7 MA/cm and a surface density of the SXR flux 1 TW/cm^2 on the lead electrodes the plasma production process is no more intensive than on the stainless steel electrodes. Under above-said circumstances the energy could be transferred to the load via MITL from the stainless steel electrodes or lead electrodes.

2.5 RTL Misalignment Sensitivity Study using a 3D Circuit Model *(D. L. Smith, SNL)*

The purpose of this study was to conduct a circuit-model-based sensitivity study to determine allowable misalignment or tolerance variation between the inner and outer recyclable transmission line (RTL) cones that results in an asymmetric Z-pinch wire array load current. It is not yet clear how much current asymmetry can be “tolerated” by the Z-Pinch wire-array/imploding plasma/hohlraum/target ignition system. Certainly the pinching tungsten plasma will do some corrective smoothing of unbalanced currents. We understand that fusion targets require a high degree of X-ray symmetry, but the X-ray sensitivity to the current irregularities can not be addressed in this summary. To acquire useful preliminary information about the possible current imbalance in a timely fashion the following assumptions and directions were taken.

- The smallest vacuum gap shall be about 2 mm. Smaller gaps would increase the risk of contact shorting or vacuum arcs.
- The maximum impedance shall be about 0.5 Ω to not limit driver efficiency.
- Sensitivity networks shall be done with Micro-Cap transmission line (T-Line) models.
- A straight conical geometry is assumed to reduce the difficulty in estimating impedances.

- MITL models will need to be added eventually to improve accuracy.
  - Operating gaps are approximately 80% of vacuum gaps.
  - A flow loss model should be included.
  - Wave front erosion should be included.
- The initial RTL 3-D simulation shall be with a 2x4 section array.
- A 4x4 section array, or larger, is desirable if the software can support it.
- A constant gap RTL means increasing impedance toward the load.
- A constant impedance RTL means a decreasing gap toward the load.
- A "rotational" misalignment may be self-compensating, not worst case.
- A laterally "translated" inner cone could be a worst case, with a reduced gap on one side and a larger gap on the opposite side.

Figure 2.34 shows the geometry and size of the basic magnetically insulated vacuum transmission line (MITL) that would be reasonable for a Z-Pinch IFE power plant. It has a height of 4 m and a base radius of 1 m with a gap between the two coaxial cones of a few millimeters. Table 2.3 lists the diameters, circumferences, and circular propagation times of interest along 1-m steps of the RTL to aid in estimating the local impedances between the conductors.

Table 2.3. RTL Parameters of Interest

Vertical Position	Dia. (cm)	Cir. (cm)	τcir (ns)
4	202	635	21.2
3	154	484	16.1
2	106	333	11.1
1	58	182	6.07
0	10	31.4	1.05

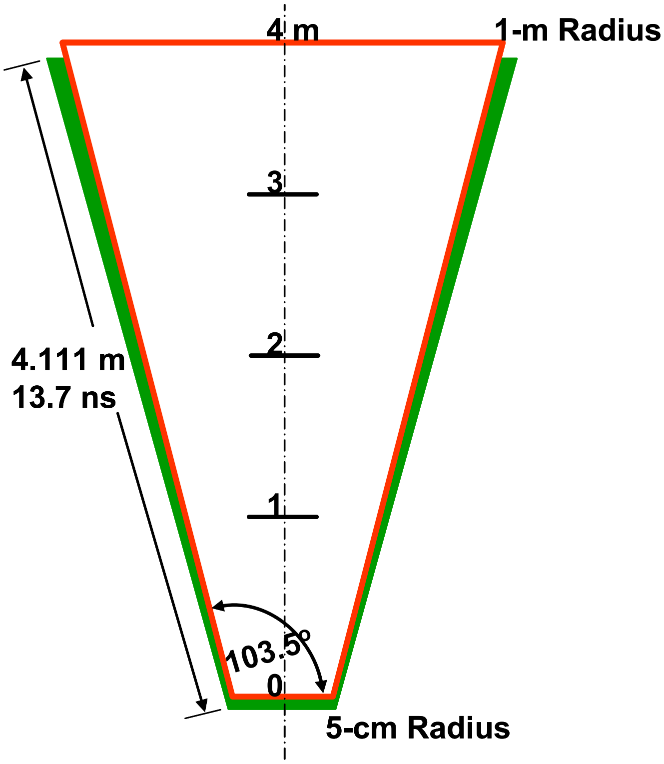

Figure 2.34. A Z-Pinch IFE power plant RTL.

Table 2.4. Constant Gap Vacuum Impedance

Gap (mm)	1.5	2	2.5	3	3.5	4	4.5	5
Z_4 (Ω)	0.089	0.12	0.15	0.18	0.21	0.24	0.27	0.30
Z_3 (Ω)	0.12	0.16	0.20	0.23	0.27	0.31	0.35	0.39
Z_2 (Ω)	0.17	0.23	0.28	0.34	0.40	0.45	0.51	0.57
Z_1 (Ω)	0.31	0.42	0.52	0.62	0.73	0.83	0.94	1.04
Z_0 (Ω)	1.83	2.45	3.08	3.71	4.35	5.00	5.66	6.32

Table 2.4 shows impedance parameters of interest along 1-m steps of the RTL for vacuum gaps between 1.5 and 5 mm. The subscripts in the first column refer to the vertical axial locations along the RTL. These values are used to build the circuit models described in this summary. The highlighted cells show how the gap must vary for a constant ~0.3-Ω impedance. The impedance estimates used in this document are derived from the basic coaxial and parallel plate geometries, which should be approximately accurate over small regions.

$$Z_{coax} = 60 \ln (b/a) \qquad Z_{//} = 377 (d/w)$$

2.5.1 Circuit Model Development

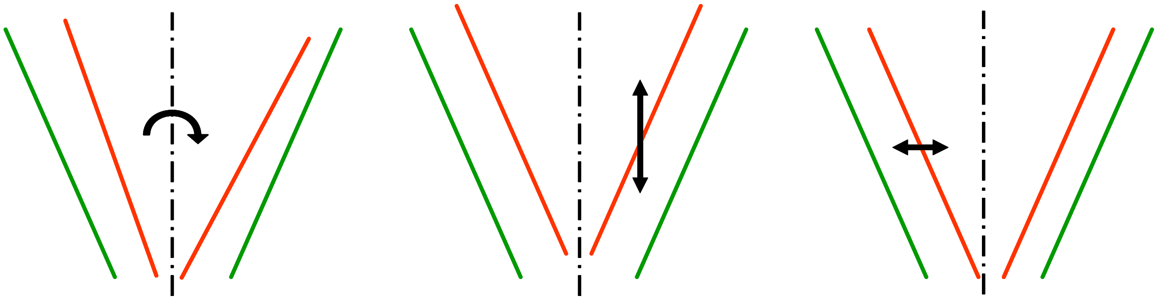

Figure 2.35. RTL misalignment configurations: Rotational, Axial Offset, and Lateral Offset.

The illustrations in Figure 2.35 represent the three primary misalignment possibilities. For the case of a rotation of the inner cone with respect to the outer cone, along any side the gap will vary from larger to smaller than the nominal gap, and the average is close to the original. Load current asymmetry is assumed small. In the case of an axial translation, the impedance is changed throughout the RTL, but it still has uniform azimuthal symmetry. The current amplitude may change, but it has no asymmetry. For the lateral translation case, the impedance is high on one side and low on the other; in between it is about the nominal value. Load current asymmetry may be the worst case under these conditions.

Figure 2.36 demonstrates an axial view of the RTL to show an initial eight-section model approach using two “annular” rings each cut into four quadrants. Each section may be represented by a “radial” inward-pointing T-line model plus azimuthal T-lines communicating with adjacent sections. In a likewise fashion, a 12-section model could have three concentric rings, each cut into quarters (3x4). The 16-section model has four concentric rings, each cut into quarters (4x4).

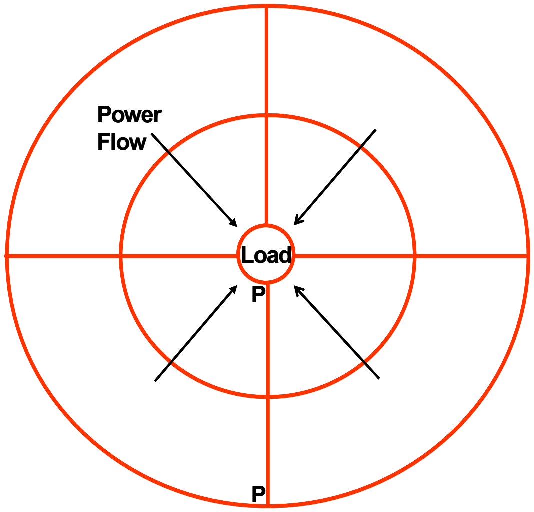

Figure 2.36. 2 X 4 section array.

The first 2x4 model of 8-sections with a constant impedance of 0.1-Ω is shown in Figure 2.37. This network simulates the RTL of Figure 2.36, which has been “cut” along P–P and folded open, but maintains electrical integrity; note the nodes labeled P1 through P8 on both sides that are effectively connected. The values on the right side of Figure 2.37 identify both the radial (or vertical) and azimuthal T-line models, a pair of which represents each section. Hence, four 0.4-Ω radial T-lines in parallel provide an overall 0.1-Ω RTL. The equivalent source is chosen to provide between 60 and 70 MA at about 6 MV within about 100 ns to the load, which is represented as a fixed 7 nH (four 28-nH inductors in parallel).

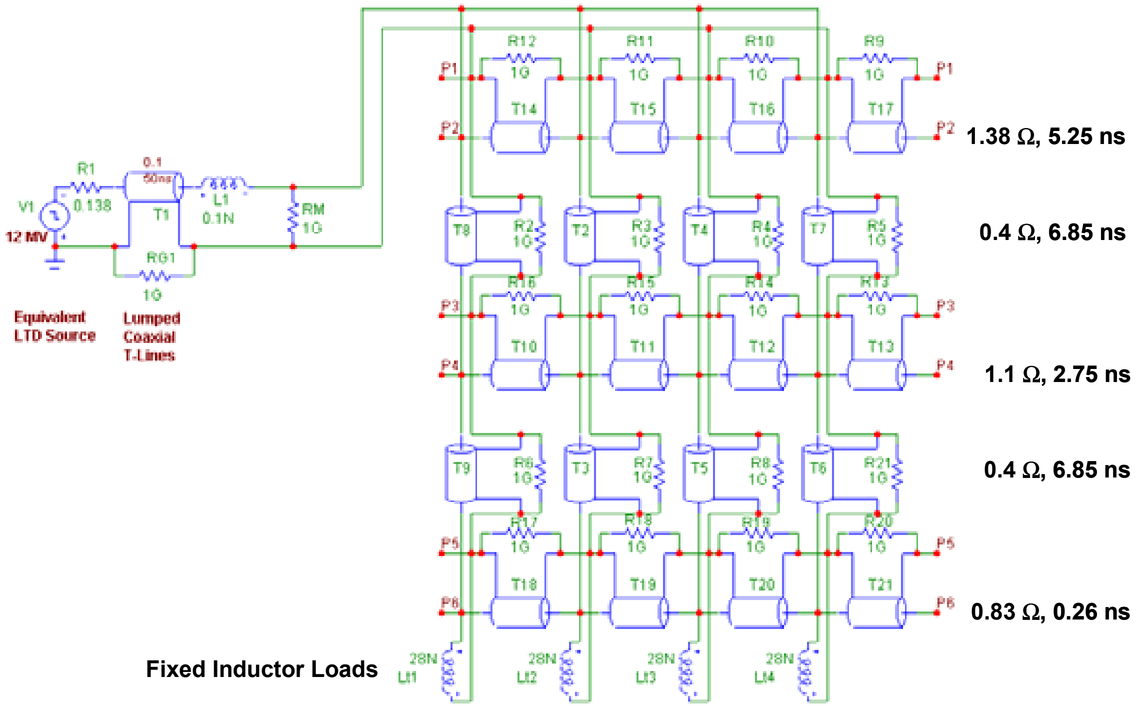

Figure 2.37. Initial 2x4 circuit model using radial and azimuthal transmission lines.

Waveforms resulting from the 2x4 balanced, 0.1 Ω constant impedance model of Figure 2.37 are seen in Figure 2.38. The horizontal scale is 100 ns per division. The load current represents all four of the inductor currents reduced by a factor of two and overlaid to show that they are identical in the nominal aligned RTL case.

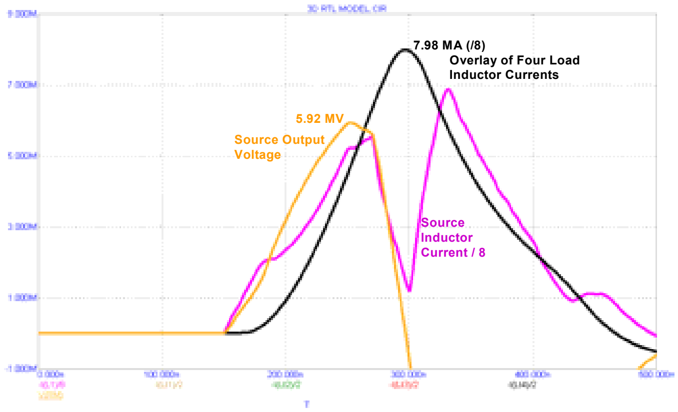

Figure 2.38. Results from the balanced 2x4 RTL circuit model.

In order to test the sensitivity of the 2x4 model, a metric or figure of merit was chosen to be the relative load current spread due to varying the impedance by ± 50% to simulate an unbalanced RTL. The impedances of vertical T-line column 4, above inductor Lt4, in the 2x4 eight-section network were increased by 50% and the adjacent "horizontal" lines increased by 25%. The impedances of vertical column 2, above inductor Lt2 (opposite side), were decreased by 50% and the adjacent horizontal lines decreased by 25%. The T-lines in columns 1 and 3 remained the nominal 0.4-Ω value. The resulting spread in the four load inductor currents is shown in Figure 2.39. Note that these curves are the magnified peaks of the load currents so that the spread is more easily distinguishable. The spread for the overall 0.1-Ω model is around 76 kA about a nominal 16.086 MA, or ~0.47%. Modifying the model for a ±50% impedance spread about an overall 0.5 Ω, resulted in a slightly smaller load current spread of ~0.39%.

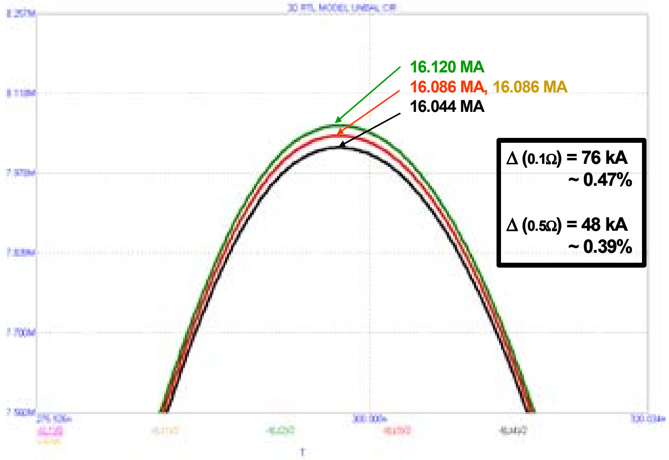

Figure 2.39. Typical spreads for the constant impedance ± 50% RTL geometry.

Since part of the load inductance is really varying with time, some simple inductor models that varied as a function of the current, between a fixed 4 nH and a peak of 12 nH, were substituted into the 2x4 network model. Modifying this model for a ± 50% impedance spread about an overall 0.3 Ω, resulted in a load current spread of ~0.67%. The time varying loads tend to push the software graphics resolution to the point where the waveform smoothness is lost creating some inherent error that needs further study.

The proper performance of the 2x4 model and the optimistic spread results prompted the development of a more detailed 4x4 model of a 16-section, varying impedance RTL with T-line values consistent for a constant 3-mm gap. A constant gap design is probably more realistic than the constant impedance case. Figure 2.40 displays the expanded architecture of the 4x4 network. The Micro-Cap software supported this network also without any difficulty and generated waveforms in approximately five seconds, suggesting that even a much more detailed circuit model is a reasonable option. The waveforms in Figure 2.41 were produced by the circuit schematic in Figure 2.40. The horizontal scale is 100 ns per division. As in Figure 2.38 but more pronounced, the large dip in the middle of the source current is due to a polarity reversed reflection.

To force some imbalance in the load currents, the impedances of vertical column 4 in the 4x4 16-section network were <u>increased</u> to that of a 4-mm gap and the adjacent "horizontal" lines to a 3.5-mm gap. The impedances of the vertical column 2 were <u>decreased</u> to that of a 2-mm gap and the adjacent horizontal lines decreased to a 2.5-mm gap. The magnified peak currents of Figure 2.42 show the spread from the unbalanced 2-3-4-mm laterally translated, constant gap, varying impedance RTL. The spread between the lowest and highest peaks is approximately 0.65% of the nominal load currents. Applying the time-varying inductor load models to the 2-3-4-mm unbalanced 4x4 constant-gap RTL network produced a spread of about 0.42%, but again on a "less smooth" waveform. (This constitutes a reduction in spread as compared to the increased spread when the time-varying inductors were included in the constant impedance model.)

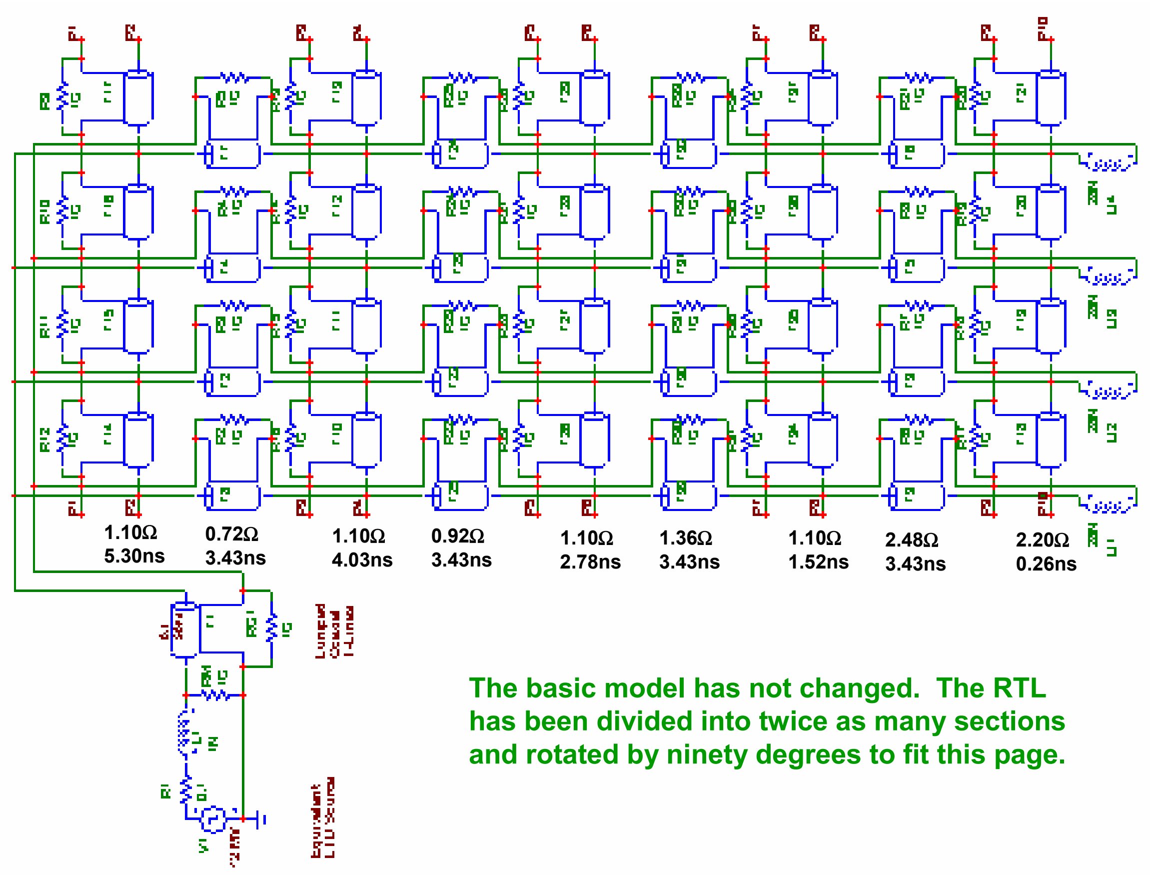

The basic model has not changed. The RTL has been divided into twice as many sections and rotated by ninety degrees to fit this page.

Figure 2.40. A 4x4 model of 16-section constant 3-mm gap, varying impedance RTL.

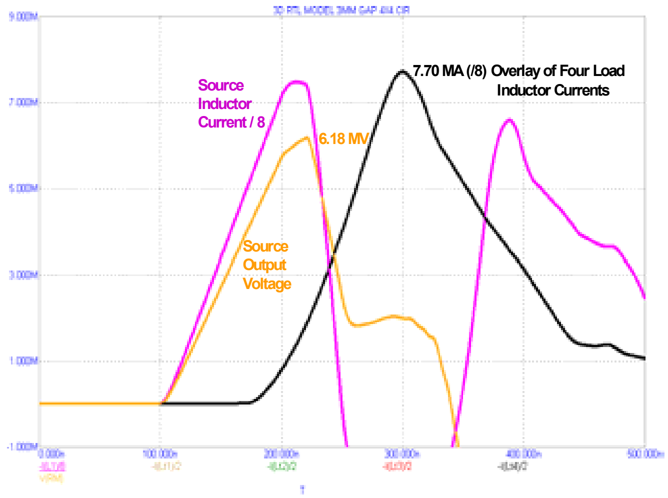

Figure 2.41. Waveforms produced by the circuit model of Figure 2.40.

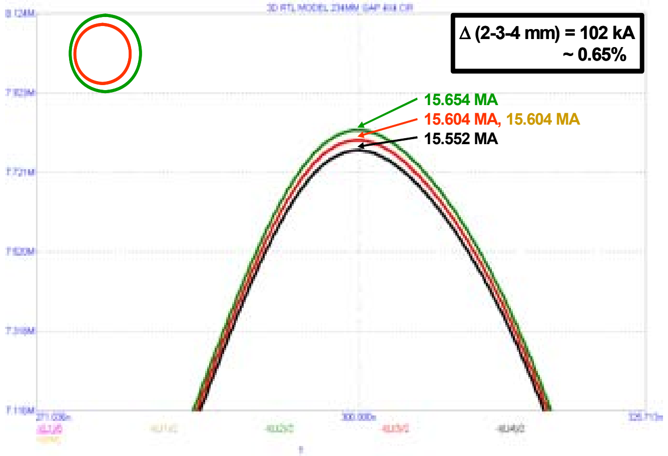

Figure 2.42. Load current spread from the 2-3-4 mm laterally translated case.

One obvious question is how does the load current asymmetry vary with smaller and larger lateral translations of the inner RTL cone as compared to the 2-3-4-mm case. To address that question the T-line values of the baseline model in Figure 2.40 were modified and the transient simulation was run again. The impedances of vertical column 4 in the 4x4 16-section network were <u>increased</u> to that of a 3.5-mm gap and the adjacent "horizontal" lines to a 3.25-mm gap. The impedances of the vertical column 2 were decreased to that of a 2.5-mm gap and the adjacent horizontal lines decreased to a 2.75-mm gap. Using the same nomenclature this new model will be designated the 2.5-3-3.5-mm case, whose resulting spread is displayed in Figure 2.43. The relative spread for this “tighter” case is about 0.32%.

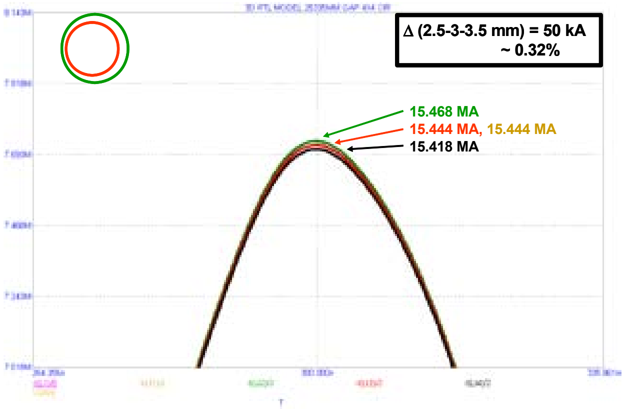

Figure 2.43. Current spread from the unbalanced 2.5-3-3.5-mm translated constant gap, varying impedance RTL.

To alternatively look at a somewhat “looser” case, the impedances of vertical column 4 in the 4x4 16-section network of Figure 2.40 were increased to that of a 4.5-mm gap and the adjacent “horizontal” lines to a 3.75-mm gap. The impedances of the vertical column 2 were decreased to that of a 1.5-mm gap and the adjacent horizontal lines decreased to a 2.25-mm gap. This new model will be designated the 1.5-3-4.5-mm case, whose results are displayed in Figure 2.44. The relative spread for this case is about 1.05%.

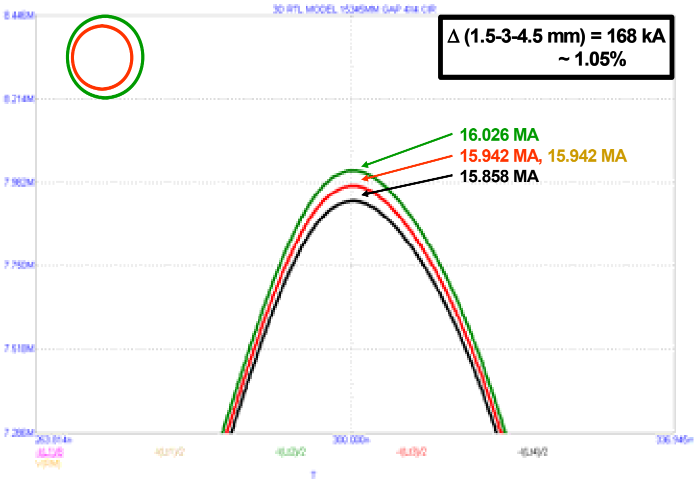

Figure 2.44. Current spread from the unbalanced 1.5-3-4.5-mm translated constant gap, varying impedance RTL.

Another possibility for misaligning the RTL conductors is for one of the cones to be out-of-round. Consider an oval-shaped inner cone for convenience. To address this situation the impedances of vertical columns 2 & 4 in the 4x4 16-section network of Figure 2.40 were increased to that of a 4-mm gap and the adjacent horizontal lines kept to a 3-mm gap. The impedances of the vertical columns 1 & 3 were decreased to that of a 2-mm gap and the adjacent horizontal lines kept to a 3-mm gap. The difference with this configuration from those previously discussed is in the fact that there are now two larger gaps and two smaller gaps with respect to the nominal spacing (instead of one each). This is partly due to choosing to break the circular load into quadrants for modeling purposes. This new model will be designated the 4-2-4-2-mm case, whose results are displayed in Figure 2.45. The relative spread for this case is about 0.33%.

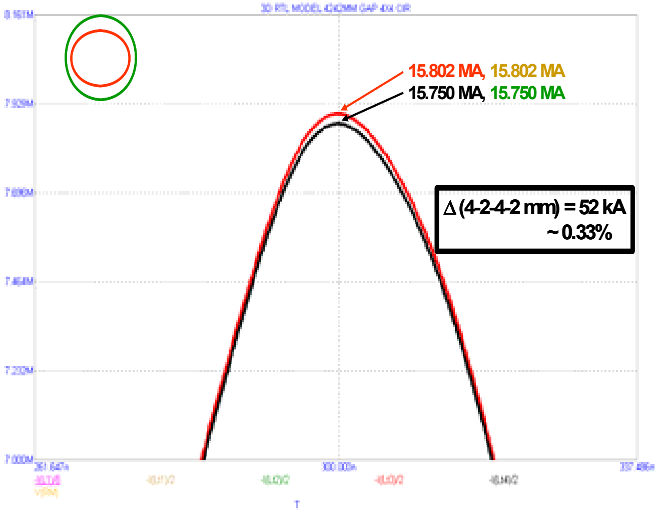

Figure 2.45. Current spread from the unbalanced 4-2-4-2-mm "oval-shaped" constant gap, varying impedance RTL.

2.5.2 Analysis of Model Performance

Only a few circuit architectures and RTL geometries have been considered at this point due to limited time, but hopefully these choices serve to bracket the issues of interest until resources are available to carry the work further. The Table 2.5 summarizes these cases and their preliminary results. The "Delta-value" items in the table are the minimum-to-maximum spreads.

Table 2.5. RTL Cases Considered Thus Far

Z-PINCH LOAD CURRENT SPREAD DUE TO MISALIGNED RTL INNER CONE
Via 2X4 and 4X4 Micro-Cap T-Line Networks -- Aug 06

Configuration [mm]	Delta-X [mm]	Delta-I [%]	Delta-I [kA]	Av Peak-I [MA]	Range-Z [Ohms]	Remarks
2.5-3-3.5	**1**	**0.32**	**50**	**15.444**	**0.15-0.73**	Lateral, Constant Gap, Varying Impedance, 4X4
2-3-4	**2**	**0.65**	**102**	**15.604**	**0.12-0.83**	Lateral, Constant Gap, Varying Impedance, 4X4
1.5-3-4.5	**3**	**1.05**	**168**	**15.942**	**0.09-0.94**	Lateral, Constant Gap, Varying Impedance, 4X4
4-2-4-2	**2**	**0.33**	**52**	**15.776**	**0.12-0.83**	Oval, Constant Gap, Varying Impedance, 4X4
2-3-4	**2**	**0.42**	**70**	**16.756**	**0.12-0.83**	**Varying Load**, Lateral, Constant Gap, Varying Impedance, 4X4
[Ohms]	**[Ohms]**					
0.05-0.1-0.15	**0.1**	**0.47**	**76**	**16.086**		Lateral, Constant Impedance, 2X4
0.15-0.3-0.45	**0.3**	**0.40**	**56**	**13.870**		Lateral, Constant Impedance, 2X4
0.25-0.5-0.75	**0.5**	**0.39**	**48**	**12.333**		Lateral, Constant Impedance, 2X4
0.15-0.3-0.45	**0.3**	**0.67**	**112**	**16.696**		**Varying Load**, Lateral, Constant Impedance, 2X4

Note again that converting the fixed load to a time-varying load resulted in a higher spread (0.67%) for the constant impedance 2x4 RTL and a lower spread (0.42%) for the constant gap 4x4 RTL. The time-varying loads require additional analysis.

The graph in Figure 2.46 plots some of the values in Table 2.5 to show the dependence of the load current spread (in percent) on the variation about the nominal gap (in millimeters). More specifically, it is the current spread due to a misaligned constant gap RTL for a lateral translation using the 4x4 network model. The nominal gap is 3 mm about which the different spreads are taken. One conclusion is that the load current

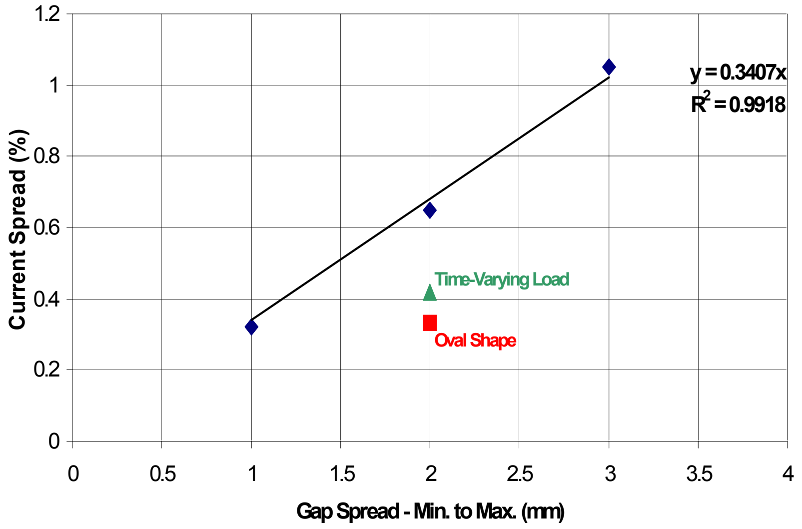

Figure 2.46. Current spread versus gap spread for the 4x4 model.

asymmetry varies linearly with the RTL gap spread, at least within this local parameter space. The deformed oval-shaped inner RTL cone case, shown as the red square, does not cause as much asymmetry as the laterally translated case.

For the constant impedance case using the 2x4 model, Figure 2.47 shows a plot of the load current spread for different impedance ranges. The horizontal axis is the nominal RTL impedance (in Ohms) about which there is a ± 50% variation to represent a misaligned cone in the circuit model. Since it is nearly flat, we can conclude that the load current asymmetry is not a strong function of the impedance over this range of interest.

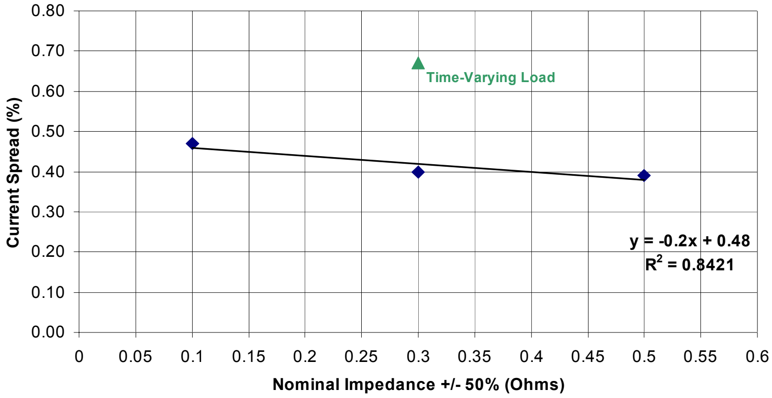

Figure 2.47. Current spread versus impedance spread for the 2x4 model.

2.5.3 Summary of RTL misalignment studies

- Representing the RTL with actual MITL models would reduce the effective operating impedance, produce additional losses, and change peak values, but the "relative" difference or current asymmetry may not be significantly changed.
- The deformed oval-shaped inner cone case does not cause as much asymmetry as the laterally translated circular case, probably because there are two high and two low impedance regions that are closer to each other (90^o instead of 180^o), and they can communicate or compensate somewhat faster.
- Some results have been generated around a nominal 3-mm gap; a similar study of nominal 2 and 4-mm gaps should be done for comparison just to ensure there are no surprises.
- Time-varying loads require additional analysis, since their results have not been very intuitive, thus far.
- Sectioning the load array into sixths (4x6) or eighths (4x8) would produce better azimuthal resolution of the load current distribution, but it would require a significant circuit network development effort, which may not be worth the diminishing returns.

- Any of the discussed Micro-Cap circuit models are available from the author for anyone who wants to duplicate these results or use them as building blocks for further analysis.

2.6 RTL Structural Analysis, Fabrication, and Pressure Testing of Z-PoP (Proof-of-Principle) RTLs *(M.Turgeon, SNL and M.E. Barkey, U. Alabama)*

The cost effectiveness of the Sandia National Laboratories concept of a pulsed nuclear fusion power generating plant hinges, in part, on "transmission lines" that provide a standoff for the target material involved in the nuclear fusion reaction. As a consequence of the pulsed fusion reaction, the transmission lines are consumed at a rate of one pair every 10 seconds. The current concept of the transmission lines is a steel conical shell that will be recycled, providing an impetus for the shell to be as thin as possible.

The operating conditions of the RTL are such that a differential pressure is applied to the surface of the conical shell, promoting a buckling failure mode of the structure that would interfere with the fusion process. In use, the RTL is designed to be subjected to a vacuum on the interior and exterior surfaces, with the larger pressure on the exterior of the RTL. The RTL may buckle if this external pressure differential is great enough. The purposes of the RTL pressure test are to experimentally determine the differential buckling pressure, and experimentally determine the buckled mode shape of the PoP-RTL.

With an external pressure approximately 20 Torr and an internal vacuum, the internal shell will experience a hoop stress. The pressure difference is small enough that it imposes no significant structural issues. However the outer shell will see an external pressure that could collapse it. Therefore it was determined to analyze that outer shell portion of the RTL.

In the following sections, we report on the structural analysis and design of Z-PoP RTLs, fabrication of Z-PoP RTLs, and pressure testing of Z-PoP RTLs.

2.6.1 Structural Analysis and Design of Z-PoP RTLs

To analyze the conical shell structure, two Eigenvalue buckling (Eigenbuckling) methods were used; Finite Element Analysis and a closed form solution, called hereafter as the Singer Solution. Both methods were used to obtain an estimate of the critical buckling load. This critical buckling load is defined as one at which the response of cone will bifurcate, and the response up until this point is essentially linear.

When conducting an Eigenbuckling analysis the purpose is to investigate singularities in a linear perturbation of the structures stiffness matrix. The resulting estimate is valuable only if the linear perturbation is a realistic reflection of the RTL's behavior prior to buckling. Therefore, Eigenbuckling analysis is useful to relative "stiff" structures, where a stiff structure is one that shows only small deformation prior to buckling.

Also with a stiff structure an inelastic response may occur before collapse. In this case, Eigenbuckling analysis provides a useful estimate of the collapse mode shape (circumferential waves, or mode shapes). Only in quite restricted cases (linear elastic, stiff response, no imperfection sensitivity) is it the only analysis needed to understand the structures collapse limit.

Conversely, in some analyses the post-buckled response is unstable and the collapse load is based on an imperfection in the original geometry, such as a ding or a dent in the Pop- RTL cone. In this case, the actual collapse load may be *significantly lower* than the bifurcation load predicted by Eigenbuckling analysis, so that a non-conservative estimate of the structures load carrying capacity is given with the analysis. Therefore, even if the pre-buckling response is stiff and linear elastic, nonlinear load displacement response analysis is generally recommended to augment the Eigenbuckling analysis.

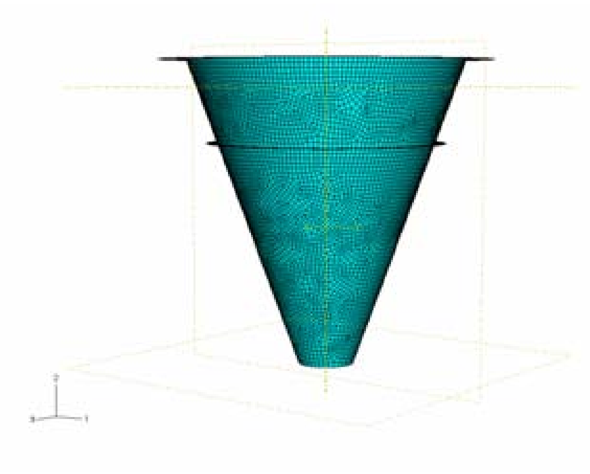

Figure 2.48. RTL (Z-PoP). FEA Finite Element Mesh with 1 stiffener.

As such in the case of a full sized RTL, "perfect" conical geometry was used in the Eigenbuckling analyses. This translates into a conical frustum with the larger radius of 50-cm, the smaller radius of 5-cm, and a cone angle of 12.68 degrees, using 25-mil (0.0635-cm) thick steel. The "perfect" geometry represented the outer shell of the RTL cone, with an added flange at the top for support (boundary conditions). While this geometry was fairly easy to incorporate into the analyses, the greater challenge was to match the "perfect" geometry requirement with available manufacturing techniques that would be introduced into the RTL Model Validation Phase in the RTL Structural Experiments. As will be discussed in that section of this report, some differences were accepted and plans are to incorporate into new, additional analyses in subsequent years.

While this geometry was fairly easy to incorporate into the analyses, the greater challenge was to match the "perfect" geometry requirement with available manufacturing techniques that would be introduced into the RTL Model Validation Phase in the RTL Structural Experiments. As will be discussed in that section of this report, some differences were accepted and plans are to incorporate into new, additional analyses in subsequent years.

The commercial program ABAQUS was used for the Eigenbuckling analysis. The model was developed with the large flange as the "top' of the structure, and fixed boundary conditions were placed here.

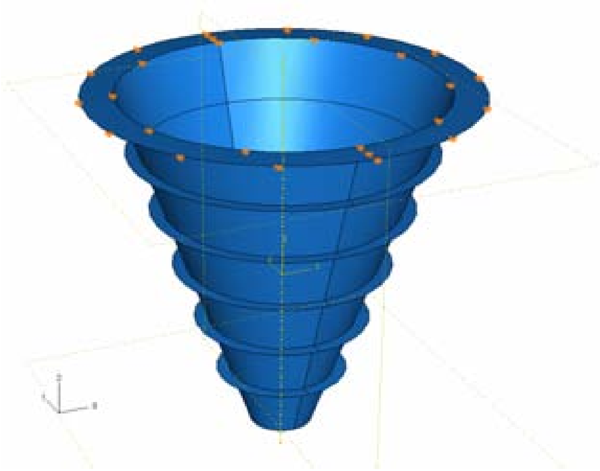

Figure 2.49. RTL (Z-PoP). Fixed boundary Conditions at Top Flange.

A dead load was first applied to the structure to define the stiffness and preload effects. This was followed by a live load representing the external pressure was applied to the buckle analysis step. The subspace iteration solver was chosen and the number of eigenmodes analyzed was generally around 20, depending on the analysis.

A few analyses using the Singer Solution were initially performed and entered into MAPLE 8.0, using both 2-term and 4-term solutions for higher order accuracy. Essentially, the higher order accuracy proved the 2-term solution to be a reasonable estimation.

In the case of the full sized RTL, it should be noted that the Singer Solution generally performed at 80-90% of the ABAQUS Eigenbuckling Analysis results. Finite Element Analyses which tend to be non-conservative, so this was expected. In addition, Singer's own experiments predicted that the experimental results will be much lower than the closed form solution because of the presence of imperfections.

A goal in the experimental phase will be to capture the imperfect geometry, as best possible for use in subsequent Eigenbuckling Analyses. The use of a laser scanner has been incorporated to capture the geometry of the various RTL cones in the stages of initial, pre-buckling, and post buckling.

A finite element model only provides a numerical approximation to the equations of calculus. The model must be based on a complete understanding of the physical system and judgment on the anticipated behavior of the structure. Also, as noted earlier FEA results tend to be non-conservative. The closed form solutions were based on assumption of 6 circumferential waves and were determined from critical mode shape in ABAQUS Eigenbuckling analysis. Also completing the basis for model validation is the fact that the current models do not incorporate imperfections (dents, dings, or out of roundness, for example) due to fabrication processes and techniques.

The following configurations were analyzed, and are shown with their dimensions.

(a) RTL (Z-PoP) (TMS) Dimensions.

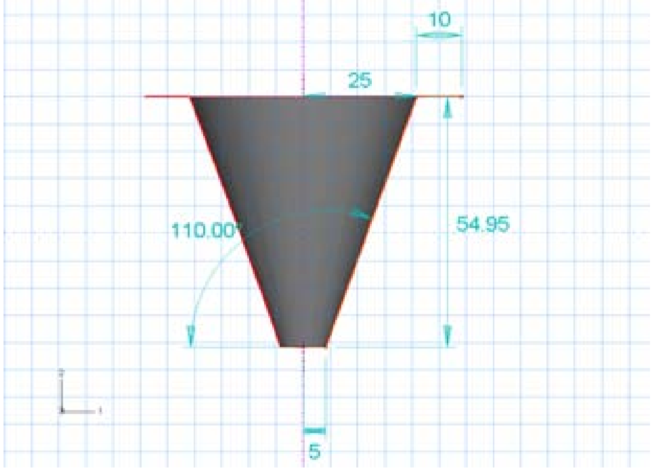

(b) RTL (Z-PoP). Dimensions (cm) shown with 1 stiffener.

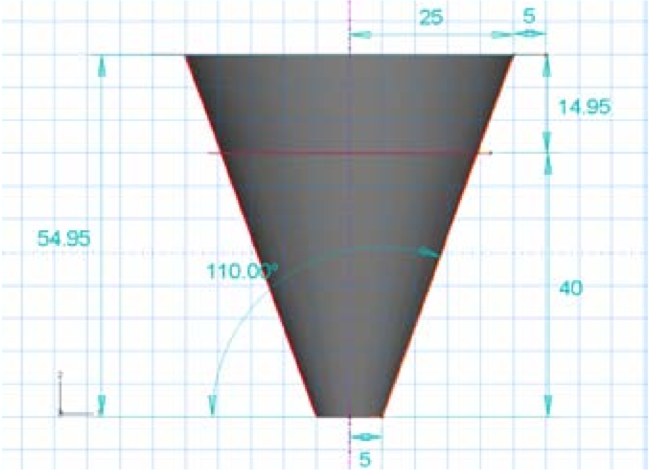

(c) RTL (Z-PoP). Dimensions (cm) shown with 2 stiffeners.

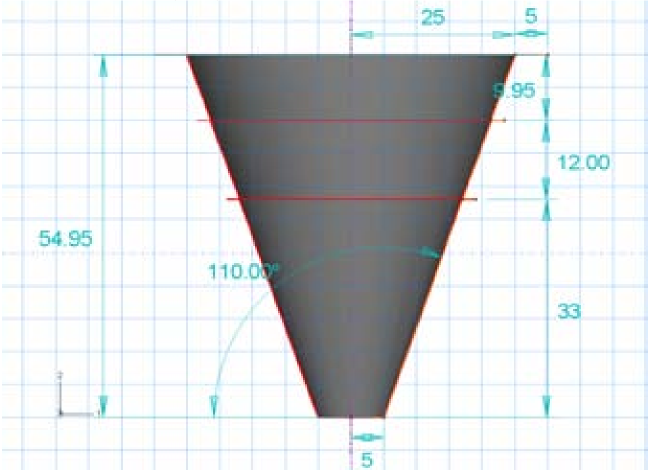

(d) RTL(Z-PoP). Dimensions (cm) shown with 3 stiffeners - a.

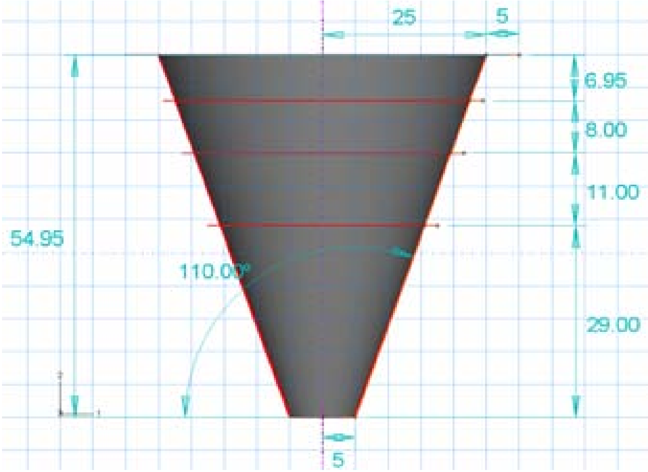

(e) RTL (Z-PoP). Dimensions (cm) shown with 3 stiffeners -b.

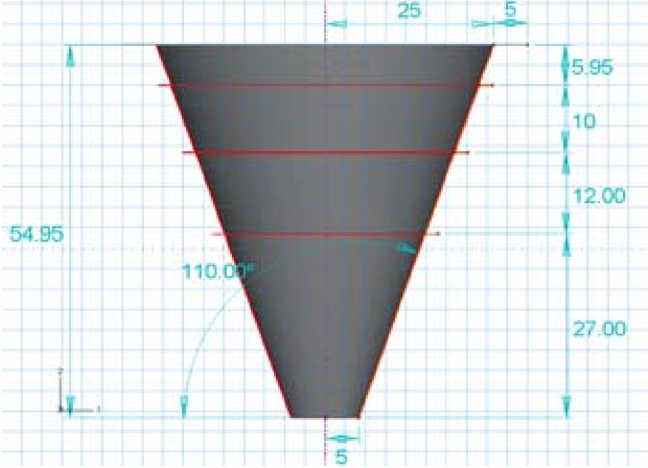

(f) RTL (Z-PoP). Dimensions (cm) shown with 4 stiffeners.

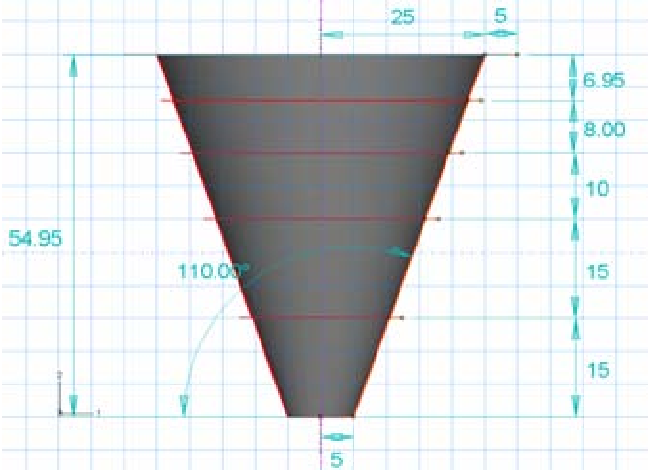

(g) RTL (Z-PoP). Dimensions (cm) shown with 5 stiffeners.

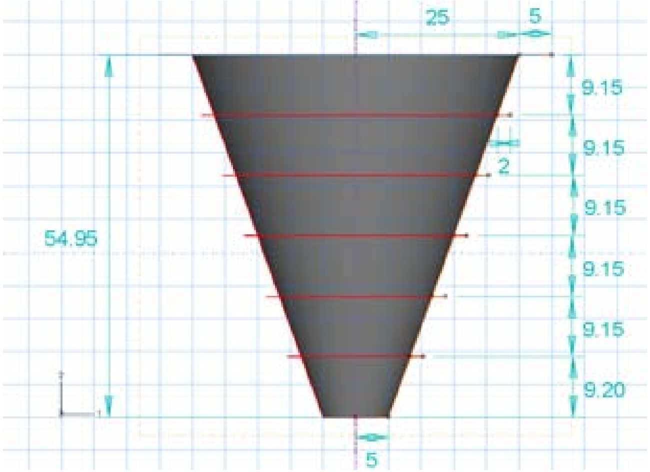

Figure 2.50. Various Z-PoP RTL configurations.

Finite Element Analysis Results;

The critical buckling pressure was calculated after solving for the Eigenvalue.

Number of Stiffeners	Eigenvalue	Critical Buckling Pressure (psi)
0	60.73	13.21
1	91.479	19.90
2	127.63	27.77
3a	162.11	35.27
3b	141.8	30.85
4	168.50	36.66
5	134.86	29.34

The models used for 1, 2, 3a, are considered as optimized locations for best performance. The location of 5 stiffeners was equally spaced, and 3b was an alternative location.

In addition, embedded stiffeners were evaluated as possible alternatives to externally mounted stiffening devices as shown in the drawings earlier. These could be formed in the sidewall of the structure by die or mandrel is metal spun.

(a) Embedded Stiffener -1 (wedge).

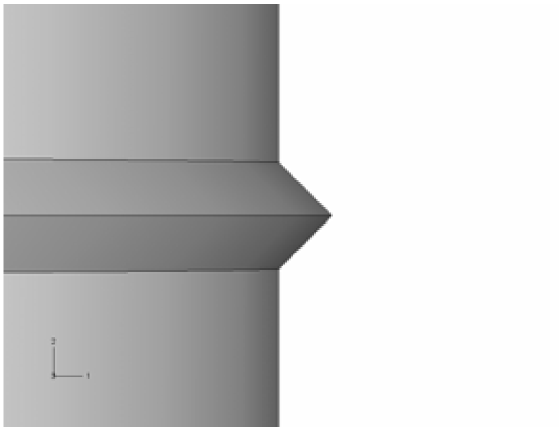

(b) Embedded Stiffener – 2 (half-circle).

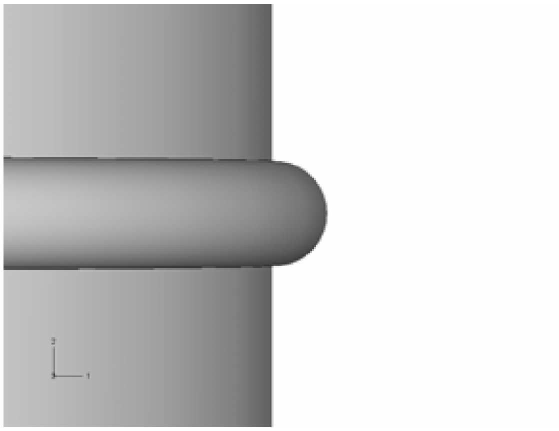

(c) Embedded Stiffener – 3 (2:1 Ellipsoid).

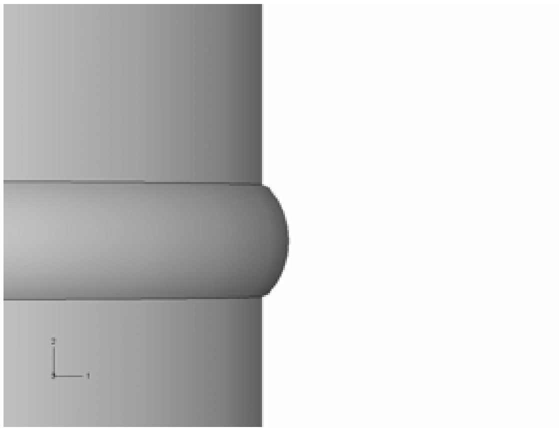

(d) External Stiffener – 4 (Ring).

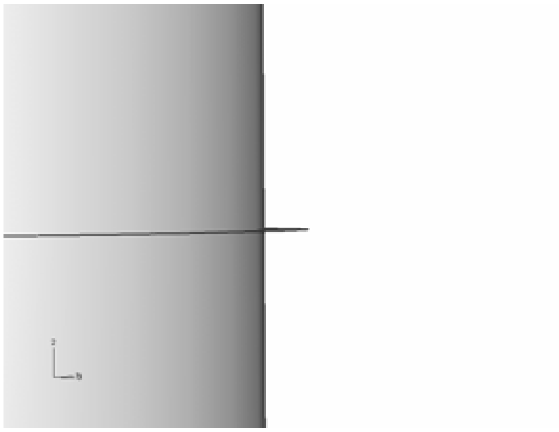

Figure 2.51. Various RTL stiffener configurations.

A model consisting of a cylindrical bucket was developed and an external pressure, similar to the PoP-RTL analyses was applied. The goal was to compare the performance of the embedded stiffeners against the external ring design which was employed for the PoP-RTL analyses and experiments. As shown in the table below, the eigenvalues for the embedded stiffeners offered a slight increase over the external ring, and therefore it appears that the use of embedded stiffeners should be considered.

Stiffener	Eigenvalue	Pcr (psi)
Embedded – wedge	82.85	18.02
Embedded – half circle	82.88	18.03
Embedded – 2:1 ellipsoid	84.33	18.34
External Ring	81.39	17.7

2.6.2 Fabrication of RTL (Z-PoP)

Two suppliers were identified for manufacturing the RTL cones; Sandia National Laboratories own metal shop and Toledo Metal Spinning (TMS) Company. A total of 22 Pop-RTL cones were developed by TMS. The conical sections were manufactured using a process called metal spinning and then welded to a top flange to be used for mounting in the testing process.

Metal spinning is a process that originates with a blank sheet of steel that is rotated on a lathe. A mandrel along with a tailstock is pressed against the rotating metal while a roller presses against the metal to form it in the desired shape. The metal takes the form of the mandrel in this process.

The initial geometry desired for the Z-PoP-RTL was determined to have a height of 50-cm, top diameter of 50-cm, bottom diameter of 10-cm (50-50-10) with a thickness of 0.0635-cm (0.025-in.). Analytical scenarios involving various stiffeners were performed using this configuration as shown below;

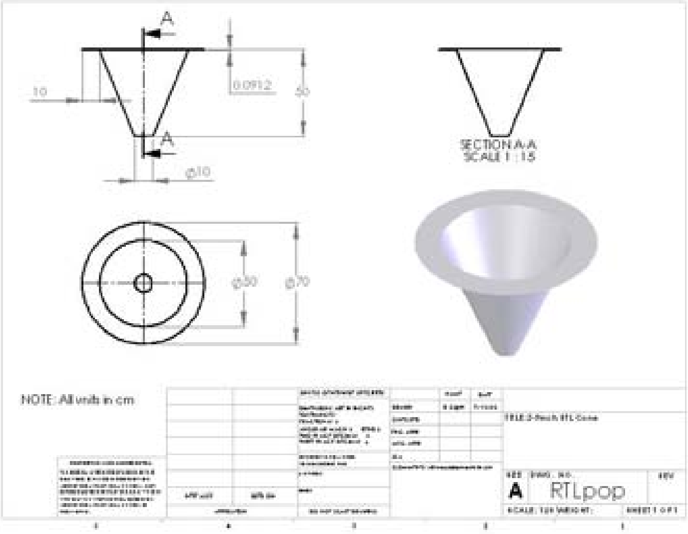

Figure 2.52. Initial Z-PoP RTL geometry.

However, this would have resulted in the requirement of a completely new fabricated mandrel. TMS had a slightly similar mandrel already in their possession and it was determined that it would be acceptable for use in the experiment. This would result in a cone with a height of 54.95-cm, top diameter of 50-cm, bottom diameter of 10-cm (55-50-10) with a thickness of 0.0635-cm (0.025-in.). As a result of this change, new analytical scenarios were calculated to accommodate the changes, which proved to be slight.

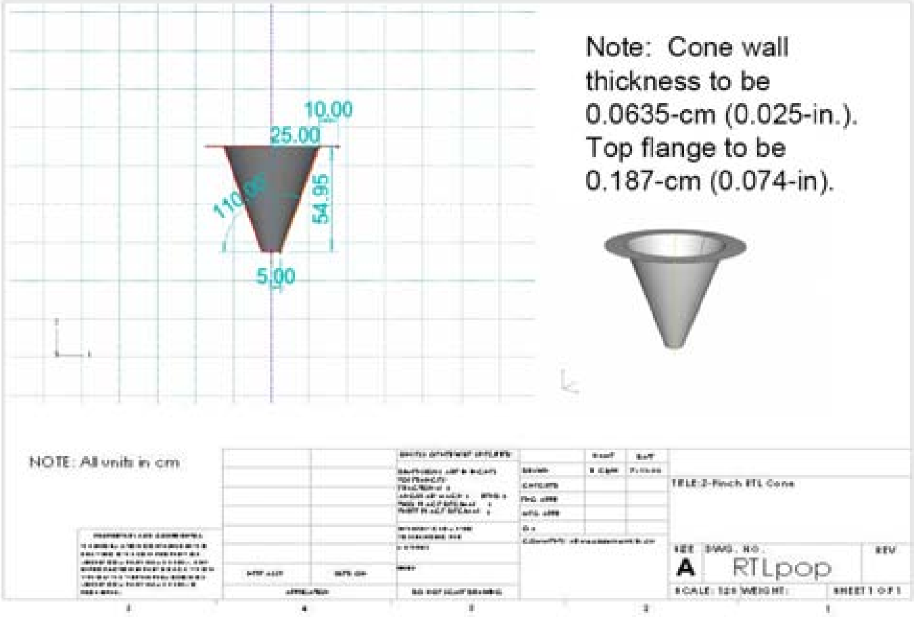

Figure 2.53. PoP-Sized RTL unit (SNL drawing).

Figure 2.54. TMS Cone, showing weld and surface quality.

The TMS produced Cones were constructed of AISI 1008 sheet metal. Properties used in analysis were obtained from www.matweb.com and are shown below.

Elastic Modulus: 200-GPa
Density: 7.872 g/cc
Yield: 170-MPa
Ultimate: 305-MPa

2.6.3 Structural Testing of Z-PoP RTLs

This section will provide an overview of the test. The test system for the full-sized RTL has been described in detail in the report for Task I. Relevant portions of the equipment description are repeated here. The system consists of several integrated components and data acquisition methods. Each subsystem will be described in detail in subsequent sections.

The main test chamber consists of a steel tube into which the RTL is inserted. The flanged portion of the RTL rests on the flange of the pressure vessel. A steel retaining-ring rests atop the flange of the RTL. The tube and facing RTL flange and are sealed with silicone sealer (GE Silicone II) and are bolted together, along with the retaining ring. Bolts, 3/8 inches in diameter are spaced at every 10 degrees around the flange of the tube. After a 24-hour cure time for silicone, a sealed, enclosed space is created around the exterior of the RTL. The interior of the RTL is open to atmospheric pressure. The test setup is illustrated below.

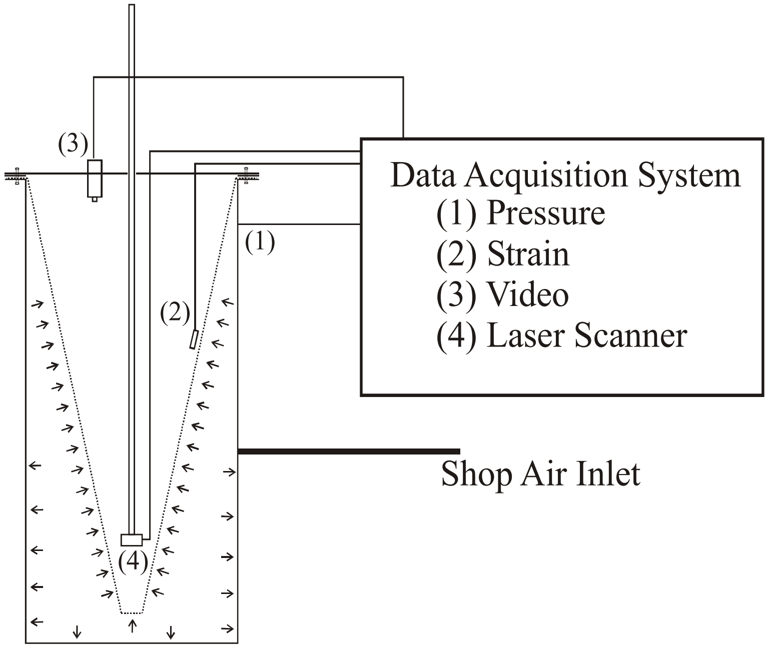

Figure 2.55. Test setup for pressure testing RTLs.

A pressure port in the tube is used to pressurize the pressure vessel-RTL system. The system uses “shop air” from a centralized air compressor that allows the application of up to 125-psi of pressure. On tests with strain gages, the strain gages were applied to the interior of the RTL (the atmospheric pressure side during testing) and were monitored, as well as the differential pressure reading. Additionally, the open end of the RTL was monitored by a video camera, and a laser scanning system is inserted into the open end of the RTL to determine the buckled mode shape.

The PoP-RTL test chamber was based on a similar design to the full-sized RTL test chamber. However, to accommodate larger internal pressures, an air compressor tank rated to 125-psi was cut and modified to become the test chamber. A photograph of the RTL test chamber is shown below.

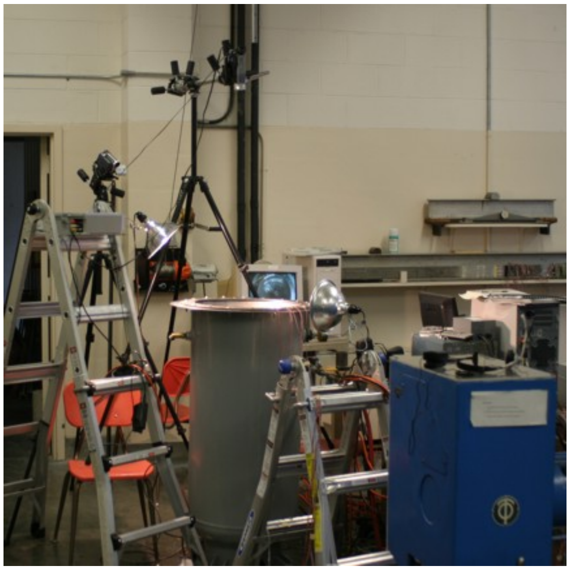

Figure 2.56. Z-PoP-RTL test chamber

The following equipment descriptions are as follows. Experimental equipment upgrades are detailed later on.

Pressure Transducers

Attached to the pressure vessel are pressure transducers. There are two digital pressure transducers (Cole-Parmer EW-68332-02) with a range of 0-30-psi differential pressure range with 0.01-psi resolution and 0.5% full scale accuracy. The purpose of these gages is to give an immediate visual indication of the current pressure value. These gages, ball valves, and a pop-off valve are seen in Figures 2.57 and 2.58.

Additionally, an FLW Southeast pressure transducer is connected to the data acquisition system. The system consists of a Transicoil 150C-P130 Differential Pressure Transducer 0-25-psi range and associated signal conditioning and power supply. The Transicoil system produces a voltage that is proportional to the pressure inside of the vessel. This voltage signal goes into a National Instruments SCXI data acquisition system (Figure 2.59).

Strain Gage Transducers

Vishay Micro-Measurements uniaxial strain gages are applied the inside (atmospheric pressure side) of selected RTL units. The signals are brought into the SCXI data acquisition system simultaneously with the pressure transducer signal. The purpose of the strain gages is to detect the onset buckling in the vicinity of the strain gages.

The gage designations that were used were:

EA-06-125BB-120
EA-06-125BT-120
EA-06-125RA-120.

Figure 2.57. Digital pressure gage, pop-off valve, and ball valve with for air inlet.

Figure 2.58. Digital pressure gage, pressure transducer, and ball valve with for air outlet/venting.

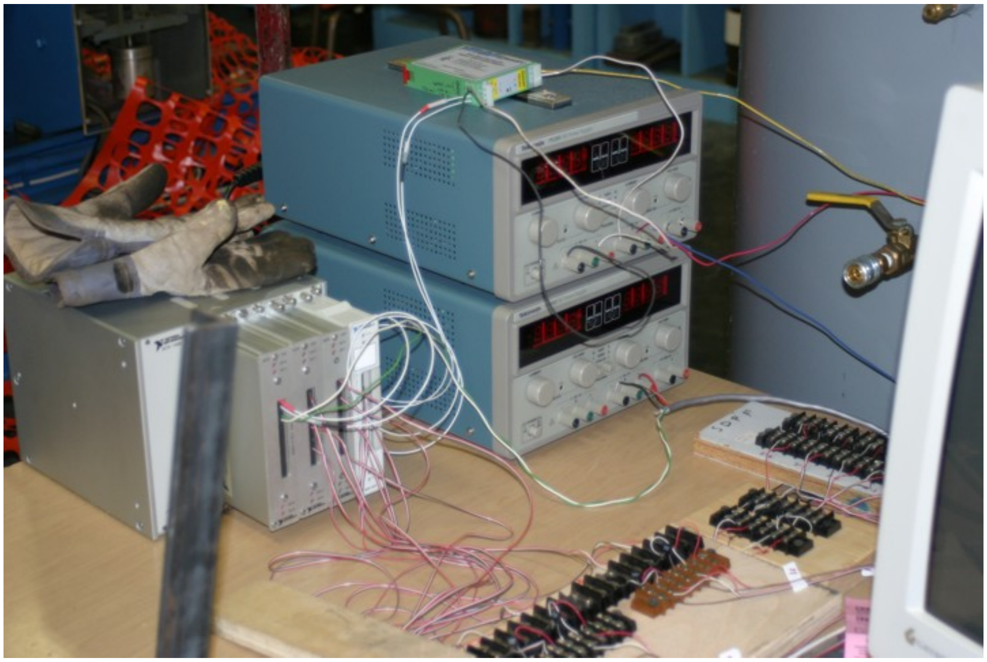

Figure 2.59. Strain gage data acquisition system and power supplies.

Video System

A visual record of the test is made by using two video cameras. One camera is mounted to the instrumentation platform on the top of the pressure vessel to visually record the deformation during the test. This video camera is attached to a VCR for redundant data capture, and a real time video feed is available for display on the data acquisition computer through the use of a PCTV tuner card. A second video camera is placed in view of the one of the digital pressure gages, and records the test procedure.

Laser Scanner

The laser scanner has the ability to measure the radial and angular distance, and depth of these measurements along the interior of the RTL. There are two purposes of the equipment. First, the cone is scanned prior to testing so that the initial state of cone can be examined for imperfections. Secondly, the laser scan is completed in the post-buckled shape so that the mode shape of the buckled cone can be determined. The scanner data is collected by the data acquisition computer.

Data Acquisition System

The data acquisition system consists of the data acquisition computer, National Instruments SCXI system, and National Instruments LabView software. SCXI 1121 strain gage modules and 1321 terminal blocks were used. The 1121 modules for the strain gages were set for a gain of 2000, with a 10 kHz filter in 3.33V quarter-bridge mode. The 1121 module used for the pressure transducer and the string pot transducer and were set for a gain of 1, with a 4 Hz filter. (These transducers were excited using an external power supply.

Equipment Upgrades

The following equipment upgrades were made from Task I:

-an additional 0-100-psi pressure transducer was acquired,
-an electric winch was obtained to raise and lower the laser scanner, and
-a computer controlled air valve was obtained to control the air flow into the test chamber

Stiffener Fabrication and Attachment

Determining a suitable stiffener material and attachment method was an early challenge in the testing program. An initial idea was to weld metal rings to the cones. However, because to the thin sheet steel used to fabricate the cones, welding was rejected due to concerns about heat input warping or damage to the RTL specimens.

DP-190 structural epoxy.

As an alternative, the stiffening rings were fabricated from ¼ inch thick luan plywood, and glued to the cones using 3-M DP-190 structural epoxy. Seamless stiffening rings were produced by cutting in the sheet of plywood with a router attached to an adjustable radial arm. In this manner the appropriate inner and outer ring diameters were obtained for the locations on the cone to which the rings were attached.

Figure 2.60. Stiffening rings mounted to cone.

PoP-RTL Experimental Results

Twenty-two PoP-sized RTL specimens were received. Nineteen have been tested, one was sent to SNL for examination, and two have been reserved for future use. A website was established to present the results of the testing, and is located at the following URL: http://mbarkey.eng.ua.edu/RTL/2005/05Toledo-PoP-cones.htm. Additional *photographs* of the specimens and *test videos* are available on the website.

Stiffener Configurations

Stiffeners were placed as close as possible to the analytical models. However, the stiffeners used were constructed of ¼-in. thick luan plywood, where as the analytical models were assigned the thickness of the sheet metal (25-mil). Because of this, slight differences exist in the exact location of the stiffener. Various stiffener configurations are shown below.

Configuration A

Configuration B

Configuration C

Configuration D

Configuration E

Configuration F

Figure 2.61. Six RTL cone configurations.

The complete results and stiffener placements are given below;

Cone Designation	Initial Buckling Pressure (psi)	Measured Thickness (in.)	Number of Stiffeners	Stiffener Configuration	Optimized Design
PoP-T01	8.45	0.025	0	n/a	Y
PoP-T02	8.36	0.025	0	n/a	Y
PoP-T03	8.07	0.025	0	n/a	Y
PoP-T04	8.26	0.025	0	n/a	Y
PoP-T18	14.0	0.025	1	F	Y
PoP-T19	14.1	0.025	1	F	Y
PoP-T16	19.2	0.025	2	E	Y
PoP-T17	18.3	0.025	2	E	Y
PoP-T11	25.6	0.025	3a	C	Y
PoP-T12	26.2	0.025	3a	C	Y
PoP-T13	26.1	0.025	3a	C	Y
PoP-T14	22.1	0.025	3b	D	N
PoP-T15	23.1	0.025	3b	D	N
PoP-T09	21.9	0.025	4	B	N
PoP-T10	21.9	0.025	4	B	N
PoP-T05	19.6	0.025	5	A	N
PoP-T06	19.4	0.025	5	A	N
PoP-T07	17.4	0.025	5	A	N
PoP-T08	18.7	0.025	5	A	N

The experimental results for the optimized, stiffened PoP RTL units showed the following performance gains as compared to the unstiffened PoP RTL cones: the average pressure to buckle the cones was increased by a factor of 3.31 for cones stiffened with 3-rings, 2.33 for cones stiffened with 2-rings, and 1.70 for cones stiffened with 1-ring, as compared to the unstiffened cone. The results are summarized in below.

Configuration	Pattern	No. of tests	Average value	Factor
Unstiffened	--	4	8.29 psi	1.00
3-rings	D	2	26.0 psi	3.13
2-rings	E	2	19.3 psi	2.33
1-ring	F	2	14.1 psi	1.70

The analytical results for the optimized, stiffened PoP RTL units showed the following performance gains as compared to the unstiffened PoP RTL cones: the average pressure to buckle the cones was increased by a factor of 3.31 for cones stiffened with 3-

rings, 2.33 for cones stiffened with 2-rings, and 1.70 for cones stiffened with 1-ring, as compared to the unstiffened cone. The results are summarized in below.

Configuration	Pattern	No. of tests	Average value	Factor
Unstiffened	--	4	13.21-psi	1.00
3-rings	D	2	35.27-psi	2.66
2-rings	E	2	27.77-psi	2.10
1-ring	F	2	19.90-psi	1.50

A comparison of the factors of stiffener influence is shown below

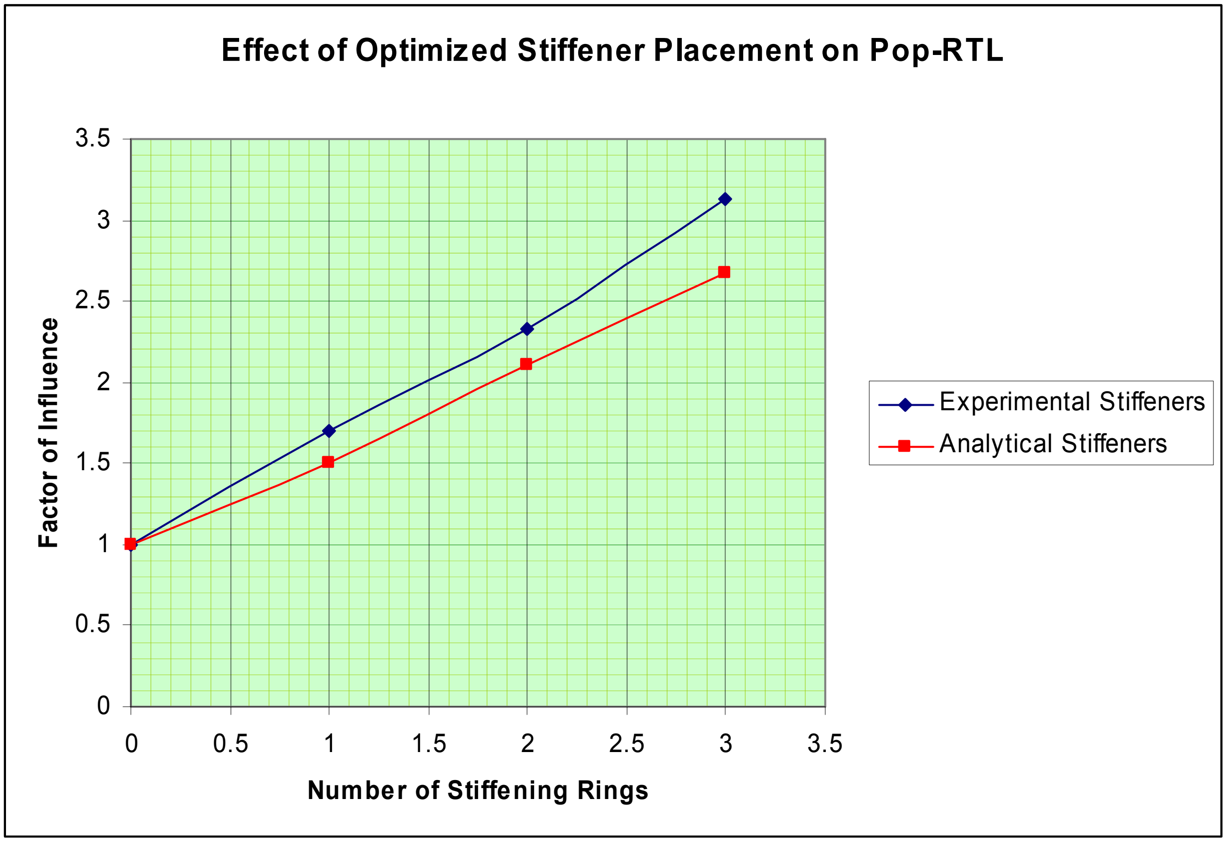

Figure 2.62. Effect of stiffener placement on Z-PoP RTL.

It appears that the effect of additional stiffeners scales linearly. The change in slope between the experimental and analytical results is most likely due to the actual thickness of the stiffeners, which while the number of stiffeners increases, the overall surface area of the cone's stiffened wall increases. Note that in the analytical model the thickness of the stiffeners was assigned the same as the cone wall thickness (0.0.25-in), and the actual stiffeners used in this analysis were the ¼-in. thick luan plywood. The influence factor is also a function of the stiffeners thickness. Since the overall goal of the RTL Optimization program is to reduce the mass of the unit, it is believed that thinner stiffeners are ultimately the goal.

Additionally the performance of the experiments as compared to the analysis shows that on average the experiments are at 66.84% or 2/3 of the analysis. This is shown graphically below.

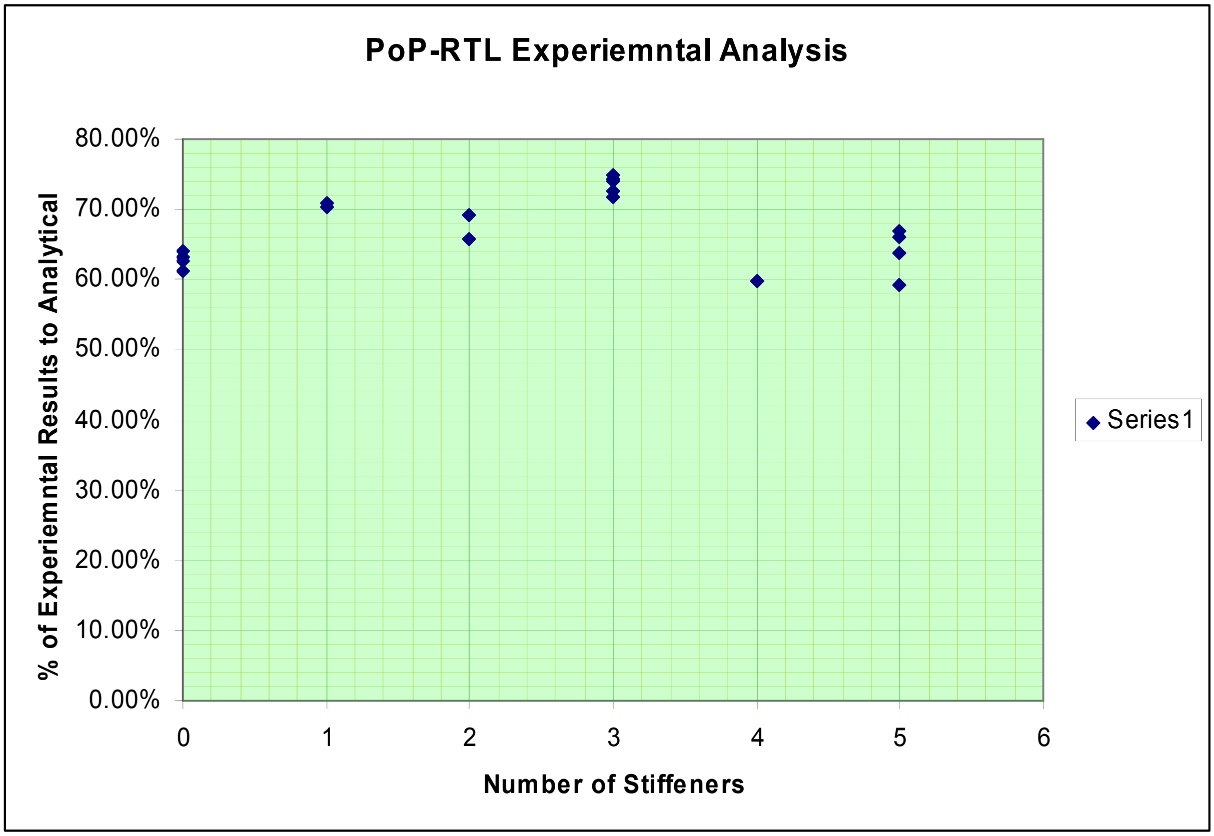

Figure 2.63. Comparison of experimental and analytical results for Z-PoP RTLs.

2.6.4 Conclusions

The use of stiffeners can significantly increase the structural performance of the Z-PoP-RTL units with adding an insignificant increase in the unit mass. Based on this, the Z-PoP-RTL wall thickness can further be reduced as more stiffeners, preferably embedded can be incorporated into the design.

2.7 Modeling of the Effect of Initial RTL Imperfections on the RTL Buckling Pressure [50] *(M. Guthrie and D. C. Kammer, U. Wisconsin)*

A methodology for obtaining probability distributions governing the buckling pressures of Recyclable Transmission Lines (RTLs) is developed. First, the basic steps for conducting a nonlinear buckling analysis in ANSYS are discussed. It is necessary to use nonlinear buckling analysis because it accounts for the initial geometric imperfections in the RTLs while its alternative, eigenbuckling analysis, does not. Next, some background on the construction of metamodels is presented. A metamodel is a functional form, typically a polynomial, that is fit to a set of data obtained from a more complicated process or analysis such as a finite element model. The metamodel can be evaluated much faster than whatever analysis produced the original data, thus allowing decoupled Monte Carlo analysis to be conducted. In this report, initial imperfections in the RTL are represented as a superposition of the first one, two, three, and four buckling modes predicted by the eigenbuckling analysis. Metamodels are constructed that map the initial deformations in each of these eigenbuckling modes to a buckling pressure. The variables governing the initial deformation in each of the eigenbuckling modes are then allowed to have some probability distribution (e.g., a normal distribution with mean μ and standard deviation σ) and the metamodel is evaluated several million times to obtain a probability distribution for the buckling pressure. It is observed that as the number of variables in the metamodel is increased, the resulting distribution of buckling pressure very closely resembles a Rayleigh distribution.

The methodology developed in this report is applied to one, two, and three segment RTL designs as well as a curved RTL design and the distributions of buckling pressure for the various designs are compared. The mean, standard deviation, 5th percentile, 95th percentile, and coefficient of variation of the buckling pressure distributions for each of the four RTL design concepts are presented in Table 2.6. It can be seen that the curved RTL design offers the greatest mean buckling pressure as well as the smallest sensitivity to imperfections as measured by the coefficient of variation. It should be noted that the results presented in Table 2.6, like all of the results and procedures presented in this report, are intended more for the purpose of obtaining a qualitative understanding of how each of the RTL design concepts maps uncertainty in initial geometry to uncertainty in buckling pressure than as exact quantitative results. In reality, the magnitude and probability distribution of the initial imperfections in the RTL geometry are unknown and this lack of knowledge maps directly into the computed buckling pressures. In addition, it was found that refinement of the mesh used in the nonlinear buckling analyses resulted in a significant change in the computed buckling pressures (13.8% in one case). Despite the fact that the quantitative values presented in Table 2.6 are somewhat suspect, they are of great qualitative value and clearly indicate that the curved RTL design is best. Future work will attempt to obtain more quantitatively accurate results by refining the mesh used in the nonlinear buckling analyses and estimating the probability distribution of the initial imperfections in the RTL geometry using experimental data. The predicted buckling pressure will then be compared with experimental results.

Table 2.6. Buckling pressure statistics for various RTL designs.

	Mean Buckling Pressure, μ_y $\left(dyne/cm^2\right)$	Standard Deviation, σ_y $\left(dyne/cm^2\right)$	5th Percentile, p_5 $\left(dyne/cm^2\right)$	95th Percentile, p_{95} $\left(dyne/cm^2\right)$	Coefficient of Variation, σ_y/μ_y
Single-Segment	213,190	11,170	193,600	230,080	0.0524
Two-Segment	352,310	49,828	264,010	425,760	0.1414
Three-Segment	474,440	45,276	399,170	545,850	0.0954
Curved	761,970	26,665	713,560	800,300	0.0350

In the following sections, the nonlinear buckling analysis approach is discussed, and the key results of how sensitive the various RTL designs are to imperfections are presented. (A complete discussion of the metamodel used is available separately.)

2.7.1 Nonlinear Buckling Analysis

Recyclable Transmission Lines (RTLs) are a key component of the Z-Pinch IFE Power Plant. This report describes the methodology and results of research aimed at assessing the uncertainty in the buckling loads of various RTL design concepts. The RTL is shown in the Z-pinch power plant chamber in Fig. 2.64.

The RTL system will consist of two conical shell structures, one nested within the other. The outer shell will have an external pressure applied to it during operation, while the inner shell structure is subjected to an internal pressure. The outer shell must be able to withstand the external pressure without buckling.

Previous analysis has focused on determining the RTL design that maximizes the buckling pressure [51]. The simplest RTL design is the single segment cone (Figure 2.65). As shown in the last report, two-segment RTLs (Figure 2.66) exhibit a higher buckling pressure than the single segment design, three-segment RTLs (Figure 2.67) exhibit even higher buckling pressures, and the curved RTL (Figure 2.68) exhibits the highest buckling pressure. The buckling pressures for the various RTL designs from the previous report are summarized in Table 2.7. Note that these buckling pressures are higher than those stated in the previous report because the shell thickness has been increased from 0.0635 cm to 0.09 cm.

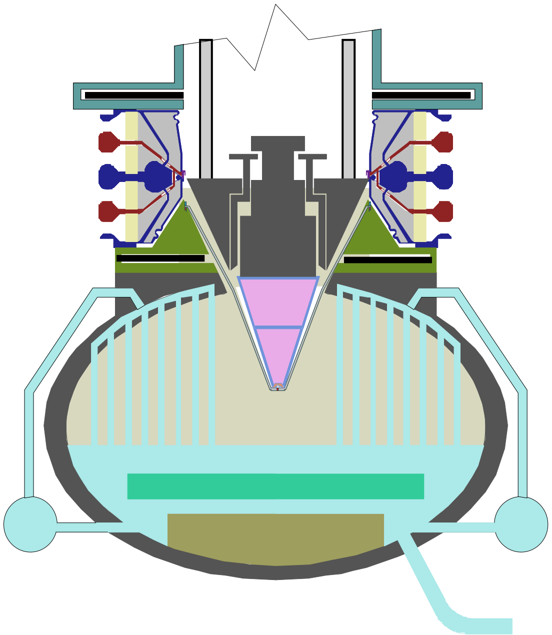

Figure 2.64. Z-Pinch Power Plant Chamber with RTL.

Table 2.7 – Eigenbuckling Pressures for Various RTL Designs.

RTL Design	**Eigenbuckling Pressure** ($dyne/cm^2$)
Single-segment	249,755
Two-segment	490,117
Three-segment	730,507
Curved	748,966

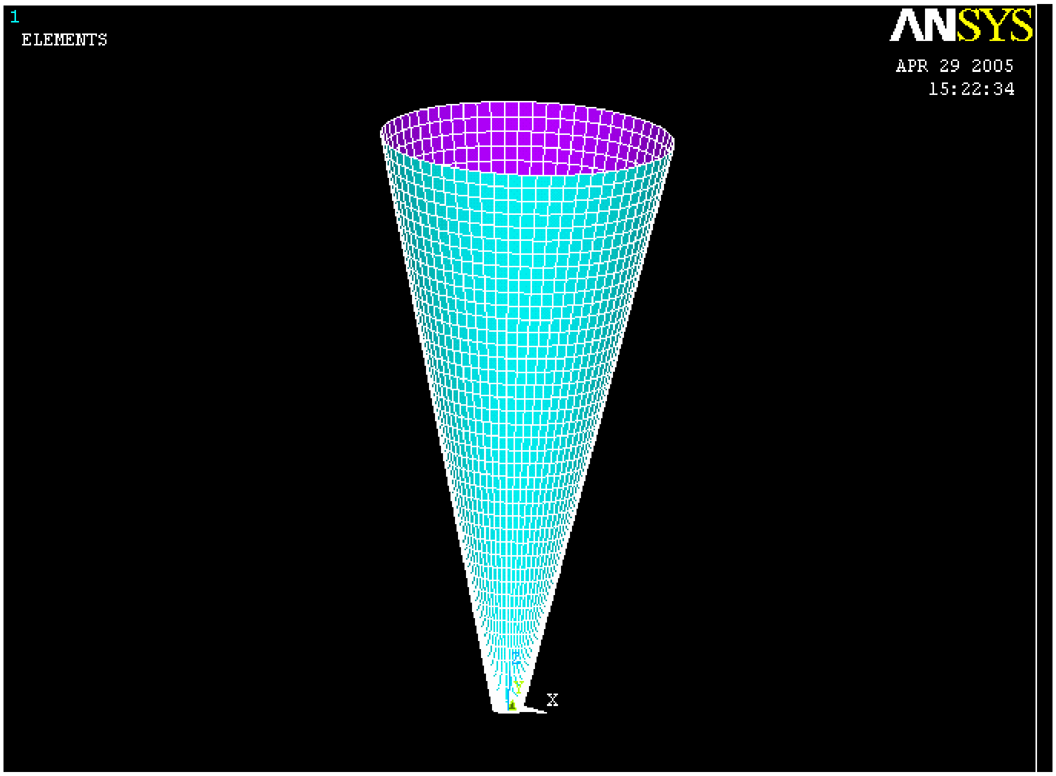

Figure 2.65. Single-Segment RTL.

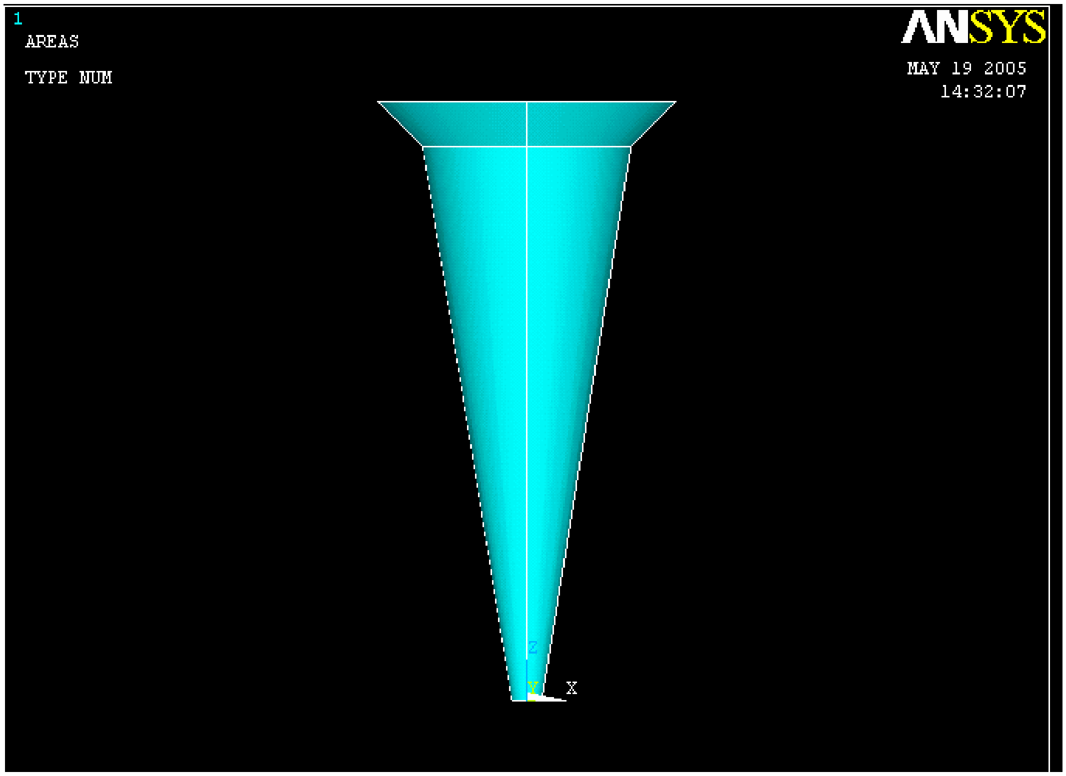

Figure 2.66. Two-Segment RTL.

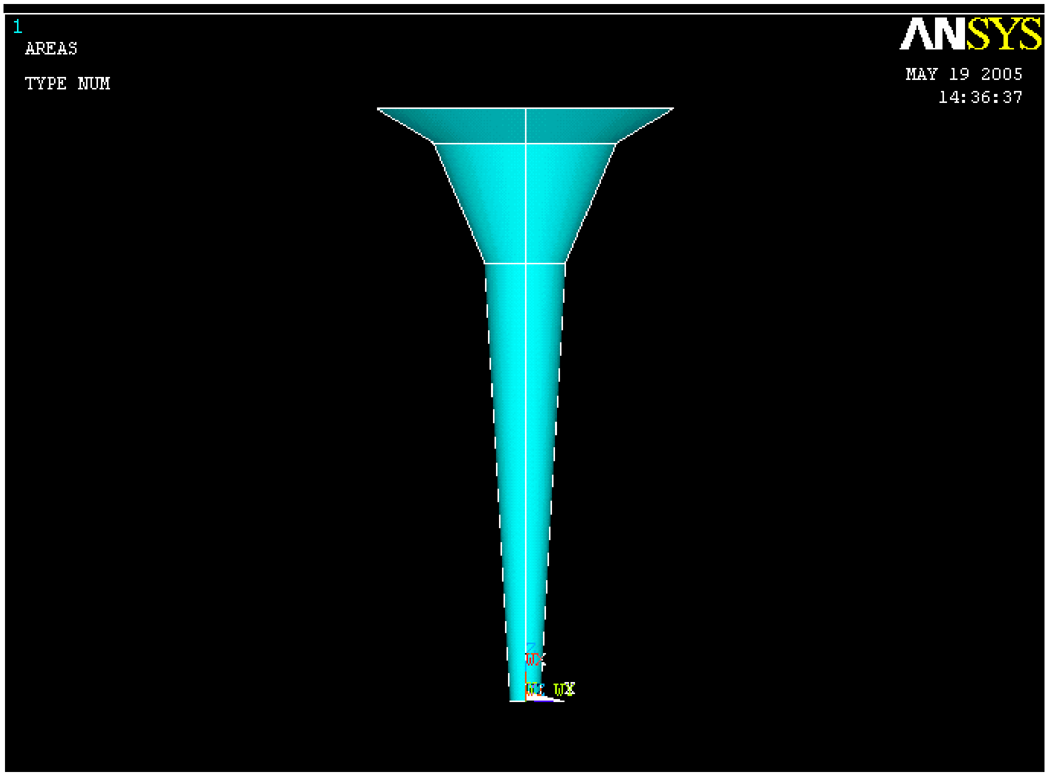

Figure 2.67. Three-Segment RTL.

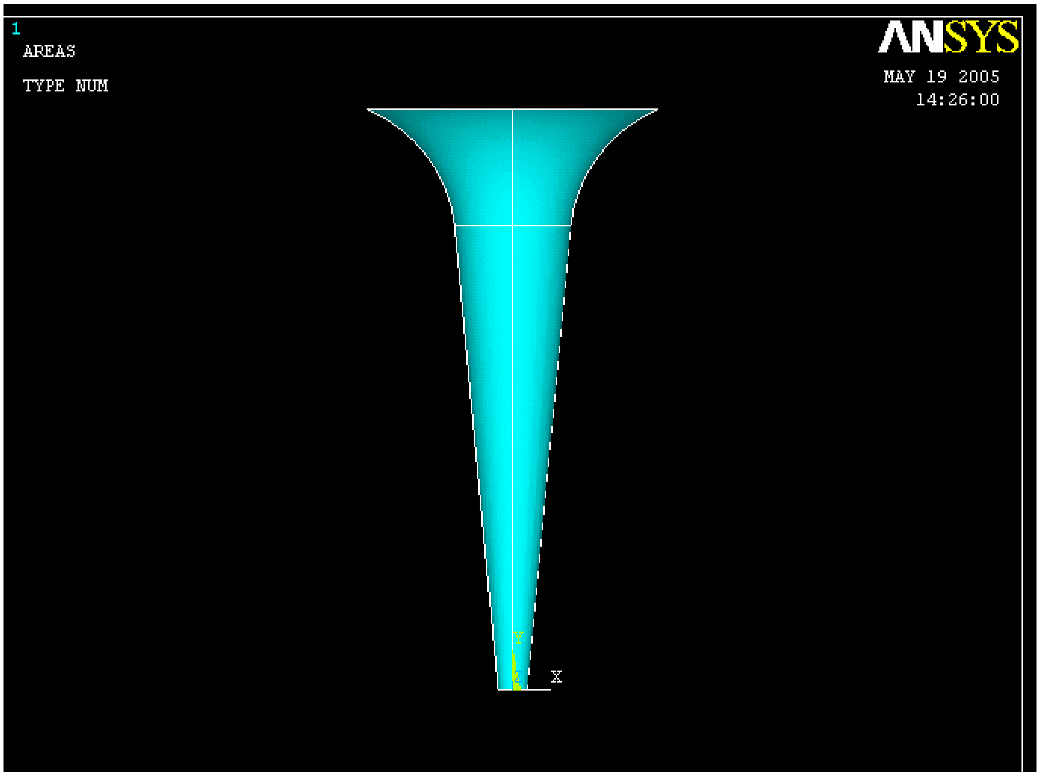

Figure 2.68. Curved RTL.

The optimization discussed in the previous report used eigenbuckling analysis to determine the buckling pressures of the RTLs. Eigenbuckling analysis only provides a rough estimate of the actual buckling pressure because it does not account for geometrical imperfections in the structure or the change in the structure's geometry, and hence stiffness, that occurs as a load is applied. In order to account for geometrical imperfections and the structure's changing geometry when determining the buckling load, it is necessary to conduct a nonlinear buckling analysis rather than an eigenbuckling analysis.

The geometrical imperfections of a structure result from countless complicated sources and so must be treated as random. Thus uncertainty in the geometry of the structure maps to uncertainty in its buckling load. The work described in this report attempts to obtain at least a qualitative understanding of the manner in which each of the RTL design concepts discussed above maps uncertainty in geometry to uncertainty in buckling pressure. Perhaps the most straightforward method of doing this would be to run several million nonlinear buckling analyses with random initial imperfections applied to the RTL. Unfortunately, each nonlinear buckling analysis requires a great deal of computation time and running several million of them would be prohibitively expensive. Instead, an approach called metamodeling is employed. A metamodel is a functional form, typically a polynomial, that is fit to a set of data obtained from a more complicated process or analysis such as a finite element model. The metamodel can then be evaluated much faster than whatever analysis produced the original data and so a decoupled Monte Carlo analysis can be conducted. In this report, initial imperfections in the RTL are represented as a superposition of the first several buckling modes predicted by the eigenbuckling analysis. A metamodel is constructed that maps the initial deformation in each of these eigenbuckling modes to a buckling pressure. The variables governing the initial deformation in each of the eigenbuckling modes are then allowed to have some probability distribution (e.g., a normal distribution with mean μ and standard deviation σ) and the metamodel is evaluated several million times to obtain a probability distribution for the buckling pressure. This methodology is applied to each of the RTL design concepts discussed above and the sensitivities of the various designs to initial imperfections are compared.

Finite Element Analysis

Three types of finite element analyses are employed in this report: linear static analysis, eigenbuckling analysis, and nonlinear buckling analysis. The procedures for conducting these various types of analysis in ANSYS will be discussed in the context of the single-segment RTL (Figure 2.65). This RTL consists of a single truncated cone with an upper radius of 50 cm, a lower radius of 5 cm, a height of 200 cm, a shell thickness of 0.09 cm, an elastic modulus of $200\times10^{10}\ dyne/cm^2$, and a Poisson ratio of $\nu = 0.27$. The model is meshed with 5000 SHELL63 elements and is fully constrained along the large top radius. The small bottom radius is constrained in the circumferential and radial directions, but not in the axial direction. The top is fully constrained because it is presumed that the RTL will be rigidly clamped to whatever mechanism is employed to bring the RTL into place. For the initial steps of the analysis, an external pressure of unit value is applied. An input file for ANSYS that creates the geometry and mesh and applies the boundary conditions and loads is included in Ref. [50].

Linear Static Analysis

Once the geometry and mesh have been generated and the loads and boundary conditions have been applied, the next step in a nonlinear buckling analysis is to solve the linear static analysis. This generates the stiffness matrix of the structure, which is needed in later analysis.

Eigenbuckling Analysis

After the linear static analysis has been solved, the nonlinear buckling analysis can be conducted. However, because we wish to predict the buckling pressure of an RTL subjected to some initial imperfection, we must first apply this imperfection. The initial imperfection applied can take many forms, but in this report, we apply some superposition of the buckling modes predicted by the eigenbuckling analysis. Therefore, it is necessary to conduct an eigenbuckling analysis before proceeding with the nonlinear analysis. In the eigenbuckling analysis, the block lanczos method is used and the first 9 buckling modes are typically extracted (BUCOPT,LANB,9,0,0). Also, prestress effects are included (PSTRES,ON). Note that the eigenmodes occur in pairs so that the 1st and 2nd are the same shape, the 3rd and 4th are the same shape, etc. Thus five independent shapes (the 1st, 3rd, 5th, 7th, and 9th) are obtained by extracting the first 9 buckling modes.

Nonlinear Buckling Analysis

The nonlinear buckling analysis is a nonlinear static analysis. This type of analysis is chosen in ANSYS by setting the analysis type to static (ANTYPE,0) and activating nonlinear geometry (NLGEOM,ON). In a nonlinear static analysis, the load is applied incrementally and the geometry of the structure is updated after the application of each load step using Newton-Raphson iterations. In this report, we use a maximum of 500 load steps, a minimum of 10 load steps, and a nominal value of 20 load steps (NSUBST,20,500,10). This means that the first load step applied to the structure will be equal to $1/20$ of the applied load and that all subsequent load steps will be between $1/500$ and $1/10$ of the applied load. The automatic time-stepping feature in ANSYS is activated (AUTOTS,ON) so that the load step will be chosen to be relatively coarse when the structure is far from buckling and very fine when buckling impends.

In order to determine when a sufficient number of Newton-Raphson iterations have been performed on a given load step, it is necessary to have convergence criteria for the Newton-Raphson iterations. The default convergence criteria in ANSYS are that the Newton-Raphson iterations have converged on a given load step if the force and moment imbalances of the structure (i.e., the differences between the applied forces and moments and the internal forces and moments due to the deflection of the structure) are both less than some small fraction, typically 0.1%, of the applied forces and moments. However, experience has shown that these criteria do not produce accurate buckling loads for the model considered here. In this report, the convergence criteria are that the Newton-

Raphson iterations have converged on a given load step if the force imbalance of the structure is less than 0.1% of the applied force (CNVTOL, F) and the norm of the displacement increment (i.e., the change in the displacement of the structure during the current Newton-Raphson iteration) is less than 0.01% of the total displacement of the structure (CNVTOL, U, ,.0001). If, on a given load step, Newton-Raphson iterations fail to converge in less than 30 iterations or if they diverge, the load step is bisected and the analysis repeated at the smaller load (NEQIT,30).

As mentioned previously, in this work we apply a superposition of the eigenbuckling shapes as an imperfection. With the results of the eigenbuckling analysis still in the postprocessor, the data set corresponding to the desired mode is selected. For example, to apply a deflection in the 3rd buckling mode, the postprocessor is entered (/POST1) and the 3rd data set is selected (SET,3). Next, one returns to the solver (/SOL) and updates the geometry (UPCOORD,2083,OFF). In this case, a deflection equal to the 3rd mode multiplied by a factor of 2083 was applied in order to obtain a maximum deflection equal to $1/2$ of the shell thickness. The maximum deflections in the 1st, 3rd, 5th, 7th, and 9th modes as well as the factors by which each of these modes must be multiplied in order to have maximum deflections equal to $1/2$ of the shell thickness are given in Table 2.8. Note that there is nothing special about a maximum deflection equal to $1/2$ of the shell thickness; it is simply taken as a physically reasonable guess at the magnitude of the structure's imperfections.

Table 2.8 – Update factors for various buckling modes.

Mode Number	**Maximum Deflection (cm)**	**Factor to Produce Max Deflection Equal to $1/2$ Shell Thickness**
1	1.99×10^{-5}	2261
3	2.16×10^{-5}	2083
5	1.84×10^{-5}	2446
7	2.32×10^{-5}	1940
9	1.69×10^{-5}	2663

The next step in performing a nonlinear buckling analysis is to delete the unit pressure load that has previously been applied (SFADELE,P51X,1,PRES) and to replace it with a load that is sufficient to make the structure buckle. In this report, we apply a pressure just slightly greater than the buckling pressure from the eigenbuckling analysis (SFA,P51X,1,PRES,-260000). ANSYS will report buckling loads as a fraction of this applied load so, for example, if the buckling load from ANSYS is 0.6, the physical buckling load is 0.6 times the applied load.

There are a few final steps that must be taken before solving the nonlinear buckling analysis. The tangent stiffness matrix formulation for the SHELL63 elements should be set to the consistent formulation (KEYOPT,1,2,1). The stress-stiffening matrix should be computed (SSTIF,ON). Finally, the Newton-Raphson options should be set to full and adaptive descent should be disabled (NROPT, FULL, ,OFF). Once these steps have been taken, the nonlinear buckling analysis can be solved. An input file for ANSYS that performs the linear static analysis, the eigenbuckling analysis, and the nonlinear buckling analysis is included in Ref. [50].

Metamodel Construction

The nonlinear buckling analysis described in the previous section requires a great deal of computation time to run. In order to obtain reliable statistical data regarding the distribution of buckling pressure for the RTL, it is necessary to find the buckling pressure of RTLs subjected to many (on the order of a million) initial imperfections. Since the nonlinear buckling analysis cannot be run this many times, it is necessary to construct a metamodel that will approximate the results of the nonlinear buckling analysis over a range of initial shapes. The set of initial shapes is parameterized by variables x_i that govern the amount of deflection in each of the eigenbuckling modes. As more eigenbuckling modes are used, more initial shapes can be represented, but the number of terms in the metamodel grows drastically. This report considers one, two, three, and four variable metamodels.

2.7.2 Metamodel Comparison of RTL Designs

In order to gain a qualitative understanding of how sensitive the buckling pressures of various RTL designs are to imperfections, the methodology developed in this report was applied to the two and three-segment RTLs as well as the curved RTL (Figures 2.69-2.71) and the results were compared with those for the single segment RTL. The optimized RTL designs from the previous report [51] were used and the parameters defining their geometry (x1, x2, z1, z2, and r from Figures 2.69-2.71) are specified in Table 2.9. Four-variable metamodels were constructed for each of the RTL designs following the procedure outlined earlier in this report. The metamodel for the two-segment RTL is:

$$y = \begin{pmatrix} 441.00 + 9.23x_2 - 1.30x_4 - 194.64x_1^2 - 206.52x_2^2 - 192.21x_3^2 \\ -15.31x_1x_2 - 8.63x_2^3 + 11.13x_1x_2x_3 + 2.87x_3x_4^2 + 81.74x_1^4 \\ +90.30x_2^4 + 76.32x_3^4 + 2.47x_1^2x_2x_4 + 37.39x_1^2x_2^2 + 28.94x_1^2x_3^2 \\ +5.50x_1x_2^2x_4 + 37.92x_2^2x_3^2 + 5.15x_2^2x_4^2 + 13.03x_1x_2^3 - 3.10x_1x_4^3 \end{pmatrix} \times 10^3 \; dyne/cm^2 \quad (2.2)$$

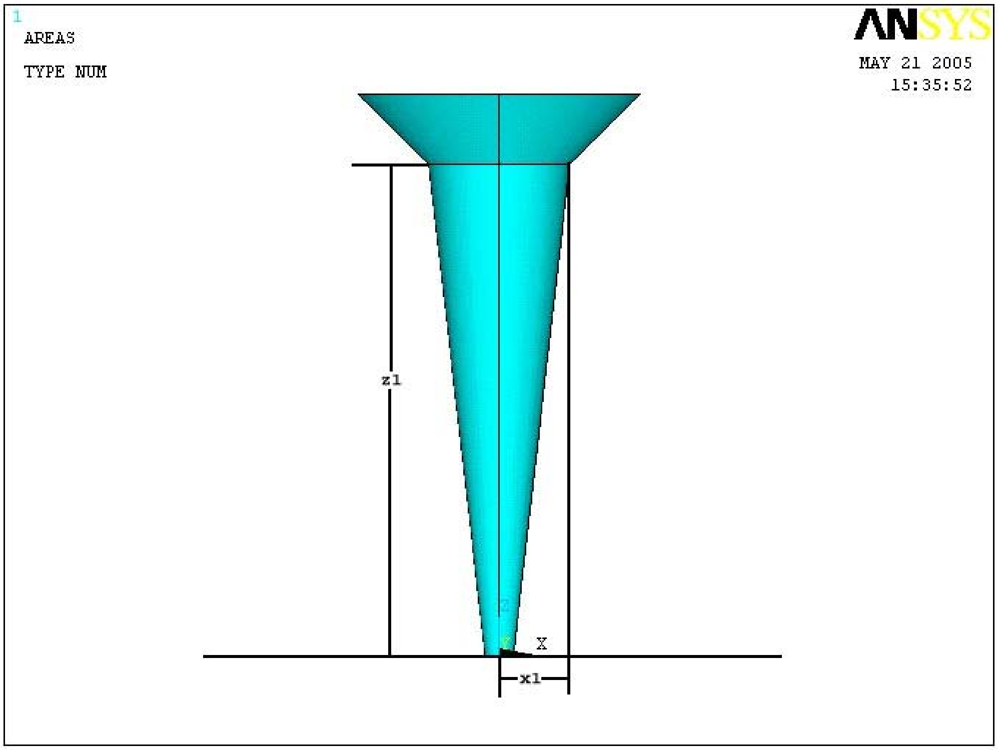

Figure 2.69. Two-Segment RTL.

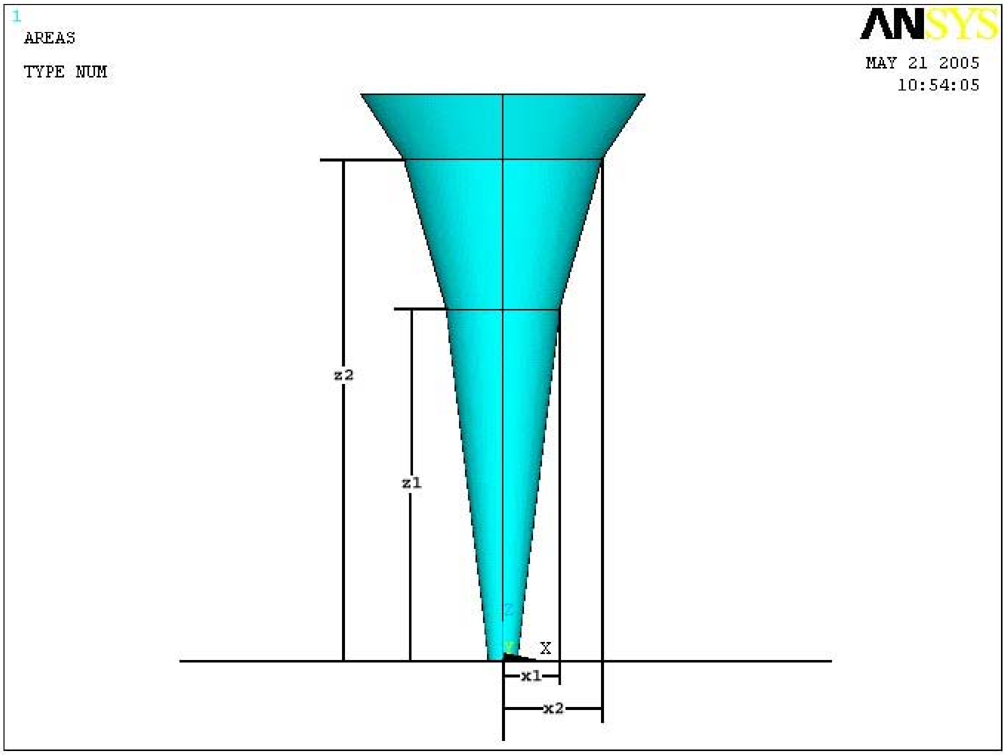

Figure 2.70. Three-Segment RTL.

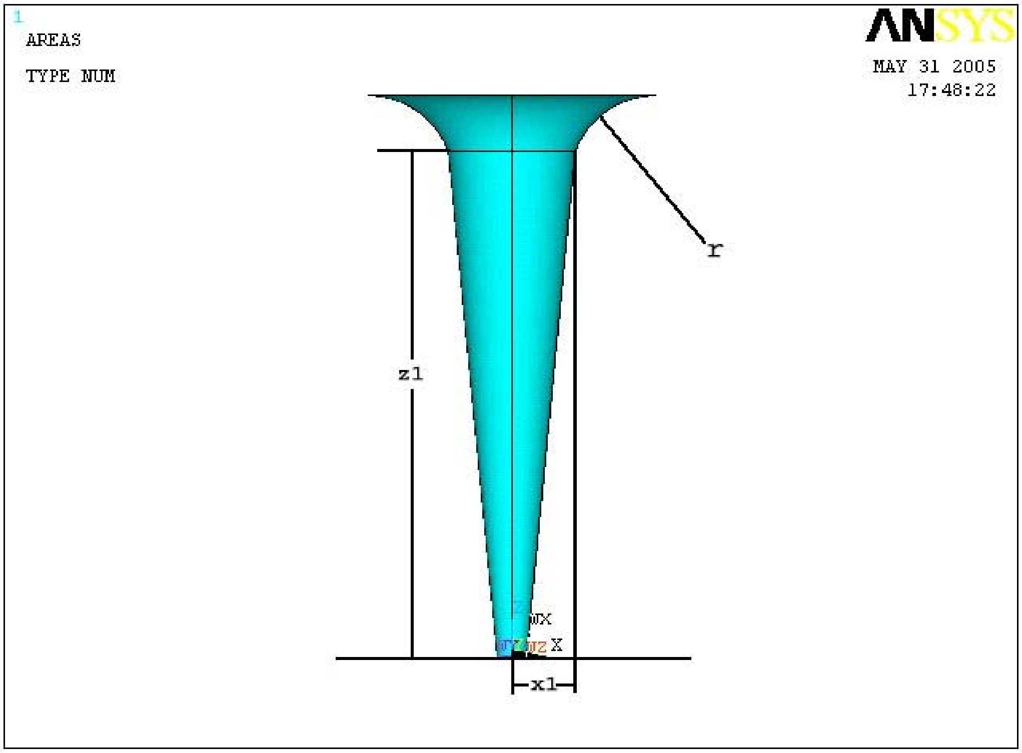

Figure 2.71. Curved RTL

Table 2.9 – Geometric Parameters of Optimized RTL Designs.

	x1 (cm)	z1 (cm)	x2 (cm)	z2 (cm)	r (cm)
Two-Segment	27.51	169.87	n/a	n/a	n/a
Three-Segment	20.99	158.14	38.79	185.25	n/a
Curved	19.78	157.13	n/a	n/a	59.51

The metamodel for the three-segment RTL is:

$$y = \begin{pmatrix} 571.08 - 14.17x_1 - 228.16x_1^2 - 147.40x_2^2 - 209.64x_3^2 \\ -109.70x_4^2 + 11.88x_1x_2 + 7.70x_1x_4 + 40.54x_2x_3 \\ +8.67x_4^3 + 22.57x_1x_2^2 + 16.66x_1x_4^2 - 12.28x_2x_4^2 \\ +98.12x_1^4 + 53.54x_2^4 + 94.38x_3^4 + 74.69x_4^4 \\ -29.67x_1^2x_2x_3 + 93.04x_1^2x_2^2 + 92.38x_1^2x_3^2 + 65.61x_2^2x_3^2 \\ -18.48x_1x_2x_4^2 - 32.19x_2^3x_3 + 24.47x_2^3x_4 - 24.02x_2x_4^3 \end{pmatrix} \times 10^3 \ dyne/cm^2 \qquad (2.3)$$

The metamodel for the curved RTL is:

$$y = \begin{pmatrix} 811.70 - 5.96x_3 - 81.29x_1^2 - 151.90x_2^2 - 34.79x_3^2 \\ - 70.96x_4^2 + 4.87x_3^3 + 40.83x_1^4 + 80.68x_2^4 + 12.53x_3^4 \\ + 29.55x_4^4 + 10.94x_1^2x_2^2 + 5.74x_1^2x_3^2 + 16.47x_2^2x_3^2 \\ - 7.58x_2^2x_4^2 + 10.65x_3^2x_4^2 - 5.15x_1^3x_2 - 5.43x_1^3x_3 + 2.06x_1^3x_4 \\ + 4.77x_1x_2^3 + 4.29x_2^3x_4 + 5.69x_1x_3^3 - 7.67x_2x_4^3 \end{pmatrix} \times 10^3 \; dyne/cm^2 \quad (2.4)$$

The measures of accuracy discussed earlier in this report are given for the four-variable metamodels of the one, two, and three segment RTLs as well as the curved RTL in Tables 2.10 and 2.11. It is seen that the measures of accuracy for the metamodels of the two-segment and the curved RTLs are similar to those for the metamodel of the single-segment RTL. Namely, all of the measures for these metamodels are acceptable except for the condition number and variance inflation factors, which indicate multicollinearity, and Hat's diagonal, which indicates that the experiments near the origin may be overinfluential. However, many of the measures of accuracy for the metamodel of the three-segment RTL are unacceptable. The values of R^2 and R_A^2 for this metamodel are unacceptably low and the value of $\tilde{e}_{\max}$ is much larger than desired. An attempt to explain these difficulties is presented near the end of this section.

Table 2.10. Measures of Accuracy for Four-Variable Metamodels for Various RTL Designs.

	R^2	R_A^2	C	$\tilde{e}_{\max}$	d
Single-Segment	0.9632	0.9571	2543	2.8%	1.96
Two-Segment	0.9870	0.9852	1748	5.5%	1.94
Three-Segment	0.7154	0.6659	2308	15.3%	2.24
Curved	0.9796	0.9764	2457	2.2%	2.02

Table 2.11. Measures of accuracy for four-variable metamodels for various RTL designs.

	Single-Segment	Two-Segment	Three-Segment	Curved
Number of terms with $VIF_i > 10$	12 (of 23)	10 (of 20)	10 (of 24)	12 (of 22)
Number of experiments with $h_i > 2p/n_e$	2 (of 163)	0 (of 163)	0 (of 163)	2 (of 163)
Number of experiments with $D_i > 1$	0 (of 163)	0 (of 163)	0 (of 163)	0 (of 163)

Decoupled Monte Carlo analysis was conducted using the metamodels for each of the RTL designs in order to obtain distributions of the buckling pressures. For each of the analyses, 50 million trials were conducted. The variables x_i were assumed to follow a normal distribution with a mean of 0 and a standard deviation of 0.5. The mean, standard deviation, 5th percentile, 95th percentile, and coefficient of variation of the resulting buckling pressure distributions are given in Table 2.12. The actual distributions of buckling pressure are plotted in Figures 2.72-2.74.

Table 2.12. Buckling pressure statistics for various RTL designs.

	Mean Buckling Pressure, μ_y $(dyne/cm^2)$	Standard Deviation, σ_y $(dyne/cm^2)$	5th Percentile, p_5 $(dyne/cm^2)$	95th Percentile, p_{95} $(dyne/cm^2)$	Coefficient of Variation, σ_y/μ_y
Single-Segment	213,190	11,170	193,600	230,080	0.0524
Two-Segment	352,310	49,828	264,010	425,760	0.1414
Three-Segment	474,440	45,276	399,170	545,850	0.0954
Curved	761,970	26,665	713,560	800,300	0.0350

By examining Figures 2.72-2.74, it can be seen that the distributions of buckling pressure obtained from the four-variable metamodels for the two-segment and curved RTLs are approximated reasonably well by the Rayleigh distribution [see Eq. (33) in Ref. 50] with s and y_0 chosen to match the mean and standard deviation. However, the distribution of buckling pressure from the four-variable metamodel for the three-segment RTL is not well approximated by the Rayleigh distribution. It is believed that this is due to the poor quality of the metamodel for the three-segment RTL and that if an accurate metamodel were obtained, it would produce a buckling pressure distribution that is well approximated by a Rayleigh distribution.

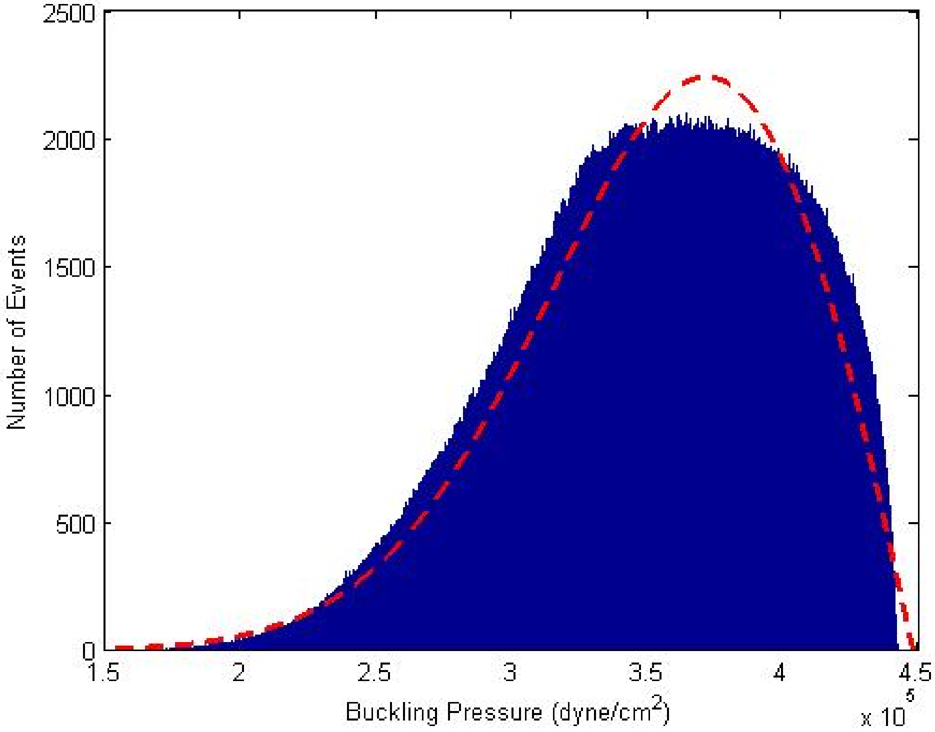

Figure 2.72. Distribution of Buckling Pressure for Two-Segment RTL (solid) and a Rayleigh Distribution Fit (red dashed line).

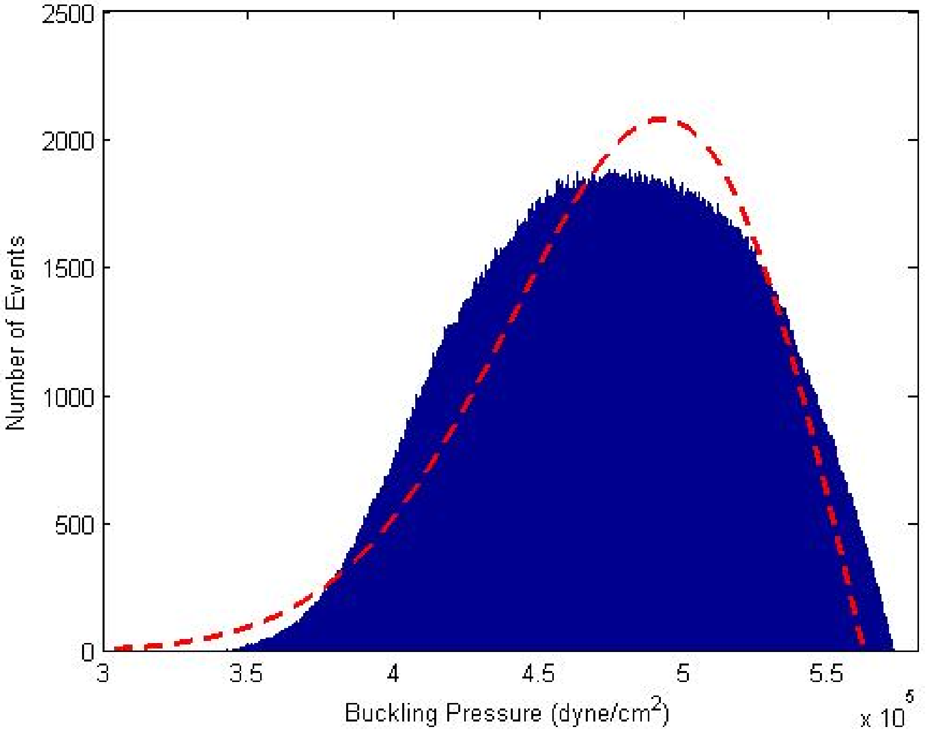

Figure 2.73. **Distribution of Buckling Pressure for Three-Segment RTL (solid) and a Rayleigh Distribution Fit (red dashed line).**

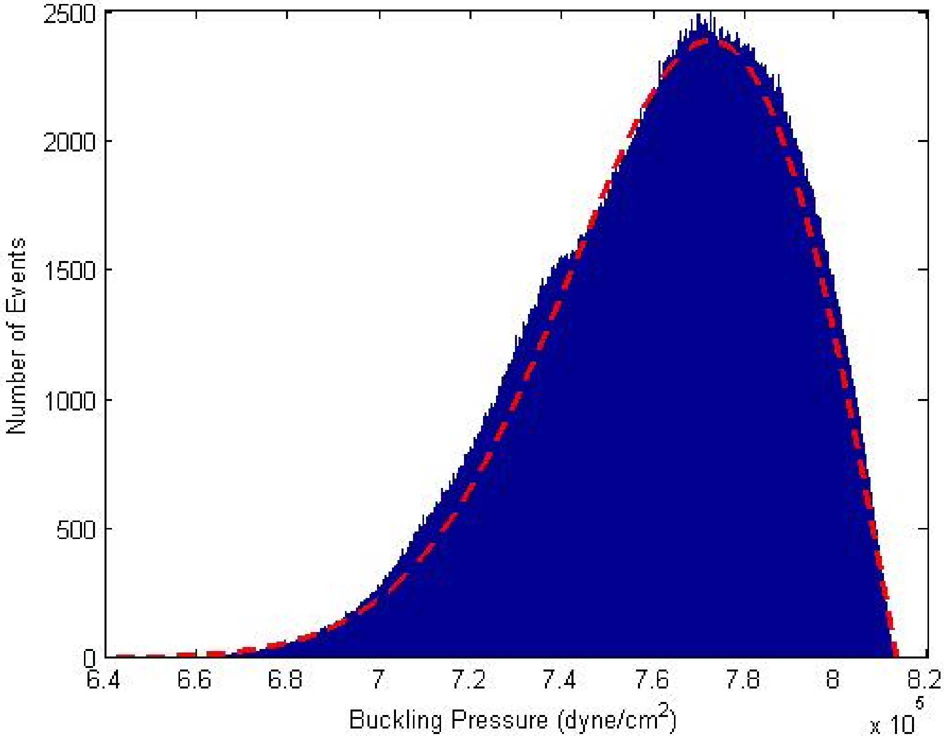

Figure 2.74. **Distribution of Buckling Pressure for Curved RTL (solid) and a Rayleigh Distribution Fit (red dashed line).**

By examining Table 2.12, it can be seen that the mean buckling pressure increases steadily as the RTL is divided into successively more segments. The curved RTL, which is the limit of the segmented RTL as the number of segments approaches infinity, offers the greatest mean buckling pressure. It can also be seen that the sensitivity of the RTL buckling pressure to imperfections, which can be represented by the coefficient of variation of the buckling pressure distribution (σ_y / μ_y), is much greater for the two and three segment RTLs than it is for the single-segment design. However, the curved RTL does not appear to be as sensitive to imperfections as the two and three segment RTLs and is even less sensitive than the single-segment RTL. The combined advantages of having a large mean buckling pressure and a relatively small sensitivity to imperfections make the curved RTL the best design of those considered here.

It should be noted that the results of the nonlinear buckling analyses for the two and three segment RTLs as well as for the curved RTL are somewhat suspect. It appears that the meshes used in the upper segments of these RTLs were too coarse. For example, when the mesh was refined in the upper portion of the curved RTL, resulting in an increase from 7,776 to 13,600 elements, the eigenbuckling pressure increased from $748{,}970 \ dyne/cm^2$ to $789{,}591 \ dyne/cm^2$, an increase of 5.1 %, while the nonlinear buckling pressure for the 1st experiment in the 4-variable metamodel decreased from $705{,}300 \ dyne/cm^2$ to $620{,}000 \ dyne/cm^2$, a decrease of 13.8 %. It is also suspected that the meshes used to model the two and three segment RTLs were too coarse and that this accounts for the poor quality of the metamodel of the three-segment RTL. It is reasonable to expect that as more segments are added to the RTL, a finer mesh will be required in the upper portion of the RTL because the segmentation causes the buckling behavior to be isolated to successively smaller regions. Thus finer and finer meshes are required in the region where buckling occurs in order to provide adequate spatial discretization of the buckling behavior. Unfortunately, it was not possible to repeat all of the nonlinear buckling analyses conducted here with sufficiently fine meshes prior to the completion of this report. However, the results presented here are still of important qualitative value and clearly show that the curved RTL design is best. In future work, the upper portions of the meshes used to model the two and three-segment RTLs as well as the curved RTL will be refined and the work described in this report will be repeated in order to obtain more accurate results.

This report has developed a methodology for obtaining probability distributions governing the buckling pressures of RTLs. First, the basic steps for conducting a nonlinear buckling analysis in ANSYS were discussed. In this report, initial imperfections in the RTL were represented as a superposition of the first one, two, three, and four buckling modes predicted by the eigenbuckling analysis. Some background on the construction of metamodels was presented and then metamodels were constructed that mapped the initial deformations in each of the eigenbuckling modes to a buckling pressure. The variables governing the initial deformation in each of the eigenbuckling modes were then allowed to have some probability distribution (e.g., a normal distribution with mean μ and standard deviation σ) and the metamodel was evaluated several million times to obtain a probability distribution for the buckling pressure. It was observed that as the number of variables in the metamodel was increased, the resulting distribution of buckling pressure very closely resembled a Rayleigh distribution. The methodology developed in this report was applied to one, two, and three segment RTL designs as well as a curved RTL design and the distributions of buckling pressure for the various designs were compared. It was seen that the curved RTL design offered a much greater mean buckling pressure as well as less sensitivity to imperfections than the other RTL designs.

Future work on this problem will attempt to obtain more quantitatively accurate results. Toward this end, the mesh used in the nonlinear buckling analyses will be refined in order to reduce the amount of error introduced by the finite element model. Secondly, the magnitude and probability distribution of the initial imperfections in the RTL geometry will be approximated using experimental data. In order to get an idea of the merit of the methodology proposed here, the predicted mean buckling pressure and its standard deviation will be compared with experimental results.

3.0 Linear Transformer Driver (LTD) *(M. Mazarakis, SNL)*

The LTD driver LDRD experimental research was concentrated this year on two aspects; first to study the repetition rate capabilities of the LTD [52], [53], [54] cavities and second to study how a number of cavities behave and add their energy, power and voltage output in a voltage adder configuration assembly.

The repetition rate studies were done in our high current LTD laboratory (Figure 3.1) utilizing our prototype 500-kA LTD cavity [55].

Figure 3.1. High Current LTD Laboratory at Sandia with the 500-kA LTD cavity shown at the center (red color).

The voltage adder experiments were conducted in Tomsk, Russia where our 1-MA cavities were built and currently are located awaiting shipment to the USA. With this year's LDRD funding we built one more cavity, the voltage adder cathode electrode and the vacuum diode. In addition, the operating expenses for individually checking the performance of each of the LTD cavities as well as the experimental investigation of the voltage adder performance with the vacuum diode load were also financed by the 2006 LDRD.

3.1 LTD Laboratory at SNL with repetitive 0.5 MA LTD cavity operating at 0.1 Hz *(M. Mazarakis, W. Fowler, R. Sharpe)*

The LTD 500-kA cavity was constructed at the High Current Electronic Institute in Tomsk, Russia as a single shot device. It was delivered to Sandia and installed at the High Current LTD laboratory pictured in Figure 3.1. Following single shot testing all the support systems such as capacitor charging, switch pressurization, switch vacuum purging, pre-magnetization and triggering systems were modified and made repetition rate capable. Figure 3.2 shows a close up view of the LTD cavity where the various cable and air hoses connecting to the cavity are visible.

Figure 3.2. Close up view of the LTD cavity, the various cable and air hoses connecting to the cavity are visible.

3.1.1 Automated Operation of 0.5 MA LTD Cavity.

In addition, a "LabVIEW" [56] software package was programmed and adapted to automatically control the above operations including the data acquisition system of the current and voltage output monitors. Figure 3.3 shows the virtual control panel on the laptop computer which runs all the systems of the cavity operation. We can preset the number of pulses required for every experimental campaign and the inter-pulse separation, press the computer key, and let the system go on firing and collecting data. In the present experiments the cavity output load is a liquid resistor installed at the center of the cavity.

This year's work had the following goals: 1. Fire a large number of shots and evaluate the longevity of the cavity active components such as capacitors and switches. 2. Determine the output current and voltage jitter, which measures the pulse-to-pulse variation of starting point as compared to the trigger pulse arrival in the switches. 3. Change the various elements of the automation systems and computer program software so the cavity firing repetition rate could approach as close as possible to that required for an Inertial Fusion Energy (IFE) power plant frequency of 0.1Hz.

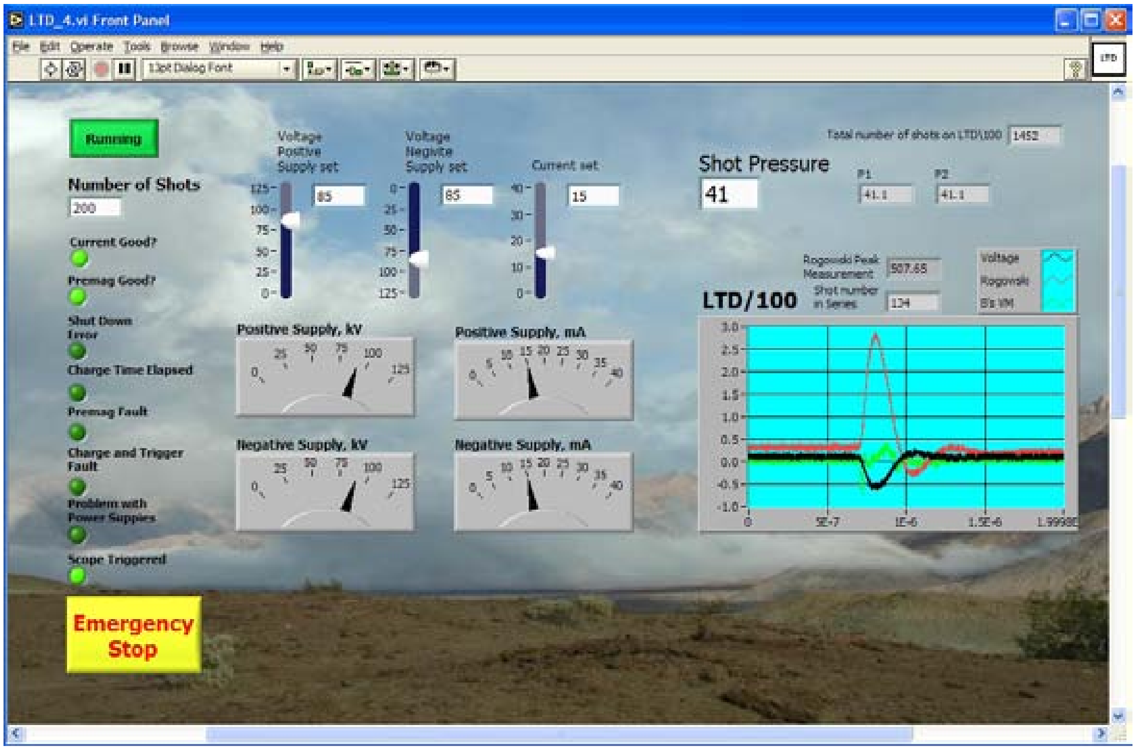

Number of Shots 200

Voltage Positive Supply set 85

Voltage Negite Supply set 85

Current set 15

Total number of shots on LTD\100 1452

Shot Pressure 41

P1 41.1

P2 41.1

Rogowski Peak Measurement 507.65

Shot number in Series 134

Figure 3.3. Virtual control panel on the laptop computer.

3.1.2 LTD Goals Achieved.

Most of the above goals were successfully completed.

1. We have fired up to now approximately 4,000 shots at rep-rate higher than 5 shots per minute without observing any component overheating or problems with the switches, the capacitors and supporting automated systems. We will continue firing the cavity until we observe any failure in order to establish the lifetime of the components. It is interesting to note that the output voltage and current pulses are extremely reproducible as witnessed by the shot overlays. Parallel with this study, a small circuit set up composed of one switch and two capacitors connected in series [similar to one of the 20 parallel circuits (named bricks) enclosed in the LTD cavity] was fired for 36,000 shots with a rep-rate of 5 shots per minute with no switch or capacitor failure. This later study was done in Tomsk HCEI under Sandia contract. It is obvious that the LTD technology is very reliable and is a good candidate for an IFE driver where a very large number of shots will be required.

2. The measured cavity output jitter is quite impressive. During a large number of shots we observed a jitter better than 2ns (1 sigma) which is much better than the one of conventional pulsed power devices.

3. We are very close to the IFE required repetition rate. At the time of the present writing we are firing every 10.3 seconds, which is equivalent to 0.097Hz! Installation of new charging power supplies are underway which we estimate that will increase the firing frequency to 0.11 to 0.12 Hz.

3.2 Testing of five 1.0 MA LTD cavities in an adder Configuration *(M. Mazarakis, A. Kim)*

Five 1-MA, 100-kV LTD cavities were assembled in a voltage adder configuration as shown in Figures 3.4 and 3.5 [56]. Only four cavities belong to Sandia. The University of Michigan owns the fifth one. We had an agreement with the University to utilize it in the present experiments before delivery to the USA. Thus we were able to have 100 kV higher voltage for the vacuum diode tests.

3.2.1 Voltage Adder Configuration for Five LTD Cavities

Figure 3.5 is an assembly drawing of the voltage adder module with the ~0.5 Ohm vacuum diode load [57]. The straight cathode stalk has the diameter of 15.15 cm; its left side is mounted on the end ground flange of the voltage adder while on it's right free standing side is mounted the ring shaped cathode electrode of the diode. The inductance of the vacuum line driving the diode is ~18 nH. The radial anode-cathode gap of the voltage adder is 6.35 cm. The peak electric field on the cathode electrode at 500 kV is ~80 kV/cm, which is well below the vacuum emission threshold of ~200 kV/cm. So the voltage adder operated in the vacuum insulated regime (no MITL regime). The current in the cathode central coaxial cylinder flowing to the anode of the voltage adder was measured by the B-dots at the ground plate located in a special groove (Figure 3.6 and detail A of Figure 3.5). The voltage across the diode was estimated by differentiating the current pulse that propagates along the inductance L_U ~ 1 μH, connected in parallel to the

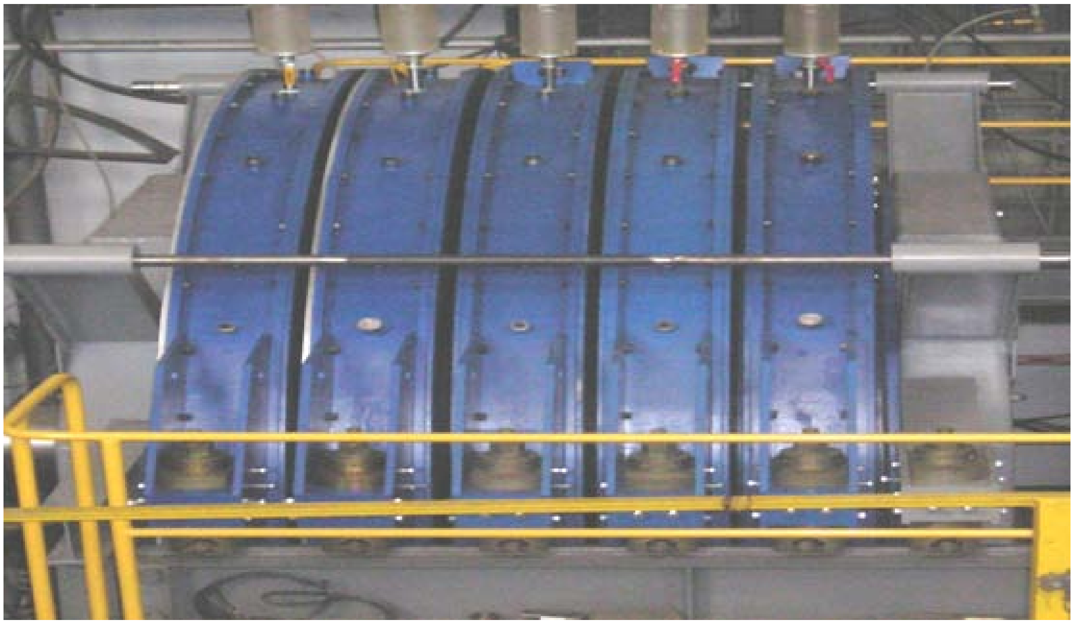

Figure 3.4. Photograph of the five 1-MA, 100-kV cavities assembled in a voltage adder configuration. The vacuum diode is not shown here but is located at the left end of the voltage adder.

load (see Figure 3.7, Figure 3.8 and detail B of Figure 3.5). The presence of such inductance reduced the output voltage by 3%, and the output power by about 5 %.

The diode is shown in Figure 3.8. It is a plane diode with cathode surface area of ~2900 cm^2. The front surface of the cathode is covered with velvet cloth to facilitate the electron emission since the cathode must operate at very low electrical fields. The AK gap can be adjusted within 1-2 cm by changing the length of cylindrical supports that hold the stainless steel anode plate.

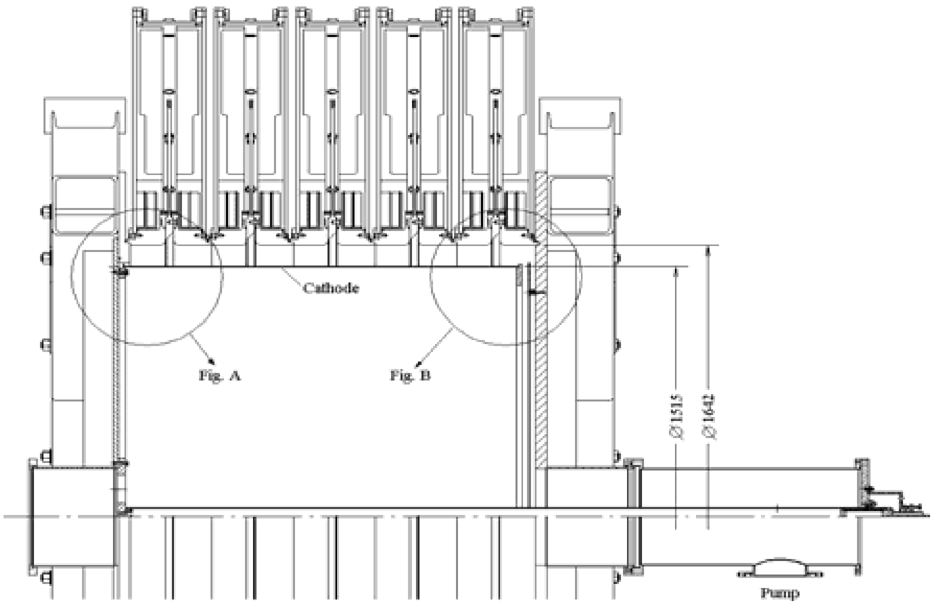

Figure 3.5. The 5-cavity LTD voltage adder module with the ~0.5 Ohm vacuum diode load at the right hand side. Only the upper half of the electrode is shown from the axis of the device.

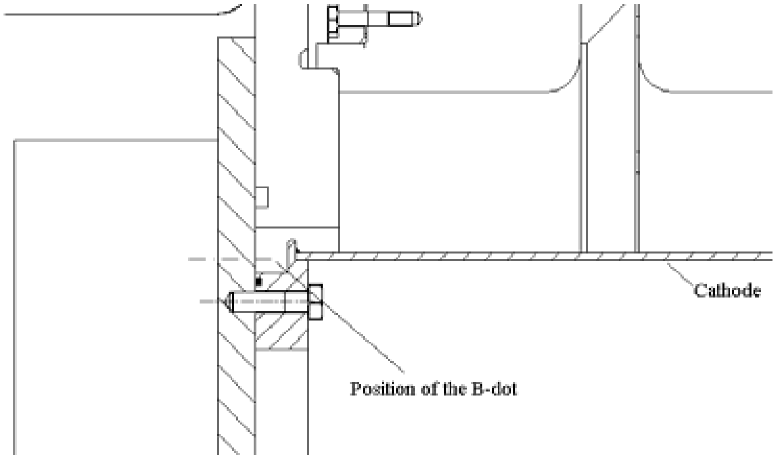

Figure 3.6. Detail A of Figure 5. Position of the B-dots measuring the current flowing on the voltage adder cathode stalk.

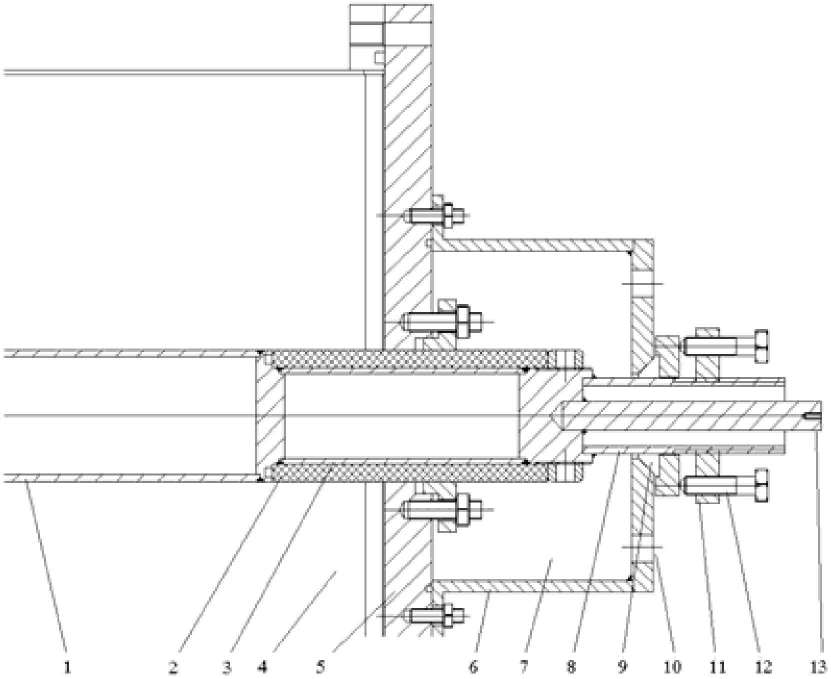

Figure 3.7. Detail B of Figure 3.5. Design of the center electrode allowing fast electric disconnection without opening the vacuum volume to atmosphere. This center electrode serve two purposes: first to measure the diode voltage and also, when isolated from the anode plate, to drive the premagnetizing current through the axis of the voltage adder.

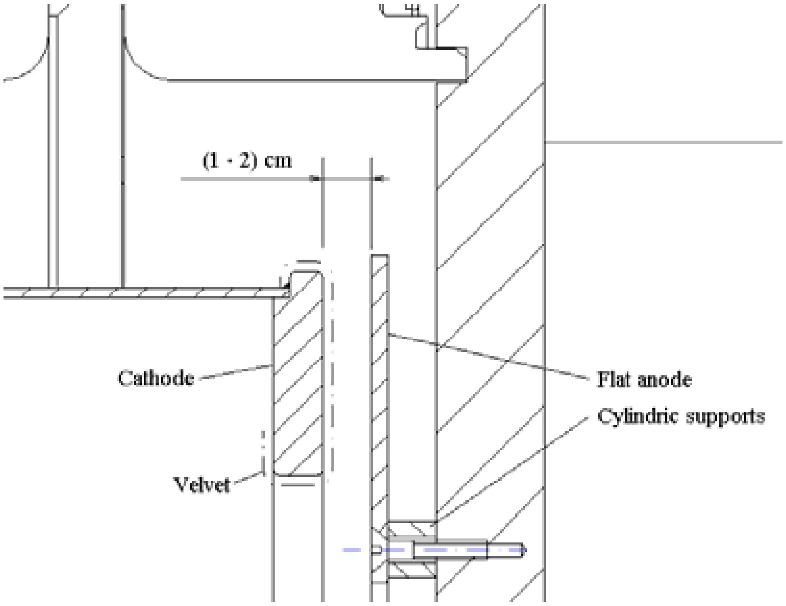

Figure 3.8. Design of the plane vacuum diode.

Figures 3.7 and 3.11 shows in detail the inductive, Lu = 1020 nH, stock which serves two purposes; first to estimate the diode voltage by measuring the current flowing through it acting as inductive voltage divider and second, when isolated from the anode plate, to drive the demagnetizing current for the cores of the LTD cavities. In Figure 3.3 only half of it is visible above the axis. In Figures 3.9 and 3.10 it is not seen because it is located on the axis of the cathode electrode and is hidden by the cylindrical wall of the cathode electrode.

In Figure 3.7, the hardware is shown in position when the electrode (8) contacts the electrode (6). This is the position for the main shot when the current in the inductance L_U ~ 1 uH is measured to define the load voltage. This current is measured with B-dots; the holes (10) show the position of the corresponding signal cable connectors.
The cores were pre-magnetized before the main shot. To do this, the bolts (12) were unscrewed, and the flange (11) with the washer (9) was removed. This procedure did not require the opening to the air of the vacuum chamber (4). A 2 mm wall dielectric pipe (not shown in Fig. 3.7) was installed into the radial gap between the side flange of the electrode (6) and the electrode (8), and the ~3 kV pre-magnetizing pulse was applied to the rod (13) which is welded to the electrode (3). In Figures 3.5 and 3.6, during the main shot the left side of the module was negative whereas the right side was positive, and the

Figure 3.9. Top view of the LTD voltage adder with the cathode electrode removed and located in front of the LTD anode vacuum cylinder.

Figure 3.10. Back view (ground plane side) of the voltage adder with the cathode electrode outside.

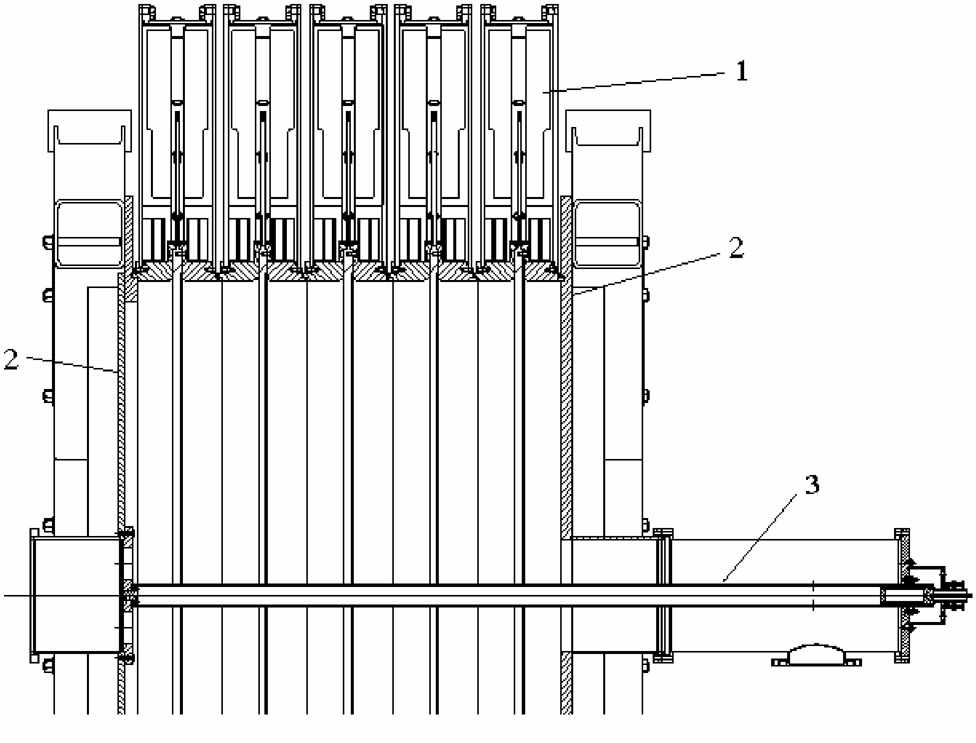

Figure 3.11. In this drawing the voltage adder cathode electrode is not shown in order to show the inductive current divider cylinder on axis (3) which, when isolated from the anode serves also as pre-magnetizing electrode. This electrode is permanently attached to the cathode or ground plate (2).

current cavities flowed on opposite direction; therefore the pre-magnetizing current must flow in the same direction as the current in the load – from the right to the left. This means the pre-magnetizing current pulse must have positive polarity. It flowed in the electrode (3) of Figure 3.11 inside the cores and returns back around the cores along the external housing of the cavities.

Design and simulations of the ~500-kV vacuum diode.

The equivalent circuit of the voltage adder and diode is presented in Figure 3.12 and the simulation results are shown in Figure 3.13. These results were used to estimate the diode parameters and predict the expected experimental results. The inductance of the load was LL = 18 nH. With such an inductance, the peak output power was obtained with a load resistance RL=0.43 Ohm. In this case the load voltage reached 360 kV (peak load current is 833 kA) in 97 ns, peak power was 299 GW, and the reversal voltage on the capacitors was 14%. The energy delivered to the diode until the voltage crossed zero was ~ 40 kJ. The current in the inductance Lu reached 77 kA in 263 ns. The simulated voltage measured with the inductive divider shows high frequency oscillations due to parasitic resonances of the circuit. These oscillations are real and not due to a software mathematical instability. They were also observed on the experimental voltage traces before the utilization of smoothing algorithm.

For a voltage of less than 500 kV the non-relativistic equations for space charge limited electron emission in a plane diode can be utilized and the A-K gap, d, can be estimated by using the expressions

$$I[A] = P(U_D[V])^{3/2}, \quad P = 2.335 \cdot 10^{-6}\frac{S}{d^2},$$

where S is the cathode emitting surface area and d is AK gap. For $U_D \sim 360$ kV and I ~ 833 kA the perveance is $P \sim 3.8 \cdot 10^{-3}$ $A/V^{3/2}$ which for S ~2900 cm^2 requires a d ~ 1.325 cm.

These estimations were confirmed by PIC simulation where for U = 500 kV and I = 1 MA an A-K gap of ~1.5 cm was required. The simulated electron flow is shown in Fig. 3.14. It indicates that in such conditions the electron flow is slightly pinched.

3.2.2 Experimental Results

A total of ~100 shots were fired with the diode load. We varied the charging voltage between 80 and 90 kV. The electron diode A-K gap was adjusted for optimum performance. A gap of 1.4 cm gave the load voltage predicted by the circuit and PIC; however, the measured current, energy and power were higher. At the beginning of the experiments we experienced some diode arcing due to lack of precise parallelism between the cathode emitting surface and the anode plate. After correcting this problem by utilizing spacers built especially in anticipation of that problem, the voltage adder and the diode performed well, but still we had to change the cathode velvet every 10 shots. Some electron losses were observed inside the voltage adder; however the plastic

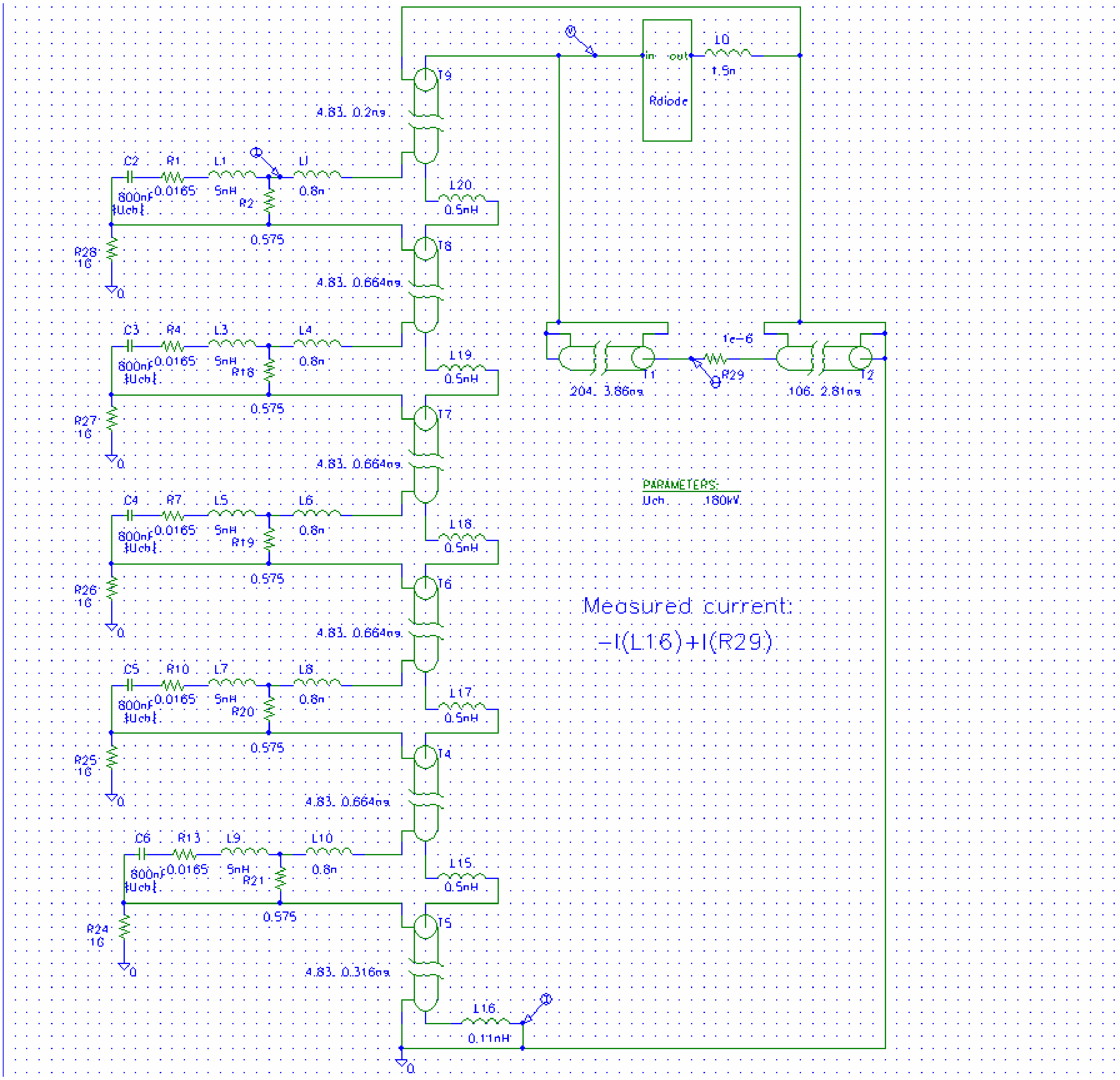

Figure 3.12. Pspice scheme of the 5-cavity, 1-MA, LTD module driving the diode load RL.

insulating rings of each cavity did not exhibit any sign of arcing. In a few shots with a larger diode A-K gap of the order of 2 cm, signs of electron emission from the cylindrical surface of the voltage adder cathode electrode at the high voltage end was observed.

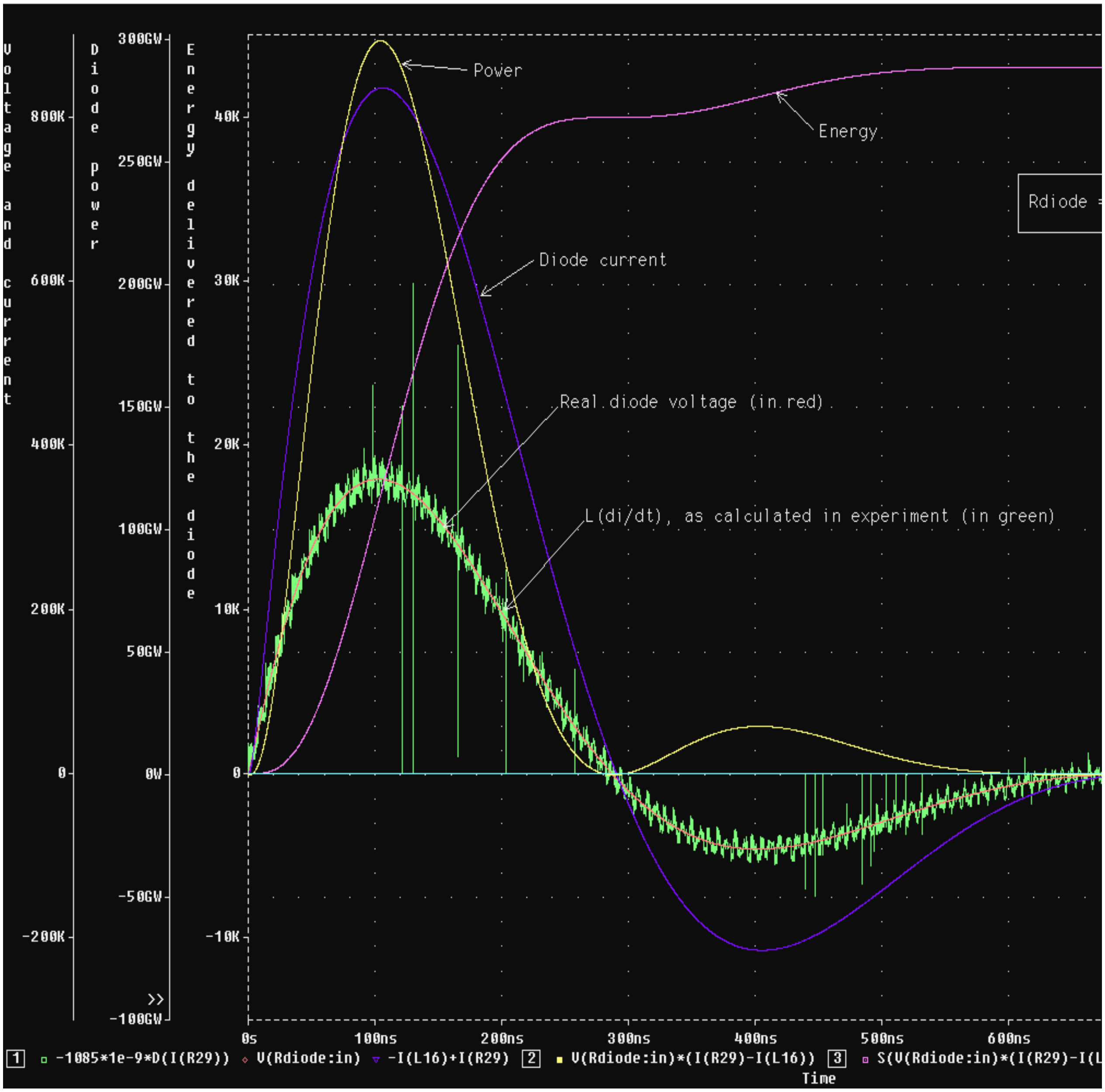

Figure 3.13. Performance of the 5-cavity LTDZ module with 0.43-Ohm diode load.

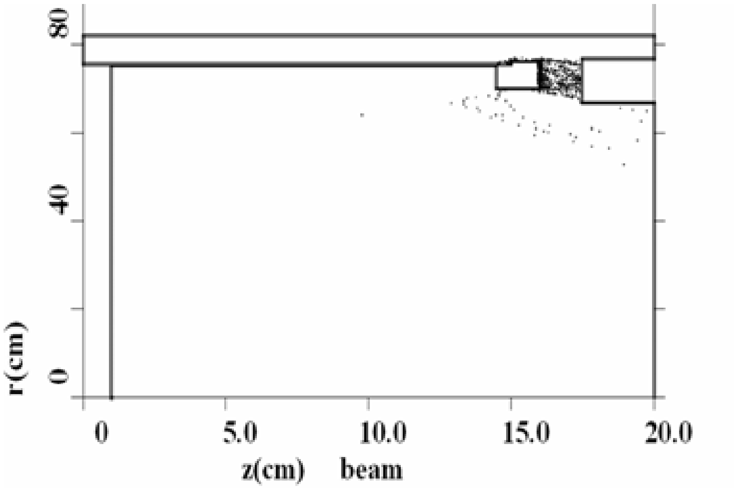

Figure 3.14. Vacuum diode PIC simulation of the electron flow 25ns into the voltage pulse for a peak voltage and current respectively of U=500 kV and I=1MA. The A-K gap is 1.5cm.

This did not have any detrimental effect on the anode surface or plastic insulators; however some superficial surface damage was observed. Closing the diode A-K gap to the PIC simulation predicted values appeared to solve the problem. The voltage adder radial anode cathode gap is much larger, 6.5cm, than the diode gap (~2cm), and we should not have observed this problem. However since the diode is located inside the voltage adder, diode plasma going upstream into the radial gap or UV and x-rays emitted from the diode and illuminating the cathode cylindrical surface, which could be the cause of radial emission. In any case in the follow up shots we refrained from using gaps of 2 cm or larger.

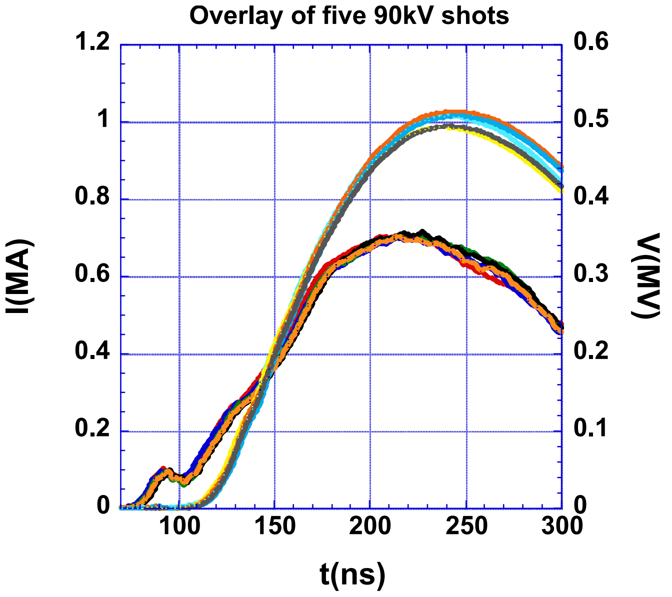

Figure 3.15. Overlay of five 90kV-charging shots.

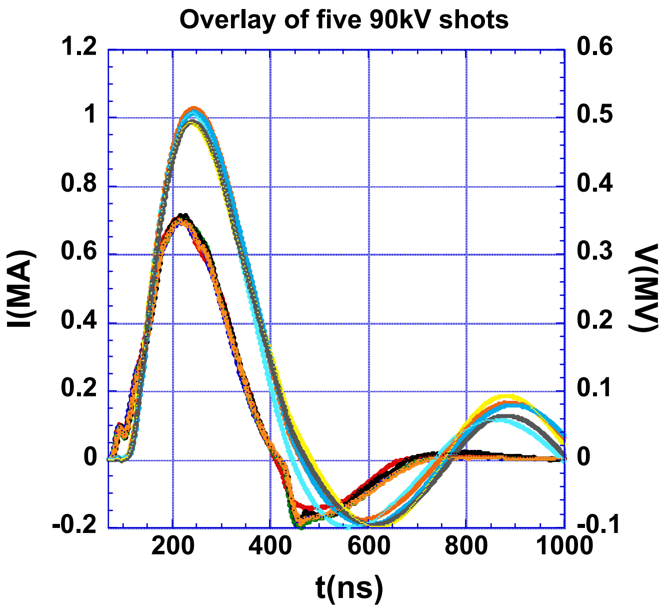

Figure 3.16. Overlay of five 90-kV charging shots in larger time base.

Figure 3.15 is an overlay of five 90kV charging shots. Figure 3.16 presents the same data in a larger time base to show the diode shorting at volt reversal and the late current ringing. These results suggest that although the diode shorted at reversal, the cavity insulators did not flash since the current kept ringing. Figure 3.17 gives a sample of the diode power and energy output for charging voltage 90kV.

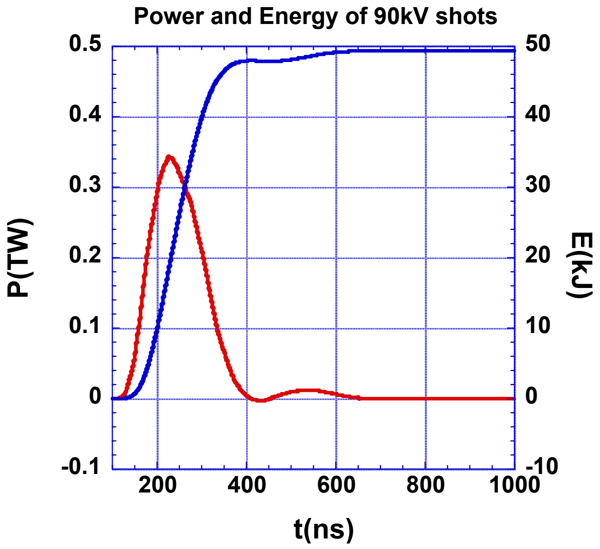

Figure 3.17. Sample of the diode power and energy output for 90-kV charging voltage.

The traces of all the above parameters are close to the ones predicted by the circuit code simulations (Figure 3.13). The current traces are having exactly the shape as expected from simulations; however, the voltage traces are somewhat different than the ones predicted by the circuit codes assuming constant diode impedance. The voltage and the current traces track each other well up to a certain value before the peak, but then the diode voltage trace rate of increase decreases and appears clipping (chewed up) and exhibits some oscillations. We believe that at this point bipolar flow takes into effect due to anode plasma formation, and the diode impedance decreases. This speculation is corroborated also with the observed larger than expected peak current and the shorter FWHM voltage trace as compared with the current traces. This phenomenon becomes more pronounced as the LTD charging voltage increases.

The observed higher peak current, energy and power could also be attributed at least to a certain extent to radial current loses inside the voltage adder. The current measuring B-dots were at the base of the cathode Stock (Figure 3.6); any radial loss would have been accounted as diode beam current.

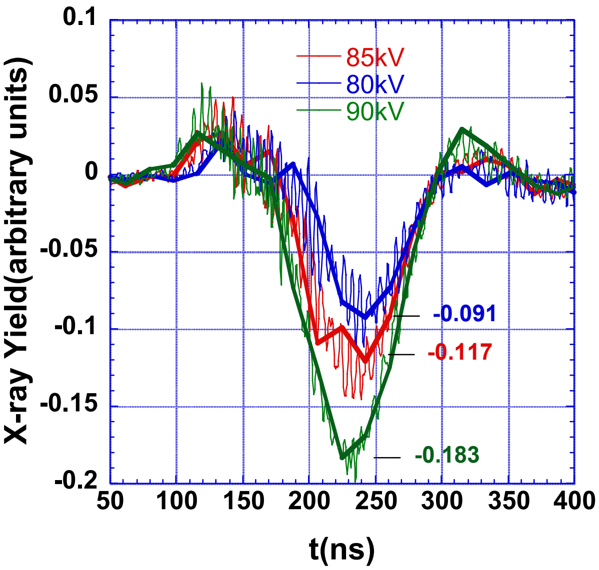

Figure 3.18. X-ray pin diode traces for three charging voltages 80kV, 85kV, and 90kV. The solid curves are from an interpolation fitting.

Figure 3.18 shows the x-ray pin diode traces for three charging voltages 80kV, 85kV, and 90kV. The pin diode was located ~ 5cm away from the diode anode plate. The x-ray peak values (relative unites) scale with the LTD charging voltage as $V^{4.8}$ (Figure 3.19) which is quite higher than expected.

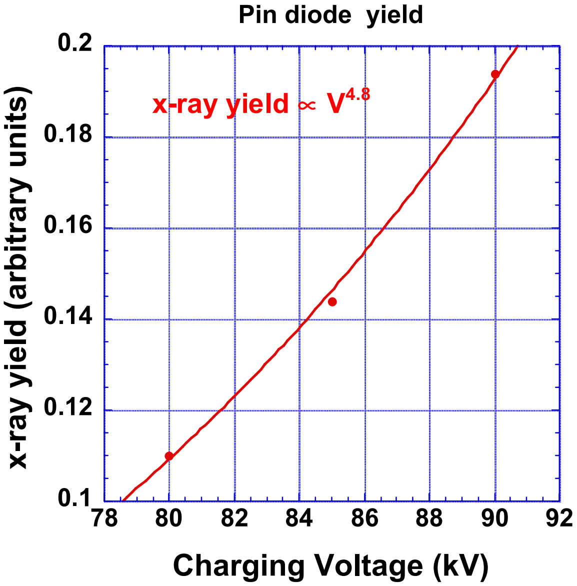

Figure 3.19. X-ray peak values (relative unites) scaling with the LTD charging voltage.

In summary, the 5 LTD, 1-MA voltage adder experiments successfully demonstrated that LTD cavities can operate in a voltage adder configuration. The diode voltage behavior is understood and should be expected from such a small A-K gap and relatively long ~ 120-ns FWHM driving voltage pulse. Despite the great challenge of testing such a low voltage adder with only a ~ 0.4 Ohm impedance electron vacuum diode, the results were successful and have proven that fast LTD voltage adders is a very promising technology for future large current driver devices.

3.3 LTD driver (60 MA) design for high yield and IFE using one layer of LTDs *(M. Mazarakis)*

The present thinking for the future high current drivers is that in order to achieve target ignition and high gain, the drivers should provide a current to the load not less than 60 MA with a rise time of 100 ns or preferably less. The load inductance could be of the order 10-15 nH. Therefore a driver capable of driving that inductance will be necessary.

3.3.1 Design of 60 MA LTD Driver

Based on the above consideration we select a 60-MA, 6-MV, driver. The building blocks are 1-MA, 100-kV, ~70-ns pulse rise time LTD cavities [58] similar to the one shown in Figures 3.20 and 3.21. Figure 3.21 is a photograph of five 1-MA, LTD cavities mounted vertically on the 10-cavity voltage adder stand. Figure 3.22 presents the measured voltage and current output of each of these cavities.

Each cavity has 40, 200-kV switches and 80 capacitors arranged in 40 individual circuits (bricks) feeding in parallel through an iron tape core the accelerating cavity gap. The capacitors of the brick are charged to opposite 100-kV polarity and are connected to the two ends of the switch. So when the switch closes approximately a 100-kV voltage pulse is applied to the accelerating gap (matched case). The total inductance of one brick, including the switch inductance and that of the two capacitors connected in series, is 232 nH. The capacitance of the two capacitors is 20 nF (40 nF each), and their internal resistance is 0.600 Ohms (0.300 Ohm each). Therefore the equivalent circuit of Figure 20 for one 1-MA, 100-kV cavity will have L = 5.8 nH, C = 800 nF, internal resistance 0.015 Ohms, and matched external, load resistance equal to 0.070 Ohms.

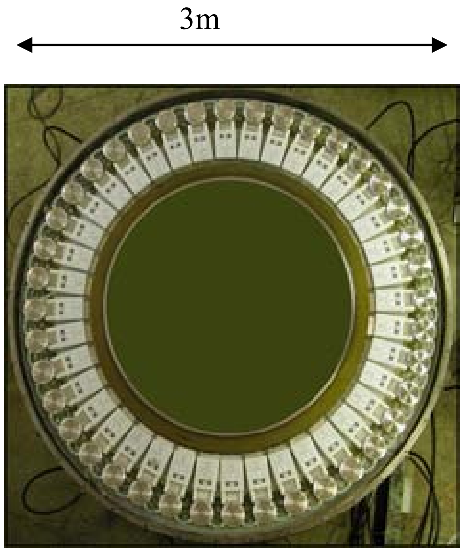

Figure 3.20. 1-MA, 100kV, 70ns LTD cavity with the top flange removed. The 40 switches and the top capacitor of the 40 individual brick circuits are also shown.

We select 60, 60-cavity voltage adders connected in parallel to a single bi-plate or tri-plate transmission line feeding the final (RTL) MITL in the center of which is located the z-pinch load and the ICF/IFE capsule. A single level arrangement of the voltage adders will be preferable for IFE since will make the system of fast replacement of the RTLs and the power flow from the IVA to the bi-plate or tri-plate to the RTL much simpler. In that case no convolutes will be required (Figure 3.23).

In the system considered here the number of cavities per module and the number of modules connected in parallel are the same. Therefore the entire 60-MV driver will have an equivalent circuit identical to that of one cavity. The total values of inductance, capacitance and resistance of the driver are estimated assuming 60 cavities connected in series in each voltage adder and 60 voltage adders connected in parallel to feed a single wire array load with final MITL inductance (L_{MITL}) of 10 nH and initial load inductance of 1 nH. Figure 3.24 presents a circuit model result for a total mass load of 55mg.
The cavity diameter is of the order of 3m. The radius of closest approach of the front of 60 voltage adders cannot be shorter than 31m, which necessitates coaxial MITLS of

Figure 3.21. Photograph of five LTD cavities assembled in a voltage adder configuration out of the planned ten 1-MA, 100-kV LTD cavities that will complete a 1-MA, 1-MV voltage adder.

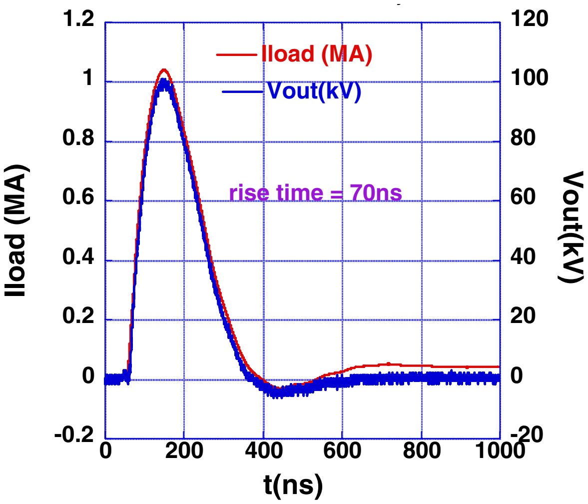

Figure 3.22. Voltage and current output of the 1-MA, 100-kV cavity.

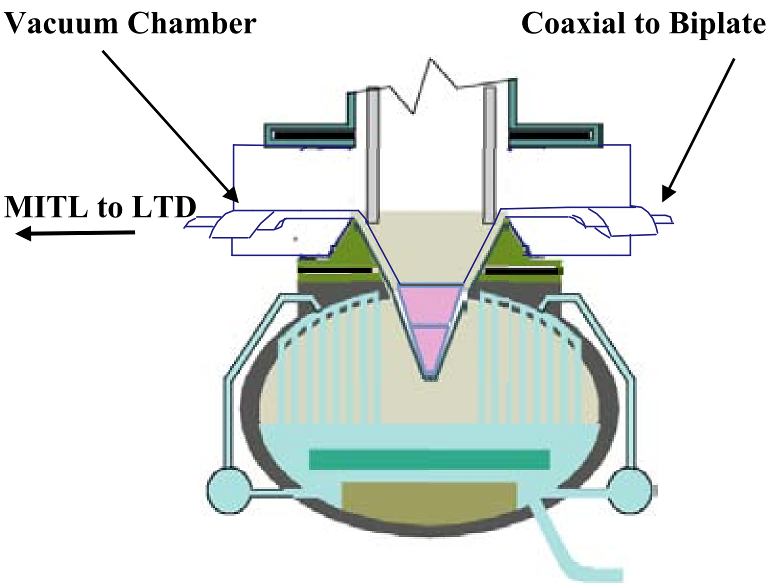

Figure 3.23. IFE Z-pinch reaction chamber fed by LTD modules connected to the load in parallel through coaxial to bi-plate transition region (single ended wire array load).

similar length to connect the output of the voltage adder to the load. Although this will erode the front of the pulse, it will also have two beneficial effects; first it will sharpen the pulse front and thus give the increased power output of the fast pinches: second it will time isolate the cavities from the load and make them unaffected by the load inductance increase during the final stages of the implosion. A 60 cavity voltage adder, including the length of pumping stations, will be approximately ~13 m long. Therefore the overall radius of the driver will be of the order of 44 m and the height including the support structure ~5 m. It will contain a total of 3,600 cavities, 144,000 pressurized air-closing switches and 288,000 capacitors.

Inde~~ed~~ the number of components is very large, however there are only four major components in the entire driver, which repeat themselves many times; a capacitor, a switch, an iron core and a cavity housing. This also provides redundancy, the great advantage of jitter reduction, and graceful degradation. In addition, of course, there is a large cost reduction in purchasing many identical components.

The above design is quite optimistic and ideal. It neglects the losses in the long MITLs and coaxial to bi-plate or tri-plate transition region.

In order to precisely estimate the losses, 2D and 3D particle in cell code modeling will be necessary. Previous similar system studies during the JUPITER and LMF projects, suggest an approximate 10%-15% total current losses in the long MITLs due to front pulse erosion and losses in the transition region due to magnetic nulls. To

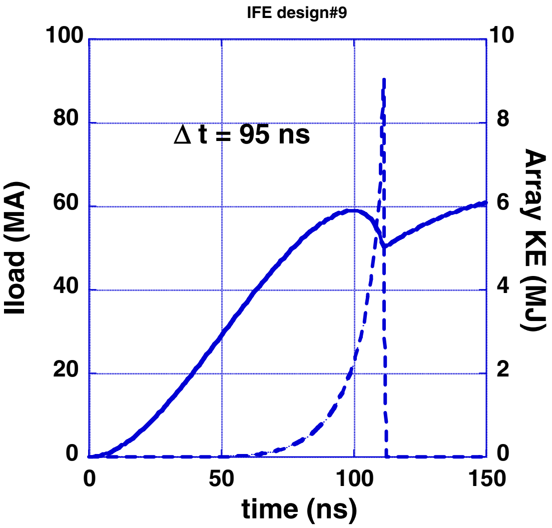

Figure 3.24. Load current and kinetic energy of an imploding 55mg single array load.

compensate for that, in a subsequent design (Figure 3.25), we increased the number of module adders from 60 to 70.

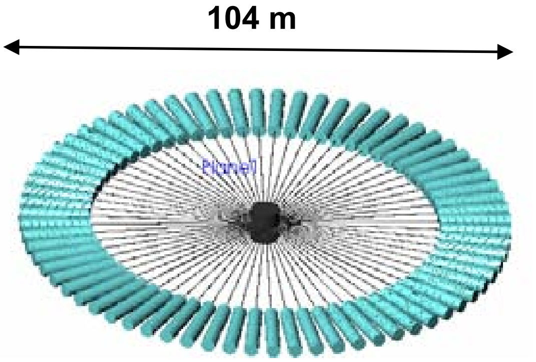

Figure 3.25. Top view of a 70 modules 70 cavity per module, LTD, driver. The overall diameter is 104 m.

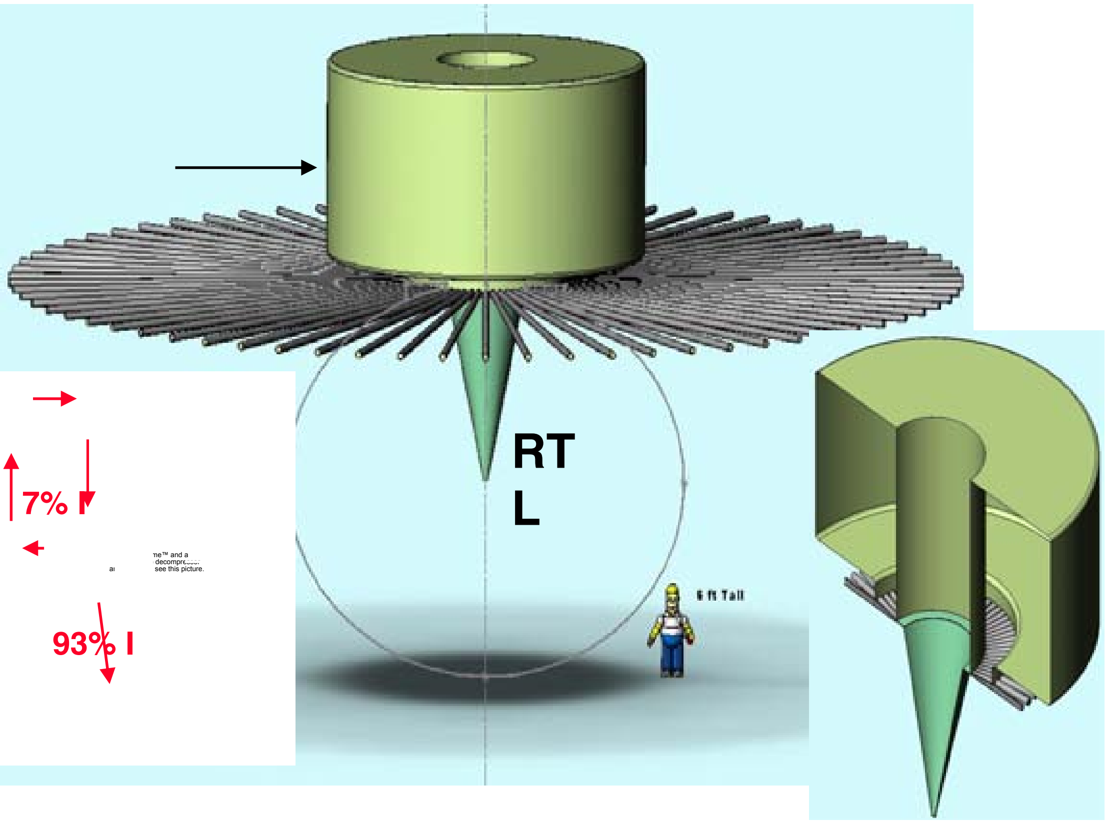

Figure 3.26. Seventy coaxial MITLs terminate at the outer wall at the bottom neck of the inductive insulating chamber.

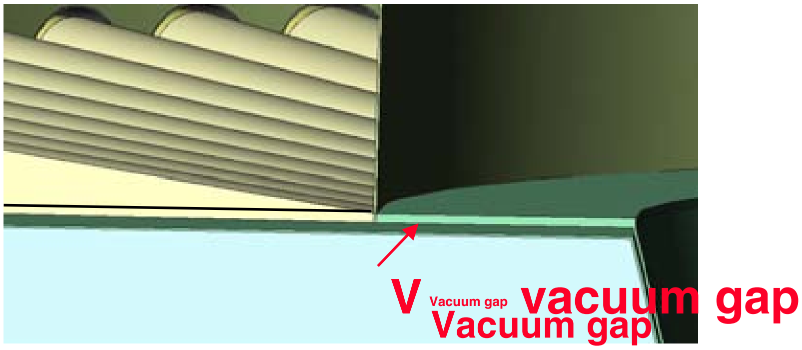

Figure 3.27. Close-up showing the merging of 70 coaxial lines to a disk bi-plate transmission line.

3.3.2 Merging of Coax MITLs to a Single Bi-Plate to an RTL

Figures 3.26 and 3.27 give a detailed view of how we merge the coaxial MITLs into a single biplate that feeds the RTL. We propose a large cylindrical electrode, which isolates and support the negatively charged cathode electrode from the ground. The anode outer cylinder of each coaxial MITL terminates at the outer wall of the large cylindrical chamber. The central cathode electrode enters into the chamber and flattens to a plate connecting together all the cathode electrodes. This plate forms a disk shaped bi-plate MITL together with the bottom wall of the large cylindrical vessel. The bi-plate then connects directly to the conical RTL and to the IEF/ICF load. For the dimensions of the vessel presented in Figure 3.27 the current losses are of the order of 10%. The disadvantage of this architecture is that the driver's footprint is large. If that becomes a serious concern, especially for a Z-pinch ICF driver, a multilevel arrangement with post –hole convolutes could be considered.

3.4 Driver Transition Geometries and Inductance Considerations Leading to Design Guidelines for a Z-IFE Power Plant *(D. L. Smith, SNL)*

A 60 MA, 7 MV, ~100-ns driver for a Z-pinch Inertial Fusion Energy (Z-IFE) power plant has been proposed [54]. In this summary we address the transition region between the 70 Linear Transformer Driver (LTD) modules and the center Recyclable Transmission Line (RTL) load section, which convolves from the coaxial vacuum Magnetically Insulated Transmission Lines (MITL) to a parallel tri-plate and then a bi-plate disk feed. An inductive annular chamber terminates one side of the tri-plate in a manner that preserves vacuum and electrical circuit integrity without significant energy losses. The simplicity is offset by the disadvantage of the chamber size, which is proportional to the driver impedance and decreases with the addition of more parallel modules. Inductive isolation chamber sizes are estimated in this paper based on an optimized LTD equivalent circuit simulation source driving a matched load with transmission line models. We consider the trade-offs between acceptable energy loss and the size of the inductive isolation chamber; accepting a 6% energy loss would only require a 60-nH chamber.

3.4.1 Transition geometries and circuit model

One proposed configuration for the center section of a Z-IFE power plant is shown in Figure 3.28. Our goals with this effort are to justify reducing the size of the inductive tri-plate termination chamber and realistically visualizing the coaxial-to-bi-plate transition.

The transition region between the LTD driver modules (not shown in Figure 3.28) and the center RTL load section represents a major reconfiguration from the large radius to the smaller radius coaxial geometries that convolve to a parallel tri-plate and then a bi-plate disk feed. One side of the tri-plate must be terminated in a manner that preserves vacuum and electrical circuit integrity without significant energy losses. The preferred method of terminating one side of the LTD output tri-plate is with an inductive loop (in 2-D) or annular chamber (in 3-D) as indicated in the sectioned top and side views of Figure 3.29. The simplicity is offset by the disadvantage of the chamber size, especially for the higher impedance drivers. Inductance is proportional to the volume enclosed by

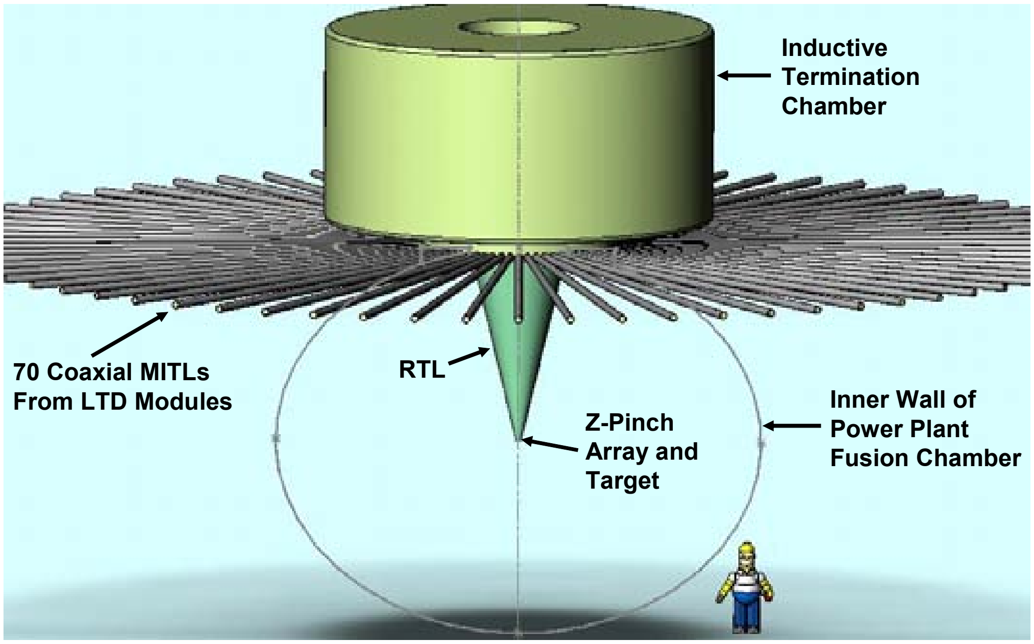

Figure 3.28. The Z-IFE power plant center region shows vacuum MITLs, large inductive tank, RTL, Z-Pinch location, and the fusion chamber with a scaled Homer model. The termination chamber is sized for a minimum loss, becoming the dominant structure.

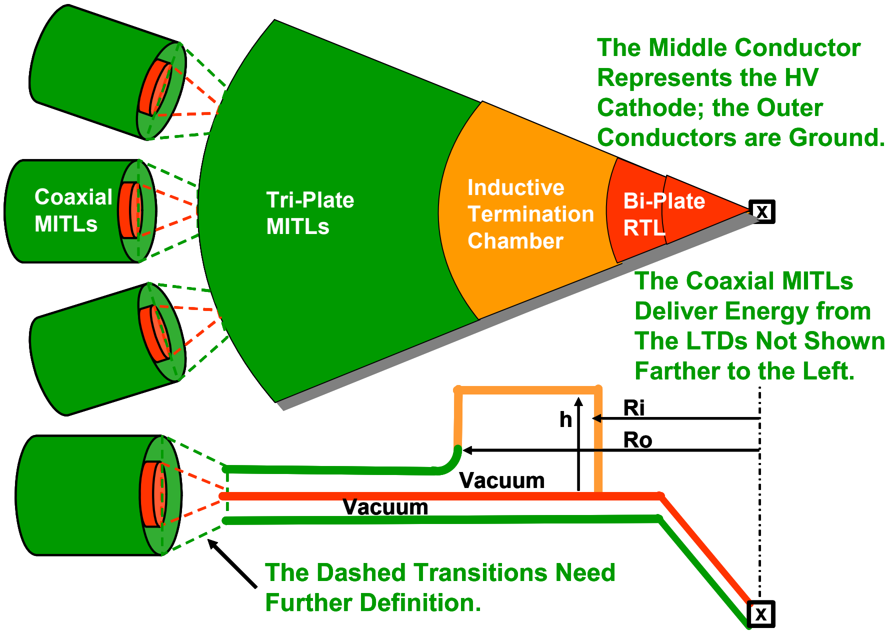

Figure 3.29. Top and side section views of the transition and center section.

the current path. The chamber inductance and size are also proportional to the driver impedance and decrease with the addition of more parallel modules. By avoiding vacuum insulators and inductive isolation cores we reduce risk, cost, and material design issues.

Inductive isolation chamber sizes are estimated here based on an LTD equivalent circuit model source driving a matched load with transmission line models. This technique largely reduces the impact of the confusing reflections coming back from the load and the source. A Micro-Cap version 7.0 circuit solving code was used to simulate the transition from the LTD coaxial T-line to the parallel-plate disk feed. The typical circuit schematic used in this study is shown in Figure 3.30.

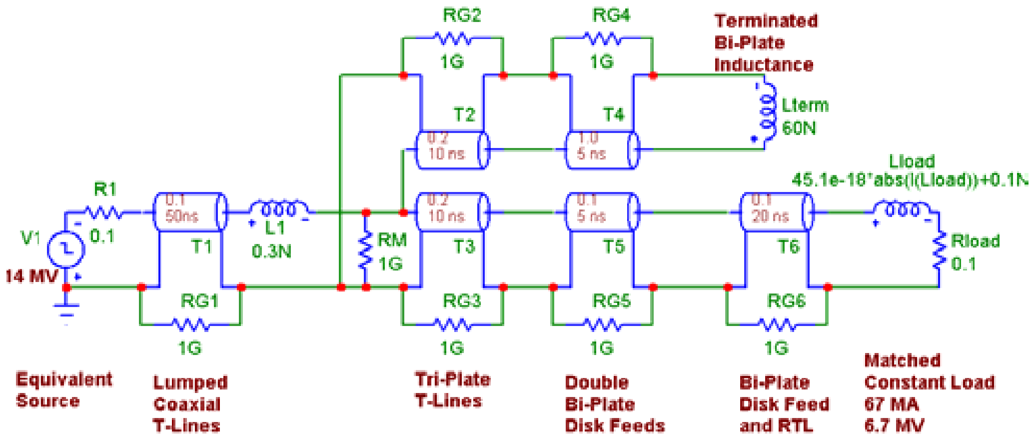

Figure 3.30. Typical Micro-Cap circuit model used for Z-IFE sensitivity studies.

Optimization is achieved by iteratively varying only one component in the simple circuit model while holding the others constant and comparing the total energy (at the time of peak current) delivered to the load. The trade-offs between simplicity, cost, acceptable energy loss, peak voltage, and the size of the inductive isolation chamber must be considered.

3.4.2 IFE Power Plant Model

Although the scale of a power plant is much larger than a one or two module Proof-of-Principle (PoP) test facility (refer to Figure 3.31), it makes sense to apply the same logical approach to address the Z-IFE plant of Fig. 1 with 70 each of seventy-cavity LTD modules and try to establish some design guidelines. Seventy stacked 0.1-**Ω** cavities make a 7.0-**Ω** module, but with 70 modules in parallel, we are back to a 0.1-**Ω** overall driver. Because of the large number of cavities in each module, the equivalent source voltage in the schematic of Figure 3.30 is 14 MV, and the nominal simulation output to the matched load becomes about 6.67 MV and 66.7 MA. Figure 3.32 shows representative waveforms produced by the model of Figure 3.30 when a time-varying load inductance is included to better simulate the imploding Z-pinch array.

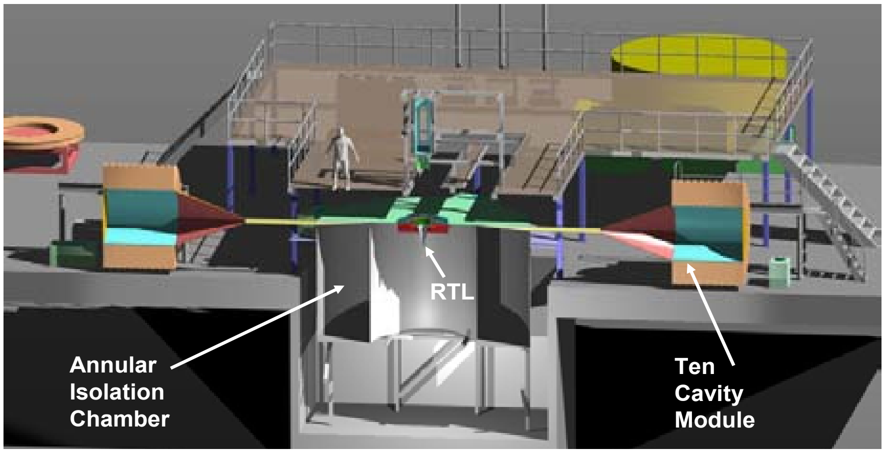

Figure 3.31. A cut-away view of the Z-PoP two module facility model emphasizes the size of the inductive isolation chamber, which is designed for low loss and inverted. Two or more compact LTD modules could demonstrate many of the performance issues of a larger facility.

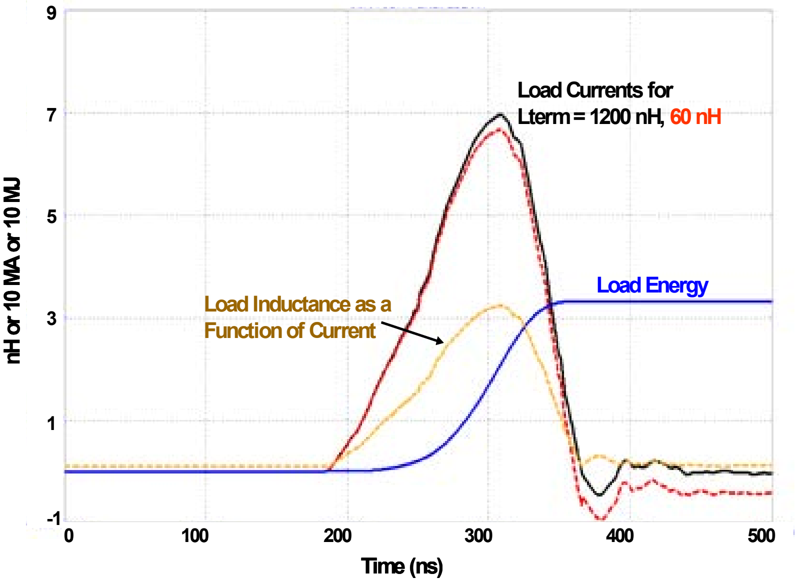

Figure 3.32. Sample waveforms from the model of Figure 3.30. The time scale is 100 ns per division. The lower current case results from a smaller, 60-nH termination of one side of the tri-plate.

A sensitivity study was conducted generating the plots of Figures 3.33, 3.34, and 3.35. Reasonable trade-offs can reduce the size and voltage of the tri-plate termination/isolation chamber. From this modeling effort there are some primary conclusions that we may draw. Accepting only 2% energy losses would require a 600-nH tri-plate termination, which would be rather large. Simulations show a 60-nH inductive isolation chamber would have ~6% energy losses for a Z-IFE plant equivalent model. Reducing the inductive isolation chamber to 25 nH results in about 12% losses. Adding the time-varying load inductance suggests a slightly more optimistic result. The peak voltage at the circuit model termination inductance varies from 8.1 MV when Lterm = 1200 nH to 7.0 MV when Lterm = 60 nH, for the matched resistive load case. For the varying inductance case, the termination inductance voltage varies between 7.0 and 8.7 MV, and the peak load current ranges from 63.2 to 70.0 MA for 40 nH ≤ Lterm ≤ 2000 nH.

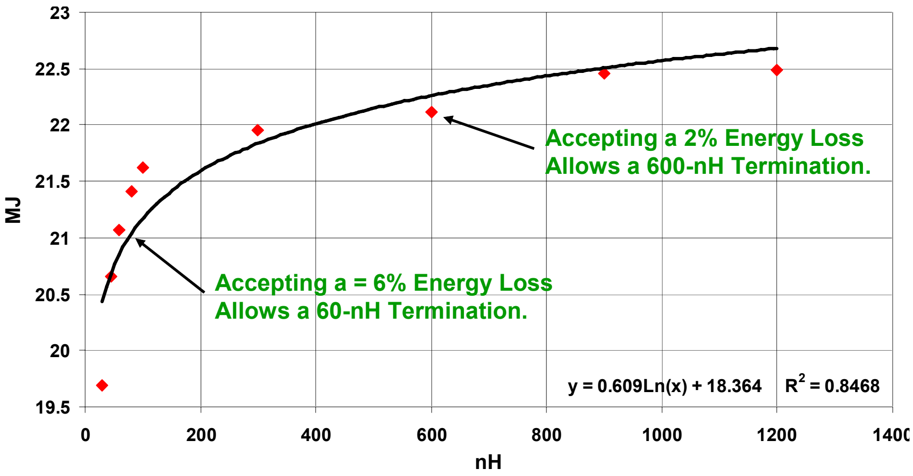

Accepting a 2% Energy Loss Allows a 600-nH Termination.

Accepting a = 6% Energy Loss Allows a 60-nH Termination.

Figure 3.33. Load energy versus tri-plate termination inductance for a matched resistive load.

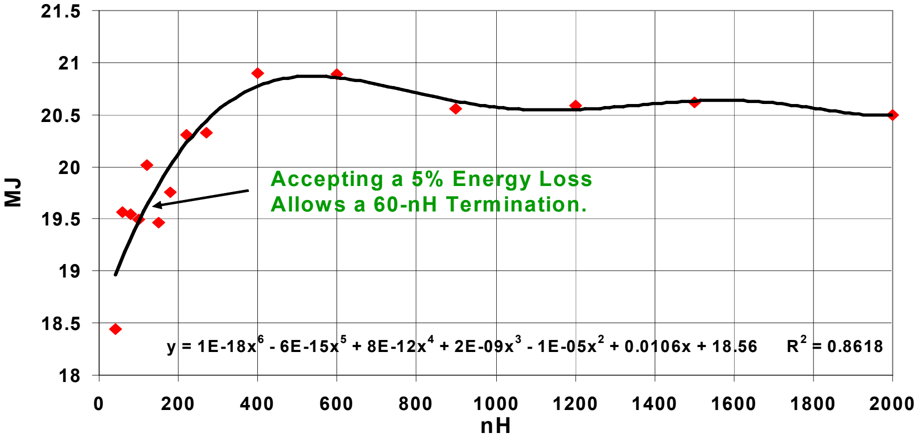

Accepting a 5% Energy Loss Allows a 60-nH Termination.

Figure 3.34. Load energy versus tri-plate termination inductance with a time-varying inductance load.

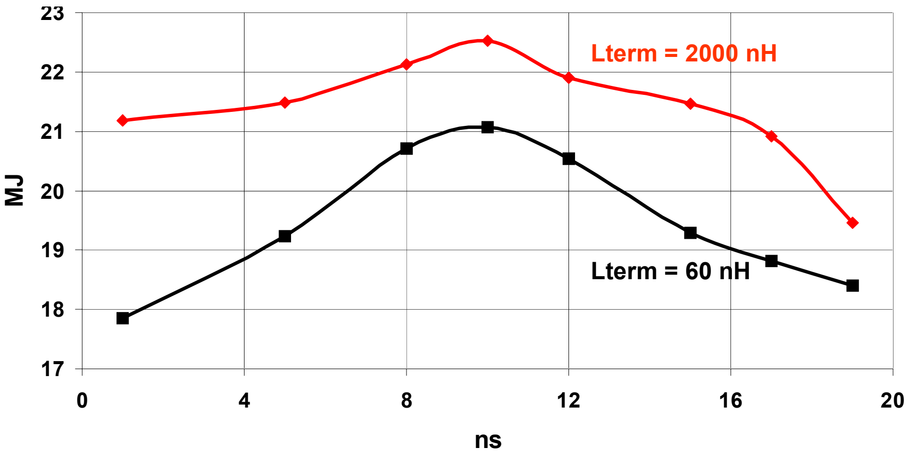

Figure 3.35. Load energy versus tri-plate propagation time (length) for two chamber sizes.

For a matched load an optimum tri-plate length between the coaxial transition and the termination/isolation chamber is about 3 m (or 10 ns) according to Figure 3.35. Shorter tri-plate transmission lines would reduce the overall machine size but also decrease the load energy efficiency. The optimum design may vary some with the pulse width and shape.

3.4.3 Chamber Size Options

Although these results come from a simple circuit model that may change as the cavities, cores, switches, and capacitors evolve to the final reactor driver design, they are probably generically correct for estimating the inductive isolation chamber sizes. It always helps to visualize hardware sizes and the impact that they may have by calculating a few example cases. That is done in the following Table 3.1 for four different chamber inductances. The emboldened items in the table are being considered as likely candidates. The three dimensions of interest are defined in Figure 3.29. The height, **h**, is estimated after choosing "typical" values for the inner and outer radii, **Ri** and **Ro**, respectively. The following equation has the units of meters and Henries.

$$h = L / [2 \times 10^{-7} \ln (Ro / Ri)]$$

Some issues are outside the scope of this summary. Where and when is the magnetic insulation lost? What is the maximum voltage drop across the chamber feed? What is the probability of a vacuum arc in the termination chamber? Figure 3.36 shows an example equipotential plot of the side view of the upper tri-plate section from the MITL into the inductive termination chamber on the right. Figure 3.37 indicates a range of possible surface field stresses along the points A, B, C, and D of Figure 3.36. The magnetic insulation should prevail in the small gaps but not in the isolation chamber. A more complex (3D), dynamic simulation may be necessary to answer these types of questions with any credibility. For instance, the leading edge of the current pulse should propagate around the inner surface of the chamber wall (~12.4 ns) before the voltage can complete its rise time, and possibly limit its peak value.

TABLE 3.1. Example chamber sizes (in meters) for four different isolation inductances.

		L =	500 nH		L =	200 nH		L =	70 nH		L =	60 nH
Ri		**Ro**	**h**		**Ro**	**h**		**Ro**	**h**		**Ro**	**h**
1.0		2.0	3.6		1.75	1.79		1.5	0.86			
1.0		2.5	2.7		2.0	1.44						
1.5		2.5	4.9		2.5	1.96		2.5	0.69			
1.5		3.0	3.6		3.0	1.44					**2.5**	**0.59**
2.0								**3.0**	**0.86**		**2.5**	**1.34**
2.0											**3.0**	**0.74**
2.5											3.5	0.89

The inner radius of the chamber will be determined by the vacuum/RTL/target center section infrastructure and access requirements. A rectangular cross-section was assumed for these examples; the final design will likely be dome shaped for strength and compactness. A 60-nH, 2-m inner radius chamber may be 1-m thick and about 1-m tall with a rounded dome.

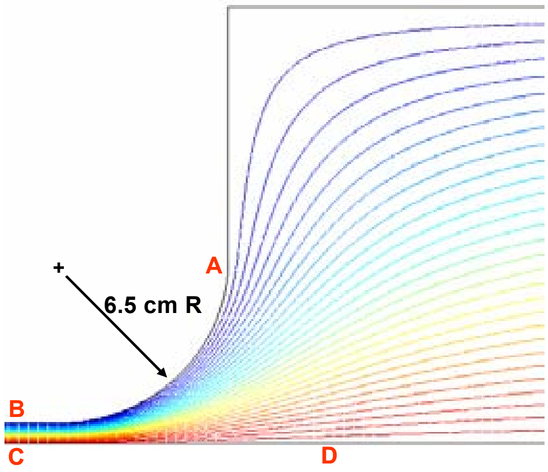

Figure 3.36. Example equipotential plot from the side view of the upper triplate MITL section (at BC) into the inductive termination chamber on the right.

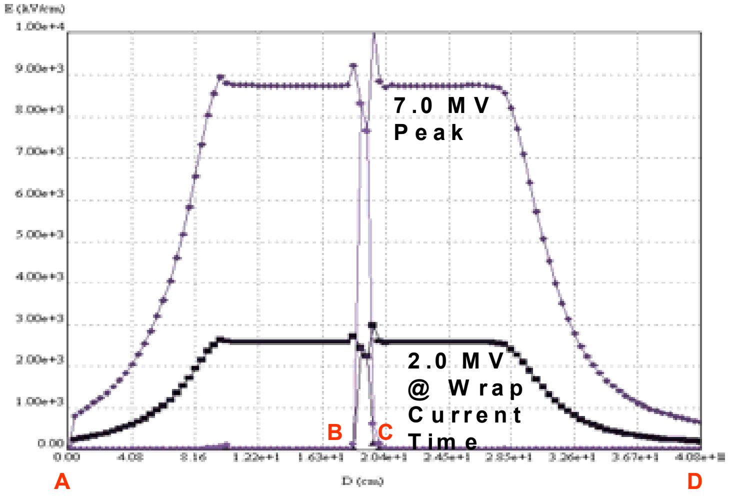

Figure 3.37. Example of the electric field stresses at two times (voltages) along the electrodes surfaces at points A, B, C, and D of Figure 3.36.

3.4.4 Coaxial-to-Disc Visualization

Certain assumptions are necessary in order to grasp a three-dimensional picture of the transition from the coaxial MITL feeds to a final parallel disk connection to the RTL:

- We want to maintain the same MITL impedance as nearly as reasonable.
- Assume a constant vacuum gap of about 1 cm throughout the transition.
- Avoid small radii and large field enhancements.
- The 3-D visualization must be supported by electric field analyses.
- Fabrication and assembly processes may require some compromises.
- The following "cartoons" are an attempt to help visualize the power flow transition from parallel coaxial lines to a monolithic disk feed.
- Graphic representations have exaggerated scales in order to show the finer details.

The two-dimensional section views of Figures 3.38, 3.39 and 3.40 are an attempt to describe the geometric transformation starting with two of the coaxial MITLs (the dashed line regions of Figure 3.29). Approximate dimensions are included to provide some scale for the reader.

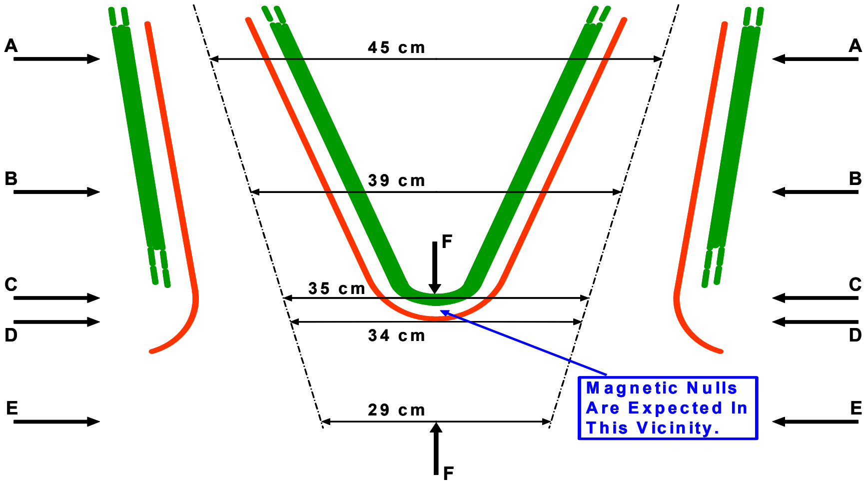

Figure 3.38. Top view of a horizontal cut through the center conductors of two of the coaxial and tri-plate geometries. The lettered arrows indicate the location of the vertical section views seen in Figures 3.39 and 3.40. As usual, the high voltage is on the inner conductors; the outer conductors are tied to ground. The circular cross-section transmission lines have a vacuum impedance of about 8.6 Ω and an operating MITL impedance of about 6.8 Ω (nominally 7 Ω).

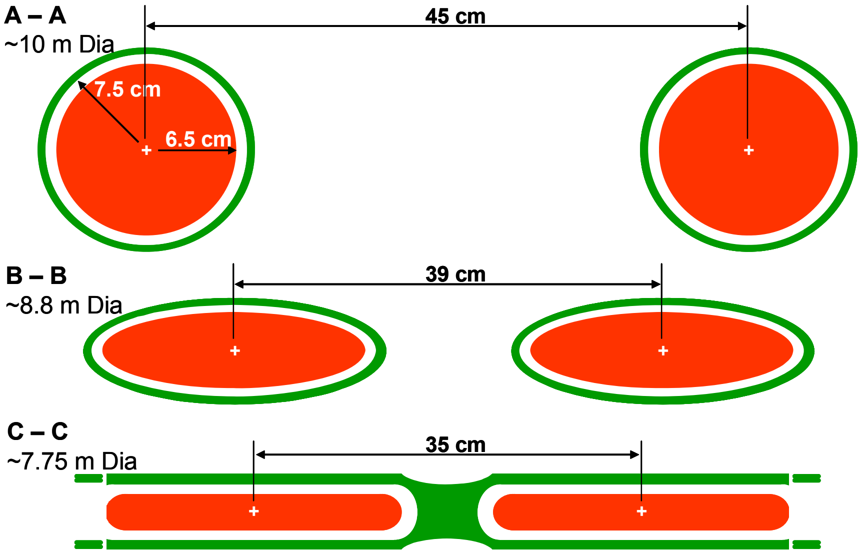

Figure 3.39. Vertical sections AA, BB, and CC from Figure 3.38 as viewed radially outward from the center.

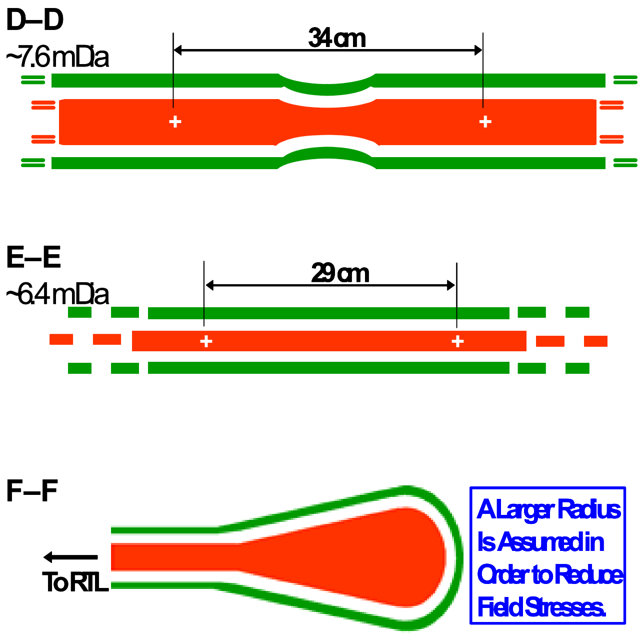

A Larger Radius Is Assumed in Order to Reduce Field Stresses.

Figure 3.40. Vertical sections DD & EE *(& FF)* from Figure 3.38 as viewed radially outward from the center *(from the right side).*

Figures 3.41, 3.42, and 3.43 are the results of applying Electro version 6.3, an electrostatic field solving code, to some of the same geometries. An elliptical transmission line at BB with the same impedance as the circular MITL of AA would have two enhanced regions with which to be concerned. This preliminary analysis showed that the regions with higher enhanced field stresses could be lowered to the typical values elsewhere by simply increasing the gap spacing by 25%, from 1 cm to 1.25 cm. The small gap increase at the enhanced region corresponds to a 7% increase in cross-section area. The increase in impedance should be comparable. The approximate 2-D slab Electro model probably exaggerates the peak stresses at the sharper radii.

The final design of these transmission lines will require confirmation that the self-magnetic insulation is indeed adequate.

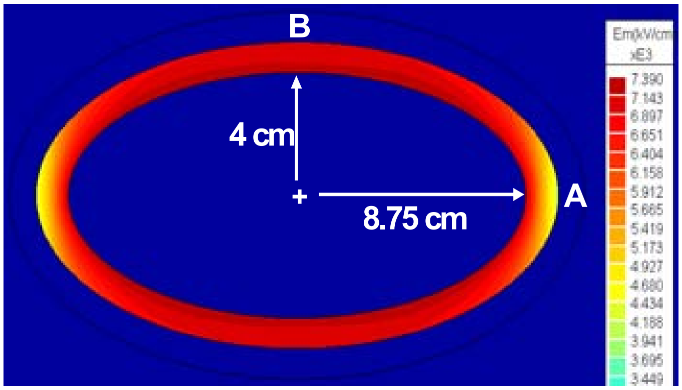

Figure 3.41. **Electric field magnitudes for the geometry of section BB of Figure 3.38.**

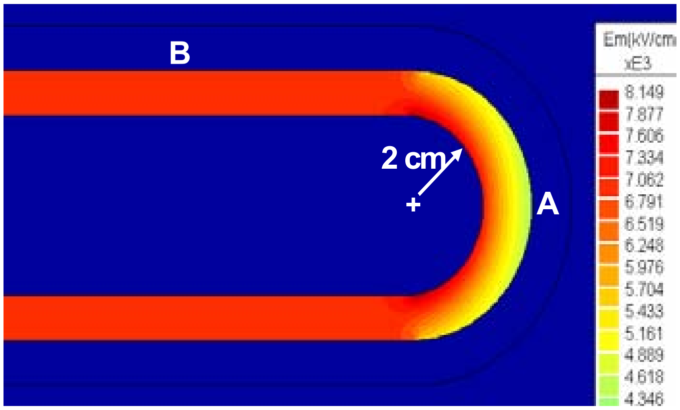

Figure 3.42. **Electric field magnitudes for the geometry of section CC of Figure 3.38.**

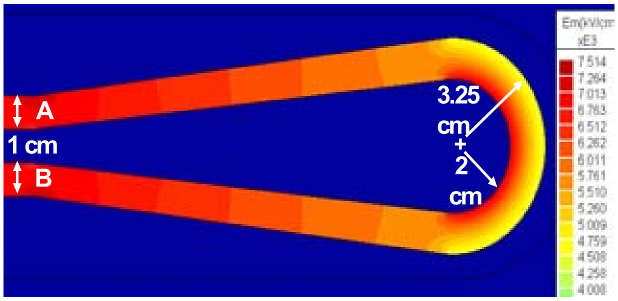

Figure 3.43. **Electric field magnitudes for the geometry of section FF of Figure 3.38.**

3.4.5 Inductive Chamber Summary

- The inductive chambers get smaller as the number of parallel modular LTD facilities grow and reduce the effective driver source impedance.
- Locating the inductive chamber as far radially inward (close to the center) as possible maximizes the inductance-to-volume ratio and minimizes the required chamber size. At some point the chamber would start crowding access to the RTL and would be limited by operationally-driven requirements.
- According to the circuit model, there appears to be an optimum length for the tri-plate transmission lines between the coaxial MITL feeds and the isolation chamber.
- The transition region, as presently visualized, appears workable in the engineering sense. The fabrication and assembly issues have yet to be addressed and may require some performance compromises.
- More detailed simulations and analyses are necessary to determine the impact of magnetic nulls and the effectiveness of magnetic insulation in the transition region and the inductive isolation chamber.
- The fundamental questions which need to be answered are: “Where and when is the magnetic insulation lost?” and “What is the probability of a vacuum arc?”
- It may be possible to design vacuum post-hole convolutes for additional support plus an 8% to 10% energy recovery advantage, provided that the other issues with them may be mitigated (i.e. material erosion, lifetime, and MITL current flow interference).
- We recommend dual-use applications for the inductive isolation chamber, such as a vacuum manifold for large volume, fast transfers to support the desired 10-s repetitive cycle and to help justify it.

3.5 3D Quicksilver simulations of electron losses for the transition from round coax LTDs to a flat triplate transmission line *(W.L. Langston and T.D. Pointon, SNL)*

Power flow from coax LTDs to a flat tri-plate transmission line has received further study in 2006. In particular, this work uses recommendations from previous work in 2005 [59] to try to reduce the electron flow current throughout the design and reduce the anode energy deposition that occurs due to the combination of the high electron flow currents and the abrupt transition from the coaxial feed lines to the disk MITL (Magnetically-Insulated Transmission Line). The *Introduction* and *Simulation Setup* sections are similar to the previous analysis [59] but brief summaries are included here for convenience and completeness.

The current conceptual design for the Z-Pinch IFE driver is based on the addition of the current from a number of LTD (Linear Transformer Driver) modules. Each module drives a vacuum coaxial line. The coaxial lines are arranged extending radially away from an annular feed disk. The coaxial lines feed the annular disk that is connected to a conical RTL (Recyclable Transmission Line) at its inner radius. This conceptual design is illustrated in Figure 3.44.

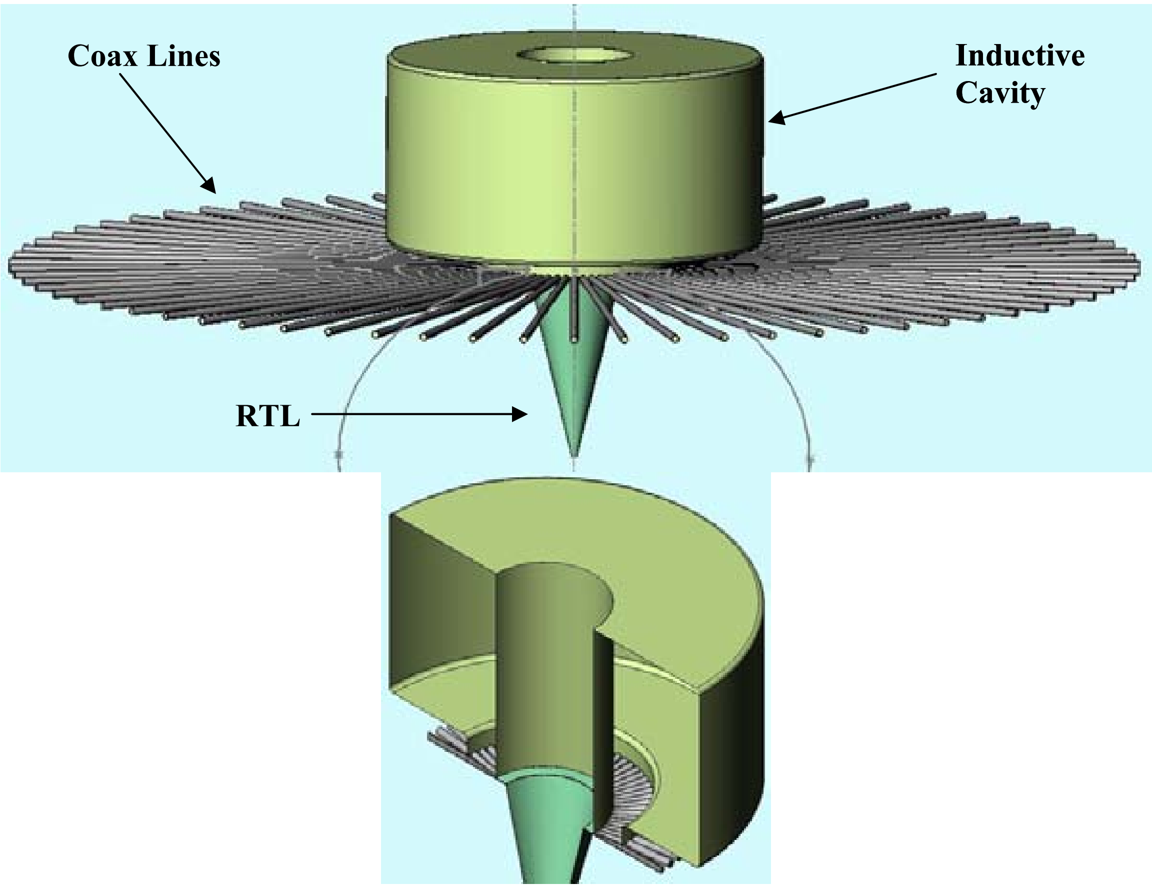

Figure 3.44. Views of the conceptual design of the Z-pinch IFE driver.

The original concept had 70 coaxial lines merging into the disk. Each of these lines delivered $I_a \sim 1$ MA at $V \sim 7$ MV. This conceptual design yielded simulation results that included electron flow currents ranging from 10 to 40 MA. As a result the design was very inefficient and the combination of the large flow currents and abrupt transitions from the feed coaxes to the disk caused an extreme amount of energy to be deposited in localized areas of the anode. This extreme amount of energy deposition would cause significant damage to the anode thus compromising the possibility of achieving the desired frequency of operation ($f \sim 0.1$ Hz) for the ZP-IFE design.

After some initial analysis by T. D. Pointon, *et al.*, it was proposed that a revised design using fewer coaxial lines (with correspondingly higher current per line) would provide better magnetic insulation and therefore reduce the electron flow currents. A revised design was constructed using 10 coaxial lines each delivering $I_a \sim 7$ MA at $V \sim 9$

MV. The line voltage was increased to ensure that a total of ~60 MA would be delivered to the load.

Computer simulations are used to continue examination of this structure. The 3-D electromagnetic, particle-in-cell (PIC) code QUICKSILVER [60] developed at Sandia National Laboratories is used for the numerical simulations. The capabilities of QUICKSILVER are especially well-suited to this problem since it has many features that were developed to model a variety of power flow issues in the Z and ZR accelerators.

3.5.1 Simulation Setup

A simplified geometry has been used to obtain simulation results as quickly as possible. The simulations are done in cylindrical coordinates but the coaxial lines have a rectangular cross section in the ϕ-z plane. The ZP-IFE structure uses 10 – 9 Ω rectangular coaxial lines feeding the inner disk MITL. Perfect symmetry is assumed for all 10 transmission lines so that the azimuthal extent of the simulations is from $\phi_{\min} = 0$ to $\phi_{\max} = \pi/10$. The disk-coax interface can be moved to smaller radius since there are fewer coaxial lines in this design of the ZP-IFE structure. In the previous designs with 70 coaxial lines, the disk-coax interface was located at $r = 5$ m with 2.5 cm A-K gaps and $r = 2$ m with 1.2 cm A-K gaps. In this design with 10 coaxial lines, the disk-coax interface will be located at $r = 1$ m with a 1.5 cm A-K gap for the disk and 3.4 cm gaps for the other three sides of the rectangular coax. The rectangular coax has uniform A-K gaps of 3.4 cm at the inlet ($r = 1.3$ m) but the bottom anode of the coax is tapered up closer to the cathode such that the A-K gap is 1.5 cm at $r = 1$ m. The inner disk is then linearly tapered to an A-K gap of 0.9 cm at $r = 0.6$ m. This new configuration is shown in Figure 3.45.

It is not practical to model the entire inductive cavity due to its large size [59]. A portion of the inductive cavity is modeled in 3-D, but the remaining inductance is modeled by a long (5 m) 1-D transmission line attached to the open end of the inductive cavity (at $r = 1.2$ m) terminated in a large inductive load.

A matched 9 Ω, 5 m long transmission line is connected to the inlet (at $r = 1.3$ m) and is driven by a forward-traveling wave $V_f(t)$ using a source impedance of R = 0.7 Ω. The inner disk is attached to another long transmission line that models the rest of the inner disk and the RTL at $r = 0.6$ m. This transmission line is terminated with a fixed 1 nH inductive load but this load can easily be replaced by a Z-pinch load. The parameters for the inner transmission line are computed from the r-z outline of the two conductors that form the RTL using the commercial IDL software package. The RTL is assumed to have inner and outer radii of $r_0 = 5$ cm and $r_1 = 50$ cm, and a height of 2 m. The A-K gap at r_0 and r_1 are g_0 and g_1, respectively. The RTL is connected to the 3-D geometry with a disk line whose A-K gap is tapered linearly from the 3-D gap at $r = 0.6$ m to the gap at the outer radius of the RTL. Table 3.2 summarizes the radii and gaps used previously and those used currently for the inner disk of the 3-D model and the RTL.

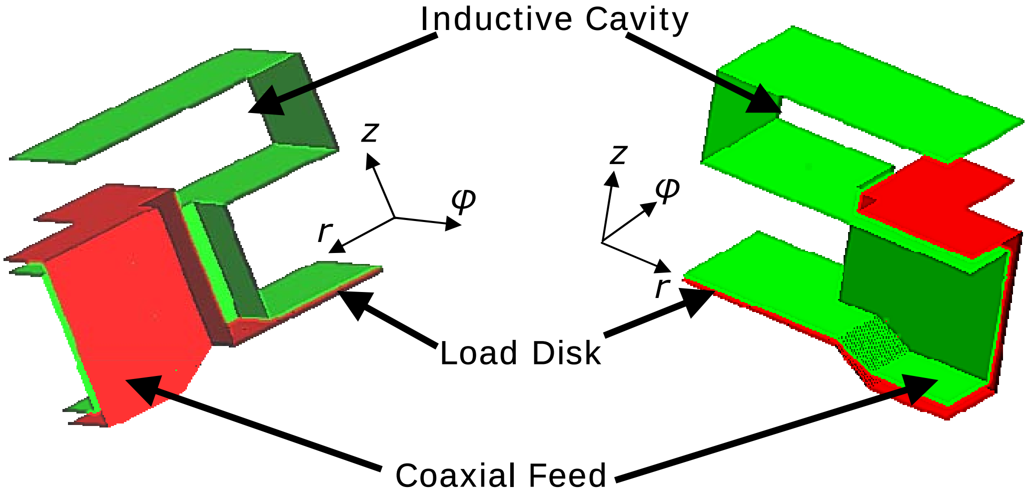

Figure 3.45. Three-dimensional geometry for the Z-Pinch IFE driver with 10 coaxial feed lines.

A simple analytic driving voltage, $V_{oc}(t) = V_0 \sin^2 \omega t$, is used to drive these simulations. The peak amplitude of the voltage $V_0 = 19.5$ MV was chosen such that the current delivered to the load is approximately 60 MA and ω is chosen for a 200 ns pulse width ($\omega = 5\pi \times 10^6$ rad/s).

Table 3.2. Radii and gaps for the inner transmission line.

	RTL				3-D Disk @ r_{min}	
	r_0 (cm)	g_0 (mm)	r_1 (cm)	g_1 (mm)	r_2 (m)	g_2 (mm)
Geom. 1 †	5	2	50	10	4.6	25
Geom. 2 †	5	1.6	50	7.5	1.6	12
Figure 2	5	2	50	7.5	0.6	9

† From [59]

3.5.2 Particle Simulations

The two major areas where the original concepts for the Z-pinch IFE driver showed problems in the initial simulations were large amounts of electron flow current and extreme energy deposition into localized areas of the anode. These areas will be a primary focus for the particle simulations for the revised structure. Time histories for the main currents and for the electron flow currents are shown in Figure 3.46. In the previous simulations the electron flow current in the 3-D model was on the order of tens of mega amperes. Figure 3.46(b) shows that the electron flow current has been greatly reduced throughout the 3-D model due to the improvement in the magnetic insulation for each of the coaxial feed lines. This fact is reinforced in Figure 3.46(a) by the similarity in form and amplitude between the current input to the 3-D model, the current in the disk section, and the current delivered to the load. Figure 3.46(a) also shows that the inductive cavity is doing a good job of diverting most of the current into the disk section. The maximum current in the inductive cavity is only about 2-3 MA.

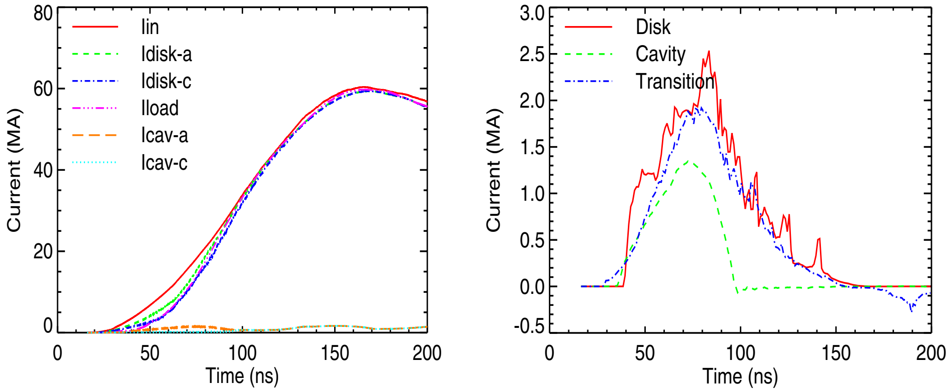

(a) (b)

Figure 3.46. Time histories for the (a) current and the (b) electron flow for a particle simulation of the revised Z-pinch IFE structure.

Reducing the number of feed coaxial lines and increasing the current on each line reduced the electron flow currents but as shown in Figure 3.47, localized anode heating is still a problem with the revised Z-pinch IFE structure. The apparent discontinuities in the anode temperature plots are due to the "stair step" approximation of the slanted anode conductor (several z values are being plotted so that the plot can include all of the anode). The model used to predict the anode temperature increase is accurate for stainless steel up to T ~ 800°C. Above T = 800°C, the "temperature" from this model should only be considered a qualitative indicator of energy deposition [59]. The peak "temperature" for this simulation is $T_{peak} \approx 9969$°C on a localized section of the anode along the centerline between adjacent coaxial feeds ($\phi = \phi_{max}$). This result is consistent with previous results with only a modest improvement in the peak anode temperature. However, anode heating is isolated to the region along $\phi = \phi_{max}$ whereas previous designs also included (less severe) anode heating on the disk anode near $r = r_{\min}$. The anode heating seen previously on the disk anode near $r = r_{\min}$ was most likely due to the large electron flow currents propagating down the disk toward the load. The anode heating along $\phi = \phi_{\max}$ however is due to the combination of the electron flow currents and a local minima of the magnetic field caused by the azimuthally asymmetric current distribution entering the disk region. The asymmetry of the current distribution is a result of the abrupt transition from the coaxial transmission lines to the disk geometry. The electron flow currents were significantly reduced but the area over which the loss is occurring has also been reduced since the transition is now at $r = 1$ m rather than $r = 2$ m or $r = 5$ m as in the previous simulations.

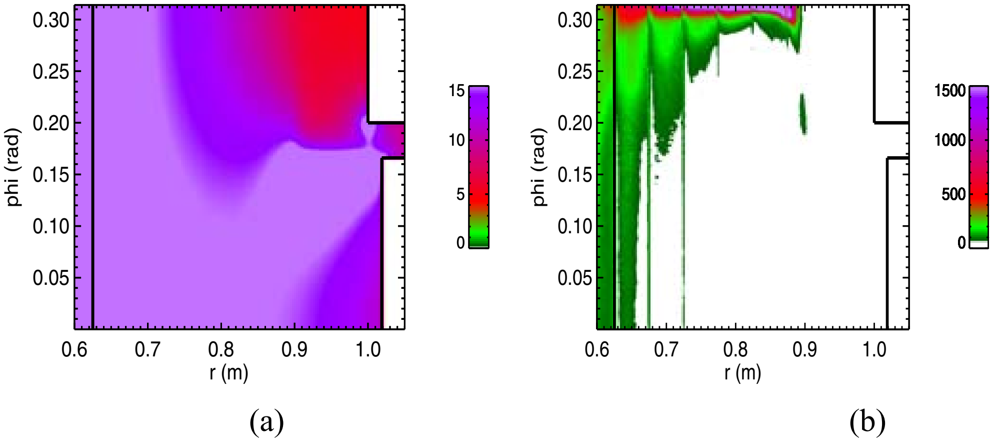

Figure 3.47. Contour plots of the transition region and the inner disk (a) B field magnitude on the anode and the (b) anode temperature ($T_{peak} \approx 9969$°C at (r, ϕ, z) = (0.8594, 0.3142, -0.1300)) at t = 200 ns for a particle simulation of the revised Z-pinch IFE structure.

One method of trying to soften the transition between the coaxial feed lines and the disk is to change the shape of the anode conductor in the transition region. Several different profiles have been simulated but the profile that yielded the best results was simply changing the angle of the original anode conductor such that the A-K gap at $\phi = \phi_{\max}$ changed from 10 cm to 2.5 cm. This modification is illustrated in Figure 3.48.

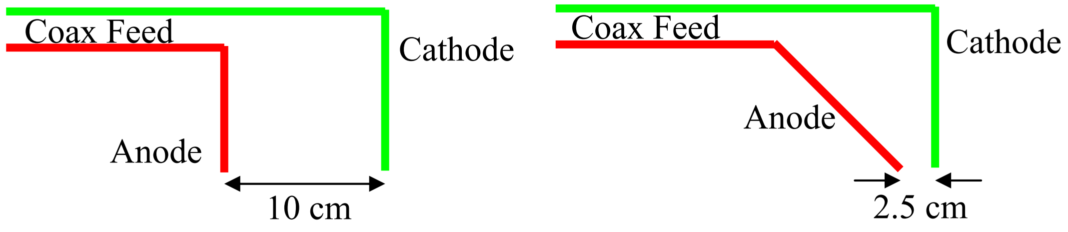

(a) (b)

Figure 3.48. (a) Original and (b) modified transition region anode and cathode profiles (top view).

The resulting simulations provided similar results for lowering the electron flow current while lowering energy deposition into localized areas of the anode by approximately a factor of 3. These results are summarized in Figures 3.49 and 3.50. The resulting peak "temperature" for the structure including the modified transition region is $T_{peak} \approx 3018°C$. Other modifications to the anode and/or the cathode conductors in the transition region reduced anode heating as well but by a less substantial amount. The reduced heating in this case can be attributed to a shift in the local minima of the magnetic field away from $\phi = \phi_{max}$ caused by the modification to the anode as seen by comparing Figures 3.47(a) and 3.50(a).

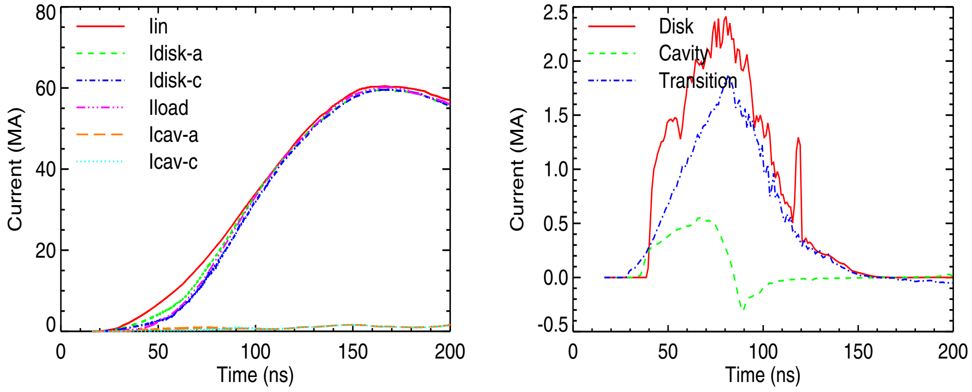

(a) (b)

Figure 3.49. Time histories for the (a) current and the (b) electron flow for a particle simulation of the revised Z-pinch IFE structure with the modified transition region anode in Figure 3.48.

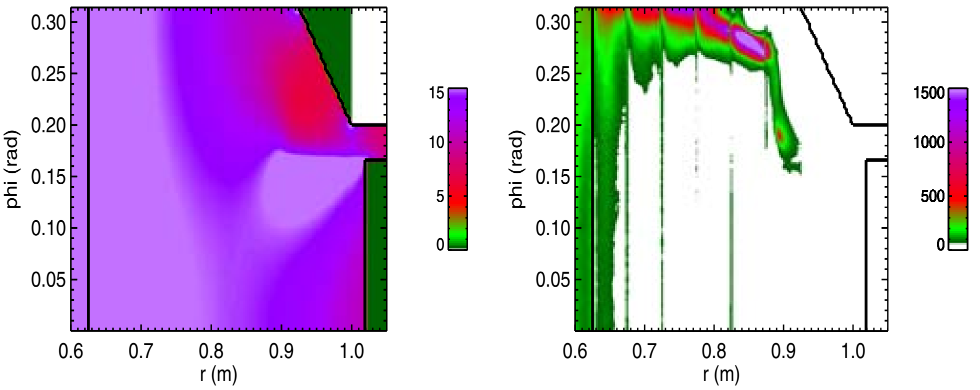

(a) (b)

Figure 3.50. Contour plots of the transition region and the inner disk (a) B field magnitude on the anode and the (b) anode temperature (T_{peak} ≈ 3018°C at (r, ϕ, z) = (0.8469, 0.2848, -0.1300)) at t = 200 ns for a particle simulation of the revised Z-pinch IFE structure with the modified transition region anode in Figure 3.48.

Some additional strategies for lowering the energy deposition to localized areas of the anode were also investigated. The effect of lengthening the A-K gap at the loss region to increase the length of the magnetic null in the electric field direction [61] was one of these additional strategies. The gap lengthening strategy was implemented by expanding the A-K gap (by modifying the anode) near $\phi = \phi_{max}$ using the combination of a triangular and a rectangular trench. The specific configuration of this anode modification is detailed in Figure 3.51. Initially, this strategy was used in addition to modifying the transition region anode. However, overall anode heating was reduced such that the maximum anode heating was occurring at the 2.5 cm A-K gap in the transition region where the anode was modified (as in Figure 3.48). Hence, the anode in the transition region was returned to its original form. This change caused only a slight change in the anode heating results in other areas of the structure. In general, the results from using the gap lengthening strategy are very promising. The results for the structure using this strategy are detailed in Figures 3.52 and 3.53. Figure 3.52 shows that the main currents and the electron flow currents have remained similar to the unmodified 10-feed line structure (shown in Figure 3.46). Figure 3.53 shows that the localized anode heating has decreased dramatically to T_{peak} ≈ 596°C.

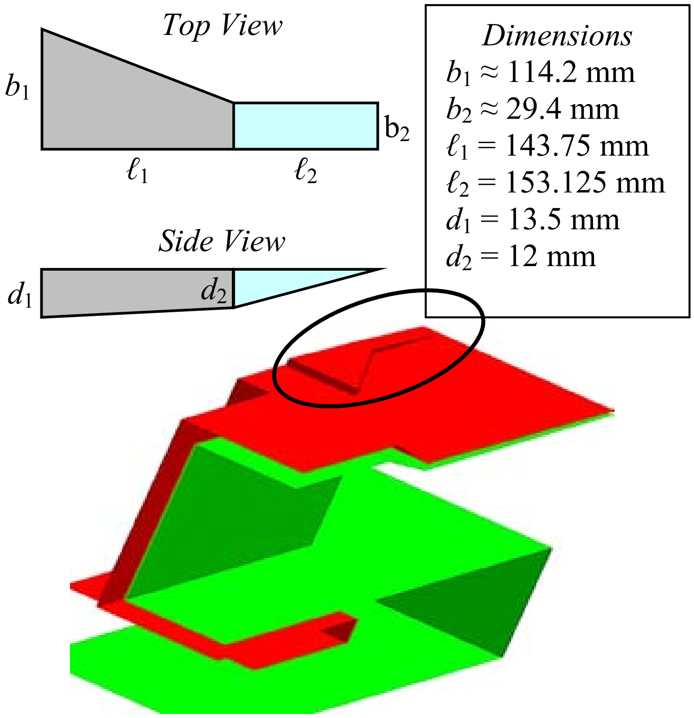

(a) (b)

Figure 3.51. (a) Detailed schematic and (b) an upside-down view of the 3-D solid model showing the anode modifications used to lengthen the A-K gaps.

The final couple of simulations presented are for a slightly different structure. The primary difference in this structure is the shape of the feed coax. At the inlet the coax has a square cross-section but the shape of the coax changes to a flatter and wider profile as it gets closer to the disk transition. The dimensions of the coax at the inlet ($r = 1.3$ m) and at the disk transition ($r = 1$ m) are listed and compared to the original 10-feed line structure in Table 3.3. The rest of the structure is scaled to match the feed coax as it connects to the disk transition. The transition from the square coax profile to the wider, flatter profile was accomplished with linear tapers due to time constraints. Ideally, this transition would be done in a smooth and seamless fashion. This modification to the geometry was made so that the current distribution would become more azimuthally symmetric in the disk section since the coax-disk transition is distributed over a larger radial distance.

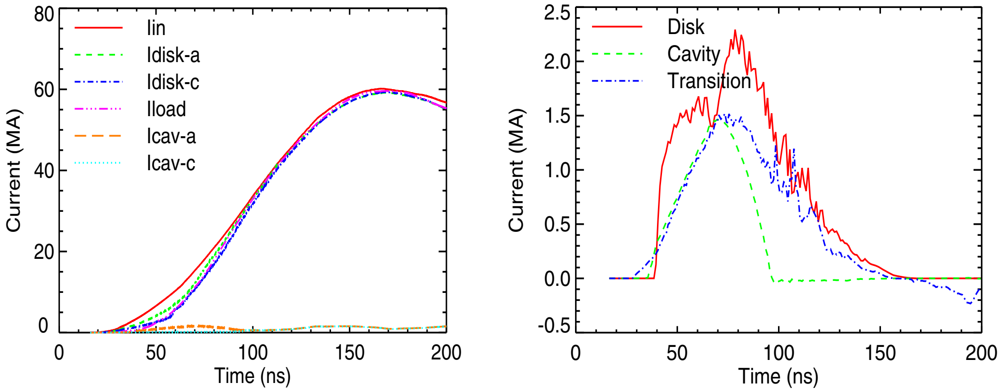

(a) (b)

Figure 3.52. Time histories for the (a) current and the (b) electron flow for a particle simulation of the revised Z-pinch IFE structure with the anode modifications used to lengthen the A-K gaps in Figure 3.51.

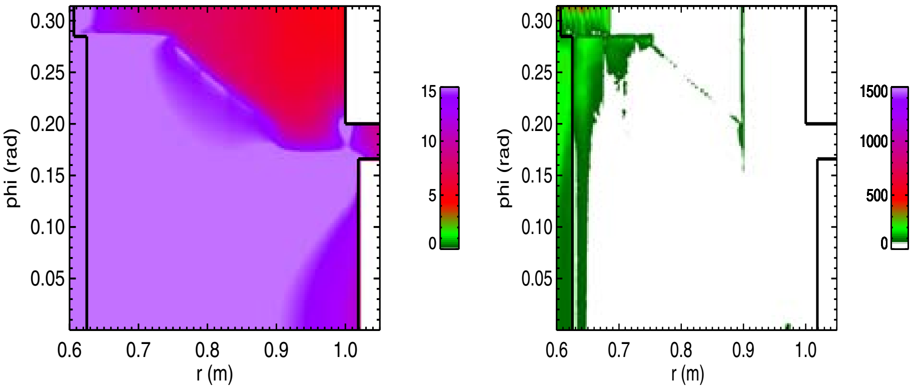

(a) (b)

Figure 3.53. Contour plots of the transition region and the inner disk (a) B field magnitude on the anode and the (b) anode temperature (T_{peak} ≈ 596°C at (r, ϕ, z) = (0.6250, 0.3142, -0.1278)) at t = 200 ns for a particle simulation of the revised Z-pinch IFE structure with the anode modifications used to lengthen the A-K gaps in Figure 3.51.

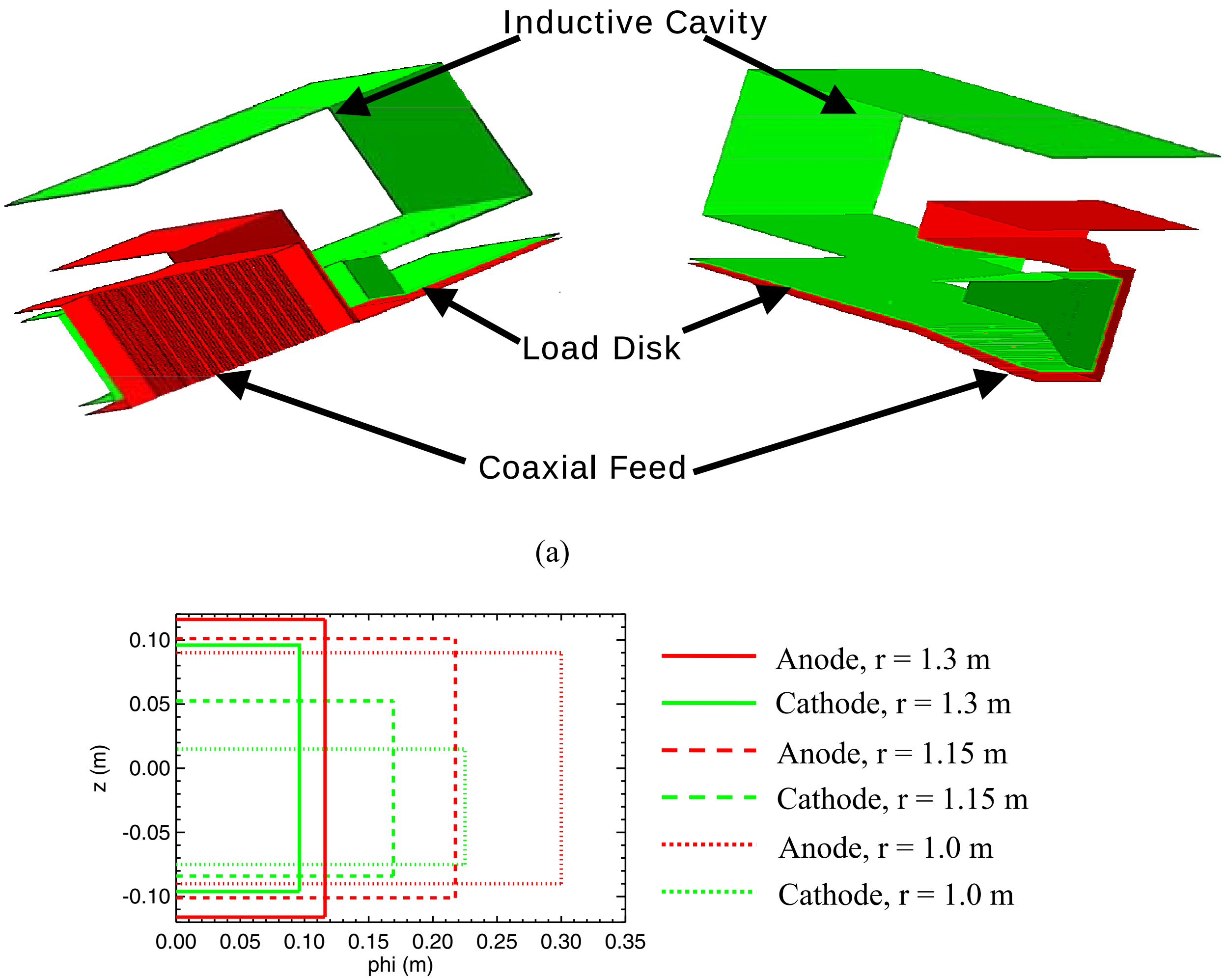

(a)

(b)

Figure 3.54. (a) Three-dimensional geometry and (b) coaxial feed cross-sectional profiles for the Z-Pinch IFE driver with 10 coaxial feed lines.

Table 3.3 Dimensions and A-K gaps for the feed transmission line.

	Inlet (r = 1.3 m)				Disk Transition (r = 1 m)			
	w_{a0} (cm)	h_{a0} (cm)	g_0 (cm)	g_{b0} (cm)	w_{a1} (cm)	h_{a1} (cm)	g_1 (cm)	g_{b1} (cm)
Fig. 2	40.0	40.0	3.4	3.4	40.0	36.625	3.4	1.5
Fig. 11	23.2	23.2	2.0	2.0	60.0	18.0	7.5	1.5

† $w_a \equiv$ anode width, $h_a \equiv$ anode height, $g \equiv$ A-K gap for top and sides, $g_b \equiv$ A-K gap for bottom

The current and electron flow time histories for this structure are shown in Figure 3.55. The currents still look very similar to the previous structures but the electron flow has decreased by an average of ~ 0.5 MA.

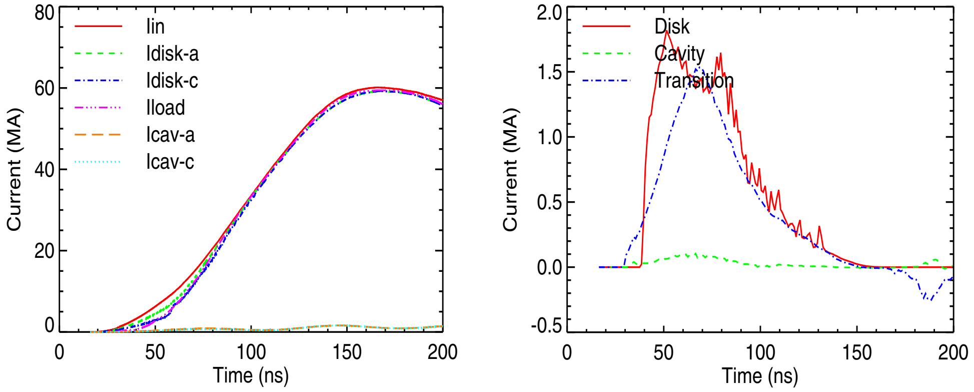

(a) (b)

Figure 3.55. Time histories for the (a) current and the (b) electron flow for a particle simulation of the revised Z-pinch IFE structure in Figure 3.54.

Figure 3.56 shows that the localized anode heating is still a problem with this structure near $\phi = \phi_{max}$. The peak temperature for this structure is $T_{peak} \approx 7592$°C. This is an improvement over the unmodified 10-feed line structure which had $T_{peak} \approx 9969$°C and the anode heating is localized in an area very close to $\phi = \phi_{max}$ so this structure is an excellent candidate for lengthening the A-K gaps in the area where the anode heating is most severe.

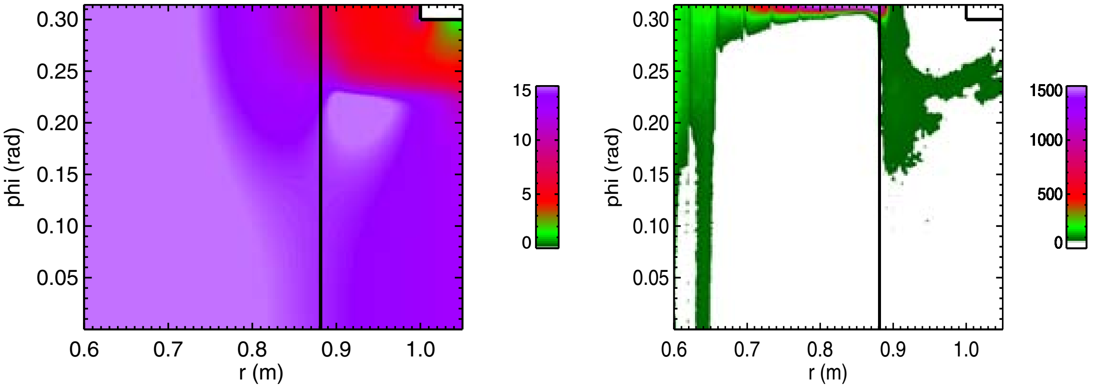

(a) (b)

Figure 3.56. Contour plots of the transition region and the inner disk (a) B field magnitude on the anode and the (b) anode temperature ($T_{peak} \approx 7592$°C at (r, ϕ, z) = (0.8687, 0.3142, -0.08925)) at t = 200 ns for a particle simulation of the revised Z-pinch IFE structure in Figure 3.54.

The details of the A-K gap lengthening for this structure are given in Figure 3.57. The area where A-K gap lengthening is required is smaller for this structure since the anode heating is confined to a relatively small area near $\phi = \phi_{\max}$.

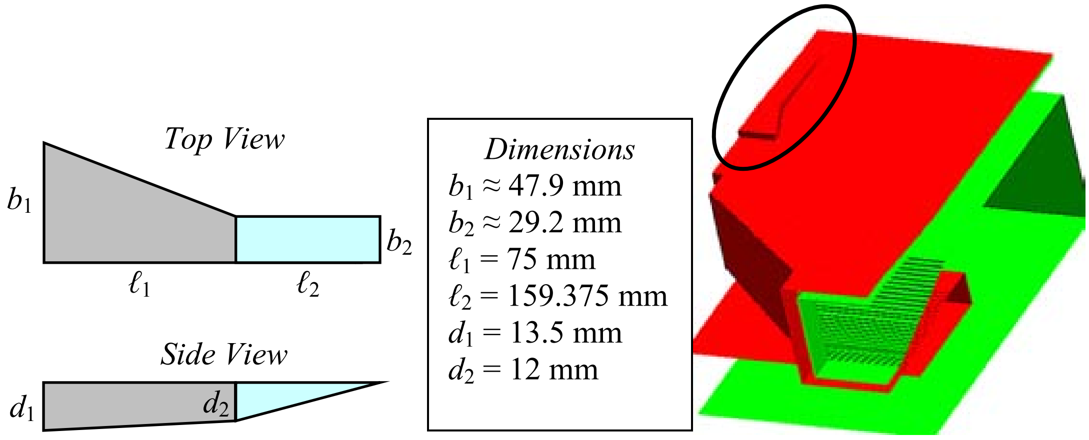

(a) (b)

Figure 3.57 (a) Detailed schematic and (b) an upside-down view of the 3-D solid model showing the anode modifications used to lengthen the A-K gaps.

Figures 3.58 and 3.59 show the time histories and contour plots for this structure. The time histories show that the current and the electron flow are largely unaffected by the lengthening of the A-K gap. The contour plot of the anode temperature shows that lengthening the A-K gap has proven to be effective in lowering the energy deposition into the anode. The peak temperature for this configuration is $T_{peak} \approx 443°C$.

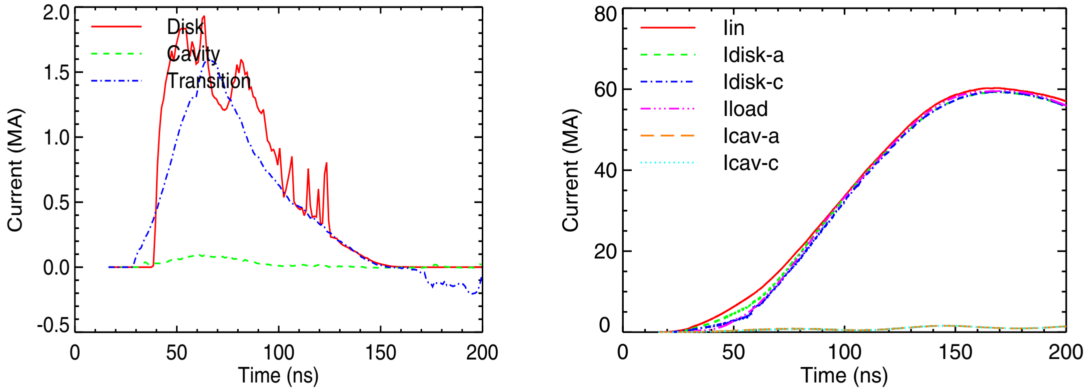

(a) (b)

Figure 3.58. Time histories for the (a) current and the (b) electron flow for a particle simulation of the revised Z-pinch IFE structure in Figure 3.54 with the anode modifications detailed in Figure 3.57.

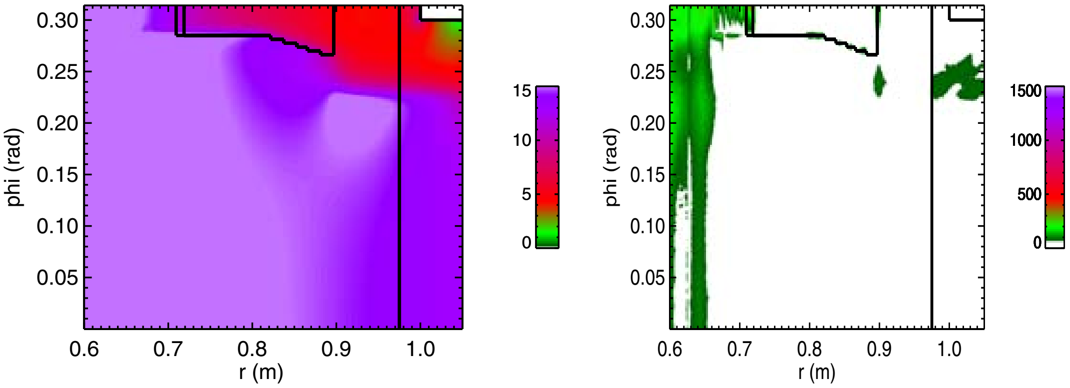

(a) (b)

Figure 3.59. Contour plots of the transition region and the inner disk (a) B field magnitude on the anode and the (b) anode temperature (T_{peak} ≈ 443°C at (r, ϕ, z) = (0.7188, 0.3142, -0.0900)) at t = 200 ns for a particle simulation of the revised Z-pinch IFE structure in Figure 3.54 with the anode modifications detailed in Figure 3.57.

3.5.3 Summary of electron losses

The simulation results show that switching to a 10-feed line structure (versus a 70-feed line structure) yields a vast improvement in (lowering of) the electron flow current. Unfortunately, this reduction in electron flow current only translates into a modest improvement in the energy deposition on the anode in the transition and disk regions. Two different methods of reducing this energy deposition were attempted. Smoothing the transition from the feed coax to the disk provides approximately a factor of 3 reduction in the peak local deposition. However lengthening the A-K gaps provides more than a factor of 16 reduction in the peak local deposition and the combination of the two methods yields a 22.5 fold reduction in the peak local deposition. Anode temperatures as low as ~ 440°C have been achieved in simulations using these methods. Even better results may still be possible by moving the disk transition out to larger radius or by using more complex geometries with smoother conductor surfaces and transitions.

3.6 Alternate LTD driver (90 MA) design (ZP-3R) for high yield and IFE using multiple layers of LTDs; and Alternate Z-PoP design based on ZP-3R design [47]

(Yu. G. Kalinin, A. S. Kingsep, S. L. Nedoseev, V. P. Smirnov, Kurchatov Institute, Moscow)

By development of ZP-3 concept, various variants of the generator of a pulse of electromagnetic energy for initiation of thermonuclear microexplosion, using Z-pinch, were analyzed. Now three basic schemes of superterawatt electric power generators with pulse duration of hundred nanosecond can really be considered – generators on forming lines with liquid insulator (the distilled water), generators with magnetic stores and plasma opening switches, and generators–drivers based on linear transformers of a current, LTD-generators. In spite of the fact that the maximal parameters of electric pulses have been reached with use of multimodular generators on forming lines with water insulation, for the conceptual scheme “ZP-3” (and then, “ZP-3R”) the multimodular LTD-generator has been chosen.

Configuration of the multimodular LTD-generator essentially differs from configuration of the generator on forming lines with water insulation. In the generator with water insulation the currents addition from separate modules develops in an insulator – water, meanwhile in the LTD-generator they are added in vacuum.
On the one hand, addition of currents in water is much easier, than in vacuum because at addition of currents in water their leakage can be easily made insignificant, if an insulator (the distilled water) is cleaned so, that its electric conductivity is small enough. On the contrary, addition of currents in vacuum, which is carried out with use of the Magnetically Insulated Transporting Lines (MITL), is inevitably accompanied by electronic leakages. They arise, first, at an establishment of magnetic self-insulation at the front increase of a current, and secondly, there, where intensity of own magnetic fields of the adding currents are small or they have significant spatial gradients.
On the other hand, the total high-voltage pulse from the generator with water insulation moves on physical load in vacuum (Z-pinch) through the water-vacuum interface, a feedthrough insulator. The analysis of the scheme “ZP-3” has shown, that the insulator is the weakest place of the scheme of a reactor from all points of view. Being an element of reactor chamber, the insulator is corruptible intensive action of energy and products of thermonuclear microexplosion with energy yield up to 3 GJ, which, according to the concept, repeat with an interval of 10 seconds. Mechanical and constructive means are not possible to protect the insulator. It is necessary to add, that electric breakdown strength of a surface of the insulator, turned into vacuum, is on a limit for modern and perspective insulating materials.

3.6.1. The Multimodulat LTD-generator of ZP-3R

Problems of addition of currents and voltages in the multimodular LTD-generator. In ZP-3R concepts the solution is searched on a way of application of the

LTD-generators collected under the multimodular scheme. Each LTD-module, generating a pulse of a voltage 10-20 MV, is formed as a stack of LTD-cells connected in series and generating pulses of 0.1 MV. Each cell has the own feedthrough insulator. Insulators settle down on an anode part of the stack, they are allocated along its length. This scheme does distribution of potential on length of the stack homogeneous; each cell is independent of others. In this sense the schemes of the LTD-generators look more perspective, than the schemes of generators based on forming lines with water insulation. However, the scheme of the generator based on LTD-modules of a stack configuration, has the problems. Two of them, connected with the insulator of LTD-cell, are discussed in the report on the Task 2. Here we shall mention only one of them, namely, about a problem of electronic leakage at addition of pulses of voltage in the stack LTD-module. In the LTD-generator consisting of stack LTD-modules, there is a consecutive addition of voltage from cells in stack LTD-module and parallel addition of currents from LTD-modules on load in reactor chamber in vacuum.

The voltage addition should occur in conditions of vacuum magnetic self-insulation, which it is carried out between an internal high-voltage electrode (cathode) and a stack of the LTD-cells, making an anode part of the LTD-module (see Fig.2.1 on the Task 2 in Ref. 47). The wave of magnetic self-insulation moves along a longitudinal axis of the LTD-module together with a wave of the voltage accruing in process of addition of voltage pulses from separate LTD-cells. As is known, the wave of an establishment of magnetic self-insulation is accompanied by electronic leakage which currents have a radial component. It means, that in exit aperture of the stack LTD-module, during establishment of magnetic self-insulation, electrons with energy of the order of a total generated voltage (megavolts!) will irradiate the anode part of the module. Currents of electronic leakage are distributed on length of scale of several interelectrode gaps, and density of electron current on an anode part and, including, on insulators will be scale 10-100 A/cm^2 at duration of ~10 ns. A conclusion: in the stack scheme of the LTD-module shielding of insulators against action of electronic leakage and hard x-ray and the gamma-radiation produced is necessary. It is a separate problem which can be solved by such change of a design of a exit aperture of the LTD-cell that insulators have been protected from direct action of a stream of electron leakage.

Necessity of addition of currents from LTD-modules on Z-pinch in vacuum in the reactor chamber defines all design of a reactor. The general view and some details of installation according to concept ZP-3R are discussed in following section.

Description of a general view and some parts of the LTD-generator and reactor chamber of ZP-3R installation. On the basis of preliminary analysis of variants, the scheme of the LTD-generator and some parts of reactor chamber, ensuring transportation and focusing of pulse on the load, Z-pinch, is proposed. The LTD-generator of installation ZP-3R is intended for formation on 0.1 Ohm load of a powerful electric pulse with amplitude 90 MA and duration of ~100 nanoseconds with frequency of 0.1 Hz repetition rate. Z-pinch, radiating x-ray, is used as the load for a hohlraum activation with a thermonuclear target. At accumulated electric energy nearby 250 MJ, energy of falling wave in MITL will make nearby 170 MJ, and in kinetic energy of the liner a little more than 35 MJ is produced. The yield of thermonuclear energy of microexplosion in unitary pulse should make 3 GJ.

The LTD-generator of ZP-3R installation, which scheme it is shown on Figures 3.60 and 3.61, consists from 30 identical LTD-sections, based on 4 LTD-modules, connected in parallel, and on the vacuum MITLs, collecting currents from LTD-modules and delivering the total current pulse to the load.

Each LTD-section consists of 4 LTD-modules located vertically on various radiuses (17, 20.5, 24 and 27.5 meters) from an axis of the liner, and reaching in the height ~60 m. Electric pulse from these LTD-modules extends on coaxial MITLs, which, being bent on a corner 90°, pass in horizontal position and incorporate in one collector, carrying out parallel addition of currents from 4 LTD-modules. The collector represents plainly-coaxial MITL. Its cross-section sizes make 2,5 m on 0,5 m. On the reactor chamber radius, equal 5 m, it is possible to place in regular intervals on a circle such 30 collectors with a backlash between them, equal 0.4 m. In the chamber of a thermonuclear reactor plainly-coaxial MITL collectors transform in flat MITLs. All these lines are intended for long use. Total impedance MITL of a path of transportation from output of LTD-modules up to outputs of the flat MITLs is supported at a level nearby 0.175 Ohm. To outputs of the flat MITL a Recycling Transportation Line (RTL) is connected with Z-pinch Target Unit (ZTU), replaced at each start-up. RTL consists from 60 flat MITLs with electrodes in the form of a trapeze, placed in regular intervals on a circle. The RTL maximal size on radius makes 0.5 m, and on height of 2 m. the Width and an interelectrode gaps of these lines decreases as approaching to ZTU, accordingly, from 50 cm up to 3 cm and from 1,25 cm up to 0,5 s. Association of all the lines in a two-electrode line with a backlash of 0.5 cm occurs on radius of 15 cm from an axis of the liner. The RTL+ZTU block connection together with the stationary component of MITL occurs remotely from above the chamber by means of the manipulator.

Calculations done in view of leakage in MITL, with a pulse of voltage $U_{[V]} = 21*10^6$ sin (t/150) where 0 <t <150 nanoseconds, and with the load, liner, having weight 4 mg/cm, height – 5 cm and initial radius - 4 cm, have shown, that about 23 % of the energy pulse passes in kinetic energy of the liner, about 45 % of energy spent on electron-ion leakage, and other part of energy is stored as magnetic energy in MITL. The analysis of losses of energy on electron-ion leakage along a path of transportation from radius of 28 meters to the axis shows, that the basic part of losses occurs in RTL (38 %) and in LTD-sections, in the region of connection of four coaxial MITL in one plainly-coaxial MITL (44 %), as there are sharp changes of wave resistance of MITL here.

RTL configuration. In the Report 2005 various variants of RTL are analyzed. The decision was made on replacement of biconical RTL, which used previously in ZP-3 concept. For the subsequent analysis two variants, shown on Figures 3.62 and 3.63, were proposed. In these schemes ring collectors (2) and (3) are used for currents collection from the stationary electrodes entering in the reactor chamber. The RTL cones (4) lean on them at positioning. In the RTL schemes, analyzed in Report 2005, for shielding of stationary MITL against neutron impact the dynamic screen (1) and local neutron

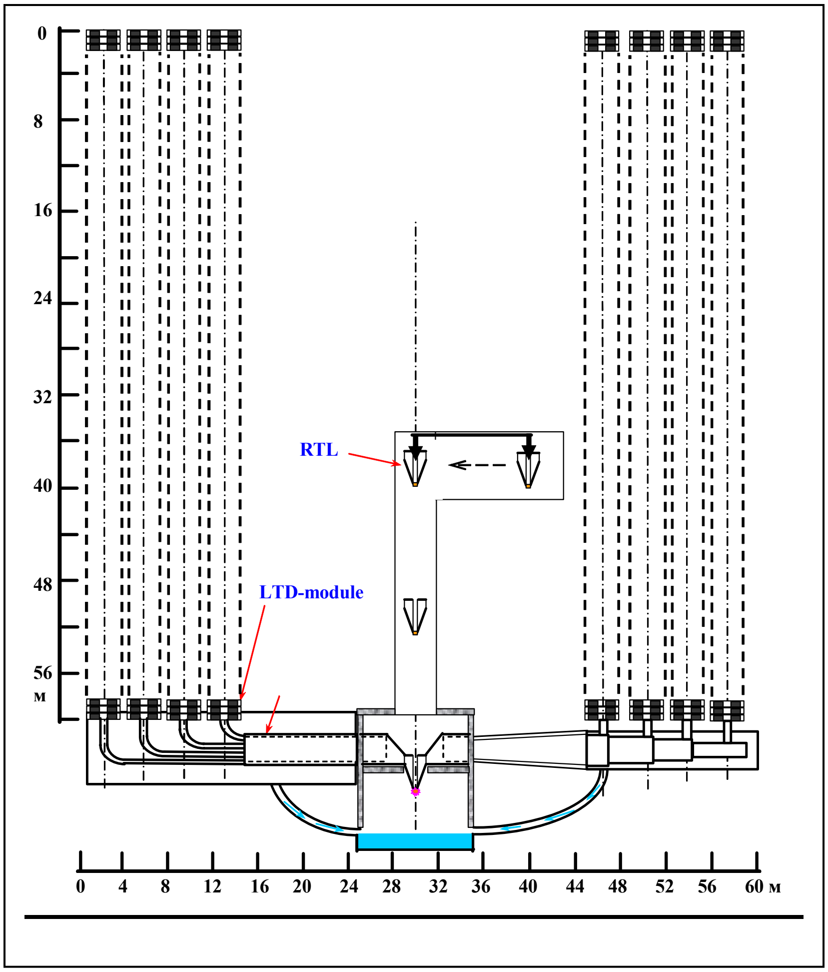

Figure 3.60. The general conceptual scheme of the generator and reactor Chamber of ZP-3R installation

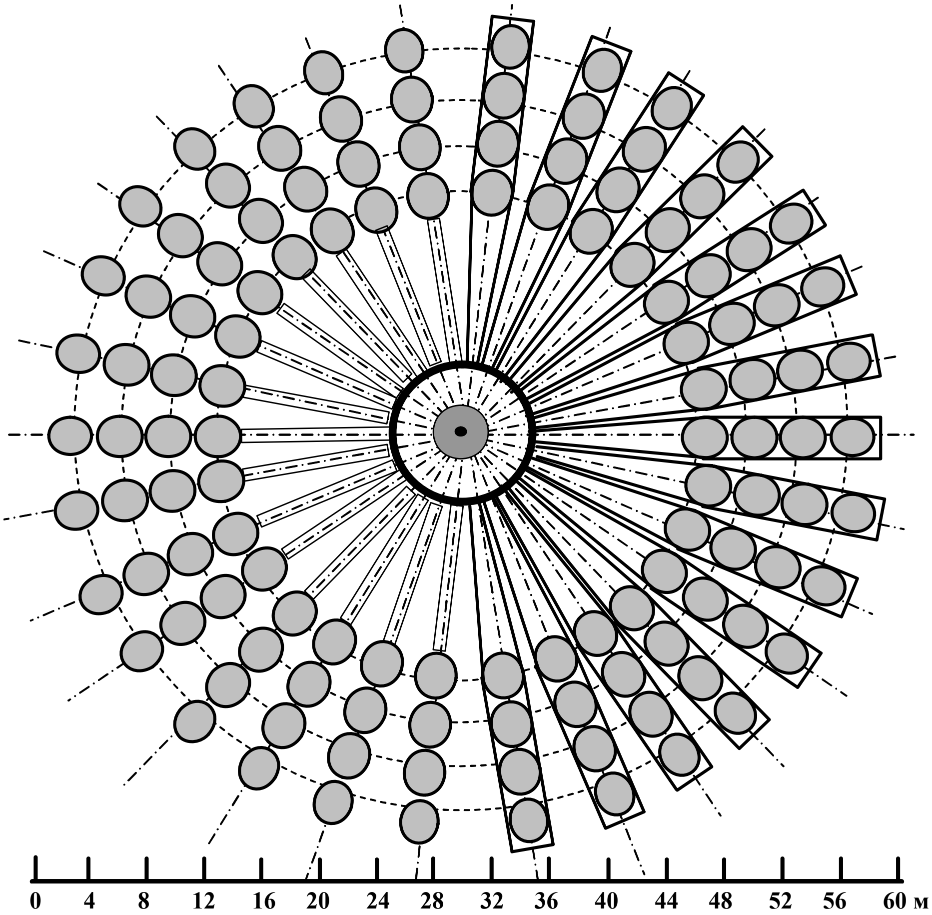

Figure 3.61. An arrangement of LTD-modules of ZP-3R installation. The top view.

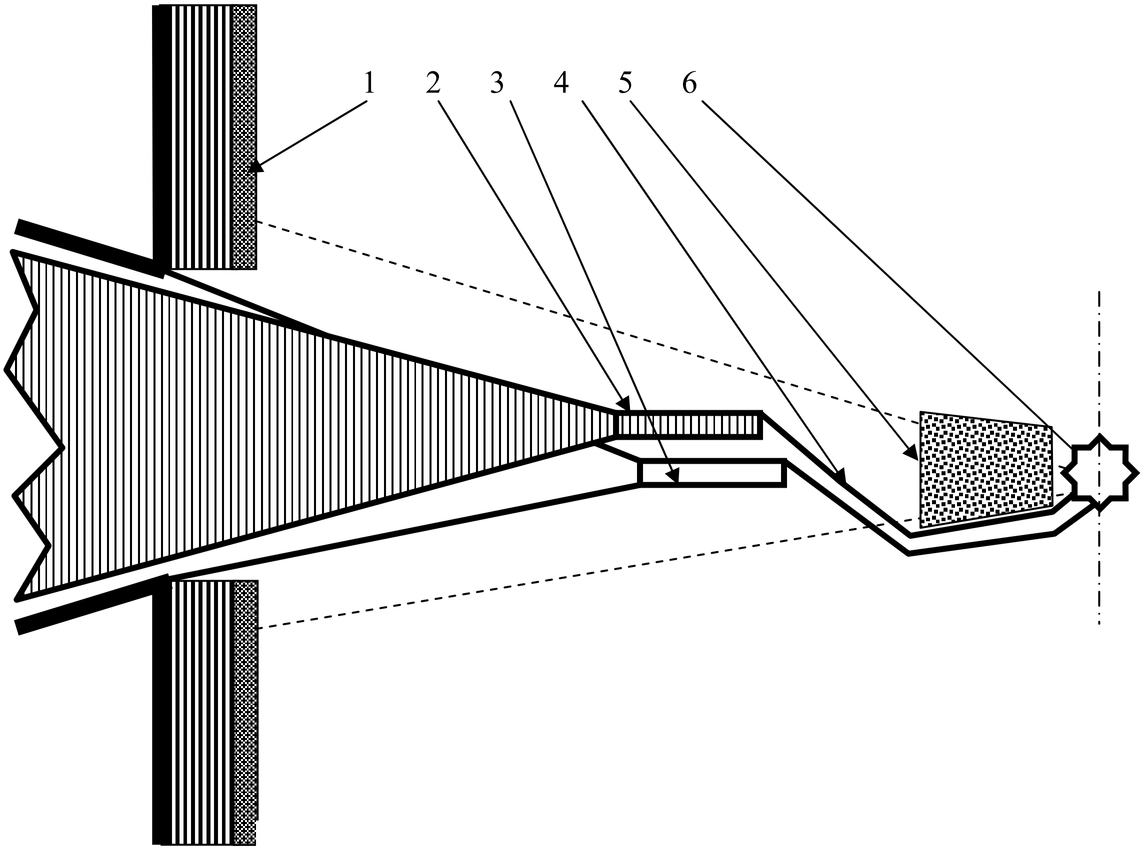

Figure 3.62. Variant of the scheme of RTL accommodation with cone-shaped electrodes in the reactor chamber (from Report 2005, scales are not observed). 1- blanket with the temporary dynamic screen (TDS), 2,3- stationary electrodes with ring collectors, 4 – RTL cones, 5-LNS, 6- target unit.

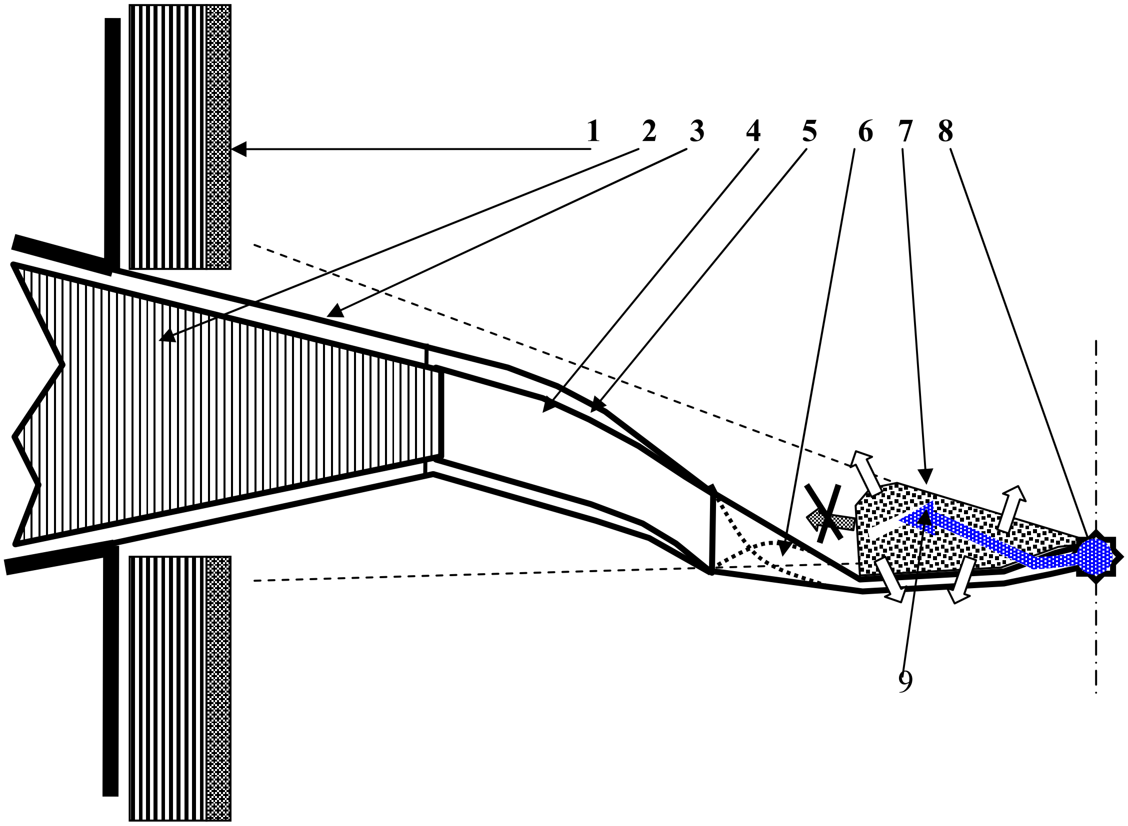

Figure 3.63. Variant of the scheme of RTL accommodation with flat inserts in the reactor chamber (from Report 2005, scales are not observed). 1-blanket with the TDS, 2,3-stationary electrodes, 4,5-flat inserts, 6-convolution zone, 7- LNS body with axial structurization to control direction of LNS body scattering at explosion, 8-target unit, 9-flux of radiation and hot plasma from microexplosion inside LNS block. Preferable and undesirable directions of LNS body scattering are shown by arrows.

shielding (LNS) (5) are applied. The LNS is of firm lead, and it is destroyed at explosion. The dynamic screen (1) is composite, from lead and a constructional material. Lead in the block (1) is liquid, proceeding through fine structure of a constructional material (a grid from a wire, or tapes). The fine structure of the composite block better resists neutron thermal shocks. Its hydrodynamical resistance to flowing lead is great. It reduces the flow rate of liquid metal. It is possible to assume, that such block will sustain many thermal shocks and its replacement will be necessary seldom. Replacement of blocks cannot serve as basic restriction because the RTL is replaced in each cycle.

In scheme of ZP-3 concepts the RTL made from a steel foil was considered. The problem of removal of exploded steel RTL from the reactor chamber, filled by fused flibe, demanded the special decision. In ZP-3R concepts the lead is chosen as material of the heat-carrier. It is proposed to do the RTL from lead, as well. In this case there is no necessity to do it from a thin foil. Moreover, technologically it will be hardly possible, especially if to apply moulding to manufacturing lines. There are two consequences:

- The RTL from rather thick material can effectively absorb the neutrons flying on the MITL stationary parts.
- The RTL can have more complicate form, for example, to contain flat vertical electrodes. It will raise the RTL assembly strength and will lower its inductance. One of possible numerous variants for the primary analysis such RTL in which on the RTL periphery inserts in the form of vertical planes are applied is shown in a Fig. 3.4. On the top view such RTL looks like a star with number of beams on number of collector electrodes of the LTD-generator. In the Report 2005 variants of RTL of flat conic form were considered (see Figures 3.62 and 3.63). It entailed greater diameters of RTL and greater weights of LNS.

The calculations of inductance and wave resistance of MITLs lead during present work have shown, that there is a possibility to increase the RTL conicity, making its electrodes in the form of two enclosed cones with internal and external ribs. A radius of RTL with ribs is only 0.5 meters at length approximately 2 meters. The picture of such electrodes is shown in a Figures 3.64 and 3.65. From the technological point of view the conic RTL with ribs possesses doubtless advantages in comparison with poorly conic form (see Figures 3.62 and 3.63). Flat lead electrodes in the conic RTL work under action of a body weight only on a stretching and do not test significant bending loadings. Therefore, the weight of block RTL+LNS, destroyed at explosion, can be essentially reduced.

3.6.2 . The Description and the General View of Z-POP Generator

Check, working off and optimization of parameters of full-scale installation ZP-3R should be carried out on installation "Z-Proof-of-Principle" (Z-PoP). As the matter of fact, the proposed Z-PoP generator is four-modular LTD-section of ZP-3R generator, which makes 1/30 part of full-scale ZP-3R generator. General scheme of Z-PoP and current collector from four LTD-modules are shown on Figure 3.66. All the elements, which are parts of LTD-section of ZP-3R installation, are presented in the scheme of

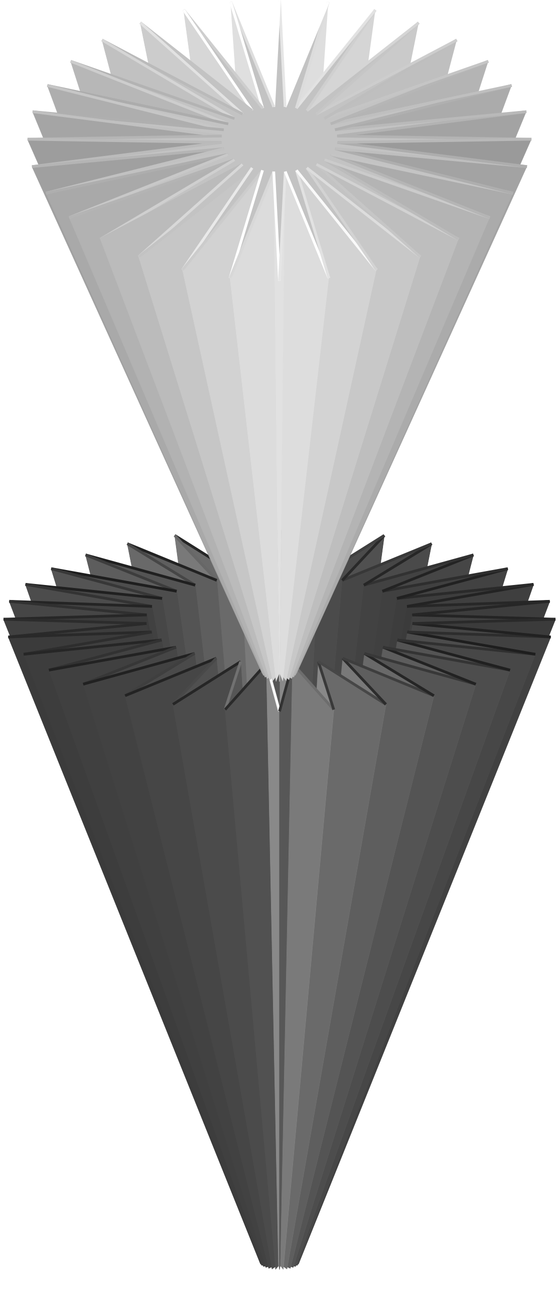

Figure 3.64. General view of the RTL electrodes in the form of cones with ribs (not the drawing). An internal cone is put up.

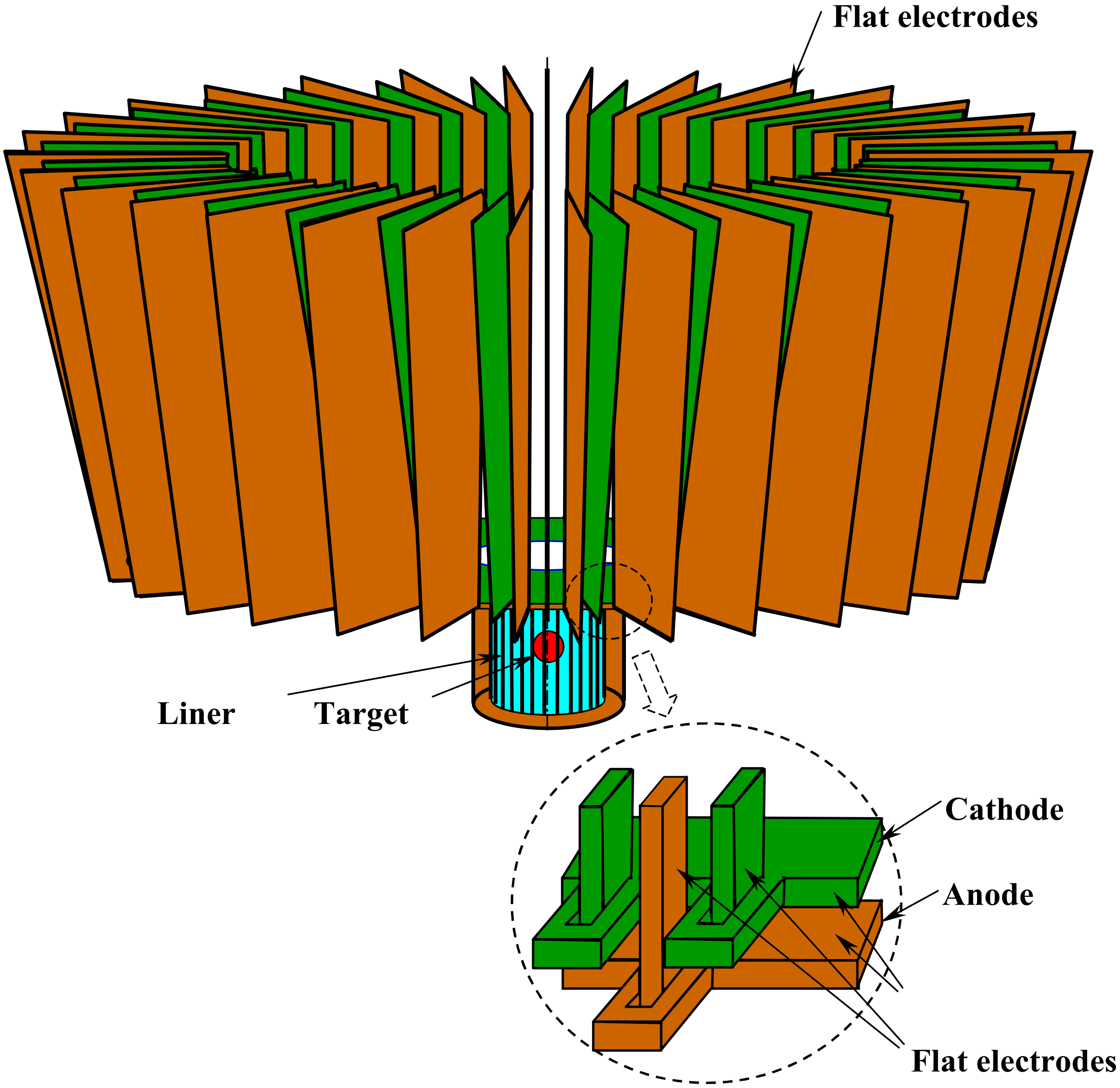

Figure 3.65. Variant of the RTL+target unit block (not the drawing)

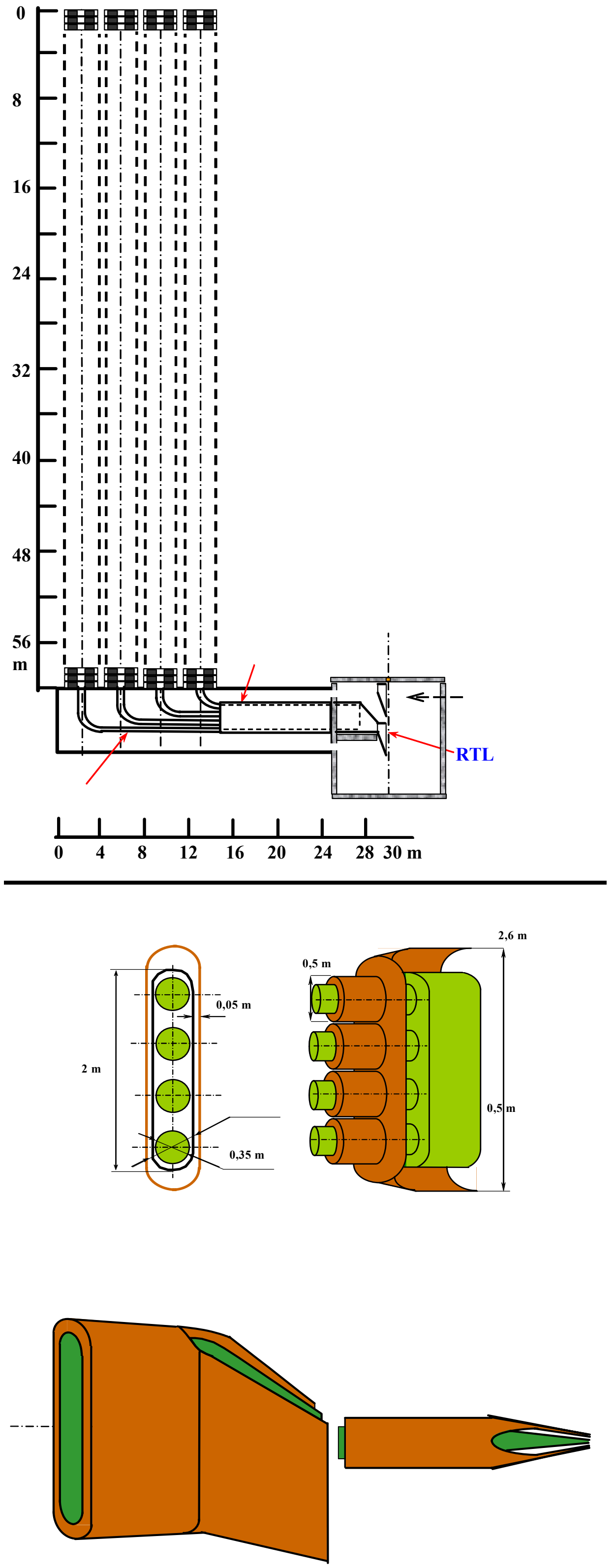

Fig. 3.66.The general conceptual scheme of the generator and some parts of ZP-3R installation.

Z-PoP generator. They are:
-4 LTD-modules located vertically and made of 240 LTD-cells everyone.
- LTD-cells with parameters:
- Amplitude of a voltage pulse 90 kV,
- Amplitude of the current 1÷1.2 MA,
- Width of the voltage pulse on the basis 150 ns,
- External diameter of the LTD-cell 3 m,
- Height of the LTD-cell 0.25 m,
- Diameter of an external electrode of a vacuum coaxial line of 0.5 m.
- 4 coaxial vacuum MITLs with wave resistance nearby 21 Ohm. They have diameter of the MITL external electrodes 0.5 m everyone, curved under a corner 90^0 and with radius of a bend about 2 m;
-Plainly-coaxial MITL with wave resistance 5 Ohm, the cross-section sizes of an external electrode being 2.5 m x 0.5 m and an interelectrode gap ~5 cm;
- A flat three-electrode MITL in the form of a trapeze beginning on radius of 2.5 m from load. The width of the line electrodes changes from 2 up to 0.5 m and an interelectrode gap changes from 5 up to 1.25 cm as approaching to the load;
- Model 1/30 part of RTL - flat three-electrode MITL with modeling physical load on the top.
Part of a plainly-coaxial MITL, stationary and replacing flat three-electrode MITL with modeling physical load on the top are positioned in a working vacuum chamber. The working chamber is not a breadboard model of ZP-3R reactor chamber. It is developed specially with the purpose of the decision of the problems put for "Z-PoP".

On an axis of the LTD-module it is positioned the internal electrode of a vacuum coaxial line, which diameter decreases in process of promotion from the first LTD-cell up to 240-th one. On an output of the LTD-module a diameter of the internal electrode should make nearby 35 cm. As a result of working off the LTD-cell scheme, its final parameters are to be defined, which would provide in the LTD-module a pulse with amplitude of a voltage 21 MV and a current 1 MA. During working off of the full scheme of one LTD-module, in process of increase in number of LTD-cells it is necessary to provide reliable synchronization of their start, because the full length of the LND-module makes about 60 m. It corresponds to time delay of an electric pulse from 1-st up to 240-th cells of ~200 nanoseconds.

The distance between axes of LTD-generators is of 3.5 m. It provides a backlash between cases of generators of 0.5 m, necessary for realization of repair work. For this reason time of start of four LTD-generators should be different, taking in account a time of distribution of an electric pulse in each vacuum coaxial MITL. Roughly time lengths of these lines differ on 13-14 nanoseconds.

As a result of Z-PoP program, the parameters of full-scale LTD-section of the generator of ZP-3R installation are to be finalized. It should be specified, in particular:
-The dimensions of four MITLs with a plainly coaxial MITL-current collector, which provide the best parameters of the pulse transportation through this place.

-The dimensions and the form of the flat three-electrode MITL, located in vacuum chamber, and also a design of sliding connection of replacing and stationary parts of these lines.
-way and the mechanism of disassembly and assembly of the generator and its parts replaced at repair.
-Methods and means of shielding of LTD-cell insulator from action of electronic leakage and from hard x-ray and gamma-radiation, arising at electron scattering in elements of LTD-module.

All these parameters can pass working off on the reduced models of generator Z-PoP with final check on the LTD-section, which is being of 1/30 part of full-scale ZP-3R generator

3.6.3 Conclusions

1. The analysis of possible variants of the multimodular LTD-generator of installation ZP-3R is lead. Problems of addition of currents and voltages in the multimodular LTD-generator are considered. On the basis of the analysis the new scheme of the LTD-generator of ZP-3R installation is offered.
2. The new scheme of the RTL configuration is given. According to the new scheme, RTL has electrodes in the form of two enclosed cones with internal and external ribs. The maximal radius of the conical RTL with ribs makes only 0.5 meters at length approximately 2 meters. From the technological point of view this RTL possesses doubtless advantages in comparison with the RTL of poorly conic form. Flat lead electrodes work under action of a body weight only on a stretching and do not expose significant bending loadings. At new RTL configuration the weight of RTL+LNZ block, destroyed at explosion, can be essentially reduced.
3. Three-dimensional calculations of neutron energy deposition in RTL block and in adjoining intrachamber units show, that the new RTL scheme allows reducing considerably weight of the local neutron shielding destroyed together with RTL at each explosion.
4. The scheme of installation Z-PoP is offered. Actually generator Z-PoP is four-modular LTD-section of ZP-3R generator, which makes 1/30 part of full-scale generator ZP-3R. In the scheme of Z-PoP generator all elements, which are the part of LTD-section of ZP-3R installation are presented. During working off of the scheme of Z-PoP generator parameters of full-scale LTD-section of ZP-3R generator should be certain and specified all.

4.0 Conclusions

Results of RTL and LTD research are reported here, that include: (1) The key physics issues for RTLs involve the power flow at the high linear current densities that occur near the target (up to 5 MA/cm). These issues include surface heating, melting, ablation, plasma formation, electron flow, magnetic insulation, conductivity changes, magnetic field diffusion changes, possible ion flow, and RTL mass motion. These issues were studied theoretically, computationally (with the ALEGRA and LSP codes), and experimentally (at the Kurchatov Institute, Moscow). Present results indicate that RTLs will work at 5 MA/cm or higher, with anode-cathode gaps as small as 2 mm. (2) An RTL misalignment sensitivity study has been performed using a 3D circuit model. Results show very small load current variations for significant RTL misalignments. (3) The key structural issues for RTLs involve optimizing the RTL strength (varying shape, ribs, etc.) while minimizing the RTL mass. Optimization studies show RTL mass reductions by factors of three or more. (4) Fabrication and pressure testing of Z-PoP (Proof-of-Principle) size RTLs were successfully reported here. (5) Modeling of the effect of initial RTL imperfections on the buckling pressure has been performed. Results show that the curved RTL offers a much greater buckling pressure as well as less sensitivity to imperfections than three other RTL designs. (6) Repetitive operation of a 0.5 MA, 100 kV, 100 ns, LTD cavity with gas purging between shots and automated operation was demonstrated at the SNL Z-IFE LTD laboratory with rep-rates up to 10.3 seconds between shots (this is essentially at the goal of 10 seconds for Z-IFE). (7) A single LTD switch at Tomsk was fired repetitively every 12 seconds for 36,000 shots with no failures. (8) Five 1.0 MA, 100 kV, 100 ns, LTD cavities have been combined into a voltage adder configuration with a test load to successfully study the system operation. (9) The combination of multiple LTD coaxial lines into a tri-plate transmission line was examined. The 3D Quicksilver code was used to study the electron flow losses produced near the magnetic nulls that occur where coax LTD lines are added together. (10) Circuit model codes were used to model the complete power flow circuit with an inductive isolator cavity. (11) LTD architectures were presented for drivers for Z-IFE and high yield. A 60 MA LTD driver and a 90 MA LTD driver were proposed.

All of the goals proposed for research on RTLs and LTDs in this FY06 LDRD have been exceeded:

Goal 1: Operate 0.5 MA LTD cavity at SNL repetitively at up to once every 25 seconds for 1000 shots or more.

Results: At SNL, this 0.5 MA cavity has been fired in repetitive mode for ~3000 shots; the last set of 50 shots with one shot every 10.25 seconds (~0.1 Hz) - we are already at the desired goal of 0.1 Hz for Z-IFE. At HCEI, Tomsk, a single switch has been fired 37,000 shots with one shot every 12 seconds (~0.08 Hz)

Goal 2: Combine four SNL LTD 1.0 MA cavities at HCEI, Tomsk, Russia to produce a 400 kV, 1 MA pulse to a load.

Results: Five 1 MA LTD cavities (four belong to SNL and one belongs to U. Michigan) have been successfully tested in a voltage-adder configuration at HCEI, Tomsk.

Goal 3: Perform detailed study of the power flow in an RTL near the load at high linear current densities (up to 5 MA/cm).

Results: Analytic results, code simulation results (LSP and other codes), and experiments have been used to study power flow at high linear current densities above 5 MA/cm.

Goal 4: Propose LTD architectures for drivers for high yield and for IFE.

Results: Two LTD architectures have been proposed: A 60 MA LTD driver with one layer of LTDs, and a 90 MA LTD driver with multiple layers of LTDs.

Goal 5: Develop and use circuit model codes and particle-in-cell codes to study power flow from the LTD driver, to the intermediate adder/transmission lines, to the RTL, to the load.

Results: Quicksilver simulations have been used to study electron losses at the magnetic nulls that occur where LTD driven coax lines add together at the entrance to a flat tri-plate transmission line. Circuit codes have been used to assess the complete circuit operation (driver, RTL, load).

Present results from all of these power flow studies validate the whole LTD/RTL concept for single-shot ICF high yield, and for repetitive-shot IFE.

References

1. C. L. Olson, “Z-Pinch Inertial Fusion Energy,” in Landholt-Boernstein Handbook on Energy Technologies (Editor in chief; W. Martienssen), Volume VIII/3, Fusion Technologies (Edited by K. Heinloth), Springer-Verlag (Berlin-Heidelberg), 495 (2005). [Includes an extensive list of references.]
2. "Z-Pinch IFE Program: Final Report for FY04," Sandia National Laboratories SAND-2005-2742P (856 pages) CD (2005). Contact clolson@sandia.gov.
3. "Z-Pinch IFE Program: Final Report for FY05," Sandia National Laboratories SAND-2006-7399P (1037 pages) CD (2006). Contact clolson@sandia.gov.
4. "Z-Pinch IFE Program: Final Report for FY06," Sandia National Laboratories SAND-2007-0419P (1032 pages) CD (2007). Contact clolson@sandia.gov.
5. S. A. Slutz, C. L. Olson, and P. Peterson, Phys. Plasmas **10**, 429 (2003).
6. This section includes portions of the NRL FY06 Z-IFE final report, which is included in its entirety in Ref. 4.
7. C. L. Olson, "Overview of RTL Research," in Ref. 2, p. 29.
8. J. P. VanDevender, “Long Self-Magnetically Insulated Power Transport Experiments,” J. Appl. Phys. **50**, 3928-3934 (1979).
9. A.W. Hull, “The Effect of a Uniform Magnetic Field on the Motion of Electrons Between Coaxial Cylinders,” Phys. Rev **18**, 31-57 (1921).
10. F. Winterberg, “The Possibility of Producing a Dense Thermonuclear Plasma by an Intense Field Emission Discharge,” Phys. Rev. **174**, 212-220 (1968).
11. A. Ron, A.A. Mondelli, and N. Rostoker, “Equilibria for Magnetic Insulation,” IEEE Trans. Plasma Sci. **1**, 85-92 (1973).

12. R.V. Lovelace and E. Ott, "Theory of Magnetic Insulation," Phys. Fluids **17**, 1263-1268 (1974).
13. J.M. Creedon, "Relativistic Brillouin Flow in the High ν/γ Diode," J. Appl. Phys. **46**, 2946-2955 (1975).
14. M.S. DiCapua, "Magnetic Insulation," IEEE Trans. Plasma Sci. **11**, 205-215 (1983).
15. D. Smith, "RTL Circuit Model. RTL Inductance Curves," in Ref. 2, p. 209 (2004).
16. C.W. Mendel, "Planar One-Dimensional Magnetically Insulated Electron Flow for Arbitrary Canonical-Momentum Distribution," J. Appl. Phys. **50**, 3830-3837 (1979).
17. C.W. Mendel, D.B. Seidel, and S.E. Rosenthal, "A Simple Theory of Magnetic Insulation from Basic Physical Considerations," Laser and Part. Beams **1**, 311-320 (1983).
18. C.W. Mendel, D.B. Seidel, and S.A. Slutz, "A General Theory of Magnetically Insulated Electron Flow," Phys. Fluids **26**, 3628-3635 (1983).
19. P.A. Miller and C.W. Mendel, "Analytic Model of Applied-B Ion Diode Impedance Behavior," J. Appl. Phys. **61**, 529-539 (1987).
20. C.W. Mendel, M.E. Savage, D.M. Zagar, W.W. Simpson, T.W. Grasser, and J.P. Quintenz, "Experiments on a Current-Toggled Plasma-Opening Switch," Appl. Phys. **71**, 3731-3746 (1992).
21. S.E. Rosenthal, "Characterization of Electron Flow in Negative- and Positive-Polarity Linear-Induction Accelerators," IEEE Trans. Plasma Sci. **19**, 822-830 (1991).
22. C.W. Mendel, and S.E. Rosenthal, "Modeling Magnetically Insulated Devices Using Flow Impedance," Phys. Plasmas **2**, 1332-1342 (1995).
23. C.W. Mendel, and S.E. Rosenthal, "Dynamic Modeling of Magnetically Insulated Transmission Line Systems," Phys. Plasmas **3**, 4207-4219 (1996).
24. P.F. Ottinger and J.W. Schumer, "Rescaling of Equilibrium Magnetically Insulated Flow Theory Based on Particle-in-Cell Simulations," Phys. Plasmas **13**, 063109 (2006).
25. R.A. Vessey, T.D. Pointon, M.E. Cuneo, T.A. Mehlhorn, J.E. Bailey, D.J. Johnson, and W.A. Stygar, "Electron-Anode Interactions in Particle-In-Cell Simulations," Phys. Plasmas **6**, 3369 (1999).
26. D.W. Swain, S.A. Goldstein, J.G. Kelly, and G.R. Hadley, "Observation of Anode Ions Associated with Pinching in a Relativistic Electron Beam Diode," J. Appl. Phys. **46**, 4604 (1975).
27. J.G. Kelly, S.A. Goldstein, and D.W. Swain, Influence of Anode Composition on Electrical Properties of Relativistic Electron-Beam Diodes," J. Appl. Phys. **46**, 4726 (1975).
28. A.E. Blaugrund, G. Cooperstein, and S.A. Goldstein, "Relativistic Electron Beam Pinch Formation Processes in Low Impedance Diodes," Phys. Fluids **20**, 1185 (1977).
29. G.M. McCracken, R.S. Barton, and W. Dillon, Nuovo Cimento, "Electron-Induced Desorption of Gas from Stainless-Steel Surfaces," Suppl. **5**, 146 (1967).
30. T.W.L. Sanford, J.A. Halbleib, J.W. Poukey, A.L. Pregenzer, R.C. Pate, C.E. Heath, R. Mock, G.A. Mastin, D.C. Ghiglia, T.J. Roemer, P.W. Spence, and G.A. Proulx, "Measurement of Electron Energy Deposition Necessary to Form an Anode Plasma Ta, Ti and C for Coaxial Bremsstrahlung Diodes," J. Appl. Phys. **66**, 10 (1989).

31. L.E. Aranchuk, E.I. Baranchikov, A.V. Gordeev, V.V. Zazhivikhin, V.D. Korolev, and V.P. Smirnov, Magnetically Self-Insulated Lines with Ion Leaks," Zh. Tekh. Fiz. **59**, 142, (1989) [Sov. Phys. Tech. Phys. **34**, 215 (1989)].
32. T.D. Pointon, W.A. Stygar, R.B. Spielman, H.C. Ives, and K.W. Struve, "Particle-in-Cell Simulations of Electron Flow in the Post-Hole Convolute of the Z-Accelerator," Phys. Plasmas **8**, 4534 (2001).
33. P.F. Ottinger and J.W. Schumer, "Magnetically Insulated Ion Flow Theory," Phys. Plasmas 13, 063101 (2006).
34. P.F. Ottinger and J.W. Schumer, "RTL Power Flow Analysis," in Ref. 2, p. 71.
35. V.L. Bailey, P.A. Corcoran, D.L. Johnson, I.D. Smith, J.E. Maenchen, K.D. Hahn, I. Molina, D.C. Rovang, S. Portillo, E.A. Puet, B.V. Oliver, D.V. Rose, D.R. Welch, D.W. Droemer, and T. L. Guy, "Re-Trapping of Vacuum Electron Current in Magntically Insulated Transmission Lines," Proceedings of the 15th International Conference on High Power Particle Beams (St. Petersburg, Russia, July, 2004).
36. J.W. Schumer, P.F. Ottinger, C.L. Olson, "Power Flow in a Magnetically Insulated Recyclable Transmission Line for a Z-Pinch-Driven Inertial-Confinement Fusion Energy System," IEEE Transaction on Plasma Science **34** (2006).
37. LSP is a software product of ATK Mission Research, Albuquerque, NM 87110.
38. D.R. Welch, D.V. Rose, B.V. Oliver, and R.E. Clark, "Simulation Techniques for Heavy Ion Fusion Chamber Transport," Nucl. Instrum. Methods Phys. Res. A **464**, 134-139 (2001).
39. "BERTHA - A Versatile Transmission Line and Circuit Code," D.D. Hinshelwood, NRL Memorandum Report 5185 (Nov. 1983).
40. This section includes portions of the VOSS Scientific FY06 Z-IFE final report, which is included in its entirety in Ref. 4.
41. W. A. Stygar, et al., "X-Ray Emission from Z-Pinches at 10^7 A; Current Scaling, Gap Closure, and Shot-to-Shot Fluctuations," Phys. Rev. E **69**, 046403 (2004).
42. D. V. Rose and D. R. Welch, "Power Flow Studies for Z-Pinch Targets," in Ref. 3, p. 24 (2005).
43. T. P. Hughes, S. S. Yu, and R. E. Clark, *Phys. Rev. ST-AB* **2**, 110401 (1999).
44. D.W. Hewitt and A.B. Langdon, *J. Comp. Phys.* **72**, 121 (1987.)
45. D. R. Welch, D. V. Rose, M. E. Cuneo, R. B. Campbell, and T. A. Mehlhorn, Phys. Plasmas **13**, 063105 (2006).
46. N. Bruner, T. C. Genoni, D. V. Rose, B. V. Oliver, and D. R. Welch, in Ref. 3, p. 30 (2005).
47. This section includes portions of the Kurchatov FY06 Z-IFE final report, which is included in its entirety in Ref. 4.
48. Z. A. Al'bikov, E. P. Velikov, A. I. Veretennikov, et al., Soviet Atomic Energy **35**, 34 (1990); translated from At. Energ. **68**, no. 1, 26 (1990).
49. G. M. Oleinik, Instruments and Experimental Techniques **43**, no. 3, 328 (2000); translated from Prib. Tekh. Eksp, no. 3, 49 (2000).
50. This section includes portions of the U.Wisconsin FY06 Z-IFE final report, which is included in its entirety in Ref. 4.
51. B. Wilson and D. C. Kammer, "Optimization of Recyclable Transmission Line Concepts for Z-Pinch Fusion Reactor," in Ref. 3, 140 (2005).

52. M.G. Mazarakis, R.B. Spielman, " A Compact, High-Voltage E-Beam Pulser." in Proc. 12th IEEE Pulsed Power Conference, Monterey, California, July 1999. IEEE # 99CH36358 1999, p. 412-415 (1999).
53. A.A. Kim, A.N. Bastricov, S.N. Volkov, V.G. Durakov, B.M. Kovalchuk, V.A. Sinebryuukkov, " 100 GW Fast LTD Stage." in Proc. 13th International Symposium on High Current Electronics IHCE SB RAS, 2004, p. 141-144 (2004).
54. M.G.Mazarakis, W.E. Fowler, F.W.Long, D.H. McDaniel, C.L. Olson, S.T. Rogowski, R.A. Sharpe, K.W. Struve, " High Current Fast 100-ns LTD Driver Development in Sandia Laboratory" in Proc. 15th IEEE Pulsed Power Conference, Monterey, California, June 2005.
55. S.T. Rogowski, W.E. Fowler, M.G. Mazarakis, C.L. Olson, D.H. McDaniel, K.W. Struve, " Operation and Performance of the First High Current LTD at Sandia National Laboratories." in Proc. 15th IEEE Pulsed Power Conference, Monterey, California, June 2005.
56. LabView Manual (National Instruments) info@ni.com.
57. A.A. Kim, LTDZ report for Task 5-1 AK (Private Communication) Tomsk, Russia, May 2006.
58. M.G.Mazarakis, W.E. Fowler, D.H. McDaniel, A.A. Kim, C.L. Olson, S.T. Rogowski, R.A. Sharpe, K.W. Struve, "A Rep-rated 100ns LTD Driver for Z-pinch Inercial Confinement Fusion (ICF) and Inertial Fusion Energy (IFE) " (invited) in Proc. 14th International Symposium on High Current Electronics, IHCE SB RAS, 2006, p. 226-231.
59. T. D. Pointon, M. G. Mazarakis, and D. B. Seidel, "Power Flow from the Coaxial Lines to the RTL", in Ref. 3, p. 237 (2005).
60. J. P. Quintenz, D. B. Seidel, *et al.* "Simulation codes for light-ion diode modeling," Lasers and Particle Beams **12**, 283 (1994).
61. C. W. Mendel, Jr., T. D. Pointon, *et al.* "Losses at magnetic nulls in pulsed-power transmission line systems," Physics of Plasmas **13**, 043105 (2006).

Distribution

2 Naval Research Laboratory
Code 6771
4555 Overlook Ave. SW
Washington, DC 20375
Attn: Paul Ottinger
Joe Schumer

1 Gerry Cooperstein
Code 6770
4555 Overlook Ave. SW
Washington, DC 20375

1 John Sethian
Naval Research Laboratory
Code 6733
4555 Overlook Ave. SW
Washington, DC 20375

1 Steve Obenschain
Naval Research Laboratory
Code 6730
4555 Overlook Ave. SW
Washington, DC 20375

5 VOSS Scientific
418 Washington SE
Albuquerque, NM 87108
Attn: Dale Welch
David Rose
Tom Genoni
Nicki Bruner
C. Thoma

1 Mark E. Barkey
Aerospace Engineering and Mechanics, Box 870280
University of Alabama
Tuscaloosa, Alabama 35487-0280

1 Gerald L. Kulcinski
Associate Dean for Research
College of Engineering
University of Wisconsin - Madison
1415 Engineering Dr., Suite 2630B
Madison, WI 53706 - 1691

5 Fusion Technology Institute
University of Wisconsin - Madison
Madison, WI 53706
Attn: Dan Kammer
Michael Guthrie
Laila El-Guebaly
Mohamed Sawan
Mark Anderson

4 Kurchatov Institute
Russian Research Center
RRC KI
Kurchatov Square
123182 Moscow, Russia
Attn: Valentin Smirnov
Alexander Kingsep
S. L. Nedoseev
Yu. G. Kalinin

1 Alexander Kim
High Current Electronics Institute
Academichesky Ave. 4
634055 Tomsk, Russia

3 Lawrence Livermore National Laboratory
P. O. Box 808, L-641
Livermore, CA 94550
Attn: Wayne Meier
Jeff Latkowski
Ralph Moir

2 University of California, Los Angeles
44-114 Engineering 4
Los Angeles, CA 90095
Attn: Mohamed Abdou
Alice Ying

1 John De Groot
University of California, Davis
Davis, CA 95616

2 Lawrence Berkeley National Laboratory
1 Cyclotron Road, MS-47R0112
Berkeley, CA 94720
Attn: Grant Logan
Will Waldron

1 David Hammer
Cornell University
Upson Hall, Room 369
Ithica, NY 14853

1 Thomas G. Finn
NNSA
U. S. Department of Energy
FORS, NA-161
Washington, DC

1 Joseph Kindel
NNSA
U. S. Department of Energy
FORS, NA-16
Washington, DC

1 Christopher Deeney
NNSA
U. S. Department of Energy
FORS, NA-11
Washington, DC

1 Christopher Keane
NNSA
U. S. Department of Energy
FORS, NA-16
Washington, DC

2 U. S. Department of Energy
GTN, SC-24.2
Washington, DC
Attn: Francis Thio
Gene R. Nardella

1 Ehsan Khan
U. S. Department of Energy
SC-5/Forrestal Building
1000 Independence Ave.
Washington, DC 20585

1 Al Trivelpiece
14 Wade Hampton Trail
Henderson, NV 89052-6635

1 Barret Rippin
U. S. Department of State
OES-STC
Washington, DC20522

1 Steve Dean
Fusion Power Associates
2 Professional Dr. Suite 24B
Gaithersburg, MD 20879

1 Wil Gauster
2 Templeton Ct.
Avon, CT. 06001-3950

1	MS0101	Thomas Hunter, 00001
1	MS0116	Al Romig, 00004
1	MS0125	Pace VanDevender, 12101
1	MS0513	Rick Stulen, 01000
1	MS0724	Les Shephard, 06000
1	MS0727	Tom Sanders, 06020
1	MS0736	John Kelly, 06770
1	MS0736	Mary Ann Walck, 06760
1	MS0748	Matt Turgeon, 06764
1	MS0748	Ben Cipiti, 06763
1	MS0748	Jason Cook, 06763
1	MS0748	Charlie Morrow, 06763
1	MS0748	Gary Rochau, 06763
1	MS0771	Dennis Berry, 06800
1	MS0839	Gerry Yonas, 07000
1	MS1129	Richard Nygren, 01658
1	MS1129	Mike Ulrickson, 01658
1	MS1129	Dennis Youchison, 01658
1	MS1136	Paul Pickard, 06771
1	MS1152	W. L. Langston, 01652
1	MS1152	Tim Pointon, 01652
1	MS1152	Mark Keifer, 01652
1	MS1178	David L. Smith, 01639
1	MS1178	Finus Long, 01637
1	MS1178	Randy McKee, 01639
1	MS1178	Doug Bloomquist, 01630
1	MS1181	Tom Mehlhorn, 01640
1	MS1181	Larry Schneider, 01650
1	MS1182	Tim Renk, 05445
1	MS1186	Stephen Slutz, 01674
1	MS1190	Keith Matzen, 01600
15	MS1190	Craig Olson, 01600
1	MS1190	Dillon McDaniel, 01600

1	MS1191	John Porter, 01670
1	MS1193	Michael Cuneo, 01673
10	MS1194	Michael Mazarakis, 01644
1	MS1194	Bill Fowler, 01644
1	MS1194	Robin Sharpe, 01644
1	MS1196	William Stygar, 01677
1	MS1196	Tom Sanford, 01677
1	MS1196	Richard Olson, 01677

2	MS9018	Central Technical Files, 08944
2	MS0899	Technical Library, 04536
1	MS0123	Donna Chavez, 01011